Large Scale Flow Characteristics of Multiple Annular Impinging Jets within a Cylindrical Chamber

Shen Long

Thesis submitted for the degree of Doctor of Philosophy
School of Mechanical Engineering
Faculty of Engineering, Computer & Mathematical Sciences
The University of Adelaide, South Australia

January 2019

Declaration

I, Shen Long, certify that this work contains no material which has been accepted for the award of any other degree or diploma in my name, in any university or other tertiary institution and, to the best of my knowledge and belief, contains no material previously published or written by another person, except where due reference has been made in the text. In addition, I certify that no part of this work will, in the future, be used in a submission in my name, for any other degree or diploma in any university or other tertiary institution without the prior approval of The University of Adelaide and where applicable, any partner institution responsible for the joint-award of this degree.

I acknowledge that copyright of published works contained within this thesis resides with the copyright holder(s) of those works.

I also give permission for the digital version of my thesis to be made available on the web, via the University's digital research repository, the Library Search and also through web search engines, unless permission has been granted by the University to restrict access for a period of time.

I acknowledge the support I have received for my research through the provision of an Australian Government Research Training Program Scholarship.

24/01/2019

Shen Long

Date

Acknowledgement

I would like to gratefully acknowledge all of the people who have helped me in my journey towards finishing this thesis.

Firstly, I would like to express my most sincere gratitude to my supervisors Professor Graham ‘Gus’ Nathan, Professor Bassam Dally and Dr Zhao Feng Tian for providing me great support in different ways.

Thanks to my principal supervisor Professor Gus Nathan for his thorough feedback and full attention on all of my PhD work, which has significantly improved my research and technical writing skills. His motivation and enthusiasm for scientific research has deeply influenced my life attitude and will continuously inspire my life in the future. I will remember his “keep up the good work” and keep up all of my good work.

Thanks to my co-supervisor Professor Bassam Dally for guiding all of my PhD work during the first six months of my candidature, as well as for his strong support to all of my papers and experiments. My experimental work would be delayed for another half year without his helpful advice.

Thanks to my co-supervisor Dr Zhao Feng Tian for his continuous support during my entire candidature. His knowledge and experience in CFD, as well as his life attitude, have significantly helped me overcome difficulties during my PhD life. I would not choose to start this journey without his guidance.

Besides my supervisors, I would also like to thank Dr Alfonso Chinnici for his great support and guidance in numerical modelling and experimental design, and to Dr Timothy Lau for patiently teaching me the PIV technique, guiding my experimental study and reviewing my papers. My PhD would not be finished on time without their kind help.

A special thank you to my landlord in Adelaide: Mr Chan Fui Yap and Ms Yen Yen Chow, and their three cute children Charlene, Serene and Rylan (the fourth one is coming!). Thanks for providing me with a real home in Adelaide since 2012. Their thoughtful kindness supports me to finish my undergraduate and PhD degrees.

In addition, I would like to give my thanks to my officemates Dr Kae Ken Foo, Dr Orddom Leav, Dr Dominic Davis, Dr Eshodarar Sureshkumar, Dr Francesco Larizza, Dr Sammuel Sobey, Dr David Haydon, Dr Amy Lewis, and to my schoolmates Dr Xiao Chen, Dr Houzhi Wang, for their company and friendship. I would also like to acknowledge the financial support from the Australian Government Research Training Program and Professor Gus Nathan through the Linkage Grant.

Finally, I would like to send my sincere thanks to my parents Mr Long Guofu and Ms Wang Yun for their priceless love and unconditional support. I cannot finish my PhD degree without them.

Abstract

The thesis presents a systematic study of the flow structure within a cylindrical chamber generated by multiple isothermal jets, under conditions relevant to a wide range of practical applications, including confined swirl combustors, ventilation systems and concentrated solar thermal devices. The system comprises a symmetric arrangement of four jets with a tangential component relevant to the Hybrid Solar Receiver Combustor (HSRC) under development at the University of Adelaide. The geometrical configuration of the HSRC is simplified here to a cylindrical cavity with four inlet jets (representing four burners), which are configured in an annular arrangement and aligned at an inclination angle to the axis with a tangential component to generate a swirl in the chamber. The use of a simple jet configuration also makes these results relevant to more complex burner arrangements, such as those comprising a central fuel jet and a co-annular air jet, by considering the total momentum associated with the combined jet. However, the greater complexity of multiple-jets over the single round jet issuing into a quiescent environment, including the additional parameters and experimental challenges, means many gaps in understanding remain. Hence, this thesis presents a detailed characterisation of the flow velocity within a Multiple Impinging Jets in a Cylindrical Chamber (MIJCC) that has geometrical relevance to the HSRC.

A joint experimental and numerical methodology was used to characterise the large-scale flow field within the MIJCC configurations, under fully turbulent flow condition with a constant nozzle Reynolds number of Re_D = 10500. A range of MIJCC devices was manufactured from acrylic and fully submerged into a water tank to provide laser access and minimise optical distortion. Particle image velocimetry was used to measure the instantaneous velocity field within the experimental MIJCC configurations, while the numerical modelling employed Reynolds-Averaged Navier-Stokes methods to provide qualitative information of the flow field in the region of the flow for which experimental data were not available.

The annular arrangement of multiple-jets was found to form a resulting jet flow downstream from the jet merging point, while the location of this point depends strongly on jet angles. The flow-field reveals strong similarity to single free and swirling jet flows downstream from the merging point, but retains significant differences upstream from this point. The key controlling parameters of multiple annular impinging jets (i.e., jet angles, number of jets and geometrical aspect ratio) were found to significantly influence the mean and turbulent velocity fields, the position and strength of the external and central recirculation zones, and also the degree of flow unsteadiness within the MIJCC configurations. In addition, the dependence of the key qualitative flow features on these controlling parameters was analysed by presenting the corresponding flow regime maps, while configurations of greatest relevance to solar thermal environments and combustion regimes were proposed. The key results and findings of the present study have been presented in four peer review papers, which have been published by the journal of “Physics of Fluids”.

Contents

List of Figures

List of Tables

Nomenclature

CST	Concentrating Solar Thermal
HSRC	Hybrid Solar Receiver Combustor
SC	Secondary Concentrator
CFD	Computational Fluid Dynamics
PIV	Particle Image Velocimetry
ERZ	External Recirculation Zone
CRZ	Central Recirculation Zone
PVC	Precessing Vortex Core
D_{th}	Throat diameter
D_c	Chamber diameter
D_{sc}	Diameter of the Secondary Concentrator
D_{pipe}	Inlet pipe diameter
L_{pipe}	Inlet pipe length
L_c	Chamber length
W_{out}	Width of the outlet gap
α_j	Jet inclination angle
θ_j	Jet azimuthal angle
γ_{sc}	Angle of the Secondary Concentrator
N_j	Jet number
Re_D	Inlet jet Reynolds number
U_e	Bulk mean velocity at the nozzle exit
$\dot{m}_{th}$	Mass flow rate through the throat
$\dot{m}_{in}$	Total inlet mass flow rate
L_{core}	Recirculation core length

P_i	Jet impingement point
P_{mer}	Jet merging point
P_s	Stagnation point
P_c	Jet combined point
K_v	Recirculation rate
r_{core}	Vortex core displacement

Chapter 1

1 Introduction

1.1 Multiple interacting jets within a confined space

Unlike the simple round jet issuing into a quiescent environment, which has received significant attention [1-5], the flow-field generated by multiple interacting jets within a confined space is still poorly understood. Nevertheless, these configurations have wide relevance to many engineering applications. For example, the aerodynamic curtains generated by multiple-jets has been used to mitigate the escape of high-temperature gases from cavities [6]. The annular jets employed in several types of gas turbine engines lead to high mixing between fuel and air [7]. Also, multiple jets are generated by multiple-fan systems for the ventilation of tunnels, in aircraft cabins and car parks to supply fresh air into confined environments [8]. In addition, combustors featuring the injection systems for multiple-burners combustors have shown the potential to reduce NOx emissions [9]. One of the applications of multiple interacting jets is for solar thermal systems utilising the Concentrated Solar Thermal (CST), which has received particular interest within the context of renewable energy.

1.2 The integration of concentrated solar thermal and combustion

In recent years, there is a growing interest in CST because it offers opportunities to generate energy at high temperatures, to allow the storage of thermal energy and to allow hybridisation with combustion devices [10]. Nevertheless, the intermittent nature of the solar source is a barrier to the penetration of solar energy technology and the cost of heliostats is high. Therefore, the overall cost of CST remains significantly higher than that of conventional energy technologies [11, 12]. In contrast to the CST, the combustion of fuels offers high availability. In the near term, fossil fuels have low cost but high emissions of CO_2 and other pollutants [13]. Thus, the complementary nature of these two thermal energy sources means that their integration is gaining interest globally [14, 15]. However, while a number of hybrid systems have been proposed to date [16], the combination of a solar cavity receiver and a combustion chamber is yet to be fully investigated. Hence there is a need to assess the conditions under which solar and combustion energy sources are integrated into a single device.

1.3 Hybrid Solar Receiver Combustor

Of particular interest here is a multiple-jets configuration featuring a symmetric arrangement of jets with a tangential velocity component relevant to the Hybrid Solar Receiver Combustor (HSRC) under development at the University of Adelaide [17-23]. The HSRC devices offer potential to reduce both the energy losses and total infrastructure requirements relative to a hybrid from stand-alone components, while providing a firm supply of energy for heat and power applications [24]. Figure 1.1 presents the schematic diagram of an HSRC configuration. It features a cavity operable as a combustion chamber, an aperture to admit concentrated solar radiation into the chamber, multiple burners to direct a flame into the chamber and a heat exchanger within it to absorb the heat from both energy sources.

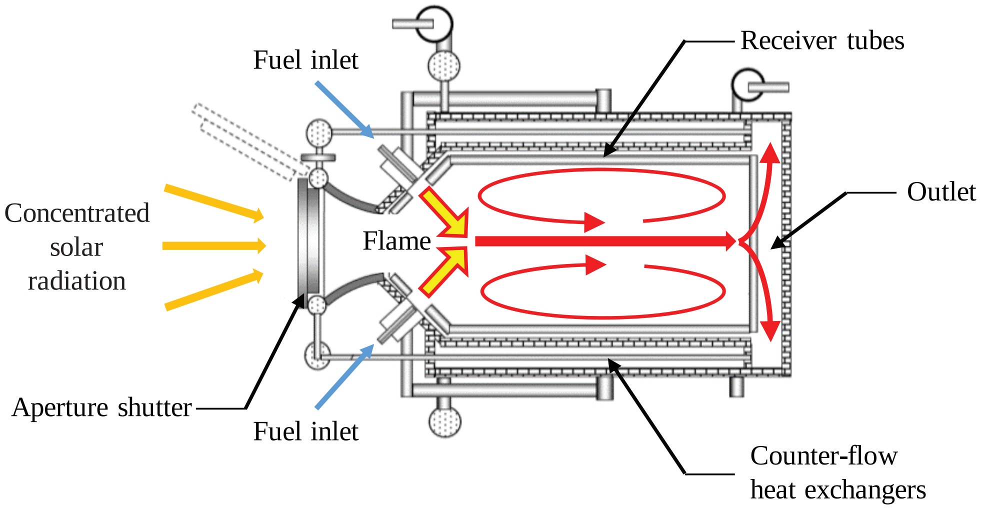

Figure 1.1: Schematic diagram of a Hybrid Solar Receiver Combustor (HSRC). Adapted from Nathan et al. [17].

Figure 1.2 presents the schematic diagram of a CST tower system, including a configuration of the HSRC, a heliostat field and a solar tower. The HSRC design allows the device to operate in any of three operational modes, namely, the “combustion only mode”, the “solar only mode” and the “mixed mode” [17]. For the “solar only mode”, the shutter of the secondary concentrator (SC) is open to allow the entrance of concentrated solar radiation, while the only heat source for the HSRC is solar energy. For the “combustion only mode”, the heat source is derived only from the burning of injected fuel and the shutter is closed. In the “mixed mode”, the power of the HSRC is derived from both solar energy and combustion, with the percentage of each being dependent on the solar intensity available at the time. The configuration of the combustion system in a solar cavity differs from that in a conventional combustor owing to the need to incorporate the aperture. This design results in an annular ring of burners, which can be configured in a symmetric arrangement and aligned at an inclination angle (α_j) relative to the axis of the chamber, and/or at an azimuthal angle (θ_j) to the axis of the burner.

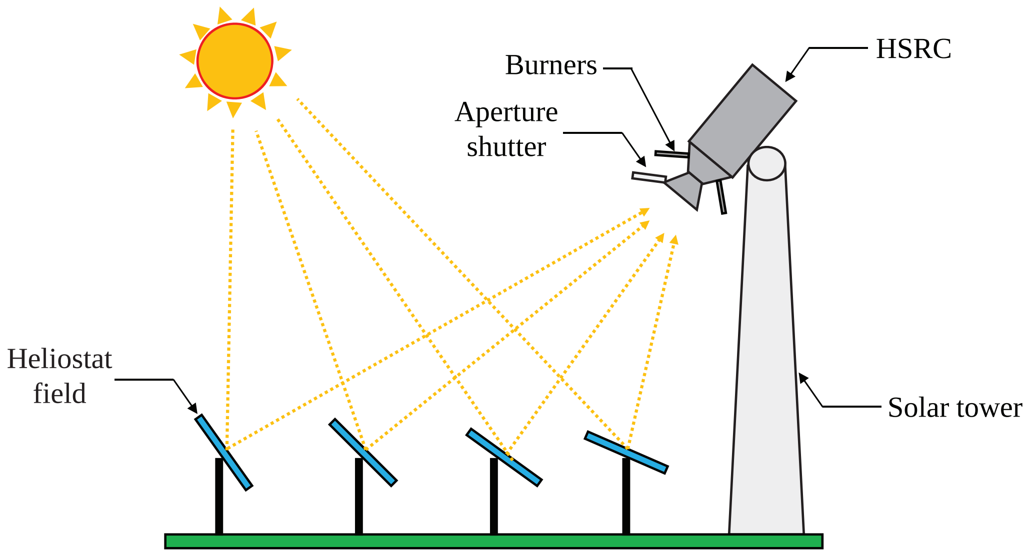

Figure 1.2: Schematic diagram of a Concentrated Solar Thermal (CST) system, showing an HSRC configuration on the top of a solar tower, together with the heliostat field. Adapted from Nathan et al. [17] .

Due to the annular arrangement of burners and the range of operational modes, it can be expected that different flow regimes, flame structures and dominant heat transfer mechanisms will occur inside the chamber depending on the mode of operation. Ideally, the optimised flow patterns would lead to an enhanced mixing while preventing fluid to escape through the aperture plane. A larger flow through the aperture would lead to a larger convective heat loss in the mixed mode of operation. Also, an optimised flow-field would be characterised by a reduced in-flow since this would alter the equivalence ratio of the flame, and therefore alter the heat transfer, fuel conversion and pollutant emissions. Nevertheless, the existing literature does not identify a suitable range of the operation angle (both α_j and θ_j) for preventing the escape of hot gases through the aperture to the secondary concentrator. Therefore, a better understanding of the flow-field generated by multiple-jets within a confined space (e.g., a cavity or chamber) is needed to allow the details of the possible HSRC configurations to be optimised.

The HSRC features multiple-jets of relevance to a wide range of CST applications, including solar-enhanced vortex gasifiers [25], solid particle solar receivers [26] and solar chemical reactors [27]. However, to my knowledge, there is no quantitative assessment that is available of the desirable flow regimes for optimizing the entrainment rates, flow instability and recirculation zones of the CST devices. Hence new data and information of the flow-field generated by multiple-jets within a cylindrical chamber are also required to develop the reliable design tools for engineers to optimise the relevant CST and hybrid combustion configurations for low-cost manufacture.

1.4 Controlling parameters of multiple confined jets

The greater complexity of the multiple-jets configurations over the single jet issuing into a quiescent environment [28], including the additional parameters and experimental challenges (e.g., jet angles [29], the extent of confinement by walls [30] and flow conditions [31]), means many gaps in understanding remain. Hence, it is important to characterise the influence of the key controlling parameters on the large-scale flow field generated by multiple-jets within a confined space or chamber.

1.4.1 Jet angles

The definition of jet angles (i.e., nozzle angles) that are used in the present study is presented schematically in Figure 1.3. The inclination (α_j) and azimuthal angles (θ_j) have been widely used to define the angular displacement between multiple inlet pipes or nozzles. The inclination angle (α_j) refers to the angle between the axis of the pipe and the enclosure, while the azimuthal angle (θ_j) refers to the relative angle from the pipe axis to the enclosure radius. The arrangement for which $\alpha_j > 0^\circ$ and $\theta_j = 0^\circ$ is termed "planar-symmetric" (Figure 1.3a), and has wide relevance to devices such as multiple-burners combustors [32] and longitudinal ventilation systems [8]. The arrangement of "rotationally-symmetric" jets is defined as having both $\alpha_j > 0^\circ$ and $\theta_j > 0^\circ$ (Figure 1.3b), and is commonly used for vortex and cyclone reactors [33]. However, although the angle of inlet-jets tends to be important for engineering applications of multiple-jets such as the HSRC, a comprehensive understanding of the influence of jet angles on the internal flow-field generated by multiple jets confined in an axisymmetric chamber is yet to be reported. That is, the existing knowledge provides an insufficient guideline for engineers to design an optimised operation angle of burners that can not only generate a large and uniform recirculation zone within a chamber, but also minimise the flow instability caused by the interaction of multiple-jets. Hence, there is a need to characterise for the first time all of the flow regimes that can be generated within a cylindrical chamber (i.e., as a confined flow) with multiple inlet-jets of arbitrary angles (α_j and θ_j) that are equal for all jets.

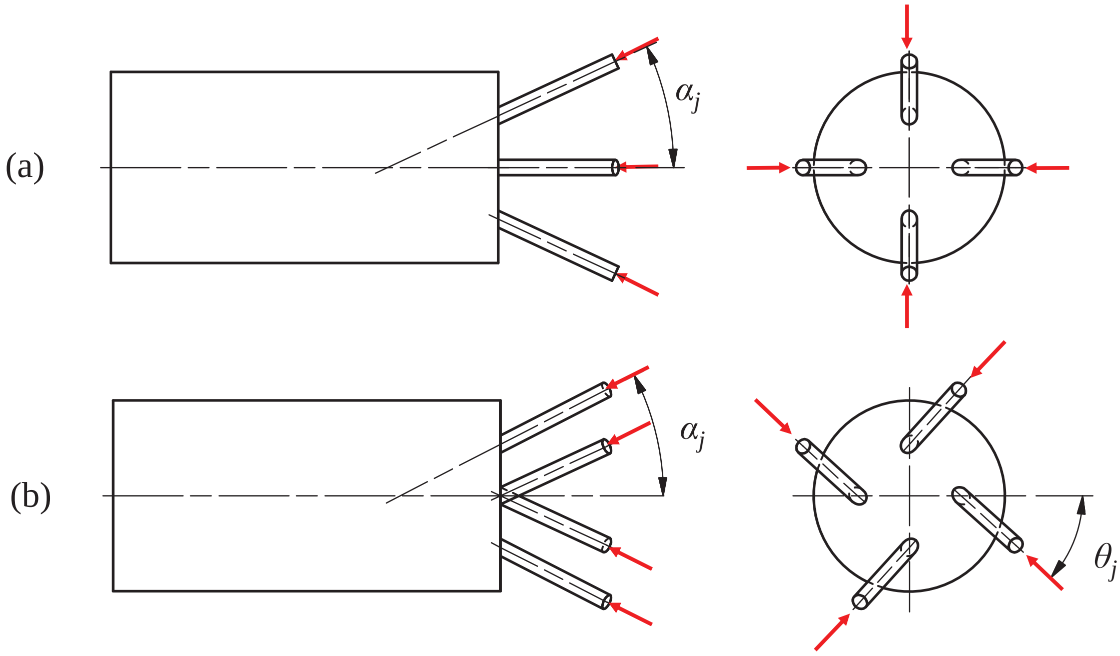

Figure 1.3: Schematic diagram of multiple inlet-pipes configurations for (a) planar-symmetric jets, and (b) rotationally-symmetric jets.

1.4.2 Jet configurations

Although a wide range of potential angles (α_j and θ_j) between jet-nozzles are possible, three configurations have received most attention previously, namely that of parallel-jets, inclined-jets and swirling jets. Parallel and inclined jets (i.e., non-swirling jets) are typically composed of multiple planar-symmetric nozzles that have the same inlet diameter (D_{pipe}), a fixed jet angle ($90^{\circ} \geq \alpha_j \geq 0^{\circ}$) and a fixed spacing between each other (S_0), while the swirling jets typically refer to the rotationally-symmetric configurations where $\theta_j > 0^{\circ}$ to generate a strong swirl within a confined space [34-36]. Previous studies of these multiple-jets configurations have found that the flow unsteadiness which is associated with the interaction between each inlet-jets (e.g., the precessing vortex core or jet precession [37]) tends to be significantly stronger than that of a single unconfined jet. This precession of jet is typically not a desirable flow feature for industrial combustion applications because it may potentially reduce the thermal performance within the chamber during the combustion process [38-40]. However, to my best knowledge, no previous assessment has been performed of flow oscillations generated by the non-swirling (parallel or inclined) and swirling jets within a cylindrical chamber for a wide range of jet angles. This gap in understanding tends to affect the engineers to finalise a suitable design of combustors or reactors for reducing the undesirable precessing flow. Hence, the key flow characteristics, including the unsteady flow features, generated by multiple confined jets also needs to be assessed.

1.4.3 Geometrical aspect ratio

The geometrical aspect ratio is one of the key parameters for a wide range of engineering applications, including air-conditioning systems [41], flow mixing [42] and combustion technologies [37]. For example, the confinement ratio of room L_{room}/H_{room} (length-to-height) was found to have a controlling influence on the efficiency of cooling and heat transfer for jet impingement [42], while the nozzle aspect ratio of a plane jet W_{nozzle}/H_{nozzle} (width-to-height) can significantly change the velocity field within a wide range of configurations, such as air curtains and cooling systems [43]. Importantly, previous studies of the HSRC revealed that the chamber aspect ratio L_c/D_c (length-to-diameter) has a strong influence on thermal efficiency and capital cost [18, 23]. Nevertheless, there is no systematic study with well-defined conditions that have been proposed to fully characterise a range of chamber aspect ratio (L_c/D_c) for multiple-jets applications. That is, the dependence of the important flow structure generated by multiple confined jets on the key geometrical parameters, such as the characteristic length of the confining wall ($L_{c.crit}$), remains unknown. This research gap is significant because in practical combustion devices, particularly for the hybrid combustion technology, the selection of an appropriate chamber size is important for maintaining high thermal efficiency and also a relatively low infrastructure cost. Therefore, there is also a need to better understand the influence of chamber aspect ratio, such as the length or diameter of the chamber, on the flow-field of multiple confined jets to guide the development of the HSRC and also relevant engineering applications.

1.5 Project aims

Based on the above background information, the overall objective of the present study is to provide a new understanding of the large-scale flow characteristics generated by multiple annular impinging jets within a cylindrical chamber. The specific aims of the present study are the following:

1. To characterise all of the flow regimes that can be generated within a cylindrical chamber with multiple planar-symmetric impinging jets.

2. To investigate the flow characteristics of multiple rotationally-symmetric jets within a cylindrical chamber configured to generate a swirl.

3. To identify the influence of the geometrical aspect ratio on the internal flow-field generated by multiple confined jets.

4. To quantify the swirling and unsteady flow features generated by multiple swirling jets (rotationally-symmetric) within a cylindrical chamber.

1.6 Thesis outline

The thesis presents eight chapters as outlined in the following:

Chapter 2 presents the literature review of the flow-field generated by multiple interacting jets within a confined space, including both experimental and numerical studies on the non-swirling jets, swirling jets, geometrical aspect ratio and flow unsteadiness. Four research gaps are identified and the corresponding scientific aims to address these research questions are presented.

Chapter 3 presents the methodology for the present study to meet the aims. The experimental configurations of “Multiple Impinging Jets in a Cylindrical Chamber” (MIJCC) investigated in the thesis are presented. A full description of the experimental arrangements is provided, including information of the Particle Image Velocimetry (PIV) arrangement, together with the data-processing methods, boundary and inlet conditions. Also included is a comprehensive discussion of the uncertainty for PIV measurements, together with a brief description of the numerical method used to perform Computational Fluid Dynamics (CFD).

Chapter 4 reproduces the first published journal paper arising from the thesis entitled “Experimental and numerical investigation of the iso-thermal flow characteristics within a cylindrical chamber with multiple planer-symmetric impinging jets”. The paper presents a joint PIV measurement and CFD investigation of the flow structure within the MIJCC configuration, including 19 jet inclination angles (α_j = 0° to 90°) and two jet arrangement (two or four jets). The measured and calculated instantaneous and mean velocity fields, turbulence intensity, Reynolds shear stress, together with the predicted recirculation rate and reversed mass flow rate were assessed. The calculated CFD results were validated against the PIV measured data, with a reasonable agreement being achieved. A map of flow regimes and their key corresponding flow features was also proposed.

Chapter 5 reproduces the second published journal paper entitled “Iso-thermal flow characteristics of rotationally-symmetric jets generating a swirl within a cylindrical chamber”. The paper presents a systematic experimental study of the interaction between four rotationally-symmetric jets within the MIJCC configuration. The value of α_j was varied over the range of 25° to 45°, while the jet azimuthal angle (θ_j) was varied from 5° to 15°. The combined effect of α_j and θ_j on the mean and root-mean-square (RMS) velocity fields, integral length scale, external and central recirculation zones (ERZ and CRZ) within the cylindrical chamber were assessed. A regimes map for identifying the influence of having both α_j and θ_j on different flow regimes was derived.

Chapter 6 reproduces the third published journal paper entitled “The influence of aspect ratio on the iso-thermal flow characteristics of multiple confined jets”. The configurations of α_j = 25° were assessed with θ_j = 5° and 15°, and a range of chamber aspect ratios (L_c/D_c = 1 to 3). The effect of the chamber aspect ratio (L_c/D_c) on the ERZ and CRZ, mean and RMS velocity fields, Reynolds shear stress and integral length scale were analysed. A detailed measurement of the recirculation rate (K_v) within the chamber was also carried out, with a strong dependence of recirculation rate on the chamber aspect ratio being identified.

Chapter 7 reproduces the fourth published journal paper entitled “Characteristics of swirling and precessing flows generated by multiple confined jets”. This paper presents a series of PIV measurements for the swirling flow generated by multiple rotationally-symmetric jets within a cylindrical chamber. New quantitative information of the tangential velocity, vortex intensity of the ERZ and CRZ, and the rotational flow patterns within the MIJCC configuration were derived. A detailed characterisation of the precessing flow, such as the precessing vortex core (PVC), within three distinctive flow regimes, was proposed. The dependence of the PVC on the multiple confined jets was identified.

In Chapter 8, a summary of all findings from Chapters 4 to 7 together with some recommendations for future work is presented.

1.7 Publications resulting from this work

List of journal papers:

- Long, S, Lau, TCW, Chinnici, A, Tian, ZF, Dally, BB and Nathan, GJ 2017, ‘Experimental and numerical investigation of the iso-thermal flow characteristics within a cylindrical chamber with multiple planar-symmetric impinging jets’, Physics of Fluids, vol. 29, no. 10, p. 105111.
- Long, S, Lau, TCW, Chinnici, A, Tian, ZF, Dally, BB and Nathan, GJ 2018, ‘Iso-thermal flow characteristics of rotationally symmetric jets generating a swirl within a cylindrical chamber’, Physics of Fluids, vol. 30, no. 5, p. 055110.

- Long, S, Lau, TCW, Chinnici, A, Tian, ZF, Dally, BB and Nathan, GJ 2018, 'The influence of aspect ratio on the iso-thermal flow characteristics of multiple confined jets', Physics of Fluids, vol. 30, no. 12, p. 125108.
- Long, S, Lau, TCW, Chinnici, A, Tian, ZF, Dally, BB and Nathan, GJ 2019, 'Characteristics of swirling and precessing flows generated by multiple confined jets', Physics of Fluids, vol. 31, no. 5, p. 055102.

List of conference papers:

- Long, S, Tian, ZF, Nathan, GJ, Chinnici, A and Dally, BB 2015, 'CFD modelling of isothermal multiple jets in a combustor', 11th International Conference on CFD in the Minerals and Process Industries, Melbourne, Australia, 7-9 December 2015.
- Long, S, Tian, ZF, Chinnici, A, Lau, TCW, Dally, BB and Nathan, GJ 2016, 'Effect of jet inclination angle on the flow field within a Hybrid Solar Receiver Combustor', 20th Australasian Fluid Mechanics Conference, Perth, Australia, 5-8 December 2016.
- Long, S, Lau, TCW, Chinnici, A, Tian, ZF, Dally, BB and Nathan, GJ 2017, 'Effect of jet azimuthal angle on the flow field within a Hybrid Solar Receiver Combustor', Asia Pacific Solar Research Conference, Melbourne, Australia, 5-7 December 2017.
- Long, S, Lau, TCW, Chinnici, A, Tian, ZF, Dally, BB and Nathan, GJ 2018, 'The effect of aspect ratio on the flow characteristics of a Hybrid Solar Receiver Combustor', 21th Australasian Fluid Mechanics Conference, Adelaide, Australia, 10-13 December 2018.

1.8 Thesis format

The thesis has been submitted in the publication format. It includes four peer review papers, which have been published by the journal of “Physics of Fluids”. I, Shen Long, is the principal author of all papers. The format of the current document is based on the formatting requirements of The University of Adelaide. The hard copy of the thesis is identical to the soft copy which is available online, and the online PDF version of the thesis can be viewed by any PDF software.

Chapter 2

2 Literature Review

Chapter 2 presents the key literature review of the flow-field generated by multiple annular impinging jets within a confined space.

2.1 The influence of multiple non-swirling jets

2.1.1 Parallel jets

The key flow regions of multiple parallel jets issuing from a wall [44-46] are presented schematically in Figure 2.1. It can be seen that the flow-field of parallel jet consists of a converging region, a merging region and a combined region. The converging region generates a recirculation zone upstream from a merging point (P_{mer}), while the two inlet-jets continue to merge until a combined point (P_c).

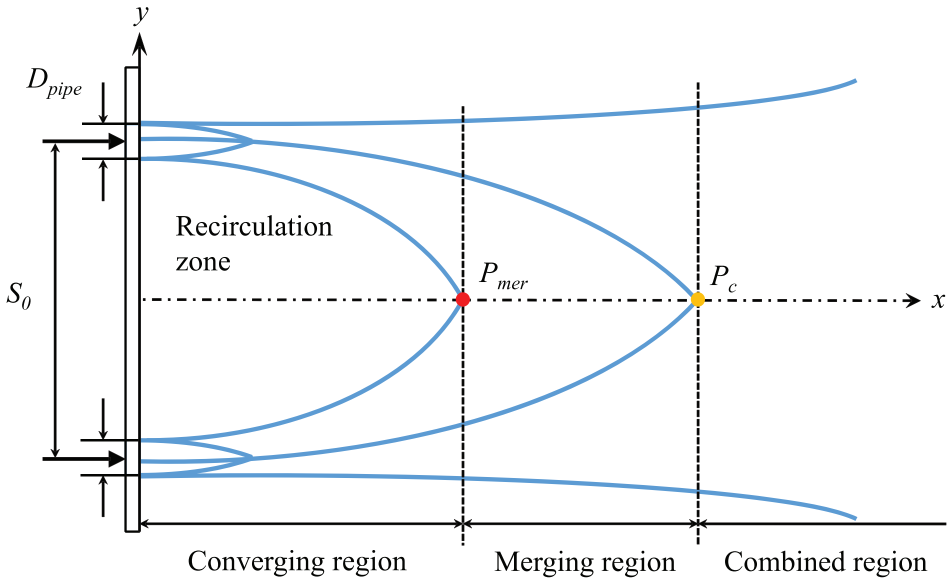

Figure 2.1: Key flow regions of multiple parallel jets generated from a free wall. The symbol of P_{mp} denotes the "merging point", while that of P_c refers to the "combined point". Adapted from Faghani et al. [45].

Table 2.1: Summary of previous studies of multiple parallel jets, including the key parameters investigated.

Study	Re_D	S_0	α_j	N_j	Downstream boundary	Method	Investigated parameters
Thong et al. [35]	$1.4 - 6.5 \times 10^3$	$9.3D_{pipe}$	90°	4	Confined	Experiment	Mean & RMS velocities
Gao et al. [54]	$1 - 2 \times 10^4$	$2.8 - 4.7D_{pipe}$	90°	2	Confined	Experiment	Mean & RMS velocities
Faghani et al. [45]	6.9×10^4	$4.25 - 18.25D_{pipe}$	0°	2	Unconfined	CFD	Mean velocity
Gavi et al. [55]	$0.7 - 2.7 \times 10^3$	$4.76D_{pipe}$	90°	2	Confined	CFD	Mean velocity & scalar field
Leite et al. [47]	$0.5 - 1.4 \times 10^4$	$5 - 20D_{pipe}$	0°	1 - 5	Unconfined	Experiment	Flame characteristics
Yimer et al. [53]	$1.6 - 1.9 \times 10^5$	$5.3 - 2D_{pipe}$	0°	1 & 7	Unconfined	Experiment	Mean & RMS velocities
Moustafa [52]	$4.2 - 13 \times 10^4$	$3 - 5D_{pipe}$	0°	2	Unconfined	Experiment	Mean velocity & pressure
Menon et al. [51]	1.5×10^4	$8 - 16D_{pipe}$	0°	2, 3 & 5	Unconfined	Experiment	Flame, temperature & scalar field
Raghunathan et al. [50]	1.4×10^5	$1.4D_{pipe}$	0°	1 - 9	Unconfined	Experiment	Mean velocity
Tanaka et al. [49]	$1.9 - 2.7 \times 10^4$	$11D_{pipe}$	0°	3	Unconfined	Experiment	Mean velocity & pressure
Tanaka [48]	$4.3 - 8.8 \times 10^3$	$8.5 - 26D_{pipe}$	0°	2	Unconfined	Experiment	Mean velocity & pressure
Tanaka [36]	$4.3 - 8.8 \times 10^3$	$8.5 - 26D_{pipe}$	0°	2	Unconfined	Experiment	Mean velocity & pressure

Previous experimental and Computational Fluid Dynamics (CFD) studies of the evolution of large-scale flow structures from multiple parallel jets, as summarised in Table 2.1, have been performed almost exclusively for unconfined environments. These showed that the flow characteristics depend strongly on the key geometrical features of the nozzles, as well as their arrangement [36, 47-55].

The following key findings can be drawn from previous studies:

- Multiple parallel jets (i.e., number of jets $N_j > 1$) was found to significantly influence the mean flow characteristics, such as the jet momentum, centreline velocity decay and jet spreading rate [36, 48-50]. The mean velocity profile of multiple parallel jets is of similar to a single circular jet for merging region, regardless the value of N_j, while a distinctive velocity profile of each inlet-jet can be observed upstream from converging region [50, 52, 53].

- The spacing between each nozzle, S_0 was found to be an important parameter for controlling the iso-thermal flow-field generated by multiple parallel jets. For example, the key mean flow statistics such as the rate of maximum decay in centreline jet velocity and the growth of jet width increase significantly with an increase in S_0 [36, 48, 53]. However, the qualitative feature of the mean velocity profile downstream from the merging point was found to be independent of S_0, although the magnitude of velocity profile depends on the inlet flow conditions [48, 52, 53].

- The turbulent or RMS (root-mean-square) flow-field of multiple parallel jets depends strongly on in-flow conditions. For a constant total inlet flow-rate ($\dot{m}_{total}$), the turbulence intensity does not change significantly between single and multiple parallel jets [53], while for a constant nozzle flow-rate ($\dot{m}_{nozzle}$), an increase in N_j tends to increase the velocity fluctuation within the merging region [48].

- Nozzle arrangement was found to significantly affect the flame and combustion characteristics of multiple parallel jets. For example, the study of multiple jet flame conducted by Menon et al. [51] showed that S_0 is the prominent parameter that influences the interaction of flame, while Leite et al. [47] revealed that, for a given S_0, the flow stability and the flame length in the merged flow from multiple unconfined reacting jets increases as N_j is increased. In addition, it was also found that the configuration of directly impinging jets ($\alpha_j = 90^\circ$) can improve flow mixing and heat transfer efficiency within a confined cylindrical chamber [35, 54, 55].

From these studies, it is clear that parameters such as the number of jet-nozzles (N_j), nozzle spacing (S_0) and nozzle arrangements have a strong influence on the flow-field generated by multiple interacting jets. Nevertheless, the research gap in multiple-jets remains significant. Firstly, the majority of previous studies only investigated the flow-field generated from parallel impinging jets (i.e., $\alpha_j = 0^\circ$) or directly impinging jets (i.e., $\alpha_j = 90^\circ$), so that few studies are available for inclined impinging jets (i.e., $0^\circ < \alpha_j < 90^\circ$) with planar-symmetric arrangements. Secondly, little information is available for multiple inclined jets within a confined space or cylindrical chamber, although confined impinging jets are directly relevant to many industrial applications, such as gas turbine combustors [7], aerodynamic curtains in solar receiver/reactors [6] and novel burner/furnaces [32]. Thirdly, the detailed in-flow and boundary conditions are not fully provided by most of the previous investigations in parallel jets due to the limitation of measurement technology (e.g., probe). Hence, a more detailed characterisation of the flow patterns within a confined environment (e.g., an axisymmetric chamber) for a systematic range of well-defined inflow and boundary conditions is needed to provide a new understanding of the flow generated by planar-symmetric multiple-jets.

2.1.2 Constant Reynolds number

The influence of Reynolds number on the mean and turbulent flow-fields has been found previously to be asymptotic for both single jet and multiple-jets configurations [28, 31, 42, 54, 56-59]. The Reynolds number at the nozzle exit plane is defined as:

$$Re_D = \frac{\rho_f U_e D_{pipe}}{\mu_f} \qquad (2.1)$$

where ρ_f is the fluid density, μ_f is the fluid dynamic viscosity and U_e is the bulk velocity at the nozzle exit. Previous work has found that the mean and turbulent flow-fields depend strongly on Reynolds number for $Re_D < 10{,}000$ but tends to be relatively weak for $Re_D \geq 10{,}000$ [31, 57-59]. However, previous studies of multiple jets have been performed for a wide range of different values of Re_D and other inlet conditions [8, 52], which makes it difficult to fully isolate the influence of other key parameters from those of Re_D. Hence it is also important to isolate the effect of Re_D to provide new understandings of large-scale flow structure generated by multiple interacting jets confined in a cylindrical chamber.

2.1.3 Inclined jets confined in a space

The investigations of multiple inclined jets ($0^{\circ} < \alpha_j < 90^{\circ}$) within a confined space are relatively newer but fewer in number than those of parallel jets. Previous research showed that the jet inclination angle (α_j) is a key parameter for controlling the flow-field generated by multiple inclined jets within a confined space [8, 9, 32, 60-63]. A summary of the studies for multiple confined inclined jets is listed in Table 2.2.

Table 2.2: Summary of previous studies of multiple inclined jets within a confined space, including the key parameters investigated.

Study	Re_D	S_0	α_j	θ_j	N_j	Method	Investigated parameters
Chammem et al. [60]	4.1×10^5	$13D_{pipe}$	10° - 90°	0°	2	CFD	Mean velocity
Chammem et al. [8]	2 - 8×10^3	$15D_{pipe}$	20° - 60°	0°	2	Experiment & CFD	Mean & RMS velocities
Boushaki et al. [9]	0.6 - 1.6×10^4	$2D_{pipe}$	0° - 30°	0°	3	Experiment	Mean & RMS velocities
Boushaki et al. [61]	1.1×10^4	$2D_{pipe}$	0° - 30°	0°	3	Experiment	Flame & mean velocity
Boushaki et al. [32]	0.8 - 1.6×10^4	3 - $5D_{pipe}$	0° - 30°	0°	3	Experiment	Flame & mean velocity

Some key findings of the influence of α_j on the flow-field generated by multiple inclined confined jets are presented below:

- The flow visualization of two inclined confined jets conducted by Chammem et al. [8] defined the “resulting jet flow” as the central, merged flow downstream from the jet merging point and the “upstream reverse flow” as that upstream from the merging point. They also found that the presence or absence of the resulting and reverse flows depends strongly on the value of α_j and Re_D. It was also found from Chammem et al. [8] that the vortex structure within the resulting jet flow is much more complex than that in a single jet, owing to the effect of the asymmetry of the inlet-jets on vortex formation.

- The CFD investigation by Chammem et al. [60] found that the reverse flow region of multiple inclined jets depends strongly on the value of α_j because this reverse flow can only be generated within a certain range of α_j. For the configurations of $\alpha_j = 10^\circ$ to 90° and $N_j = 2$, the upstream reverse flow occurs only for the cases where $\alpha_j \geq 50^{\circ}$, while the jet merging point is only present for $\alpha_j \geq 30^{\circ}$. However, no experimental data is presently available with which to validate these calculated results.

- Boushaki et al. [9, 32, 61] conducted a series of experiments to measure the mean and turbulent velocity fields within a multiple-burners combustor. They found that an increase in α_j from 0° to 30° can significantly accelerate the impinging and combining of individual inlet-jets for the mean velocity field, which is crucial for achieving desirable mixing performance for combustion applications. The Particle Image Velocimetry (PIV) results of Boushaki et al. [9] also showed that the turbulence intensity along the axis of the chamber increases significantly with an increase in α_j, although the comparison of turbulence intensity between multiple-jets and the single jet was not provided in their study.

While these previous works provide useful insight, they are of limited value for model validation because none of them reports detailed in-flow information and boundary conditions. More importantly, none of the previous measurements of inclined jets provides a comprehensive understanding of the influence of jet arrangement for all of the regimes of flow-fields that can be generated. That is, no flow regime map has been provided for multiple impinging inclined jets within a cylindrical chamber. Instead, all previous investigations have been limited to a relatively small range of conditions, such as a limited range of α_j and a fixed number of jets (N_j). Therefore, there is poor understanding of the influence of the key dominant parameters, particularly of α_j, on the resulting flow and recirculation region for confined impinging jets in planar-symmetric arrangements (e.g., N_j = 2 and 4). This is a significant research gap for identifying the operation angle of jet-nozzles to provide a large and uniform recirculation region within the industrial combustors or chemical reactors. A critical jet angle ($\alpha_{j.crit}$) is also needed for the CST devices to avoid the transport of high temperature gases from the cavity to the outside environment. In addition, the existing data sets for planar-symmetric jets provide insufficient information for the unambiguous development and validation of computational models across the full range of angles $0^\circ < \alpha_j < 90^\circ$, resulting in the lack of fully validated CFD models for multiple confined jets. Hence, there is also a need to obtain sufficient reliable experimental data to fully characterise the flow-field of multiple planar-symmetric impinging jets in a confined space and to assess the validity of CFD models through this range.

2.2 The influence of swirl on confined jets

2.2.1 Annular swirling jets

The swirl within a confined space is typically generated by an azimuthal angle (θ_j) relative to either the axis of the jet for multiple-jets, or the vane for annular jet systems. The influence of θ_j on the iso-thermal flow-field has been widely investigated for configurations of annular swirling jets [34, 64-74]. These studies showed that the value of θ_j, associated with a swirl number, S_w, significantly influences the large-scale recirculation zones within a confined chamber. The swirl number S_w is defined as:

$$S_w = \frac{\int_0^R \rho_f U_x U_\theta 2\pi r^2 dr}{R\int_0^R \rho_f {U_x}^2 2\pi r dr} \tag{2.2}$$

where U_x and U_θ denote the axial and azimuthal velocities, respectively, while R is the radius of the geometry. One of the key flow features within a swirling jet flow is the central recirculation zone (CRZ) generated by the azimuthal angle θ_j with a sufficient swirl number. Another key flow feature is the external recirculation zone (ERZ), which is typically found in configurations of jet impingement. Figure 2.2 presents a schematic diagram of the CRZ and ERZ generated by jets within a confined chamber. It can be seen that the CRZ is defined as a large-scale vortex with inward rotation (Figure 2.2a), while the ERZ refers to the vertex with outward rotation (Figure 2.2b). Syred et al. [73] and Gupta et al. [72] proposed a detailed review of swirling flow and found that the CRZ is particularly important for the stabilization of a flame, notably by the recirculation of reactants during the combustion process. However, while previous studies provide useful qualitative information of the CRZ, they are limited to a relatively few configurations since they have been performed almost exclusively for the single annular jet ($N_j = 1$) within vane swirled systems. That is, no previous studies quantitatively measured the key information such as the length and the core location of the CRZ and ERZ (L_{core}) as a function of the jet-nozzles' angles, although these parameters are critical for quantifying the mixing and heat transfer efficiency within the chamber of multiple-jets burners. Hence, the influence of the azimuthal angle θ_j from multiple-jets (i.e., multiple inlet-jets configured with annular arrangement) on the large-scale recirculation regions, such as the CRZ and ERZ, requires further investigations.

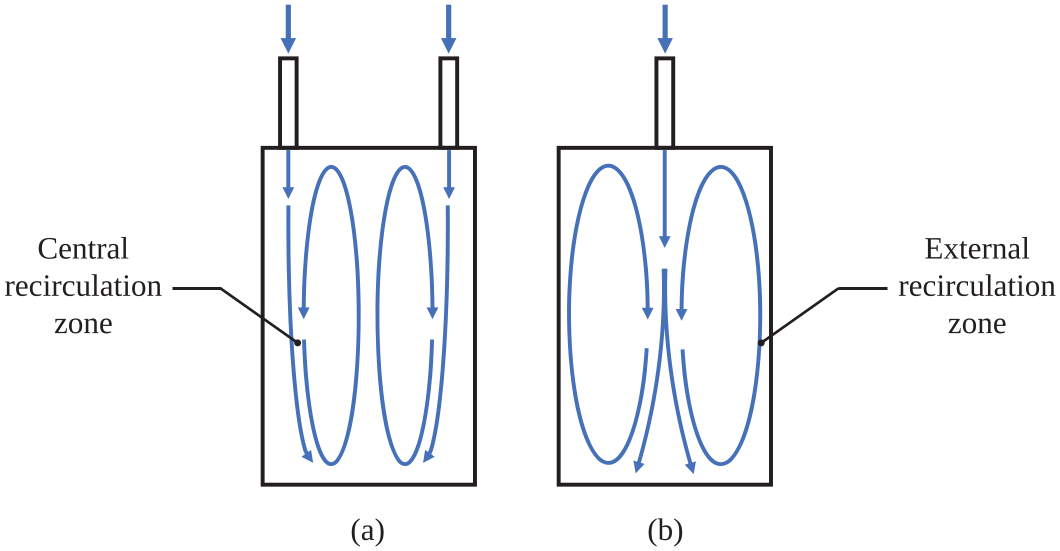

Figure 2.2: Schematic diagram of the large-scale vortex generated by confined jet configurations, showing (a) central recirculation zone, and (b) external recirculation zone.

The characteristics of the large-scale recirculation zone can strongly influence the mean and turbulent flow-fields generated by swirling jets, as reported by Syred et al. [73] and Syred [37]. The recirculation zone is particularly important for configurations of swirling jets within an axisymmetric chamber. For example, it was found that an increase in the size of the CRZ can significantly increase the level of turbulent fluctuations and Reynolds stress anisotropy within the central region of a confined chamber [34, 67], although the decay rate of turbulence intensity and turbulent kinetic energy within the CRZ was also found to be increased [68]. The turbulent flow characteristics such as turbulence intensity and Reynolds stress are important for the development of combustion and solar thermal technologies because these parameters quantify the flow instability generated by the interaction between multiple-jets. However, while these previous studies provide new data of swirling flow in a cylindrical chamber, the value of θ_j used in these studies was not explicitly presented. Therefore, the influence of θ_j on the mean and turbulent characteristics is still not fully understood. In addition, the definition of the swirl angle (i.e., azimuthal angle θ_j) in each study is slightly different due to the inconsistent coordinate for these configurations (e.g., Cartesian or polar systems), which also makes them difficult to be analysed together. Hence, a detailed investigation of θ_j for swirling jets confined in a cylindrical chamber under a well-defined boundary condition is also needed.

2.2.2 Multiple impinging jets generating a swirl

There are limited studies that have investigated the effect of multiple impinging swirling jets ($\theta_j > 0^\circ$ and $N_j > 1$) on the iso-thermal flow field within a confined space, particularly for conditions where jets are confined in an axisymmetric chamber [33, 75-79]. A summary of these studies is given in Table 2.3.

Table 2.3: Summary of previous studies of multiple impinging jets generating a swirl in a cylindrical chamber.

Study	θ_j	α_j	N_j	Method	Investigated parameters
Chinnici et al. [33]	90°	90°	2	Experiment & CFD	Mean velocity
Chinnici et al. [76]	90°	90°	2	Experiment & CFD	Mean & RMS velocities
Tian et al. [77]	90°	90°	2	CFD	Mean velocity
Krishna et al. [79]	45°	90°	18	CFD	Mean velocity & scale fields
Ozalp et al. [78]	45°	90°	18	CFD	Mean velocity
Ridluan et al. [75]	90°	90°	12	CFD	Mean velocity

The majority of these previous studies have investigated the dependence of the flow-field on the geometrical features and inlet conditions of multiple impinging jets. For example, Chinnici et al. [33] and Chinnici et al. [76] investigate the mean flow characteristics within a Solar Enhanced Vortex Reactor (SEVR) equipped two tangential inlet-pipes ($\theta_j = 90^{\circ}$ and $N_j = 2$). They found that an increase in the cone angle (β_{con}) and the length of the main cavity (L_c) leads to a decrease in the swirl strength within the SEVR. The numerical and experimental studies of Ozalp et al. [78] for a multiple-jets cyclone reactor ($\theta_j = 45^{\circ}$ and $N_j = 18$) revealed that a decrease in the nozzle exit velocity (U_e) results in a reduction in the magnitudes of axial velocity (U_x) and vorticity (ζ) within the cyclone cavity. Nevertheless, none of these studies has considered the effect of θ_j on the flow-field generated by multiple impinging jets because most of them have investigated a single value of θ_j. The lack of a comprehensive investigation for θ_j leads to the incomplete data-set to fully identify the entire range of operational azimuthal angles for achieving preferred swirling flow within industrial vortex applications. Therefore, the influence of θ_j on the mean and turbulent flow-fields generated by multiple swirling jets requires further investigations.

It is also important to note that most of the previous studies of multiple impinging jets ($N_j > 1$) considered only the influence of the α_j between each inlet-jet (see also Table 2.2), so that almost no information is available of the influence of the jet azimuthal angle θ_j for which $\alpha_j > 0^{\circ}$. This gap in understanding is significant because the combination of α_j and θ_j for multiple-jets (rotational-symmetric) has wide relevance to the development of swirl jets applications, including novel vortex combustors [27, 65, 75], cyclone reactors [78, 80] and solar thermal applications [81, 82]. Owing to the lack of sufficient reliable experimental data from previous investigations, the details of the flow structure generated by multiple swirling jets (rotationally-symmetric) confined in a cylindrical chamber is still poorly understood. This is a significant impediment to the continuous development of computational models for multiple swirl jets configurations [83]. Therefore, a more detailed and quantitative understanding is needed of the combined effects of θ_j and α_j on the flow-field generated by multiple rotationally-symmetric jets confined in a cylindrical chamber.

2.3 The influence of geometrical aspect ratio

The influence of geometrical aspect ratio on the flow-field generated by jet has been investigated for a wide range of applications, including jet impingement, single annular jet and multiple-jets [42, 43, 54, 70, 84-88]. A summary of previous studies of the aspect ratio for both the swirling and non-swirling jets is listed in Table 2.4.

Table 2.4: Summary of previous studies of the geometrical aspect ratio for swirling and non-swirling jets configurations.

Study	Aspect ratio	N_j	Configuration	Method	Investigated parameters
Guo et al. [87]	H_{con}/D_{pipe} = 2 - 8	1	Non-swirling	Experiment	Mean velocity
Khalil et al. [70]	D_c/D_{pipe} = 1.7	1	Swirling	Experiment	Mean velocity
Kao et al. [88]	L_c/D_c = 1.5 - 3	1	Swirling	Experiment	Mean velocity
Gao et al. [54]	H_{con}/D_{pipe} = 1.5 to 4	2	Non-swirling	Experiment	Mean & RMS velocities
Al-Sanea et al. [42]	L_{room}/H_{room} = 0.5 - 6	1	Non-swirling	CFD	Mean velocity & heat-transfer efficiency
Deo et al. [43]	W_{nozzle}/H_{nozzle} = 15 - 72	1	Non-swirling	Experiment	Mean & RMS velocities
Morris et al. [84]	H_{con}/D_{pipe} = 1 - 4	1	Non-swirling	CFD	Mean velocity & pressure
Morris et al. [85]	H_{con}/D_{pipe} = 2 - 4	1	Non-swirling	CFD	Mean velocity
Garimella et al. [86]	H_{con}/D_{pipe} = 1 - 14	1	Non-swirling	Experiment	Heat-transfer coefficient

For configurations of non-swirling jet ($\theta_j = 0^{\circ}$), it has been found that the distance between the jet exit and an end plate, termed “confinement height” (H_{con}), can significantly influence the position and strength of the large-scale recirculation regions, wall jet development and the distribution of the jet velocity [84-87]. For example, the PIV measurements of Guo et al. [87] for a confined jet impingement revealed that an increase in H_{con} from H_{con}/D_{pipe} = 2 to 8 leads to a significant movement of the vortex-core of an ERZ from the bottom to the top edge of the confining wall within the range of Re_D = 1000 to 9000, although the growth rate of the wall jet thickness is significantly decreased.

However, these studies have been performed almost exclusively for a single jet ($N_j = 1$), which makes it difficult to directly apply to multiple swirling or non-swirling jets within a cylindrical chamber.

For configurations of swirling jet investigated previously ($\theta_j > 0^{\circ}$), it was found that the confinement by cylindrical wall tends to increase the velocity fluctuation, velocity magnitude and the recirculation within swirl flow burners [88, 89]. For example, the experimental study of Kao et al. [88] showed that the influence of the chamber aspect ratio (L_c/D_c) on the mean and RMS velocity fields is significant for near-field (e.g., $x/D_c = 0.12$), although they also found the influence to be negligible in the far-field (e.g., $x/D_c = 1.77$) within a swirled jets combustor. However, due to the lack of information available of the inflow and boundary conditions, these previous studies are of limited value for model validation.

For configurations of multiple confined jets ($N_j > 1$), Gao et al. [54] investigated the effect of the confinement height H_{con} on the turbulent flow field within a confined impinging jets reactor using PIV. Their results showed that a decrease in H_{con}/D_{pipe} from 4 to 1.5 leads to an increase in turbulent kinetic energy and mixing efficiency within the jet impinging region. Nevertheless, the important flow parameters such as the recirculation zones and RMS velocity field were not be assessed in their study. Hence, the dependence of the key mean and turbulent flow characteristics within multiple confined jets on geometrical parameters such as the chamber aspect ratio is yet to be fully understood.

The presence of large-scale recirculation zones (e.g., the ERZ and CRZ) can significantly influence the flow and flame characteristics of multiple confined jets. For example, it was found that the ERZ and CRZ are associated with the recirculation rate K_v (the ratio between the circulated and total mass flow-rate) within the chamber, which is important for combustion stabilization and thermal efficiency [90-92]. However, to my knowledge, the influence of the geometrical parameters such as the chamber length-to-diameter ratio (L_c/D_c) on the size and the strength of the dominant recirculation zone remains unknown due to the lack of comprehensive investigations. Hence, a more detailed characterisation is also needed to identify the influence of the chamber aspect ratio L_c/D_c on the ERZ and CRZ generated by multiple jets within a cylindrical chamber.

2.4 Flow unsteadiness of multiple impinging jets

The characteristics of flow unsteadiness that associated with multiple impinging jets have been widely investigated by previous researchers [33, 35, 37-40, 54, 67, 73, 93-97]. One of the major features is the precessing vortex core (PVC) within the recirculation zone, which has been identified for a wide range of vortex applications [33, 37, 96, 97]. The PVC is a large-scale coherent and time-dependent flow structure embedded within a vortex, which is defined as the precession of the vortex-core relative to the geometrical axis of an axisymmetric device, as described in the detailed review by Syred [37] and presented schematically in Figure 2.3. Their study showed that the PVC can significantly influence flow behaviour, mixing performance and combustion efficiency for vortex devices such as cyclones and swirl burners. Previous investigations revealed that the extent of the PVC depends strongly on the geometrical confinement [98], recirculation zone [72] and thermal conditions [73]. For example, the experimental studies of Syred et al. [98] and Gupta et al. [72] found that a decrease in the confinement ratio of jet leads to a significant increase in the intensity of the ERZ and CRZ, which increases the degree of the PVC and other instabilities within a swirl combustor. Syred et al. [73] reviewed the characteristics of PVC under reacting flow conditions and found that the combustion process tends to amplify the amplitude of the PVC by an order of magnitude compared with isothermal conditions. In addition, the experimental and numerical studies of Chinnici et al. [33] confirmed the presence of a PVC within a multiple-jets solar cavity receiver. Their study also showed that an increase in either the value of cone angle (β_{con}) or the length of the chamber (L_c) leads to a significant reduction in the significance of the PVC. However, while the dynamics of the PVC in a swirling or single jet has been widely documented [37], none of the previous investigations provided a comprehensive understanding of the influence of the key controlling parameters (i.e., α_j and θ_j) on the PVC, so that the dependence of the PVC on large-scale recirculation zones (i.e., ERZ and CRZ) generated by multiple-jets remains unclear. Hence, there is also a need to better understand the characteristics of the PVC generated by multiple jets within a confined space.

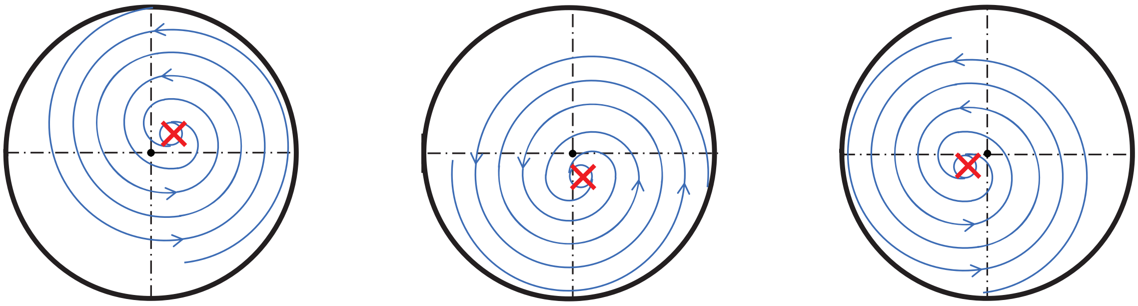

Figure 2.3: Schematic diagram of typical streamline of the precessing vortex cores (PVC) within the recirculation zone. The black-dot denotes the central of the geometry, while the red-cross denotes the core of the vortex.

Previous studies of multiple-lateral jets (α_j = 90° and θ_j = 0°) revealed that the strong interaction of multiple impinging jets tends to amplify the extent of flow precession and oscillation, resulting in the presence of a precessing flow downstream from the jet merging or impingement point [35, 54, 99]. For those configurations, a significant offset in the instantaneous position of the impingement point from the axis, which was termed "flapping", was observed. However, although these studies provided useful insights about jet precession, they are almost exclusively performed for multiple impinging jets without an azimuthal component θ_j, with the inclination angle is typically fixed at a constant single value (α_j = 90°). That is, none of the previous investigations provided a comprehensive understanding of the influence of the combination of α_j and θ_j on the extent of flow unsteadiness. This suggests that the key unsteady flow features, such as the PVC or jet precession, within these configurations remains unknown. Hence, there is also a need to fully characterise the precessing flows generated by multiple jets within a cylindrical chamber.

2.5 Research gaps and scientific aims

Based on the literature review, the following research gaps have been identified and the corresponding research aims to address these gaps are provided.

2.5.1 Research gaps

1. Previous studies provide insufficient information about inlet-flow and boundary conditions to fully characterise the dependence of flow structure on the inclination angle (α_j) for multiple impinging jets within a cylindrical chamber. Hence, there is poor understanding of the influence of the jet inclination angle (α_j) on the mean and turbulent flow-fields generated by multiple planar-symmetric ($\alpha_j > 0^\circ$ and $N_j > 1$) jets in a cylindrical chamber.

2. The majority of previous investigations of multiple-jets considered either the configurations for which $\alpha_j > 0^\circ$ (impinging jets) or $\theta_j > 0^\circ$ (swirling jets), resulting in the lack of reliable experimental data sets for the development of multiple rotationally-symmetric jets ($\alpha_j > 0^\circ$, $\theta_j > 0^\circ$ and $N_j > 1$) where both α_j and θ_j are employed to generate a swirl within a cylindrical chamber.

3. Previous research revealed a significant dependence of the iso-thermal flow-field on a wide range of geometrical aspect ratio for multiple-jets configurations. However, none of the previous studies has performed a systematic experimental investigation to fully assess the effect of geometrical aspect ratio on the mean and turbulent flow-fields generated by multiple rotationally-symmetric jets in a cylindrical chamber ($\alpha_j > 0^\circ$, $\theta_j > 0^\circ$ and $N_j > 1$).

4. Previous investigations have provided useful information to understand the effect of geometrical parameters and in-flow conditions on the characteristics of swirling and precessing flows generated by either single jet ($N_j = 1$) or multiple jets ($N_j > 1$). However, the combined effect of α_j and θ_j on the swirling and precessing flows (e.g., the PVC and tangential velocity) has not been fully explored. That is, the understanding of key flow features occurs in multiple swirling confined jets is still very limited.

2.5.2 Scientific aims

1. The first scientific aim of the present study is to characterise all of the flow regimes that can be generated within a cylindrical chamber with multiple planar-symmetric impinging jets. Specifically, The thesis aims:
   (a) to provide a detailed characterisation of the flow-field for planar-symmetric arrangements of impinging jets with well-defined inflow conditions within a cylindrical chamber;
   (b) to identify the influence of the inclination angle of jets α_j from 0° to 90° for two or four jets ($N_j = 2$ or 4), on large-scale flow structure;
   (c) to provide a map of flow regimes for planar-symmetric arrangements of impinging jets in a cylindrical chamber.

2. The second scientific aim of the thesis is to investigate the flow characteristics of multiple rotationally-symmetric jets within a cylindrical chamber configured to generate a swirl. The three sub-aims are:
   (a) to characterise the mean and RMS flow-fields for a series of rotationally-symmetric arrangements of multiple interacting jets;
   (b) to identify the influence of the small azimuthal angle of jets ($\theta_j = 5^{\circ}$, 10° and 15°) in addition to the inclination angle of jets $\alpha_j = 25^{\circ}$, 35° and 45°, on the dominant recirculation zones within a cylindrical chamber;
   (c) to characterise the dependence of flow regimes on rotationally-symmetric arrangements of multiple jets within a cylindrical chamber.

3. The third scientific aim of this investigation is to identify the influence of the chamber aspect ratio (length-to-diameter L_c/D_c) on the internal flow-field generated by multiple jets within a cylindrical chamber. More specifically, it aims:
   (a) to provide a detailed characterisation of the flow generated by multiple rotationally-symmetric inlet-jets within a cylindrical chamber for aspect ratios $L_c/D_c = 3, 2.5, 2, 1.5$ and 1;
   (b) to identify the influence of aspect ratio L_c/D_c on both the mean and RMS flow-fields within a cylindrical chamber with multiple-jets;
   (c) to characterise the dependence of aspect ratio L_c/D_c on the large-scale recirculation zones for multiple-jets configurations.

4. The fourth scientific aim of the current study is to quantify the swirling and unsteady flow features generated by multiple swirling jets (rotationally-symmetric) confined in a cylindrical chamber. The specific sub-aims are:

(a) to provide a quantitative description of the mean and RMS flow-fields in both the axial and tangential directions for multiple confined jets;

(b) to identify the characteristics of swirl within the ERZ and CRZ generated within a confined chamber with multiple-jets;

(c) to characterise the dependence of the precessing vortex core (PVC) on the configurations of multiple confined jets.

Chapter 3

3 Methodology

Chapter 3 presents the experimental and numerical methods that were chosen to address the research gaps and to meet the scientific aims presented in Chapter 2.

3.1 Configurations selected in the present study

Figure 3.1 presents the schematic diagram of the configuration investigated in the present study, namely, the Multiple Impinging Jets in a Cylindrical Chamber (MIJCC). This geometry is simplified relative to the HSRC to facilitate understanding and to increase relevance to other devices. The most significant components of practical burner systems are a central jet of fuel and a co-annular stream of air. The details of geometrical shapes vary greatly from one combustor to another, so that they typically have different levels of swirl, different relative velocities and geometrical configurations. Despite these differences, to first order, the complex co-annular burner can be represented as a single jet of equivalent momentum. This simplification is desirable because it avoids the complexity of assessing every possible combination of the many details of burner configurations, whilst still allowing the large-scale dynamics associated with the multiple-jets to be evaluated. For these reasons, the simplified arrangements were selected for the current study. The data set obtained from the present MIJCC configuration is relevant not only to the applications of combustion technology but also to several engineering applications where combustion is not necessarily needed, such as solar thermal devices, ventilation systems and chemical reactors.

The key geometrical features of the MIJCC are the main cavity, consisting of a cylindrical chamber with a conical expansion, and a secondary concentrator (SC), used to further concentrate the solar radiation from the heliostat field (as shown in Figure 1.2). The SC in the model was closed at the largest end with a flap (labelled with a green line) to prevent flow to the ambient environment, but open at the plane of the throat (labelled with a red dashed-line) to admit flow between these sections. This corresponds to the configuration of the HSRC within the combustion-only mode, where the aperture is closed with a flap to prevent heat loss [17].

Two nozzle arrangements were proposed for the MJICC configurations investigated here. These are the "planar-symmetric jets" (Figure 3.1b) and the "rotationally-symmetric jets" configurations (Figure 3.1c). Four inlet-pipes were distributed around the conical expansion of the main chamber with an inclination angle (α_j) to the axis of the chamber and/or at an azimuthal angle (θ_j) to the axis of the pipe. The flow leaves the chamber in the radial direction through an annular gap around a bluff end wall of uniform thickness, W_{out}. The dimensions of the key geometrical parameters of the MIJCC configurations investigated here are given in Table 3.1.

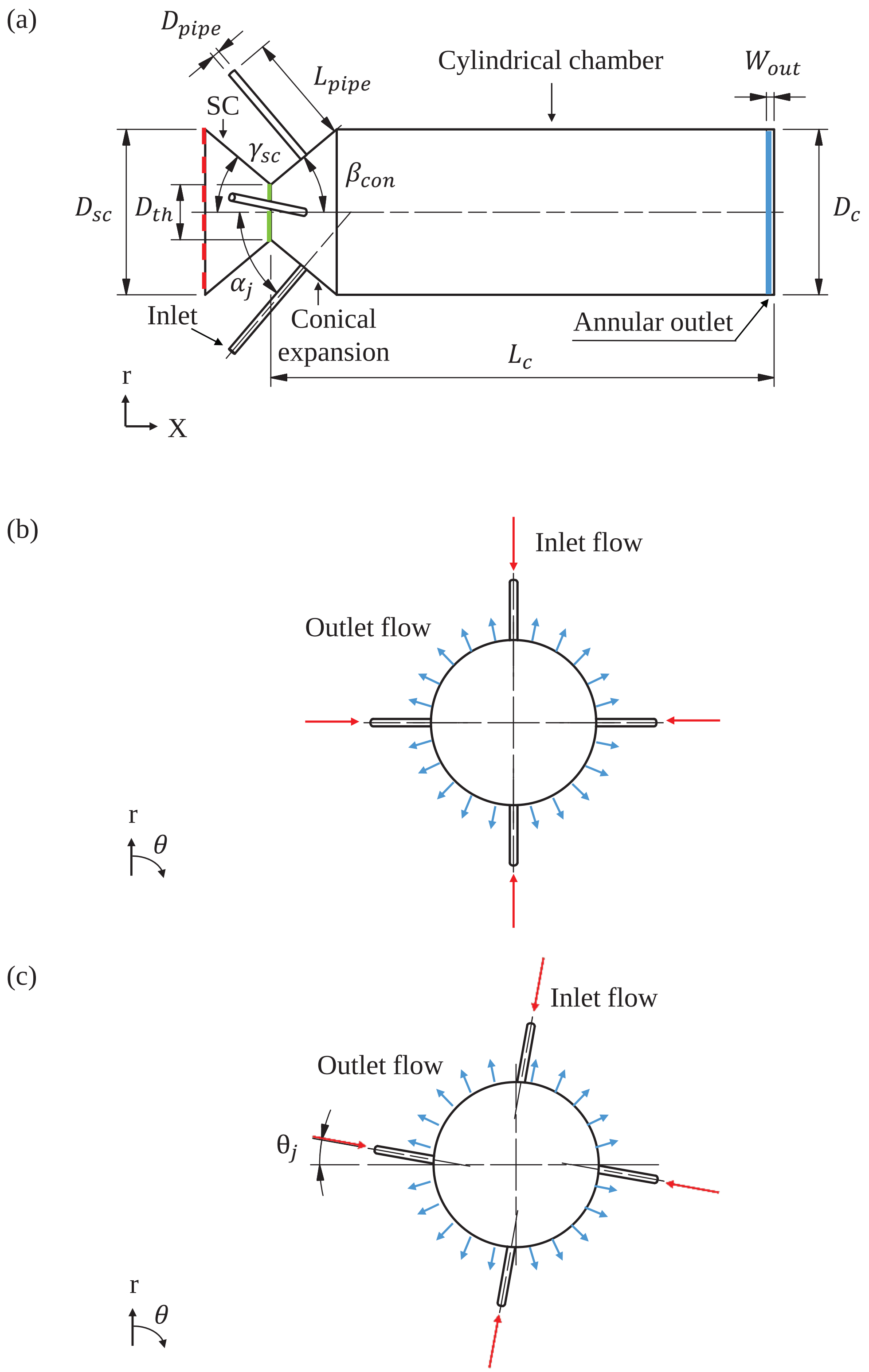

Figure 3.1: Schematic diagram of the configurations of the Multiple Impinging Jets in a Cylindrical Chamber (MIJCC) investigated here, showing the key geometrical features from the (a) axial cross section and (b) radial cross section for planar-symmetric jets, and (c) rotationally-symmetric jets. Here the flap plane, the throat plane, and the annular outlet are highlighted with red (dashed), green (solid), and blue lines, respectively. The SC refers to the Secondary Concentrator.

Table 3.1: Values of the geometrical parameters of the MIJCC configurations investigated in the present study.

Dimensions	Description	Value
D_c	Chamber Diameter (mm)	74
D_{sc}	Diameter of the Secondary Concentrator (mm)	74
D_{th}	Throat Diameter (mm)	24.6
D_{pipe}	Inlet Pipe Diameter (mm)	3.35
L_c	Chamber Length (mm)	74, 111, 148, 185 and 225
L_{pipe}	Inlet Pipe Length (mm)	150
W_{out}	Width of the Outlet Gap (mm)	3
α_j	Jet Inclination Angle (degree)	0° to 90°
θ_j	Jet Azimuthal Angle (degree)	5°, 10° and 15°
β_{con}	Conical Expansion Angle (degree)	40°
γ_{sc}	Angle of the Secondary Concentrator (degree)	40°

3.2 Experimental cases

Table 3.2 lists all of the experimental cases investigated in the present study. The experimental configuration of the MIJCC was manufactured from acrylic to provide optical access and a close match between the refractive index of the chamber and that of the working fluid (water). These configurations have inclination angles of $\alpha_j = 25^\circ, 35^\circ, 45^\circ$ and 50° and azimuthal angles of $\theta_j = 5^\circ$, 10° and 15°, together with a manufacturing tolerance of $\pm$ 0.1 mm (linear) and $\pm$ 0.5° (angular). The angles of jet-nozzles were selected to ensure the jet merging point (or jet impingement point in some cases) for all experimental cases is within the cylindrical chamber, as is necessary for optical access, and to achieve sufficiently large increment of α_j and θ_j required to provide distinct flow-features. The diameter of the MIJCC chamber was fixed at D_c = 74 mm, while the length of the chamber was set at either L_c = 225 mm, 185 mm, 148 mm, 111 mm or 74 mm, resulting in aspect ratios of L_c/D_c = 3, 2.5, 2, 1.5 or 1. These ratios were selected to span a sufficient range of flow-features and to cover realistic geometrical dimensions for relevant applications.

Table 3.2: The notation for the MIJCC configurations investigated experimentally.

Configurations	Inclination angles, α_j	Azimuthal angles, θ_j	Number of jets, N_j	Chamber aspect ratio, L_c/D_c	Investigated Chapters
MIJCC-25-2J	25°	0°	2	3	4
MIJCC-25-4J	25°	0°	4	3	4
MIJCC-50-2J	50°	0°	2	3	4
MIJCC-50-4J	50°	0°	4	3	4
MIJCC-25-05	25°	5°	4	3	5 and 7
MIJCC-25-10	25°	10°	4	3	5
MIJCC-25-15	25°	15°	4	3	5 and 7
MIJCC-35-05	35°	5°	4	3	5
MIJCC-35-10	35°	10°	4	3	5
MIJCC-35-15	35°	15°	4	3	5
MIJCC-45-05	45°	5°	4	3	5
MIJCC-45-10	45°	10°	4	3	5
MIJCC-45-15	45°	15°	4	3	5 and 7
MIJCC-05-LD25	25°	5°	4	2.5	6
MIJCC-05-LD20	25°	5°	4	2	6
MIJCC-05-LD15	25°	5°	4	1.5	6
MIJCC-05-LD10	25°	5°	4	1	6
MIJCC-15-LD25	25°	15°	4	2.5	6
MIJCC-15-LD20	25°	15°	4	2	6
MIJCC-15-LD15	25°	15°	4	1.5	6
MIJCC-15-LD10	25°	15°	4	1	6

3.3 Measurement techniques

Planar Particle Image Velocimetry (PIV) was employed to investigate the mean and RMS flow-fields within the MIJCC configurations. The PIV technique offers a wide range of advantages over traditional point measurements to measure the instantaneous velocity field of turbulent flow, such as a relatively high accuracy for measuring the integral length scales, the anisotropy of the velocity fluctuations and the Reynolds normal and shear stresses [100, 101]. Measurements were performed under iso-thermal conditions at ambient temperature using water as the working fluid to avoid deposition of seeding particles onto confining walls and also to provide a relatively high Reynolds number at a lower in-flow velocity condition. To limit optical distortion, the entire experimental model was fully submerged into a rectangular water tank with dimensions of 500 mm (L) × 400 mm (W) × 390 mm (H). This water tank was also made from acrylic. The water from the outlets was discharged into the water tank, which overflowed to a reservoir. The discharged fluid was reinjected through the jets using a variable-speed-drive enabled water pump (Pan World NH-200PS), a frequency converter (Danfoss VLT 2800) and flowmeters (ABB D10A11), resulting in a closed-loop system.

The bulk mean velocity at the nozzle exit (U_e) was fixed at 2.8 m/s for each nozzle, resulting in an inlet jet Reynolds number $Re_D = 10500$. This ensures that the inlet flow is within the fully turbulent regime where the influence of Re_D is considered to be small [43]. The jets were generated with a supply system that was carefully designed to ensure both overall flow symmetry and fully developed pipe flow at the exit. A symmetric manifold system was employed to ensure equal flow distribution to each jet, which fed 150 diameters of gently-curved flexible piping, feeding 46 diameters of perfectly straight pipe. The perfectly straight section exceeds the 40 diameters found by Nikuradse [102] to be the minimum needed to establish a fully developed pipe flow. Hence, the customised manifold system is sufficient to ensure that the present configuration achieves, or closely approximates fully developed pipe flow.

The symmetry of the flow was carefully reconfirmed in a series of sensitivity study prior to the actual PIV measurement. Briefly, the data from “0° - plane” P_{00} (jet inlet plane) and “45° - plane” P_{45} (the plane rotated 45° relative to 0° - plane) were measured for the reference configuration of $L_c/D_c = 3$ with $\alpha_j = 25^\circ, 35^\circ, 45^\circ$ and $\theta_j = 5^\circ, 10^\circ, 15^\circ$. Figure 3.2 presents a schematic diagram of the measurement planes for the study of symmetry. The results showed that all investigated cases feature significant symmetric or axisymmetric flow-fields for both "0° - plane" and "45° - plane". A detailed description of the measurement is presented in Chapter 5.

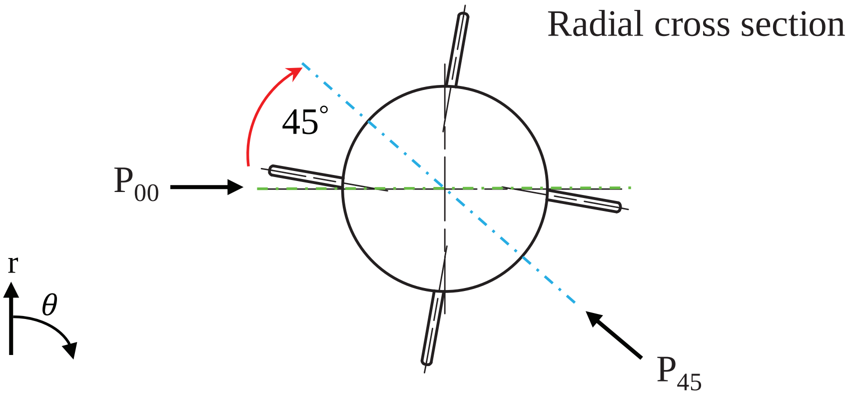

Figure 3.2: Schematic diagram of the radial cross section, showing the measurement planes of "0° - plane" P_{00} and "45° - plane" P_{45}.

The flow was seeded with hollow glass spheres of 12 μm diameter and with a specific gravity of 1.1. The resultant Stokes number (Sk_D), based on the bulk exit velocity and exit diameter of the nozzle was $Sk_D = 0.003$ ($Sk_D = \rho_p D_p^2 U_e / 18 \mu_f D_{pipe}$ where ρ_p is the particle density and D_p is the particle diameter), which is sufficiently low to enable the particles to follow the flow down to length scales that can be resolved with the PIV measurement. Owing to the closed-loop design of the entire system, continuous seeding of particles was not required.

The optical arrangement and the measurement region are shown schematically in Figure 3.3. The source of illumination for the PIV measurements was a double-head, pulsed Nd:YAG laser (Quantel Brilliant B), operating at a fixed pulsing frequency of 10 Hz and a maximum power of approximately 400 mJ. The laser was operated in the frequency-doubled mode to provide a wavelength of 532 nm. The laser beam was formed into a sheet with a combination of three cylindrical lenses (Thorlabs) that were aligned with the centreline of the cylindrical chamber and positioned to illuminate the measurement region, as shown in Figure 3.3. The thickness of the light sheet was measured by using both the burn marks and image data-processing, resulting in a thickness of 1.5 mm at the focal line.

The PIV raw images were captured with a Charged Coupled Device (CCD) camera (Kodak Megaplus ES2093) with an array of 1920 × 1080 pixels. The frame rate of CCD camera for the PIV measurements was set to match that of the laser at 10 Hz. The x-r plane (see Figure 3.3b), which provides the axial (x) and radial (r) instantaneous velocity components, was approximately 123 mm (L_i) × 66 mm (W_i) in size, while the r-θ plane (see Figure 3.3c) was approximate 37 mm in radius to measure the tangential component (θ) within the MIJCC configuration. This measurement region was chosen to avoid interference from reflections caused by curved acrylic sections and interfaces between different sections. The shape of the conical component within the chamber prevented optical access there, so that measurements were performed only within the cylindrical part of the chamber, downstream from the edge of the cylinder for approximately $S_i = 2 \sim 10$ mm, depending on the configuration (See Figure 3.3b).

A minimum of 1500 PIV image pairs (12 bits) was recorded for each experimental condition. An in-house PIV code in MATLAB R2015a (Mathworks) was employed to process the raw images. A single-pass, Fast Fourier Transform (FFT) algorithm, together with an interrogation window size of 32 × 32 pixels was used for the data-processing, resulting in an effective probe volume of 2 mm × 2 mm × 1.5 mm. It should be noted that the current PIV measurement cannot resolve small-scale velocity field (e.g., Kolmogorov scales) and this is also not an objective of the present study. In addition, a multi-grid correlation algorithm with 50% overlap was applied to calculate the displacement of seeding particles and also to minimize noise. Outliers (erroneous vectors) were identified by using an in-house PIV code in the post-processing, which compares the value difference between the absolute and relative velocities. The average number of outliers was less than approximately 5% of the total vectors, and all outliers were removed from the ensemble.

The overall uncertainty associated with the PIV measurements comprises both systematic and measurement errors. The systematic errors arise both from geometrical uncertainty, derived from manufacturing tolerances, and from measurement uncertainties. The volumetric flow rate of each inlet-pipe was measured independently by using a flowmeter prior to each single measurement. The averaged difference between each inlet-pipe was calculated to be ≈ 1.6 - 1.8%, resulting in a 2% uncertainty of the desired flow rate. The spatial resolution of the PIV and cylinder, which incorporates the effect of optical distortion, was assessed by calibration with a customized grid that was inserted into the cylindrical chamber before each experiment. On this basis, the uncertainty of position was estimated to be ± 0.05mm within the measurement region, which is around 0.03%. The time separation between successive image pairs in the PIV measurement was chosen to achieve an average particle displacement of about 8~10 pixels (1/3 of the interrogation window size), as estimated from the centreline region of images, with the highest expected mean velocity. The bias error associated with the time separation between the laser pulses was estimated to be ± 2%. The uncertainty due to the sample size was calculated from value difference in the velocity fields along the centreline and selected radial profiles of the chamber for sample size within the range of 100 to 2000 image pairs, with an increment of 100. The difference was below 1% for a sample size of ≥ 1500. Based on the inaccuracies in calibration and observed scatter in present measurements, the overall uncertainty of the measured mean and RMS velocities for the present study is estimated to be $\epsilon_{overall} \approx 5\%$.

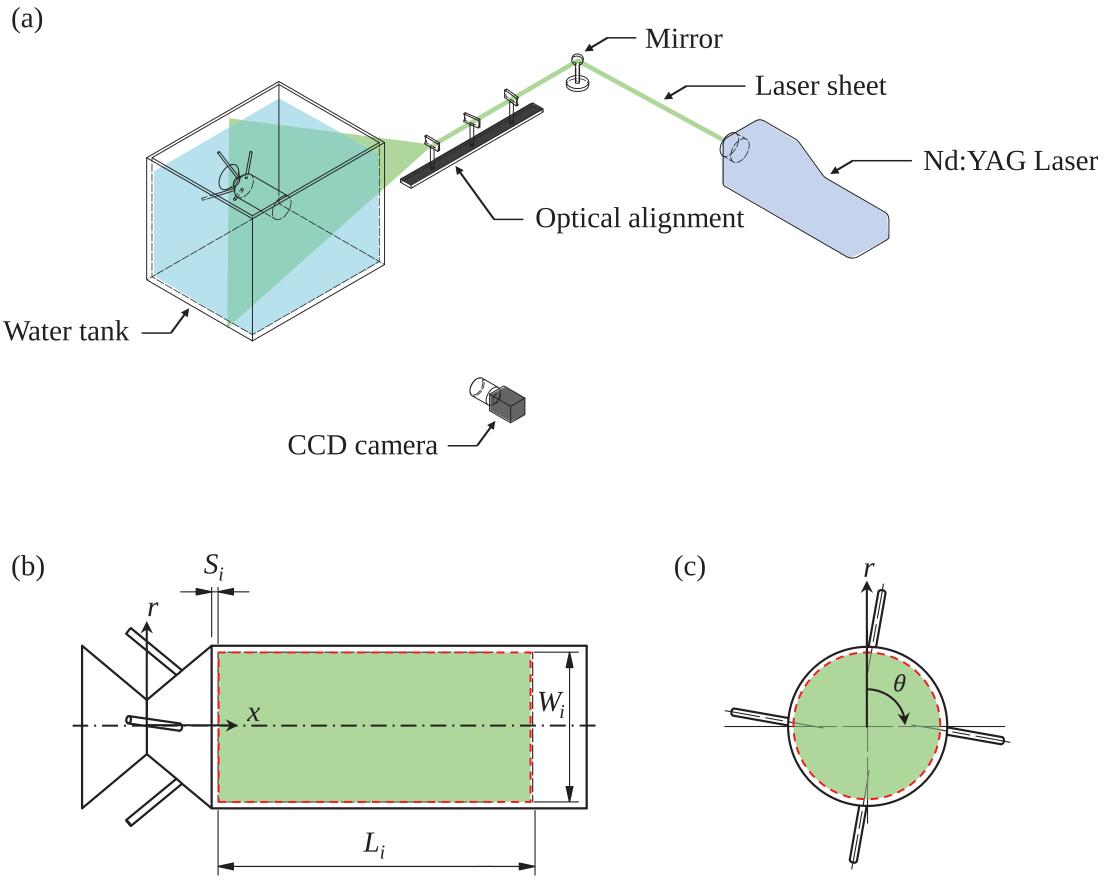

Axial cross section

Radial cross section

Figure 3.3: (a) The PIV setup, showing the Nd:YAG laser, optics arrangement, light sheet and camera, (b) Axial measurement region (green box enclosed by a red dashed line) relative to the chamber, and (c) Radial cross-section, showing the radial measurement region.

3.4 Numerical methods

Numerical simulation was conducted to provide qualitative information on the flow field in regions of the flow for which experimental data are not available. The commercial Computational Fluid Dynamics (CFD) code ANSYS/CFX 16.1 was employed to simulate the flow-field, utilising the Reynolds-Averaged Navier-Stokes (RANS) method. The three-dimensional computational model of the device, shown in Figure 3.4, was generated with the commercial Computer Aided Design (CAD) package PTC Creo. Due to the axis-symmetric geometry and to reduce the computational cost, only a quarter of the full domain was modelled utilising the symmetry boundary option in the code. This simplification relies on the assumption that no circumferential instability, such as a precession, can occur. This, as is shown below (Figure 3.4), is true for most conditions but not all.

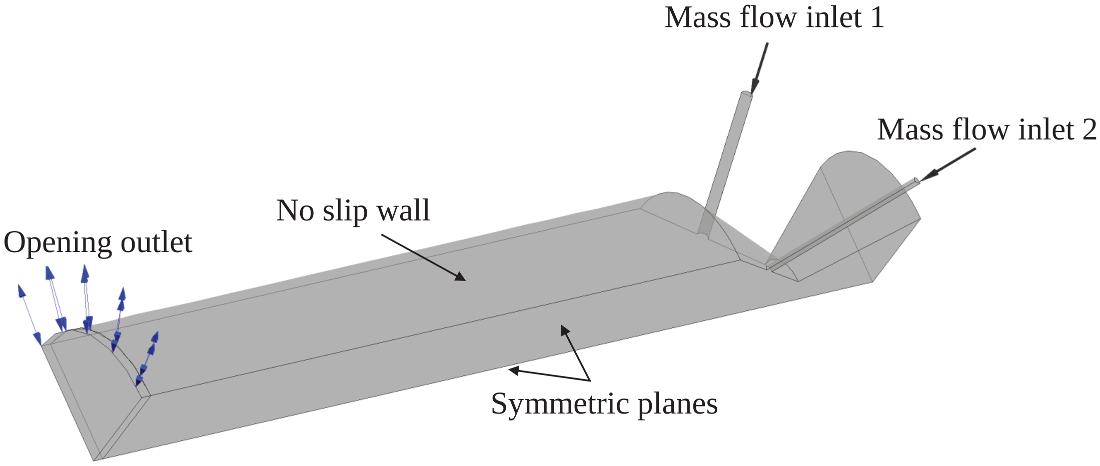

Figure 3.4: The CFD domain of the MIJCC configuration investigated in the present study.

The uncertainties associated with the CFD simulation arise mostly from limitations in mesh quality and simplification of the turbulence models. The influence of uncertainty of the boundary conditions was small because of the care taken to ensure fully developed pipe flow at the inlet (described in Section 3.3), but was nevertheless assessed systematically by a sensitivity analysis for both the inlet and outlet conditions. This showed that the difference in the calculated mean velocity field changed by less than 1% with changes to the boundary condition. The selected boundary conditions are shown in Figure 3.4.

The ANSYS/Meshing 16.1 CFD code was used to generate the computational mesh. A structured mesh was chosen for all circular components (nozzles, cylindrical chamber), while non-uniform unstructured grids were chosen for the conical components. The mesh quality was checked for expansion factor, aspect ratio, skewness and orthogonality. The influence of the number of mesh nodes on the CFD results was evaluated through a mesh independence test. Figure 3.5 presents the radial profiles of the calculated mean axial velocity U_x, normalised by inlet bulk velocity U_e, for mesh nodes number 2×10^6, 4×10^6, 8×10^6 and 12×10^6 at the jet impingement point for the case of $N_j = 4$ and $\alpha_j = 25^\circ$ (MIJCC-25-4J). It can be seen that the grid was sufficiently converged for 8 million mesh nodes (8×10^6) with a maximum difference of 2% compared to 12 million mesh nodes. This result indicates that 8 million mesh nodes represent a good compromise between the accuracy of the calculated results and computational cost.

The convergence criterion for all CFD cases was set to be 1×10^{-5} (RMS). A total of 38 configurations of the planar-symmetric MIJCC were assessed, comprising inclination angles from $\alpha_j = 0^\circ$ to 90° in 5° increments for both the 2-Jet ($N_j = 2$) and 4-Jet ($N_j = 4$) configurations. The working fluid and the inflow conditions assessed in the numerical simulations were chosen to match those of the PIV measurements (i,e., water as working fluid and $Re_D = 10500$).

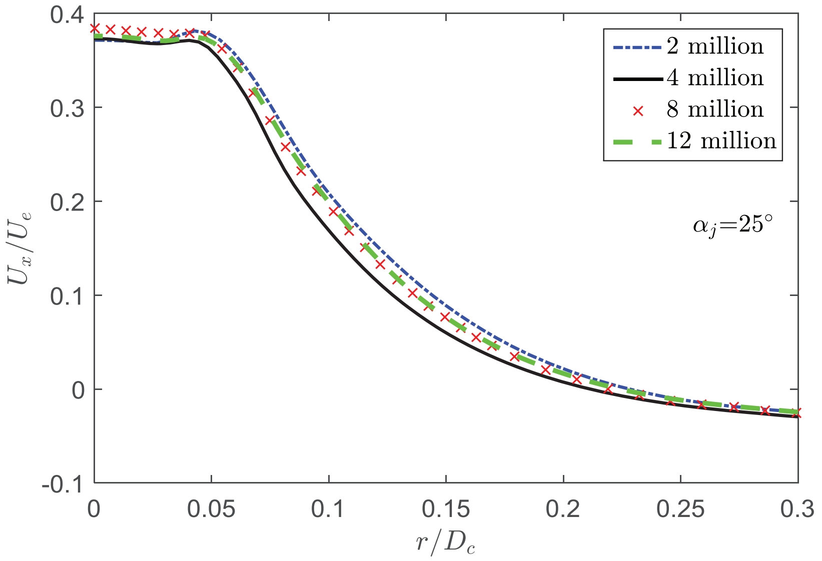

Figure 3.5: Radial profiles of the calculated mean axial velocity U_x, normalised by inlet bulk velocity U_e, at the jet impingement point for the MIJCC configuration of N_j = 4 and α_j = 25° for four different computational meshes.

Previous CFD modelling studies [77, 103, 104] have shown that the Reynolds Stress model (RSM) can be used to provide a reasonable prediction of the mean velocity field of multiple-jets flow within a confined space. Figure 3.6 presents the evolution of normalized mean axial velocity (U_c/U_e) along the centreline of the MIJCC chamber as calculated with three turbulence models, namely, the Baseline Reynolds Stress model (BSL RSM), Standard k-ε (SKE) model and Shear Stress Transport (SST) model, in comparison with the PIV data for the case where α_j = 25° and N_j = 2 (MIJCC-25-2J). It can be seen that both the SST and SKE models fail to reproduce the trend and magnitude of the centreline velocity, while the BSL RSM model shows good quantitative and qualitative agreements with the measured data, together with a maximum difference of 13% at x/L_c = 0.4. The inaccuracy of the SST and SKE models for the present case is attributed to the modelling of the Reynolds stresses as isotropic stresses in these models. The BSL RSM has additional six transport equations for Reynolds stresses that is expected to model the Reynolds stresses more accurately than the SKE and SST models. Hence, the Baseline Reynolds Stress model in ANSYS/CFX gives a reasonable agreement of the centreline velocity evolution for the current MIJCC configuration compared with the Standard k-ε model and Shear Stress Transport model.

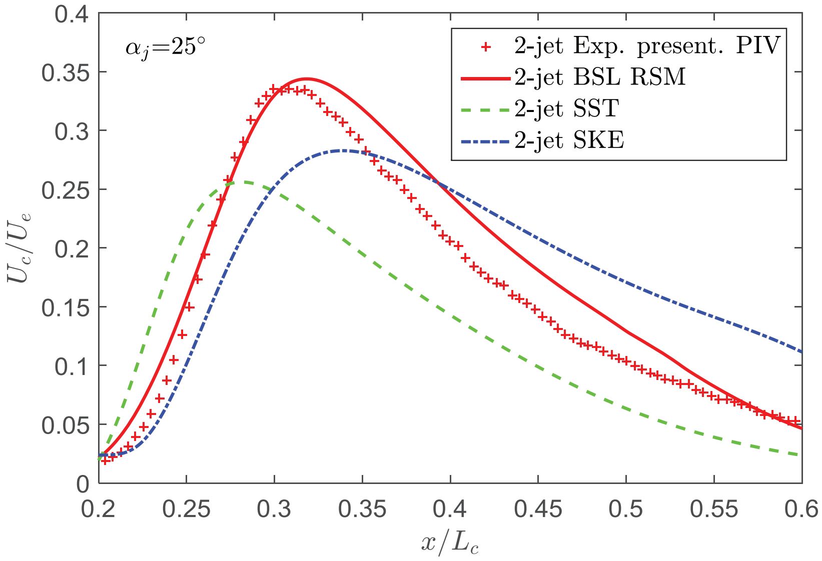

Figure 3.6: Evolution of the mean axial velocity along the centreline of the MIJCC configuration for the case of α_j = 25° and N_j = 2 (MIJCC-25-2J) for both the experimental data (plus sign) and the results calculated with three turbulence models (lines), namely, the Baseline Reynolds Stress (BSL RSM), Standard k-ε (SKE) and Shear-Stress-Transport (SST) models.

A preliminary comparison of the relative performance of five alternative RSM models [83, 105-108] available in ANSYS/CFX was also undertaken for one configuration of confined jets. These models are the “Baseline Reynolds Stress”, the “SSG (Speziale, Sarkar, Gatski) Reynolds Stress”, the “LRR (Launder, Reece and Rodi) Reynolds Stress”, the “Omega Reynolds Stress” and the “QI (Quasi-Isotropic) Reynolds Stress” models. The models were assessed on the basis of the mean velocity field and the Reynolds stresses. Figure 3.7 presents the comparison of the evolution of normalized mean axial velocity (U_c/U_e) along the centreline of the MIJCC chamber (Figure 3.7a), and the radial profile of non-dimensional Reynolds stress ($<uv>/U^2_c$) at the jet impingement point (Figure 3.7b), for the case of $\alpha_j = 25^\circ$ and $N_j = 2$ (MIJCC-25-2J). Figure 3.7a shows that the LRR RSM, QI RSM and SSG RSM models over-predict the peak velocity by about 15%, 11% and 32%, respectively, while the OMEGA RSM under-predicts the peak velocity at the impingement point by 11%. The BSL RSM model achieves the best agreement with the experimental data, with an average 10% over-prediction thought the centreline velocity.

In Figure 3.7b, the BSL RSM model gives a reasonable agreement with the trend and location of the peak value of $<uv>/U^2_c$. The reasonable difference (10%) between the BSL RSM prediction and the measured data is mainly caused by the unsteadiness and “out-of-plane” motion in the resulting jet (refer to Chapter 4 for details). Hence, it can be concluded that the BSL RSM model provides the best prediction to the mean velocity and Reynolds stress for the MIJCC configurations. The Baseline RSM model was selected as the turbulence closure model for the present study, which is hereafter referred to as the “RSM model” for brevity in Chapter 4.

All CFD simulations were performed with a supercomputing cluster (Dell PowerEdge R815 Rack Mount Server) with two AMD 12-Core Opteron 6174 Processors and 40GB of RAM. An average of 5 hours of CPU-time was required to achieve the desired convergence of 1×10^{-5} (RMS).

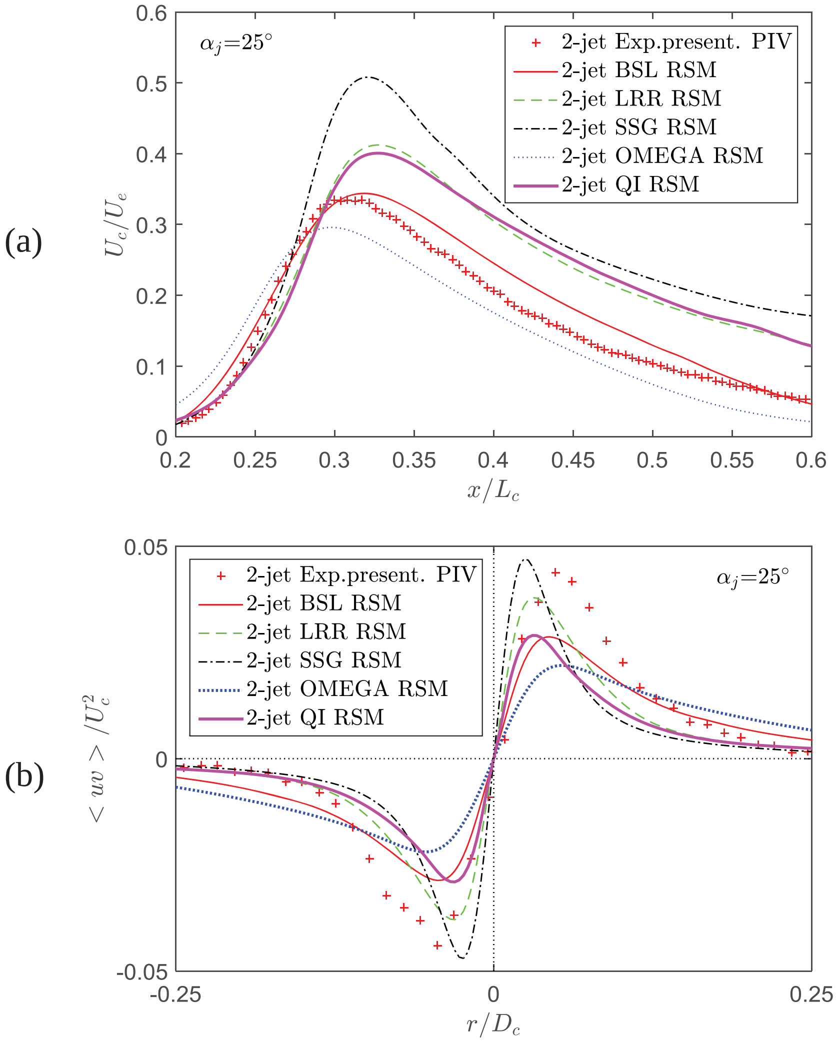

Figure 3.7: Evolution of the (a) normalised mean axial velocity along the centreline of the MIJCC (U_x/U_e), and (b) radial profiles of non-dimensional Reynolds stress ($<uv>/U^2_c$) at the jet impingement point for the case of $\alpha_j = 25^{\circ}$ and $N_j = 2$ (MIJCC-25-2J) for both the experimental data (plus sign) and the calculated results from five Reynolds Stress models (lines).

Chapter 4

Experimental and Numerical Investigation of the Iso-thermal Flow Characteristics within a Cylindrical Chamber with Multiple Planar-symmetric Impinging Jets

Statement of Authorship

Title of Paper	Experimental and numerical investigation of the iso-thermal flow characteristics within a cylindrical chamber with multiple planar-symmetric impinging jets
Publication Status	☑ Published ☐ Accepted for Publication ☐ Submitted for Publication ☐ Unpublished and Unsubmitted w ork w ritten in manuscript style
Publication Details	Long, S., Lau, T.C., Chinnici, A., Tian, Z.F., Dally, B.B. and Nathan, G.J., 2017, 'Experimental and numerical investigation of the iso-thermal flow characteristics within a cylindrical chamber with multiple planar-symmetric impinging jets', Physics of Fluids, vol. 29, no. 10, p. 105111.

Principal Author

Name of Principal Author (Candidate)	Shen Long		
Contribution to the Paper	Conducted literature review, collected all experimental data, conducted all CFD modelling, performed data processing and analysis, wrote manuscript and acted as corresponding author.		
Overall percentage (%)	65		
Certification:	This paper reports on original research I conducted during the period of my Higher Degree by Research candidature and is not subject to any obligations or contractual agreements with a third party that would constrain its inclusion in this thesis. I am the primary author of this paper.		
Signature	[redacted]	Date	07/01 /2019

Co-Author Contributions

By signing the Statement of Authorship, each author certifies that:

i. the candidate's stated contribution to the publication is accurate (as detailed above);

ii. permission is granted for the candidate in include the publication in the thesis; and

iii. the sum of all co-author contributions is equal to 100% less the candidate's stated contribution.

Name of Co-Author	Timothy Lau		
Contribution to the Paper	Supervised the experiments, performed data processing and edited manuscript.		
Signature	[redacted]	Date	7/01/2019

Name of Co-Author	Alfonso Chinnici		
Contribution to the Paper	Helped to develop the work, provided ideas and edited manuscript.		
Signature	[redacted]	Date	7/01/19

Name of Co-Author	Zhao Feng Tian		
Contribution to the Paper	Supervised the CFD modelling work and provided comments.		
Signature		Date	7-1-2019

Name of Co-Author	Bassam Dally		
Contribution to the Paper	Supervised the development of work, provided comments and edited manuscript.		
Signature		Date	7-1-19

Name of Co-Author	Graham 'Gus' Nathan		
Contribution to the Paper	Supervised the development of work, helped in data interpreting, provided comments and edited manuscript.		
Signature		Date	7/1/19

PHYSICS OF FLUIDS **29**, 105111 (2017)

Experimental and numerical investigation of the iso-thermal flow characteristics within a cylindrical chamber with multiple planar-symmetric impinging jets

Shen Long,[a] Timothy C. W. Lau, Alfonso Chinnici, Zhao Feng Tian, Bassam B. Dally, and Graham J. Nathan
Centre for Energy Technology, School of Mechanical Engineering, The University of Adelaide, Adelaide, South Australia 5005, Australia

(Received 2 June 2017; accepted 5 October 2017; published online 30 October 2017)

We present a joint experimental and numerical study of the flow structure within a cylindrical chamber generated by planar-symmetric isothermal jets, under conditions of relevance to a wide range of practical applications, including the Hybrid Solar Receiver Combustor (HSRC) technology. The HSRC features a cavity with a coverable aperture to allow it to be operated as either a combustion chamber or a solar receiver, with multiple burners to direct a flame into the chamber and a heat exchanger that absorbs the heat from both energy sources. In this study, we assess the cases of two or four inlet jets (simulating the burners), configured in a planar-symmetric arrangement and aligned at an angle to the axis (α_j) over the range of 0°–90°, at a constant inlet Reynolds number of $Re_D = 10\,500$. The jets were positioned in the same axial plane near the throat and interact with each other and the cavity walls. Measurements obtained with particle image velocimetry were used together with numerical modeling employing Reynolds-averaged Navier-Stokes methods to characterize the large-scale flow field within selected configurations of the device. The results reveal a significant dependence of the mean flow-field on α_j and the number of inlet jets (N_j). Four different flow regimes with key distinctive features were identified within the range of α_j and N_j considered here. It was also found that α_j has a controlling influence on the extent of back-flow through the throat, the turbulence intensity, the flow stability, and the dominant recirculation zone, while N_j has a secondary influence on the turbulence intensity, the flow stability, and the transition between each flow regime. *Published by AIP Publishing.* https://doi.org/10.1063/1.4986132

I. INTRODUCTION

Unlike the simple round jet issuing into a quiescent environment, which has received significant attention,[1–4] the flow-field of multiple impinging jets within a confined space is poorly understood. Nevertheless, these configurations have wide relevance to many engineering applications, including gas turbine engines for modern aircraft,[5] separated-jet combustors for combustion technology,[6] and longitudinal ventilation systems for large enclosures.[7–9] Of particular interest here is a multiple-jet configuration with a planar-symmetric arrangement for the design of the Hybrid Solar Receiver Combustor (HSRC) under development at the University of Adelaide.[10–14] The HSRC offers the potential to reduce both the energy losses and total infrastructure requirements relative to a hybrid from stand-alone components (such as start-up and shut-down of the back-up combustor), while providing a firm supply of energy for heat and power applications. It features a cavity operable as a solar receiver and/or a combustion chamber with multiple burners to direct a flame into the chamber and a heat exchanger within it to absorb the heat from either energy source. The burners are configured in a planar-symmetric arrangement and aligned at an angle to the axis of the chamber, so that they interact with each other within the chamber. The presence of walls (confinement) has an additional influence in restricting the entrainment of the surrounding fluid, changing the pressure field and hence also the direction of flow.[15] Although a wide range of potential inclination angles (α_j) between jet nozzles are possible, two configurations have received the most attention previously, that of parallel-jets and opposed-jets. However, multiple impinging jets are much more complex than a single jet because of the additional parameters, so that many gaps in understanding remain. The overall objective of the present paper is therefore to characterize for the first time all of the flow regimes that can be generated within a cylindrical chamber (i.e., as a confined flow) with multiple planar-symmetric impinging inlet-jets of an arbitrary inclination angle that is equal for all jets.

Previous studies of the evolution of large flow structures from multiple impinging jets have been performed almost exclusively for unconfined environments. These have shown that the flow characteristics depend strongly on the key geometric features of the nozzles as well as their arrangement.[16–23] For example, Tanaka[17,18] found that, for a transitional/turbulent flow regime ($4300 < Re_D < 9000$), the rate of maximum decay in centerline jet velocity (U_m) increases with an increase in the distance between each nozzle, S_0, normalized with the nozzle width. Menon and Gollahalli[21] and Leite *et al.*[16] revealed that, for a given S_0 within the range

---

[a] Author to whom correspondence should be addressed: shen.long@adelaide.edu.au

$4000 < Re_D < 15\,000$, the flow stability and the flame length in the merged flow from multiple unconfined reacting jets increase as the number of jets (N_j) is increased. Nevertheless, the majority of previous investigations only investigated the flow-field from parallel impinging jets (i.e., $\alpha_j = 0°$) or directly impinging jets (i.e., $\alpha_j = 90°$), so that few studies are available for inclined impinging jets with planar-symmetric arrangements (i.e., $0° < \alpha_j < 90°$). Little information is available for confined jets, although confined impinging jets are directly relevant to many industrial applications, such as gas turbine combustors,[5] aerodynamic curtains in solar receivers/reactors,[24] and novel burners/furnaces.[6] Furthermore, previous studies have been performed for a wide range of different values of the inlet jet Reynolds number (Re_D) and other inlet conditions, which makes it difficult to isolate the influence of Re_D from other parameters, owing to the asymptotical dependence of Re_D on the turbulent flow field.[25] Hence, a more detailed characterization of the flow patterns within a confined chamber for a systematic range of well-defined and consistent inflow and boundary conditions is needed to provide new understanding of the flow generated by inclined confined jets. The present paper aims to meet this need.

From previous research of inclined, confined, and impinging jets, it can be found that the inclination angle (α_j) can significantly influence the flow-field. The flow visualization experiments of Chammem *et al.*[26] showed that the impingement of planar-symmetric inclined confined jets ($N_j = 2$) generates a central, merged jet downstream from the impingement point, termed the "resulting jet." Their work also showed that the vortex structure in the resulting jet is much more complex than that in a single jet, owing to the effect of jet-interaction on vortex formation. The Computational Fluid Dynamics (CFD) investigation by Chammem *et al.*[27] found that the vortex structure upstream from the impingement point, dubbed the "reverse flow" region, can only be generated within a certain range of α_j. However, while this work provides useful insight, it is of limited value for model validation because it does not report detailed inflow information and boundary conditions. Similarly, Boushaki and Sautet[28] showed that α_j has a significant influence both on the mixing and instantaneous velocity fields of multiple-jets configurations for a separated-jet combustor with α_j = 0°, 10°, 20°, 30°, but they also did not report details of the inflow and boundary conditions for inclined-jets cases. Furthermore, none of the previous measurements of inclined, confined, and impinging jets provide a comprehensive understanding of the influence of jet arrangement for all of the regimes of flow-fields that can be generated. Instead, all previous investigations have been limited to a relatively small range of conditions, such as a limited range of α_j. Therefore, there is poor understanding of the influence of the key dominant parameters, particularly of α_j and N_j, on the resulting flow field for confined impinging jets in planar-symmetric arrangements (e.g., N_j = 2 and 4). In addition, the existing data sets for planar-symmetric jets provide insufficient information for the unambiguous development and validation of computational models across the full range of angles $0° < \alpha_j < 90°$. Hence, there is also a need to obtain sufficient reliable experimental data to fully characterize the flow field of multiple planar-symmetric impinging jets in a confined space and to assess the validity of CFD models through this range.

To meet the aforementioned needs, the current investigation aims (a) to provide a detailed characterization of the flow-field for planar-symmetric arrangements of impinging jets with well-defined inflow conditions within a cylindrical chamber; (b) to identify the influence of the inclination angle of jets α_j from 0° to 90° for two or four jets (N_j = 2 or 4), on large-scale flow structure; and (c) to provide a map of flow regimes for planar-symmetric arrangements of impinging jets in a cylindrical chamber. The present paper, which forms part of a larger research program, reports a joint experimental and numerical investigation of the iso-thermal flow-field generated by Multiple Impinging Jets in a Cylindrical Chamber (MIJCC) under configurations most relevant to HSRC technology. The primary objective of the CFD work are, firstly, to provide qualitative understanding of the flow-field in regions of the flow for which experimental data are not available (due to experimental constraints) and, second, to assess accuracy and limitations of commercially available models with a view to guiding the development of further CFD modeling endeavors.

II. METHODOLOGY

A. Configurations selected in the present study

A schematic diagram of the MIJCC configuration is shown in Fig. 1. This geometry is simplified relative to the HSRC to facilitate understanding and to increase relevance to other related devices. Its key features are the main cavity, consisting of a cylindrical chamber with a conical expansion, and a secondary concentrator (SC), used to concentrate solar radiation in a solar receiver, which is of conical shape. The SC was closed at the largest end with a flap (labeled with a green line), preventing flow to the ambient environment, but open at the plane of the throat (labeled with a yellow line) to admit flow between these sections. This corresponds to the configuration

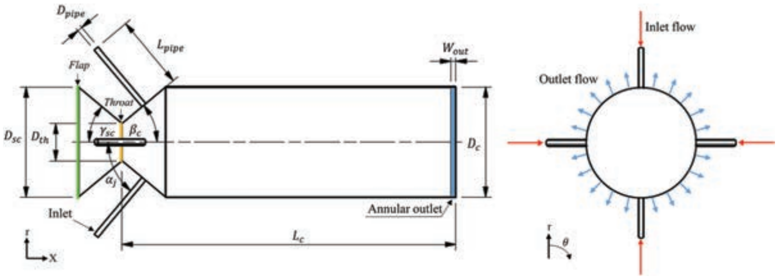

FIG. 1. Schematic diagram of the Multiple Impinging Jets in a Cylindrical Chamber (MIJCC) configurations investigated here, showing the key geometric features from the axial cross section (left) and a radial cross section (right). Here the flap plane, throat plane, and annular outlet are highlighted with green, yellow, and blue lines, respectively.

TABLE I. Values of the geometric parameters of the MIJCC (see Fig. 1) that have been investigated in the present study.

Dimensions	Description	Value
D_c	Chamber diameter	74 mm
D_{sc}	Diameter of the secondary concentrator	74 mm
D_{th}	Throat diameter	24.6 mm
D_{pipe}	Inlet pipe diameter	3.35 mm
L_c	Chamber length	225 mm
L_{pipe}	Inlet pipe length	150 mm
W_{out}	Outlet gap	3 mm
α_j	Jet inclination angle	0°–90°
β_c	Conical expansion angle	40°
γ_{sc}	Angle of the secondary concentrator	40°

of the HSRC within the combustion-only mode, where the aperture is closed with a flap to prevent heat loss. The MIJCC is configured with four planar-symmetric inlet jets distributed around the conical expansion of the main chamber with an inclination angle (α_j) to the axis of the chamber. The flow leaves the chamber in the radial direction through an annular gap around a bluff end wall of uniform thickness, W_{out}. The dimensions of the key geometrical parameters of the MIJCC configurations investigated here are given in Table I.

B. Experimental arrangement

Planar Particle Image Velocimetry (PIV) was employed to investigate the instantaneous and mean flow-fields within selected configurations. Measurements were performed under iso-thermal conditions at ambient temperature using water as the working fluid to avoid deposition of tracer particles onto confining walls. Two laboratory-scale models with inclination angles of $\alpha_j = 25°$ and 50° were manufactured from acrylic to provide optical access and a close match between the refractive index of the chamber and that of the working fluid, with tolerances of ±0.1 mm (linear) and ±0.5° (angular). These two angles were selected to ensure the impingement point for experimental cases is within the cylindrical chamber, as is necessary for optical access, and to achieve a sufficiently large increment of α_j required to provide distinct flow-features. These were assessed for the cases with equal flows to either two or four planar-symmetric jets, as shown in Table II.

To limit optical distortion, the entire experimental model was fully submerged into a rectangular water tank with dimensions of 500 mm (L) × 400 mm (W) × 390 mm (H). This water tank was also made from acrylic. The water from the outlets was discharged into the water tank, which overflowed to a reservoir. The discharged fluid was reinjected through the jets using a variable-speed-drive enabled water pump (Pan World NH-200PS), a frequency converter (Danfoss VLT 2800) and flowmeters (ABB D10A11), resulting in a closed-loop system.

TABLE II. The notation for the configurations investigated experimentally in the present study.

Experiment case no.	Configurations	Jet inclination angles, α_j (°)	Jet number, N_j
1	MIJCC_25_2J	25	2
2	MIJCC_25_4J	25	4
3	MIJCC_50_2J	50	2
4	MIJCC_50_4J	50	4

The inlet jet bulk injection velocity (U_b) was fixed at 2.8 m/s for each nozzle, leading to an inlet jet Reynolds number $Re_D = 10\,500$ ($Re_D = \rho_f U_b D_{pipe}/\mu_f$, where ρ_f is the fluid density and μ_f is the fluid dynamic viscosity). This ensures that the inlet flow is within the fully turbulent regime. The jets were generated with a supply system that was carefully designed to ensure both overall flow symmetry and fully developed pipe flow at the exit. A symmetrical manifolding system was employed to ensure equal flow distribution to each jet, which fed 150 diameters of gently curved flexible piping, feeding 46 diameters of perfectly straight pipe. The perfectly straight section exceeds the 40 diameters found by Nikuradse[29] to be the minimum needed to establish a fully developed pipe flow. Hence, the combination of the long gently curved supply to the straight section is sufficient to ensure that the present configuration achieves or closely approximates a fully developed pipe flow.

The flow was seeded with hollow glass spheres of 12 μm in diameter and with a specific gravity of 1.1. The resultant Stokes number (Sk_D), based on the bulk exit velocity and exit diameter of the jet, was Sk_D =0.003 ($Sk_D = \rho_p {D_p}^2 U_b/18\mu_f D_{pipe}$, where ρ_p is the particle density and D_p is the particle diameter), which is sufficiently low to enable the particles to follow the flow down to length scales that can be resolved with the PIV measurement. Owing to the closed-loop design of the entire system, continuous seeding of particles was not required.

The optical arrangement and the measurement region are shown schematically in Fig. 2. The illumination for the PIV measurements was sourced from a double-head, pulsed Nd:YAG laser (Quantel Brilliant B), frequency doubled to provide a wavelength of 532 nm at a fixed pulsing frequency of 10 Hz. The laser beam was formed into a sheet with a combination of three cylindrical lenses (Thorlabs plano-convex and plano-concave lenses) that were aligned with the axis of inlet nozzles and positioned to illuminate the measurement region, as shown in Fig. 2. The thickness of the light sheet was estimated to be 1.5 mm at the focal line.

The images were captured with a Charged Coupled Device (CCD) camera (Kodak Megaplus ES2093) with an array of 1920 × 1080 pixels. The frame rate of the CCD camera for the PIV measurements was set to match that of the laser at 10 Hz. The x-r plane (see Fig. 2), which provides the axial (u) and radial (v) instantaneous velocity components, was 118 mm (L_i) × 66 mm (W_i) in size. This measurement region was chosen to avoid interference from reflections caused by curved acrylic sections and interfaces between different sections. The shape of the conical component within the chamber prevented optical access there, so that measurements were performed only within the cylindrical part of the chamber, downstream from the edge of the cylinder for approximately S_i = 2–10 mm, depending on the configuration [note that the investigation of the flow-field within the two conical sections was performed using computational fluid dynamics (CFD), as is described in Sec. II C].

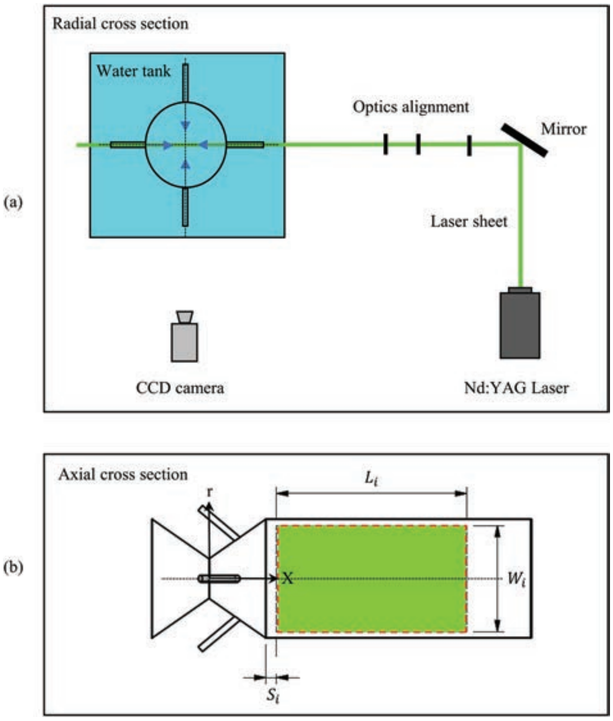

FIG. 2. (a) The optical arrangement, showing the laser, optics, light sheet, and (b) measurement plane (green box enclosed by a red dashed line) relative to the chamber.

A minimum of 3000 PIV images (12 bits) were recorded for each measurement. The image-processing was performed with an in-house PIV code in MATLAB (Mathworks), with an interrogation window size of 32 × 32 pixels, leading to a spatial resolution of 2 mm in each direction. A multi-grid correlation algorithm with 50% overlap was applied to all cases. Outliers (erroneous vectors) were identified in the post-processing using an in-house code to compare both absolute velocity and relative velocity differences. All erroneous vectors were removed from the ensemble.

The overall uncertainty associated with the PIV measurements comprises both systematic and measurement errors. The systematic errors arise both from geometric uncertainty, derived from manufacturing tolerances, and from measurement uncertainties. The measurement uncertainties from the flowmeter was measured to be ±1.6% of the desired flow rate, resulting in an estimated uncertainty of the exit velocity from the four pipes of less than 2%. The spatial resolution of the PIV and cylinder, which incorporates the effect of optical distortion, was assessed by calibration with a customized grid that was inserted into the cylindrical chamber before each experiment. On this basis, the uncertainty of position was estimated to be ±0.05 mm within the measurement region. The time separation between successive image pairs in the PIV measurement was chosen to achieve an average particle displacement of about 8–10 pixels (1/3 of the interrogation window size), as estimated from the centerline region of images, with the highest expected mean velocity. The bias error associated with the time separation between the laser pulses was estimated to be ±2%, while the uncertainty due to the sample size was less than 1% for a sample size of 3000. Based on the evaluation of systematic and measurement errors, the overall uncertainty of the measured mean and r.m.s. (root-mean-square) velocities for the present study is estimated to be less than ±2%.

C. Computational modeling

The commercial computational fluid dynamics (CFD) code ANSYS/CFX 16.1 was employed to simulate the flowfield, utilizing the Reynolds-Averaged Navier-Stokes (RANS) method. The three-dimensional computational model of the device, shown in Fig. 3, was generated with the commercial computer-aided design (CAD) package PTC Creo. Due to the axisymmetric geometry and to reduce computational cost, only a quarter of the full domain (Fig. 3) was modeled utilizing the symmetry boundary option in the code. This simplification relies on the assumption that no circumferential instability, such as a precession, can occur. This, as is shown below (Fig. 3), is true for most conditions but not all.

The uncertainties associated with the CFD simulation arise mostly from limitations in mesh quality and simplification of the turbulence models. The influence of uncertainty of the boundary conditions was small because of the care taken to ensure fully developed pipe flow at the inlet (described above) but was nevertheless assessed systematically by a sensitivity analysis for both the inlet and outlet conditions. This showed that the difference in the calculated mean velocity field changed by less than 1% with changes to the boundary condition. The selected boundary conditions are shown in Fig. 3. The ANSYS/Meshing 16.1 CFD code was used to generate the computational mesh. A structured mesh was chosen for all circular components (nozzles, cylindrical chambers), while non-uniform unstructured grids were chosen for the conical components. The mesh quality was checked for expansion factor, aspect ratio, skewness, and orthogonality. The influence of the number of mesh nodes on the CFD results was evaluated through a mesh independence test, which showed that approximately 8×10^6 mesh nodes represent a good compromise between the accuracy of the calculated results and the simulation time. The convergence criterion for all cases was set to be 1×10^{-5} (r.m.s.). A total of 38 configurations of the MIJCC were assessed, comprising inclination angles from $\alpha_j = 0°$ to 90° in 5° increments for both the 2-jet (19 models) and 4-jet (19 models) configurations. The working fluid and the inflow conditions assessed in the numerical simulations were chosen to match those of the PIV measurements (i.e., water as working fluid and $Re_D = 10\,500$).

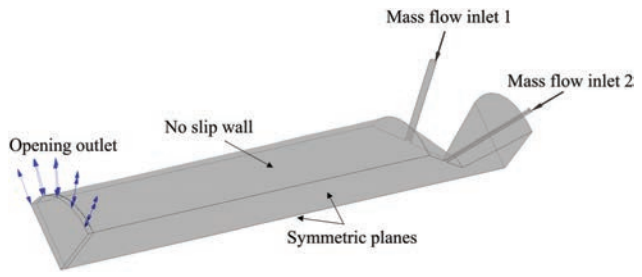

FIG. 3. The CFD domain of the Multiple Impinging Jets in a Cylindrical Chamber (MIJCC) configuration.

TABLE III. Axial positions of the radial profiles for which data are reported, together with the methods employed to investigate them. The circumferential plane is shown in Fig. 4.

Transect	Location, x/L_c	Methods	Investigated case no.
1	0.14	PIV, CFD	3, 4
2	0.18	PIV, CFD	3, 4
3	0.22	PIV, CFD	1, 2, 3, 4
4	0.26	PIV, CFD	1, 2, 3, 4
5	0.31	PIV, CFD	1, 2, 3, 4
6	0.35	PIV, CFD	1, 2, 3, 4
7	0.40	PIV, CFD	1, 2
8	0.44	PIV, CFD	1, 2
9	0.53	PIV, CFD	1, 2
10	N/A	PIV, CFD	1, 2, 3, 4

The results from previous CFD modeling studies of multiple-jet flow within a confined space[30–32] have shown that the Reynolds Stress model (RSM) can be used to provide a reasonable prediction of the mean velocity field. This is consistent with our own preliminary CFD model assessment, which found that the Baseline RSM model in ANSYS/CFX gives a reasonable agreement of the centerline velocity evolution for the current MIJCC configuration compared with the standard k-ε model and shear stress transport model. In addition, a preliminary comparison of the relative performance of five alternative RSM models[33–37] available in ANSYS/CFX was also undertaken for one configuration of confined jets. These models are the "Baseline Reynolds Stress," "SSG (Speziale, Sarkar, Gatski) Reynolds Stress," "LRR (Launder, Reece, and Rodi) Reynolds Stress," "Omega Reynolds Stress," and the "QI (Quasi-Isotropic) Reynolds Stress" models. The models were assessed on the basis of the mean velocity field and the Reynolds stresses, as shown in the supplementary material. The best prediction was provided with the Baseline RSM model. Hence, the Baseline RSM model was selected as the turbulence closure model for the present study, which is hereafter referred to as the "RSM model" for brevity.

The validity of the RSM model for the selected MIJCC configuration (four cases) was assessed at the six radial profiles and one axial profile shown in Table III by comparing the PIV measurements with the CFD calculations, as is shown in Fig. 4. All CFD simulations were performed with a supercomputing cluster (Dell PowerEdge R815 Rack Mount Server) with two AMD 12-core Opteron 6174 Processors and 40 GB of RAM. An average of 5 h of CPU-time was required to achieve the desired convergence.

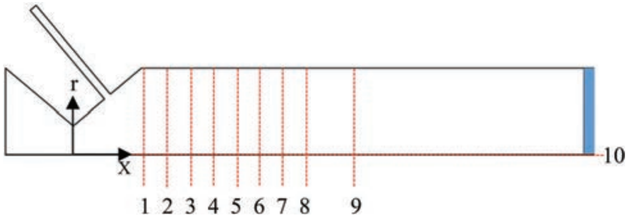

FIG. 4. Selected positions for the investigations of the radial profiles investigated with PIV measurements and/or CFD simulations. See Table III for the exact location of each axial station.

III. RESULTS AND DISCUSSION

A. Instantaneous velocity fields

Figure 5 presents four sets of three typical instantaneous images of velocity vectors, showing direction (black) and magnitude (colored) for the cases in which $\alpha_j = 25°$ and $N_j = 2$ (MIJCC_25_2J), $\alpha_j = 50°$ and $N_j = 2$ (MIJCC_50_2J), $\alpha_j = 25°$ and $N_j = 4$ (MIJCC_25_4J), and $\alpha_j = 50°$ and $N_j = 4$ (MIJCC_50_4J). It can be seen that the flow is characterized by the unsteady impingement of the turbulent jets onto a single point that is located at or close to the principle axis ($r/L_c = 0$), where they merge into the "resulting jet,"[26] as described above. For a given number of jets (N_j), the location of the impingement point progresses upstream with an increase in the inclination angle (α_j), while for a given value of α_j, the velocity magnitude and flow lateral extent of the resulting jet increases as the number of jets is increased from 2 to 4. This suggests that the turbulence characteristics, including the extent of unsteadiness, will also depend both on the inclination angle and on the number of inlet jets.

The instantaneous results in Fig. 5 also reveal that the location of the impingement point (determined visually for each image shown and marked with a white cross) varies with time, which in turn causes oscillations in the flow downstream from the impingement point. This is most notable for the higher inclination angle case ($\alpha_j = 50°$) and is consistent with previous studies, for which lateral flow oscillations and flow precession were identified for multi-lateral jets with large jet inclination angles ($\alpha_j = 90°$).[38–42] For those configurations, a significant offset in the instantaneous position of the impingement point from the axis, which was termed "flapping," was observed. Importantly, this flapping mode cannot be captured with existing steady-state RANS models.[38] Hence, the increased significance of flow oscillations with inclination angles explains the larger differences between the experimentally measured and numerically calculated mean velocities for configurations of $\alpha_j = 50°$ than for the smaller angles, as is discussed in Sec. III B.

It can also be seen that the lateral (cross-stream) offset of the impingement point is less significant for the case where $N_j = 4$ than for $N_j = 2$, although the flapping was still observed downstream from the impingement point. The reason for this is possibly due to the increased strength of the flow from the two additional "out-of-plane" jets. More work is required to determine if this trend is consistent for a greater number of jets ($N_j > 4$) and higher inclination angles ($\alpha_j > 50°$).

B. Mean velocity fields

Figure 6 presents the normalized mean velocity (U_x/U_b) contours for the cases (a) MIJCC_25_2J, (b) MIJCC_25_4J, (c) MIJCC_50_2J, and (d) MIJCC_50_4J. It can be seen that the mean flow field for all four cases is planar-symmetric, despite the presence of some flow unsteadiness in the instantaneous flow as described above. The mean flow of the resulting jet spreads out gradually and symmetrically beyond the impingement point, in a trend consistent with a single free jet.[43] In order to quantitatively characterize the mean flow field in more detail, we plot the mean centerline axial velocity profiles (U_c/U_b), inverse mean centerline velocity decay of resulting

(a) MIJCC_25_2J

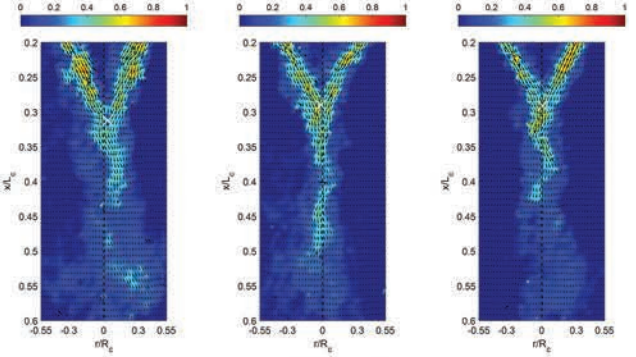

(b) MIJCC_50_2J

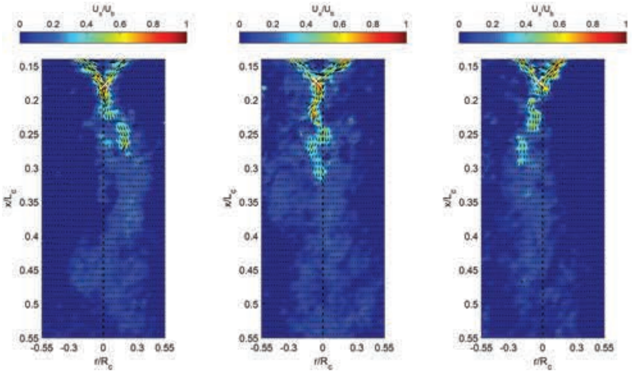

(c) MIJCC_25_4J

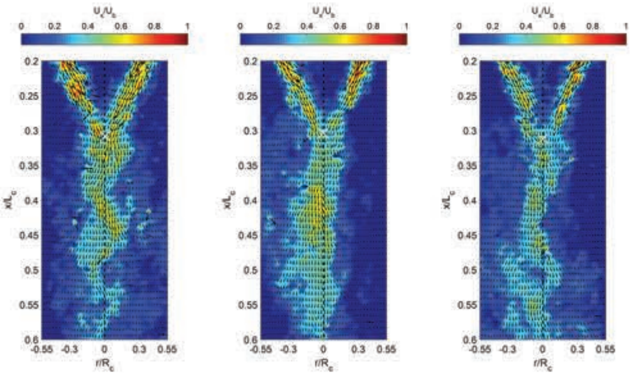

(d) MIJCC_50_4J

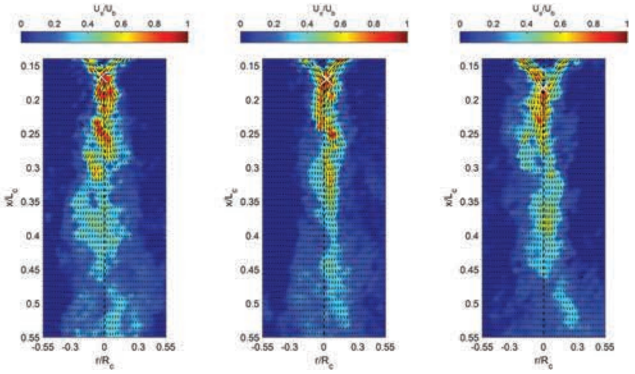

FIG. 5. Typical instantaneous velocity vectors (black) and magnitude contours (colored) for the configurations of (a) α_j = 25° and N_j = 2 (MIJCC_25_2J), (b) α_j = 50° and N_j = 2 (MIJCC_50_2J), (c) α_j = 25° and N_j = 4 (MIJCC_25_4J), (d) α_j = 50° and N_j = 4 (MIJCC_50_4J). Here U_x and U_b denote the mean axial velocity and the jet injection velocity, respectively. L_c denotes the length of the MIJCC chamber, and white cross denotes the approximate jet impingement point determined visually.

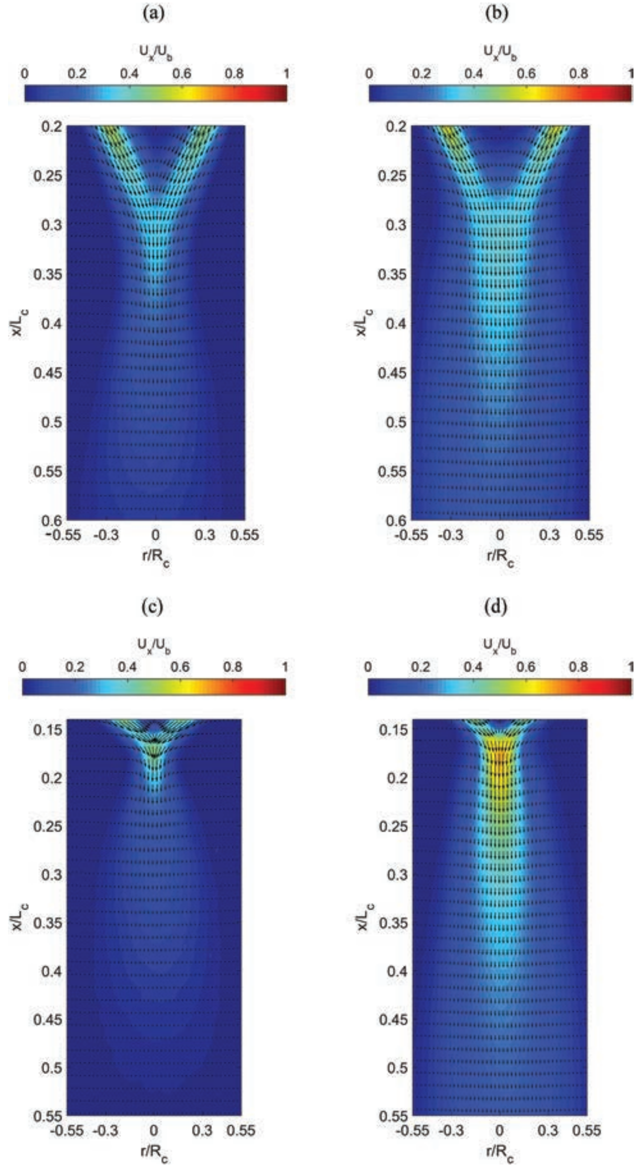

FIG. 6. Normalised mean velocity (U_x/U_b) contours for the cases of (a) MIJCC_25_2J, (b) MIJCC_25_4J, between x/L_c = 0.2 and 0.6, and for the cases of (c) MIJCC_50_2J and (d) MIJCC_50_4J, between x/L_c = 0.13 and 0.55.

jet (U_b/U_c), and radial profiles of mean axial velocity (U_x/U_b) in Figs. 7, 8, and 10. All data are obtained directly from Fig. 6.

Figure 7 presents the evolution of dimensionless mean axial velocity (U_c/U_b) along the centerline of the MIJCC obtained from the CFD model in comparison with the experimental measurements for the cases of MIJCC_25_2J, MIJCC_50_2J, MIJCC_25_4J, and MIJCC_50_4J. The impingement point is defined as the location of maximum mean velocity $(U_c/U_b)_{max}$. It can be seen that all cases feature similar trends in the mean axial centerline velocity decay, although the locations and magnitudes of their peak values differ. The jet impingement point is located at $x/L_c \approx 0.30$ for MIJCC_25_2J, $x/L_c \approx 0.17$ for MIJCC_50_2J, $x/L_c \approx 0.31$ for MIJCC_25_4J, and $x/L_c \approx 0.18$ for MIJCC_50_4J. This result is consistent with the observation in Fig. 5. That is, an increase in α_j for constant D_{pipe} leads to the upstream progression of the jet impingement

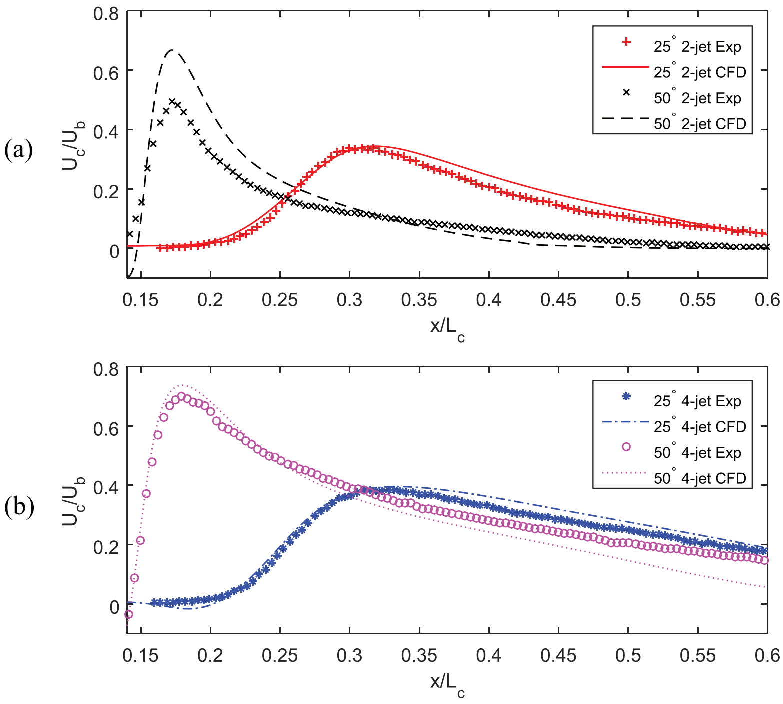

FIG. 7. Evolution of the mean axial velocity (U_c/U_b) along the centerline of Multiple Impinging Jets in a Cylindrical Chamber (MIJCC) normalized by the inlet velocity as functions of chamber length for (a) $\alpha_j = 25°$ and $N_j = 2$ (MIJCC_25_2J), $\alpha_j = 50°$ and $N_j = 2$ (MIJCC_50_2J), (b) $\alpha_j = 25°$ and $N_j = 4$ (MIJCC_25_4J), $\alpha_j = 50°$ and $N_j = 4$ (MIJCC_50_4J). The impingement point is defined as the location of peak mean velocity $(U_c/U_b)_{max}$.

point, while the number of jets (N_j) increases only slightly the axial distance to the impingement. In addition, it can also be seen that the measured peak velocity for $N_j = 4$ is higher than for $N_j = 2$ cases by 15% ($\alpha_j = 25°$)–30% ($\alpha_j = 50°$), implying that an increase in jet number (N_j), for constant D_{pipe}, reduces the unsteadiness in the resulting jet flow.

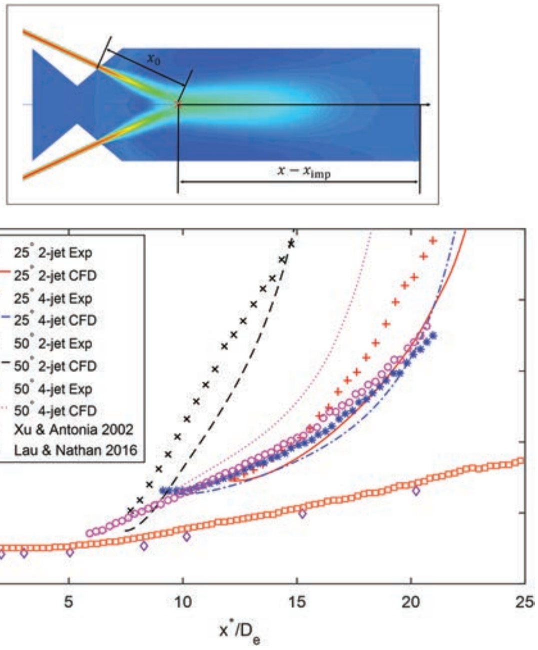

FIG. 8. Inverse mean velocity decays (U_b/U_c) along the centerline of the MIJCC for the cases of MIJCC_25_2J, MIJCC_25_4J, MIJCC_50_2J, and MIJCC_50_4J. The equivalent axial coordinate, x^*, can be expressed as $x^* = x_0 + (x - x_{imp})$, where x_{imp} denotes the distance between the throat and the impingement point, x_0 denotes the distance along the curved axis of each jet between the pipe exit and the impingement point as shown in the inset, and D_e is the diameter of an equivalent circular pipe with the same total exit area. For a better image resolution, experimental data are presented with each of the two data points.

For all cases, the RSM model predicts the overall trends in the experimental data and also gives quantitative agreement to within 10% for all $\alpha_j = 25°$ cases. However, the quantitative agreement for the $\alpha_j = 50°$ cases is relatively poor, particularly at the impingement point region ($x/L_c \approx 0.17$) for MIJCC_50_2J, where the peak velocity is overpredicted by 25%. Nevertheless, the axial locations of the velocity peak are well produced even for this case. The most likely explanation for these two observations is the presence of significant unsteady oscillations in the flow at the point of impingement, as discussed in Sec. III A. This unsteadiness will not influence the average position of the point of impingement but will decrease relative to the model both the magnitude of the peak and the downstream centerline velocity decay.

Figure 8 presents the evolution of the measured and calculated inverse mean velocity of the resulting jet (U_b/U_c) along the centerline of the MIJCC. The equivalent jet exit diameter, D_e, can be expressed as $D_e = \sqrt{N_j}D_{pipe}$, which is the diameter of an equivalent circular pipe with the same exit area. The equivalent axial coordinate, x^*, along the axis of the local jet can be approximated as being $x^* = x_0 + (x - x_{imp})$, where x_{imp} denotes the distance between throat and impingement point and x_0 denotes the distance along the local axis of each jet between the pipe exit and impingement point (shown in the inset of Fig. 8). For comparison with previous measurements of the single unconfined jet, the HWA (Hot-wire anemometry) data of Xu and Antonia[44] for a free pipe jet and the PIV measurement of Lau and Nathan[45] for a turbulent, round jet, issuing from a long pipe, are also included in Fig. 8. It can be seen that the evolution of U_b/U_c for the central resulting jet for present experimental cases is significantly greater than a single unconfined jet within $7 \le x^*/D_e \le 22$, regardless the value of α_j and N_j. This implies that the combination of the presence of walls (confinement), the jet curvature upstream from the impingement point, and the additional unsteadiness caused by the impingement substantially increase the decay of the resulting jet.

Figure 8 also shows that the evolution of U_b/U_c over the measured region is different for each of the four configurations. For the cases of $N_j = 2$, an increase in the inclination angle (α_j) from 25° to 50° leads to a great increase in the decay of the resulting jet. For example, the case of MIJCC_50_2J decays faster than MIJCC_25_2J, for which $U_b/U_c = 10$ at $x^*/D_e = 15$, while U_b/U_c for MIJCC_25_2J reaches 10 at $x^*/D_e = 21$. However, for the cases of $N_j = 4$, the slope of inverse centerline velocity is lower than the $N_j = 2$ cases and is also similar for $\alpha_j = 25°$ and 50°, although a slightly greater slope was found for $\alpha_j = 50°$ within the range $11 \leq x^*/D_e \leq 22$. The most likely cause for this is the increased unsteadiness in the resulting jet arising from the lateral offset of the impingement point for all $\alpha_j = 50°$ cases, as discussed in Sec. III A. Hence, it can be concluded that, firstly, for constant D_{pipe}, the centerline velocity decay of the resulting jet increases as α_j is increased, and second, the extent of unsteadiness for $N_j = 2$ cases is greater than for $N_j = 4$ for a given value of α_j—at least for these planar-symmetric impinging jets configurations.

The RSM model predicts the centerline velocity decay of the resulting jet reasonably well for most cases, particularly for the two cases of $\alpha_j = 25°$, where the maximum difference is 15%. However, a relatively poor agreement was found for the case of MIJCC_50_4J in the region downstream from $x^*/D_e \approx 15$, although quantitative agreement is good upstream from this location. This is further evidence of the influence of unsteadiness for this case.

Figure 9 presents the calculated inverse mean centerline velocity decays of the resulting jet (U_b/U_c) along the centerline of the MIJCC for the cases of MIJCC_25_4J$_{Dpipe=2.37}$ and MIJCC_50_4J$_{Dpipe=2.37}$, where the subscript $D_{pipe=2.37}$ denotes a pipe diameter of 2.37 mm. The total exit area from these four pipes ($A_{pipe.tot}$) is therefore the same as for the original MIJCC_25_2J and MIJCC_50_2J cases, allowing the influence of the pipe diameter (D_{pipe}) on the flow-field to be assessed. The calculated results for the original four cases ($D_{pipe} = 3.35$ mm) are also reported here for reference. It can be seen that, for a constant total exit area $A_{pipe.tot}$ (Case 1, 3, 4, 6), an increase in the number of jets (N_j) from 2 to 4 leads to a significant decrease in the velocity decay of the resulting jet, although the value of U_b/U_c at the impingement point for $N_j = 4$ cases is higher than that for $N_j = 2$. This trend is consistent with the velocity decay shown in Fig. 8, which shows that the decrease in the decay of the resulting jet that arises from an increase in N_j from 2 to 4 is not caused by the change in the area of the nozzles. The most likely reason for this is that the two additional "out-of-plane" jets restrict the radial spread of the resulting jets, consistent with observations from a previous study.[46]

It is also worth noting that, for all cases with D_{pipe} = 3.35 mm (Case 1, 2, 4, 5 in Fig. 9 and the associated experimental data in Fig. 8), an increase in N_j from 2 to 4 causes a significant decrease in the centerline velocity decay for $\alpha_j = 50°$, while only a slight decrease occurs for the two $\alpha_j = 25°$ cases. This suggests that a higher "out-of-plane" spread of the resulting jet occurs in MIJCC_50_2J than that in MIJCC_25_2J, also consistent with previous research.[47]

The calculated results in Fig. 9 also show that, for the cases of $N_j = 4$ (Case 2, 3, 5, 6), an increase in D_{pipe} from 2.37 mm to 3.35 mm leads to an increase in the centerline velocity decay of the resulting jet, regardless of the change in α_j. This is attributed to the increased entrainment of the surrounding fluid arising from the extra confinement for larger D_{pipe}.

Figure 10 presents radial profiles of the measured and calculated mean axial velocity, normalized by the inlet velocity, U_b, at six axial distances along the chamber for the cases (a) MIJCC_25_2J, (b) MIJCC_25_4J, (c) MIJCC_50_2J, and (d) MIJCC_50_4J. The left-hand-side figure presents three profiles near the impingement point, and the right-hand-side figure presents three profiles in the downstream region. The black dashed-dotted line denotes the location of $U_x/U_b = 0$ for each case, for which the exact locations of the measurements is reported in Table III. For $\alpha_j = 25°$ [Figs. 10(a) and 10(b)], it can be seen that there are no significant qualitative differences in the velocity profiles between $N_j = 2$ and $N_j = 4$ cases. Significant positive velocity peaks are found upstream from the impingement point ($x/L_c = 0.22, 0.26$), while a central resulting jet with single velocity peak occurs downstream from the impingement point ($x/L_c = 0.31, 0.35, 0.44, 0.53$). It can also be seen that no negative velocity peaks occur for these two cases, which implies that no reversed flow is present on the axis for these cases. For the cases of $\alpha_j = 50°$ [Figs. 10(c) and 10(d)], the impingement point is further upstream at $x/L_c \approx 0.17$–0.18.

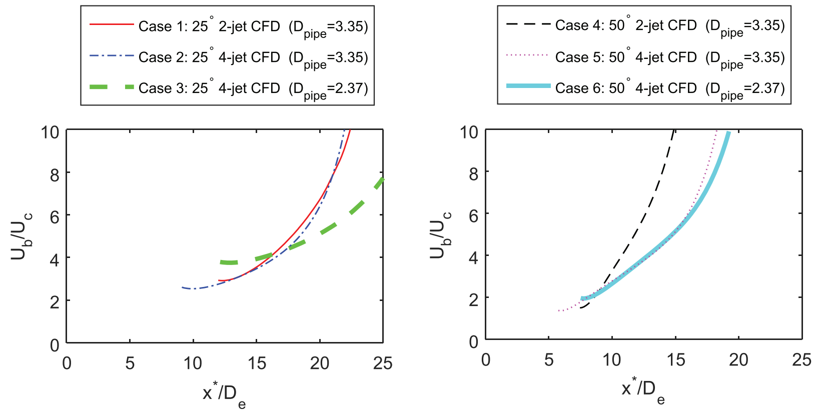

FIG. 9. Calculated inverse mean velocity decays (U_b/U_c) along the centerline of the MIJCC for the cases of MIJCC_25_4J$_{Dpipe=2.37}$ (case 3) and MIJCC_50_4J$_{Dpipe=2.37}$ (case 6), where the exit pipe area (A_{pipe}) is identical to MIJCC_25_2J (case 1) and MIJCC_50_2J (case 4). The cases of MIJCC_25_4J (case 2) and MIJCC_50_4J (case 5) are also included for comparison. The equivalent axial coordinate, x^*, can be expressed as $x^* = x_0 + (x - x_{imp})$, where x_{imp} denotes the distance between throat and impingement point, x_0 denotes the distance along the curved axis of each jet between the pipe exit and impingement point as shown in the inset of Fig. 8, and D_e is the diameter of an equivalent circular pipe with the same total exit area.

(a) MIJCC_25_2J

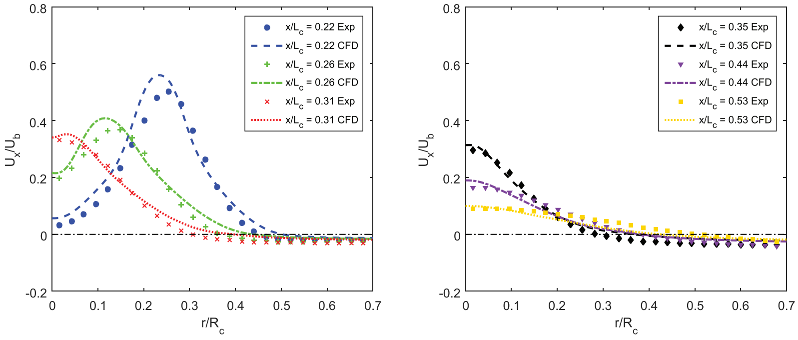

(b) MIJCC_25_4J

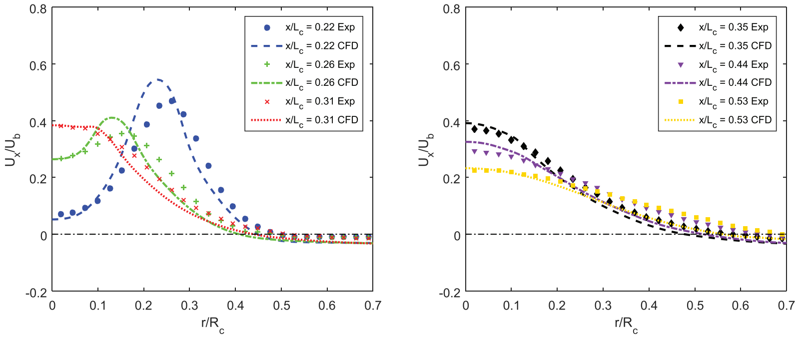

(c) MIJCC_50_2J

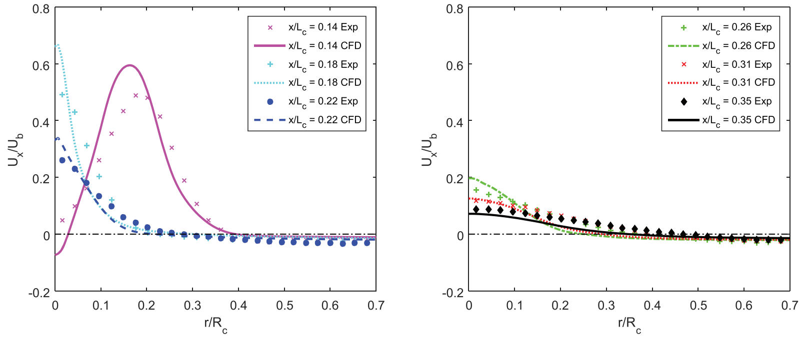

(d) MIJCC_50_4J

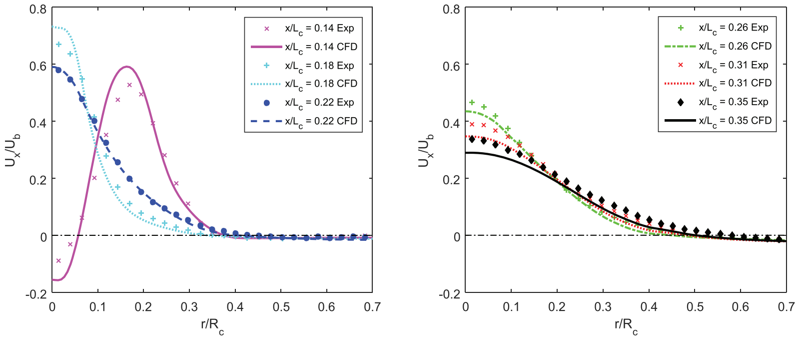

FIG. 10. Radial profiles of measured and calculated mean axial velocity, U_x, at six cross sections through the Multiple Impinging Jets in a Cylindrical Chamber (MIJCC) for (a) MIJCC_25_2J, (b) MIJCC_25_4J, (c) MIJCC_50_2J, (d) MIJCC_50_4J. The left-hand-side figure presents three profiles near the impingement point, and the right-hand-side figure presents three profiles in the downstream region. Here R_c denotes the radius of the MIJCC. Note that the impingement point is located at approximately $x/L_c \approx 0.3$-0.31 and 0.17–0.18 for $\alpha_j = 25°$ and $\alpha_j = 50°$ cases, respectively. The dashed-dotted line denotes the location of $U_x/U_b = 0$.

A negative velocity peak is found in the central region of the chamber ($r/R_c < 0.1$) upstream from the impingement point ($x/L_c \approx 0.17$), which implies the presence of a reverse flow for these cases. In addition, the magnitude of the negative velocity peak of $x/L_c = 0.14$ for the $N_j = 4$ [Fig. 10(d)] is approximately 75% higher than that for $N_j = 2$ [Fig. 10(c)], which is consistent with the strength of the flow increasing with the number of inlet jets.

Figure 10 also shows that, for a given value of D_{pipe}, the flow-field for the 2-jet configuration is qualitatively similar to the 4-jet configuration but typically has a lower magnitude of velocity. For α_j = 25°, the radial profile of U_x/U_b for the N_j = 4 case at x/L_c = 0.35 (downstream region) is approximately 10% higher than that for the N_j = 2 case, while for α_j = 50°, the velocity profile for the N_j = 4 case at x/L_c = 0.35 is 70% higher. This implies a greater decay of centerline velocity and more "out-of-plane" expansion in the flow-field for N_j = 2 than for the N_j = 4 cases, as discussed above. This trend in the mean velocity field is also consistent with the observations from the experimentally measured instantaneous velocity fields (Fig. 5), which shows that the greater mean decay is not the result of precession but also occurs instantaneously.

It is important to note that there are regions of negative axial velocity in the outer region of the chamber for all cases downstream from the impingement point. For example, reverse flow is found at $r/R_c \gtrsim 0.3$ for x/L_c = 0.31 for the case MIJCC_25_2J and $r/R_c \gtrsim 0.3$ for x/L_c = 0.18 for the case MIJCC_50_2J. This implies the presence of a large-scale circulation region within the main cavity, extending to the wall of the chamber.

As with previous comparisons, the results of the RSM model show good qualitative agreement with the experimental results for all cases and a quantitative agreement to within 15% for three of the four cases, both upstream and downstream from the impingement point. However, poorer agreement was found for the MIJCC_50_2J case, for which a maximum difference of 25% was found on the axis at x/L_c = 0.18. Hence it can be concluded that the RSM model gives good qualitative agreement with the experimental data for all cases assessed here and gives good quantitative agreement for all cases in which no significant precession in the merged flow is generated, namely, for MIJCC_25_2J and MIJCC_25_4J.

The validity of the RSM model for α_j = 0° was also assessed by comparing the simulated results with the experimental data of three confined parallel jets investigated by Boushaki and Sautet,[28] which shows that the RSM model also predicts the qualitative trends and gives similar quantitative agreement to the non-precessing cases reported there. This assessment is reported in the supplementary material. Similarly, other researchers have reported that the RSM model also provides good prediction of impinging jets with α_j = 90° in several relevant configurations, such as jet impingement[48,49] and confined impinging jet reactors.[50] Hence, taking our measured data of α_j = 25° and 50° together, it can be deduced that the RSM model reproduces velocity fields sufficiently well for multiple jets configurations in the range of $0° \leq \alpha_j \leq 90°$ to identify the large-scale flow structure within the MIJCC configuration.

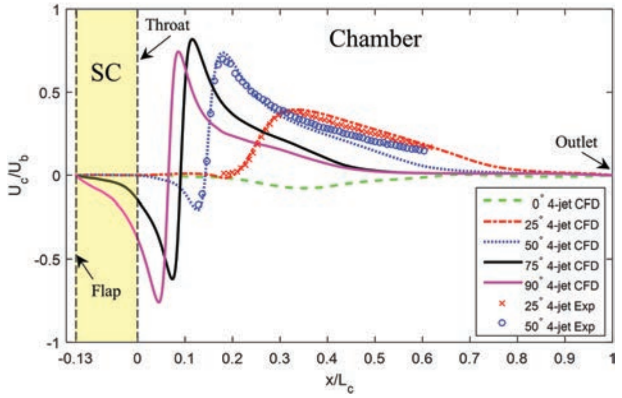

FIG. 11. Calculated mean axial velocity (U_c/U_b) profiles along the centreline of the Multiple Impinging Jets in a Cylindrical Chamber (MIJCC), from the flap to the annular outlet ($-0.13 \leq x/L_c \leq 1$). Here x/L_c = 0 corresponds to the location of the throat plane. The yellow area denotes the secondary concentrator, and the two black dashed-lines denote the flap (left) and throat planes (right), respectively. For a better image resolution, experimental data are presented with each of the two data points.

Figure 11 presents the axial distribution of calculated mean axial velocity (U_c/U_b) through the whole region of the MIJCC ($-0.13 \leq x/L_c \leq 1$) for the five inclination angles α_j = 0°, 25°, 50°, 75°, and 90° and for the N_j = 4 configuration. The experimental data of α_j = 25° and 50° are also included for reference. The results for the N_j = 2 cases are not reported for conciseness because they are qualitatively similar to the N_j = 4 cases (refer to Fig. 7). It can be seen that for all cases in which inlet jet impingement occurs (α_j = 25°, 50°, 75°, and 90°), the location of the impingement point progresses upstream with an increase in α_j, from x/L_c = 0.31 for α_j = 25° to x/L_c = 0.06 for α_j = 90°. In contrast, for the α_j = 0° case, a small negative velocity profile is found between $0.2 \leq x/L_c \leq 0.6$, revealing a reverse flow. This is consistent with previous experimental research.[51,52]

It can also be seen that a region of significant negative axial velocity occurs on the axis upstream from the impingement point for the cases of α_j = 50°, 75°, and 90°. This reveals that a fraction of the jet flow from the impingement point travel upstream, which in turn indicates that a secondary recirculation region with a strong reverse flow is established within this region. More importantly, the peak negative axial centerline velocity occurs downstream from the plane of throat (x/L_c = 0), which implies that the flow decelerates toward the throat and recirculates again in this region. For the cases of α_j = 75° and 90°, the negative axial velocity along the centerline extends upstream into the secondary concentrator ($x/L_c \leq 0$), which indicates that a strong reverse flow from the main chamber into the secondary concentrator is generated under these conditions. Furthermore, it is clear that a stagnation plane occurs at the flap plane (x/L_c = –0.13) for the cases of α_j = 75° and 90°, since the axial centerline velocity approaches zero there. This also implies that an annular recirculation zone is generated within the SC moving upstream on the axis.

Figure 12 presents radial profiles of the calculated mean (time-averaged) axial velocity, normalized by the jet inlet velocity, U_b, at five axial distances along the chamber of the α_j = 0° and 75°, for both N_j = 2 (left) and N_j = 4 (right) MIJCC configurations. It can be seen that for the parallel impinging jets configuration, α_j = 0° [Figs. 12(a) and 12(b)], there is no direct interaction between the inlet jets, resulting in the radial location of the peak velocity being approximately constant with axial distance within the cylindrical chamber. Nevertheless, the trajectory of the jets is not exactly constant, since they converge slightly at the end of the chamber. Consistent with conventional parallel-jets, the peak in each radial velocity profile decays with axial distance.[20] Furthermore, the minimum value of velocity for MIJCC_00_4J, which occurs on the axis, becomes negative for $x/L_c \geq 0.22$, implying the presence of

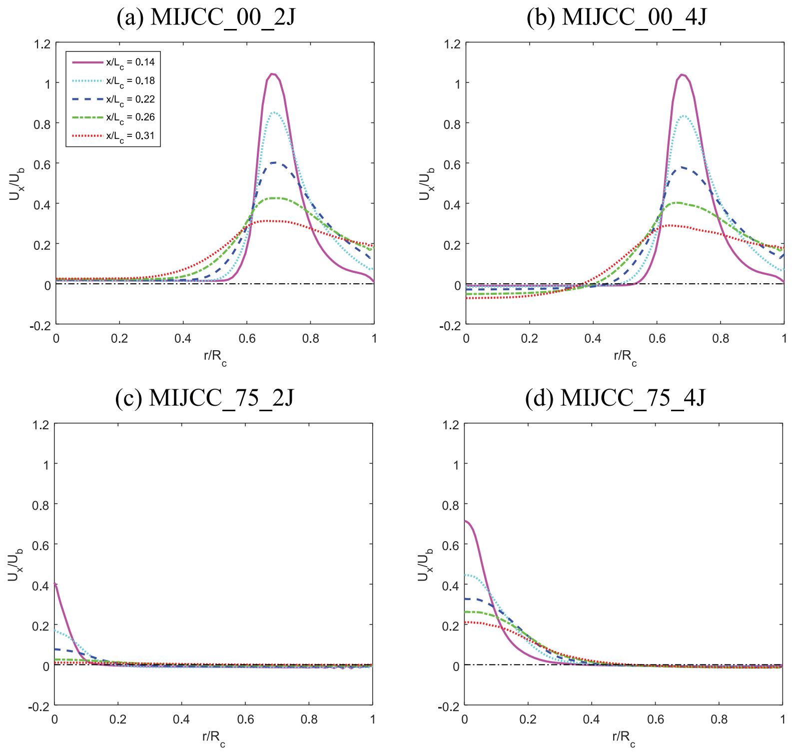

FIG. 12. Calculated radial profiles of mean axial velocity, U_x at five cross sections through the Multiple Impinging Jets in a Cylindrical Chamber (MIJCC) for the cases of (a) MIJCC_00_2J, (b) MIJCC_00_4J, (c) MIJCC_75_2J, and (d) MIJCC_75_4J. Here R_c denotes the radius of the MIJCC. The dashed-dotted line denotes the location of $U_x/U_b = 0$.

a reversed flow there. This feature is not observed for larger inclination angles, $\alpha_j \geq 25°$.

Where the inclination angle is increased sufficiently, the inlet jets interact with each other, causing the location of the peak velocity to move toward the centerline. For the $\alpha_j = 75°$ case, the velocities are non-negative throughout the radial extent of the chamber for $x/L_c \geq 0.14$. This is because the impingement point is located where $x/L_c < 0.14$. The calculated velocity profiles in the central region are consistent with conventional unconfined jets. That is, the peak velocity, which is located on the axis, decreases with the axial distance along the chamber.[20] The upstream reverse flow inferred from the $\alpha_j = 50°$ case, as discussed in Fig. 10, if it exists, is expected to be located outside the calculated regions shown in Figs. 12(c) and 12(d).

It is also worth noting that the parallel impinging jet case, $\alpha_j = 0°$, does not generate a central merged jet at any axial location within the chamber, while for the $\alpha_j = 75°$ case, a central jet is measured from $x/L_c = 0.14$ (i.e., close to the throat plane). This highlights the sensitivity of the presence or absence of central jet to the inlet jet inclination angle.

C. Turbulent flow fields

Figure 13 presents the measured and calculated (a) axial turbulence intensity (u'/U_c) and (b) radial turbulence intensity (v'/U_c) of the resulting jet along the centerline of the MIJCC for the cases of MIJCC_25_2J, MIJCC_50_2J, MIJCC_25_4J, and MIJCC_50_4J. Here $u' = \langle u^2 \rangle^{0.5}$ and $v' = \langle v^2 \rangle^{0.5}$ where u and v denote the fluctuating components of the velocity along the axial and radial directions of the chamber, respectively. The detailed description of the equivalent jet exit diameter, D_e, and the equivalent axial coordinate, x^*, can be found in Fig. 8. The PIV measurement of Lau and Nathan[45] for a turbulent, round jet, issuing from a long pipe, is also included. It can be seen that the evolution of both axial and radial turbulence intensities for present experimental cases is always higher than a single unconfined jet within $7 \leq x^*/D_e \leq 22$, consistent with the centerline velocity decay trend from Fig. 8. This is likely to be caused by the combined effects of jet impingement, wall confinement, and flow unsteadiness. For multiple-jet configurations under fully turbulent flow conditions, the coherent structures downstream from the impingement point are more evident than for a single unconfined jet. This implies a strong interaction between the large-scale flow structures within the upstream jets, so that impingement amplifies the large-scale unsteadiness within the natural jet. It is plausible that these oscillations may be further amplified by wall confinement, although this was not assessed here.

It can also be seen that for $N_j = 2$ cases, an increase in the inclination angle (α_j) from 25° to 50° leads to a significant increase in both u'/U_c and v'/U_c. A similar evolution of u'/U_c and v'/U_c was also found for all $N_j = 4$ cases. However, for a given α_j, the extent of u'/U_c and v'/U_c decreases with the increase in N_j. This occurs for both the measured data and CFD predictions and is also more significant for the MIJCC_50_2J case than for the other cases. Hence, it can be concluded that an increase in N_j can significantly reduce the turbulent fluctuations, while an increase in α_j is expected to increase the extent of turbulence intensity for $N_j = 2$ configurations.

Figure 14 presents the measured and calculated radial profiles of the normalized axial r.m.s. velocity (u'/U_c), normalized radial r.m.s. velocity (v'/U_c) and the non-dimensional Reynolds stress ($\langle uv \rangle / U^2{}_c$) downstream from the jet impingement point for the cases of MIJCC_25_2J, MIJCC_50_2J, MIJCC_25_4J, and MIJCC_50_4J. The calculated r.m.s. velocity along the "out-of-plane" direction (w) is relatively small, which has been excluded in the present study. It can be

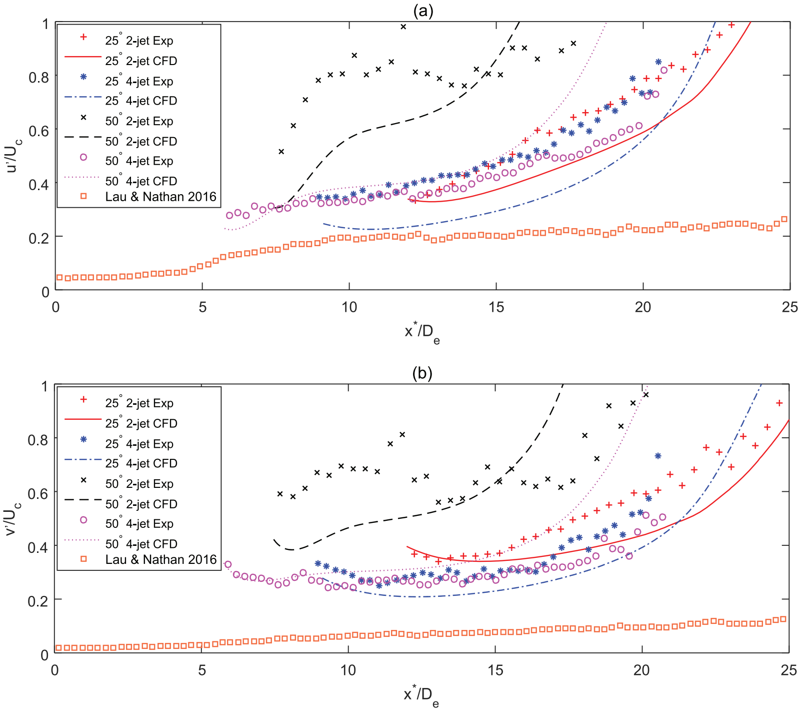

FIG. 13. Measured and calculated axial evolution of (a) axial turbulence intensity (u'/U_c), (b) radial turbulence intensity (v'/U_c) of the resulting jet along the centerline of the MIJCC for cases of MIJCC_25_2J, MIJCC_25_4J, MIJCC_50_2J, and MIJCC_50_4J. The equivalent axial coordinate, x^*, can be expressed as $x^* = x_0 + (x - x_{imp})$, where x_{imp} denotes the distance between throat and impingement point, x_0 denotes the distance along the curved axis of each jet between the pipe exit and impingement point as shown in the inset of Fig. 8, and D_e is the diameter of an equivalent circular pipe with the same total exit area. For a better image resolution, experimental data are presented with each of the two data points.

seen that for $\alpha_j = 25°$, the radial evolution of both u'/U_c and v'/U_c in the resulting jet does not change significantly with an increase in N_j from 2 to 4, while for $\alpha_j = 50°$, a notable magnitude reduction in both u'/U_c and v'/U_c at the jet impingement point ($r/R_c = 0, x/L_c = 0.18$) was observed. This indicates that the fluctuating components may contribute more unsteady characteristics to the resulting jet of $\alpha_j = 50°$ than $\alpha_j = 25°$, and particularly for $N_j = 2$ configuration, which is consistent with Fig. 13.

The results in Figs. 14(a)–14(d) also show the magnitude of u'/U_c is typically 20%–30% higher than v'/U_c for most cases, consistent with previous research of the single unconfined jet.[43–45] However, the value of v'/U_c at the impingement point $r/R_c = 0$ ($x/L_c = 0.31$ for $\alpha_j = 25°$ cases and $x/L_c = 0.18$ for $\alpha_j = 50°$ cases) is higher than u'/U_c, particularly for $\alpha_j = 50°$ cases. The most likely cause for this is the interaction between jets with inclination angles, which generates a high radial fluctuating component (v') at the impingement point. Hence, the turbulent fluctuation is expected to be characterized by α_j for multiple-jets configurations.

It can also be seen from Figs. 14(e)–14(h) that, for a given α_j, the Reynolds stresses $\langle uv\rangle/U^2{}_c$ for $N_j = 2$ cases are always higher than that for $N_j = 4$ cases. This difference is particularly large for $\alpha_j = 50°$ cases, consistent with the finding from u'/U_c and v'/U_c [Figs. 14(a)–14(d)]. This in turn indicates a much higher turbulent fluctuation, including the normal ($\langle u^2\rangle$) and shear ($\langle v^2\rangle$) stresses existing in the fluid momentum for $N_j = 2$ cases than that for $N_j = 4$ cases. More importantly, the difference between u'/U_c and v'/U_c, together with the different magnitudes of Reynolds stresses $\langle uv\rangle/U^2{}_c$ for different N_j, indicates a high degree of Reynolds stress anisotropy in the current MIJCC configurations. This can also be clearly observed from the radial [Fig. 13(a)] and axial [Fig. 13(b)] turbulence intensities along the centerline of the chamber. Taken together, it can be concluded that a high degree of anisotropy exists within the flow field generated by planar-symmetric impinging jets within a cylindrical chamber. This finding is important for the selection and future development of CFD models since the assumption of the isotropic condition has been widely used for existing RANS models.[34] In addition, this also explains the improved reliability of the RSM model relative to the other RANS models in predicting the mean flow field for the current study since this model solves the Reynolds stresses individually for each direction.

Overall, the RSM model predicts the qualitative trends of turbulence intensity and the Reynolds stress anisotropy reasonably well for all cases, although there are significant discrepancies in the quantitative values, as is to be expected for RANS models. The discrepancy is particularly significant for $\alpha_j = 50°$ cases, which can be attributed to the unsteadiness within the flow, discussed in Sec. III A.

D. Characterization of flow regimes

Figure 15 presents schematic diagrams of the configuration and the calculated streamlines for the four dominant flow regimes that have been identified within the MIJCC configuration. These are illustrated by the cases $\alpha_j = 0°$, 25°, 50°, and 90°. The calculated streamlines for the $N_j = 2$ cases are not reported for conciseness due to their similarity to the $N_j = 4$ cases. The experimentally measured streamlines for the cases of MIJCC_25_4J [Fig. 15(b)] and MIJCC_50_4J [Fig. 15(c)] are also included for comparison. Here the recirculation core location (L_{core}) denotes the axial distance between the throat and the centre of the dominant recirculation region (often termed "vortex core"[53,54]). The key features of the four flow regimes are described in turn, below:

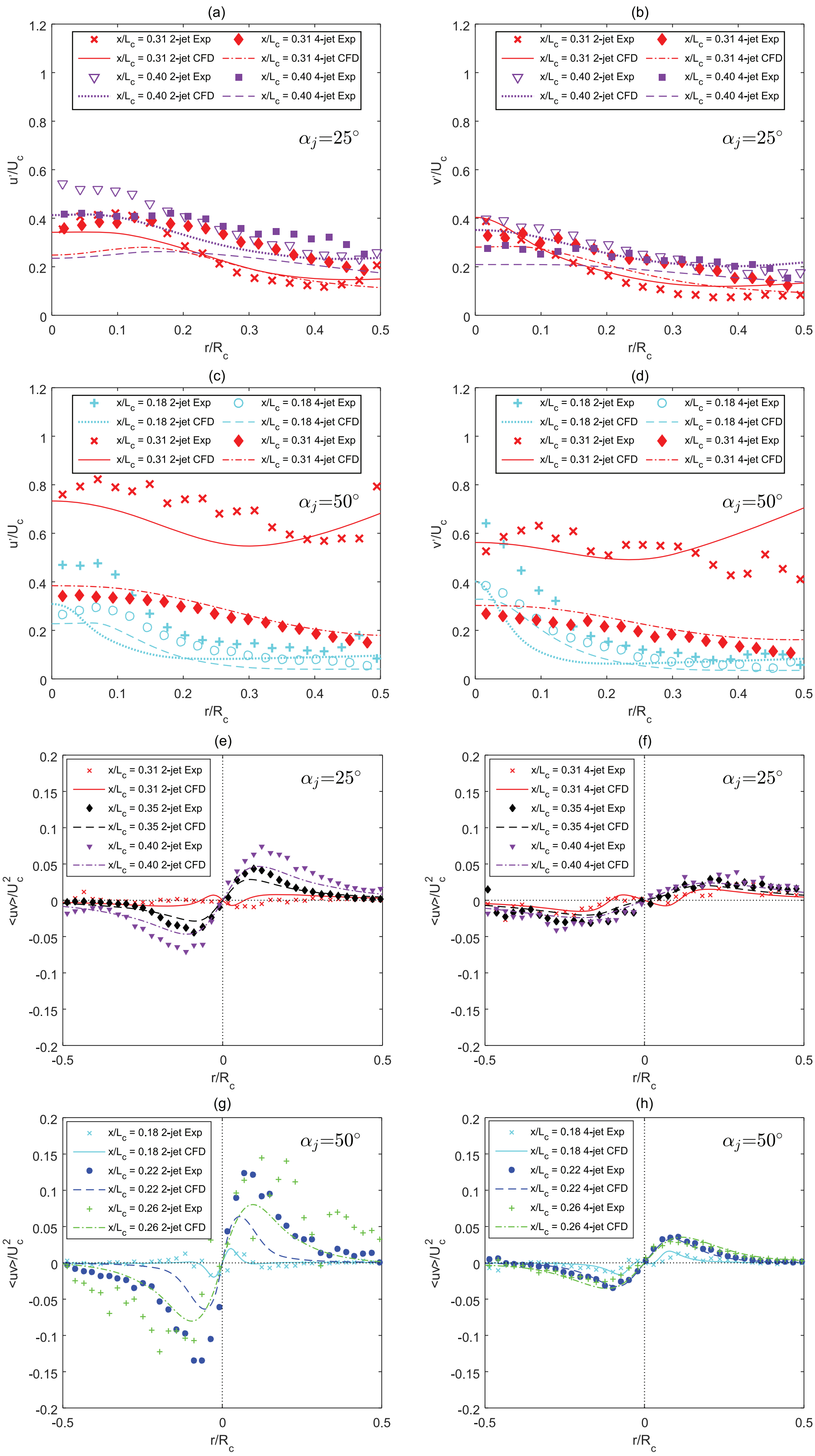

FIG. 14. Radial profiles of measured and calculated normalized axial r.m.s. velocity (u'/U_c), normalized radial r.m.s. velocity (v'/U_c), and the non-dimensional Reynolds stress ($\langle uv\rangle/U^2{}_c$) downstream from the jet impingement point for the cases of MIJCC_25_2J, MIJCC_50_2J, MIJCC_25_4J, and MIJCC_50_4J. Here R_c denotes the radius of the MIJCC. The impingement point is located at approximately $x/L_c \approx 0.3$-0.31 and 0.17–0.18 for $\alpha_j = 25°$ and $\alpha_j = 50°$ cases, respectively.

1. Regime I: Dominant central recirculation flow regime

Regime I, which occurs for $0° \leq \alpha_j < 10°$, is dominated by the axial momentum from the outer jets toward the rear of the chamber that converge onto a saddle point, S_A, to generate a large central recirculation zone (CRZ) within the cylindrical chamber. Downstream from the saddle point, toward the cylinder walls ($r/R_c \approx 0.8$), a small vortex can be observed. This

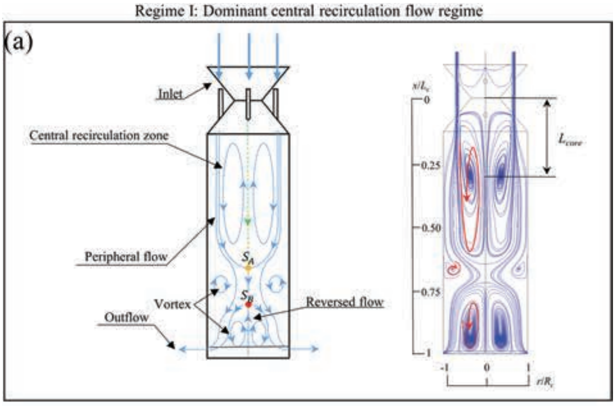
Regime I: Dominant central recirculation flow regime

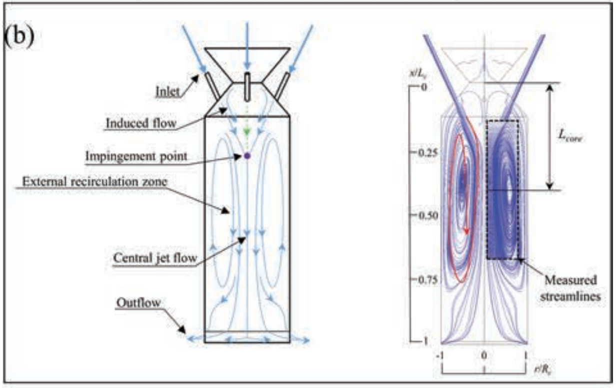
Regime II: External recirculation dominated flow regime

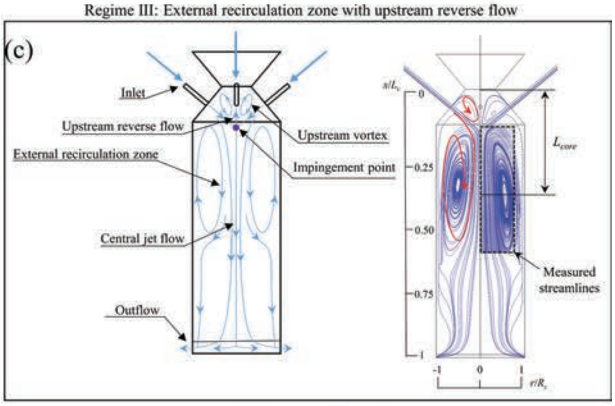
Regime III: External recirculation zone with upstream reverse flow

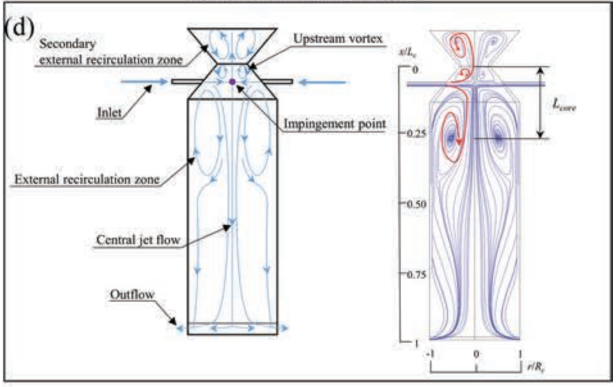
Regime IV: Jet impingement regime

FIG. 15. Simplified diagrams showing the major flow features within the Multiple Impinging Jets in a Cylindrical Chamber (MIJCC) configurations (left) and calculated flow patterns of 4-jet MIJCC configurations with $\alpha_j = 0°, 25°, 50°, 90°$, as generated with the CFD model validated with the PIV measurements. (a) Regime I: dominant central recirculation flow regime, (b) Regime II: external recirculation dominated flow regime, (c) Regime III: external recirculation zone with upstream reverse flow, (d) Regime IV: jet impingement regime.

vortex is linked to the stream-line curvature of the peripheral flow, generated by the interaction between the jets and the walls, drawing fluid from the outer region ($r/R_c > 0.8$) to the inner region ($0 < r/R_c < 0.8$) of the cylinder at $x/L_c \approx 0.7$, before the flow exits from the chamber via the annular outlets. At the downstream end of the cylinder, close to the axis, a reversed flow is observed. This leads to the generation of the second vortical region at the end of the chamber and the second saddle point, S_B.

2. *Regime II: External recirculation dominated flow regime*

Regime II, which occurs for $10° \leq \alpha_j < 35°$, is characterized by a merged central jet within upstream half of the chamber and a dominant external recirculation zone (ERZ) around it. The merged central jet is a dominant feature of this regime. Unlike Regime I, no reversed flow is present on the axis in the region downstream from the point of impingement. At the upstream region of the chamber, near the throat plane, an induced flow toward the impingement point can be observed. However, the intensity of flow in this region is low.

3. *Regime III: External recirculation zone with upstream reverse flow*

Regime III, which for $35° \leq \alpha_j < 60°$, is characterized by a region of reverse flow upstream from the nozzle inlets in addition to the ERZ within the main chamber. This is termed the "upstream vortex." The upstream reverse flow is also associated with an annular vortex within the conical section of the chamber. Also significant are the instantaneous PIV measurements, shown in Figs. 5(b) and 5(d), which reveal that this regime tends to generate an unstable impingement point, so that resultant jet exhibits significant flow oscillations. This was observed experimentally to constitute a precession, so that the turbulent characteristics in the flow-field are more variable in this regime than the other two.

4. *Regime IV: Jet impingement regime*

Regime IV, which occurs for $60° \leq \alpha_j < 90°$, is associated with the increase in the size and strength of the vortex region upstream from the impingement point to extend through the throat plane and into the secondary concentrator (SC). This penetration of the secondary ERZ through the throat is associated with significant transport of fluid between the conical chamber and the SC, which is typically undesirable for solar thermal devices.

Table IV presents the measured and calculated dimensionless recirculation core location (L_{core}/L_c) for four experimental cases. The value of L_{core} was determined with the method

TABLE IV. Measured and calculated dimensionless recirculation core location (L_{core}/L_c) for the cases of MIJCC_25_2J, MIJCC_50_2J, MIJCC_25_4J, and MIJCC_50_4J.

Configurations	Calculated L_{core}/L_c	Measured L_{core}/L_c	Difference (%)
MIJCC_25_2J	0.43	0.45	4.4
MIJCC_50_2J	0.26	0.29	11
MIJCC_25_4J	0.40	0.42	4.7
MIJCC_50_4J	0.36	0.38	5.3

TABLE V. Definition of flow regimes in the MIJCC configuration.

Flow regime	Characteristics
Regime I	1. The dominance of a central recirculation zone (CRZ) within the cylindrical chamber, so that its length exceeds half the chamber length
Regime II	1. Characterized by an impingement point within the upstream half of the chamber; 2. the dominance of an external recirculation zone (ERZ) within the cylindrical chamber
Regime III	1. A significant reverse flow ($U_c \lesssim 0$) upstream from the impingement point (the value of $\lvert U_c/U_b \rvert \gtrsim 5\%$ upstream from the impingement point); 2. a small vortex is generated upstream from the impingement point but does not extend into the secondary concentrator (SC)
Regime IV	1. A significant reverse flow extends through the throat plane into the SC section ($\dot{m}_{th}/\dot{m}_{in} \gtrsim 5\%$); 2. a secondary ERZ is generated within the SC section

described by Grosjean *et al.*[53] and Volkert *et al.*,[54] in which the vortex core is defined as the crossing point for lines of zero u_x, v_x, $u_x + v_x$, and $u_x - v_x$ on the *x*-*r* coordinate system (2-dimensional). It can be seen that the calculated results of L_{core}/L_c agree with the experimental results to within an average of 7%. It can also be seen that, for a given value of N_j, an increase in α_j leads to a decrease in L_{core}/L_c. That is, the centre of the dominant recirculation (vortex core) moves upstream within an increase in α_j. This finding is also consistent with the calculated streamlines for Regime I, II, III, and IV (Fig. 15).

Table V presents the definition of flow regimes within the MIJCC configuration, which is obtained from the fluid visualization and quantitative data from both PIV and CFD results presented in Fig. 15.

Figure 16 presents a map of the geometric configurations for which the various flow regimes are generated as a function of the jet inclination angle, α_j, for the cases N_j = 2, 4, and 8 cases. The data have been derived from a combination of experimental data, where they are available, and additional numerical data, showing explicitly those cases for which data are available to directly validate the model and those cases for which the model has been extended to conditions where no experimental data are yet available, notably for $N_j = 8$. It can be seen that the transition between the different flow regimes occurs for $\alpha_j \approx 10°, 35°, 60°$ for the $N_j = 4$ configuration and $\alpha_j \approx 10°, 50°, 70°$ for the $N_j = 2$ configuration. This indicates that Regime I occurs in the range $0° \leq \alpha_j < 10°$ for both $N_j = 2$ and $N_j = 4$ configurations, while the other three regimes do not occur consistently at the same inclination angles as N_j is increased from 2 to 4. Therefore, an increase in jet number from 2 to 4 could have a substantial effect on the flow-field for $\alpha_j > 10°$. This trend is more notable for $N_j = 8$ configuration, in which the transition between the different flow regimes occurs at $\alpha_j \approx 10°$, 25°, and 50°. This indicates that the transition between regimes occurs at lower jet inclination angles for an increase in the number of jets (N_j) or with an increase in the area of jets ($A_{pipe.tot}$). Hence, it can be concluded that, for configurations in which $0° \leq \alpha_j \leq 90°$, the jet inclination angle (α_j) is expected to be the dominant parameter that characterizes the flow-field within a cylindrical chamber, while for a given value of D_{pipe}, the number of inlet jets (N_j) is expected to influence the transition of flow regimes for configurations in which $10° \leq \alpha_j \leq 90°$.

E. Quantification of the recirculation rate

Figure 17 presents the effect of α_j on the calculated local recirculation rate ($K_v = \dot{m}_e/\dot{m}_{in}$) within the MIJCC configuration for five different inclination angles $\alpha_j = 0°$, 25°, 50°, 75°, and 90° for the $N_j = 4$ configuration. Here $\dot{m}_e$ denotes the total mass flow rate of fluid entrained by all inlet jets transported upstream through a plane orthogonal to the axis at the plane x/L_c, while $\dot{m}_{in}$ refers to the total inlet mass flow rate of fluid. All values were obtained using the built-in "Iso-Clip" function in ANSYS/CFX. For reference, we also plot the blue cross marker to denote the normalized location of the core of the recirculation zone (L_{core}/L_c) for five calculated

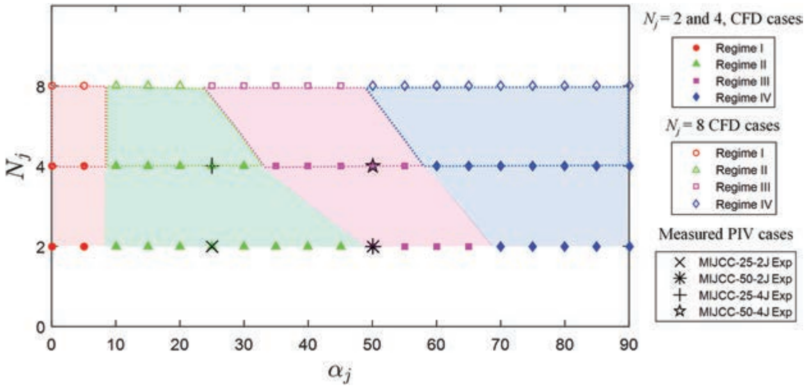

FIG. 16. Map of flow regimes as a function of the inclination angles (α_j) for N_j = 2, 4, and 8 of the Multiple Impinging Jets in a Cylindrical Chamber (MIJCC) configurations.

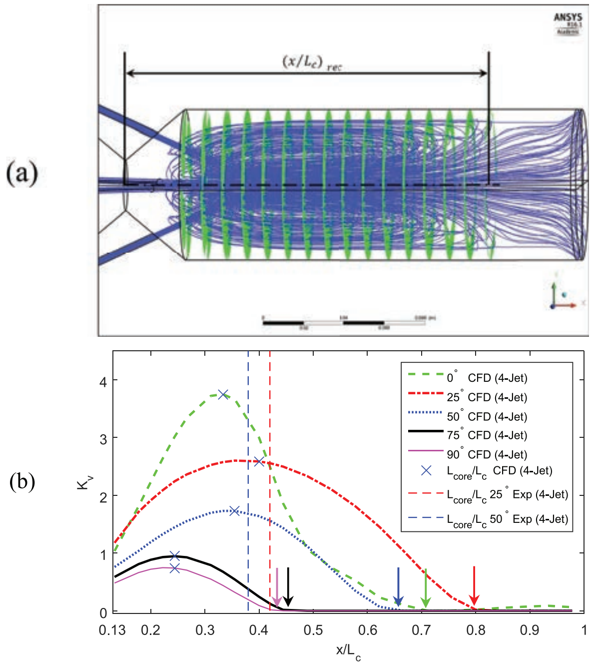

FIG. 17. Calculated axial evolution of the normalized recirculation rate ($K_v = \dot{m}_e/\dot{m}_{in}$) for the 4-jet configuration of the Multiple Impinging Jets in a Cylindrical Chamber (MIJCC) with five inclination angles, together with a schematic diagram of the ANSYS/CFX "iso-clip" function for MIJCC_25_4J as shown in part (a). Here $\dot{m}_e$ denotes the total mass flow rate of fluid transported upstream through a plane orthogonal to the axis at a selected location x/L_c and $\dot{m}_{in}$ refers to the inlet mass flow rate of fluid through all jets. The length of the recirculation zone location $(x/L_c)_{rec}$, derived from (a), is denoted with an arrow, color matched for each case. The blue cross marker denotes the normalized location of the core of the recirculation zone (L_{core}/L_c) for five calculated cases, while the two vertical dashed lines (red and blue) denote the location of the measured values of L_{core}/L_c for MIJCC_25_4J and MIJCC_50_4J. Note $x/L_c = 0.13$ refers to the upstream edge of the cylindrical section of the chamber.

cases, while we plot the two vertical dashed lines (red and blue) to denote the location of the measured values of L_{core}/L_c for MIJCC_25_4J and MIJCC_50_4J (refer to Fig. 15 and Table IV).

A schematic diagram of the planes within the MIJCC_25_4J for which K_v was calculated is shown in Fig. 17(a), as green lines, while the blue lines are streamlines. It can be seen that the maximum downstream location for which $K_v \geq 0$ coincides well with the downstream-end of the recirculation zone, $(x/L_c)_{rec}$, as also shown in Fig. 17(a). The downstream axial location where K_v approaches zero corresponds well to the location of $(x/L_c)_{rec}$ for all cases, as shown in Fig. 17(b) with colored arrows.

The results of Fig. 17(b) show that, for cases where jet impingement occurs ($\alpha_j = 25°, 50°, 75°$, and $90°$), the location of $(x/L_c)_{rec}$ for which K_v is positive progresses upstream from $(x/L_c)_{rec} = 0.8$ to $(x/L_c)_{rec} = 0.43$ as α_j is increased from 25° (Regime II) to 90° (Regime IV). This implies that an increase in α_j leads to a reduction in the distribution of the external recirculation zone (ERZ). However, from the case $\alpha_j = 0°$ (Regime I) to 25° (Regime II), a 10% increase in the distribution of the recirculation zone was found for which K_v is positive moving from $(x/L_c)_{rec} = 0.7$ to $(x/L_c)_{rec} = 0.8$. This is also consistent with the qualitative trend of measured and calculated streamlines illustrated in Fig. 15. Taken together, it can be concluded that the integrated recirculated flow within the recirculation zone is greatest for Regime II ($\alpha_j = 25°$), and the axial variation is also more uniform than that it is for Regimes I, III, and IV ($\alpha_j = 0°, 50°, 75°$, and $90°$). This finding is important for the development of practical combustion applications employing MILD (moderate or intense low oxygen dilution) combustion because the presence of a large and uniform recirculation zone is crucial for achieving desirable mixing, heat transfer, and quasi-homogeneous temperature within the chamber.[55,56]

It is also worth noting that the calculated value of L_{core}/L_c for these five cases coincides fairly well with the location of the peak in K_v. This implies that the maximum amount of recirculation coincides with the location of the centre of dominant recirculation zone, consistent with expectation. That is, $L_{core} \approx x_{Kv.max}$.

F. Reverse flow through the throat

Figure 18 presents the influence of α_j on the calculated normalized mass flow rate through the throat ($\dot{m}_{th}/\dot{m}_{in}$). Here $\dot{m}_{th}$ denotes the mass flow rate through the throat plane ($x/L_c = 0$) into the SC, which was obtained with the "Iso-Clip" function in ANSYS/CFX, while $\dot{m}_{in}$ is the total inlet mass flow rate of fluid. For both the $N_j = 2$ and 4 cases, it can be seen that the percentage of the mass flow rate through the throat plane is approximately zero for $\alpha_j < 55°$. Importantly, this means that there is negligible flow entering the SC within the range of $0° \leq \alpha_j < 55°$. This is a significant finding because in practical combustion devices, particularly of the HSRC technology, the limitation of heat and fluid flow from the main cylindrical chamber into the SC (where they may be lost to the environment), is crucial for maintaining high thermal efficiency of the reactor.

The results also show that an increase in α_j above the threshold causes a significant increase in $\dot{m}_{th}/\dot{m}_{in}$ from 0.3% ($\alpha_j = 55°$) to 66% ($\alpha_j = 90°$) with the $N_j = 4$ case. While the trend is similar for the $N_j = 2$ case, the values are slightly lower for $\dot{m}_{th}/\dot{m}_{in} = 0.3\%$ for $\alpha_j = 65°$, while the maximum value of $\dot{m}_{th}/\dot{m}_{in} = 59\%$ for $\alpha_j = 90°$. This suggests that the inclination angle should be chosen to be $\alpha_{j.op} > 65°$ for $N_j = 2$ and $\alpha_{j.op} > 55°$ for $N_j = 4$ to avoid significant induction of flow through the aperture. This value maintains the relative mass flow rate of upstream reversed flow to be less than 0.3% ($\dot{m}_{th}/\dot{m}_{in} \leq 0.3\%$). These angles are also smaller than the

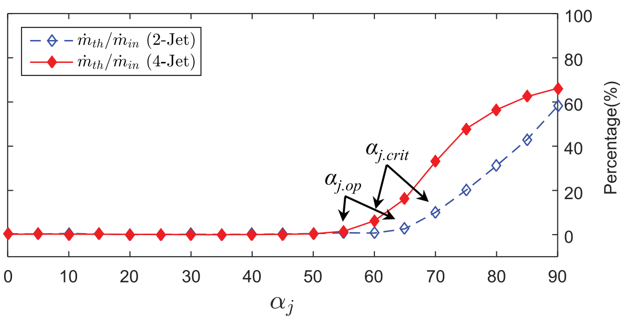

FIG. 18. Comparison of the calculated mass flow rate through the throat to the secondary concentrator ($\dot{m}_{th}/\dot{m}_{in}$) of the Multiple Impinging Jets in a Cylindrical Chamber (MIJCC), normalized by the total inlet mass flow rate ($\dot{m}_{in}$), as a function of inclination angles (α_j).

critical inclination angles for which $\dot{m}_{th}$ becomes significant ($\dot{m}_{th}/\dot{m}_{in} \gtrsim 5\%$), i.e., $\alpha_{j.crit} = 70°$ for $N_j = 2$ and $\alpha_{j.crit} = 60°$ for $N_j = 4$, corresponding to the transition between Regimes III and IV (Fig. 15).

IV. CONCLUSIONS

A joint experimental and numerical investigation was carried out to characterize the iso-thermal flow patterns within a cylindrical geometry configured with planar-symmetric jets (two or four jets) inclined at several different angles (α_j), termed the Multiple Impinging Jets in a Cylindrical Chamber (MIJCC) relevant to Hybrid Solar Receiver Combustor (HSRC) technology. The key outcomes of the study are as follows:

1. The characteristics of the flow field exhibit a primary dependence on the inclination angle, α_j, and a secondary dependence on the number of inlet jets (N_j). The location of the jet impingement point progresses upstream with an increase in α_j from 25° to 90°, while an increase in N_j from 2 to 4 causes a smaller upstream translation of the jet impingement point. In addition, significant flow oscillations and precession of the resulting jet were observed from both the instantaneous and mean velocity fields for $\alpha_j = 50°$.
2. The decay of the mean centerline velocity of the resulting jet is significantly greater than a single unconfined free jet. This is partly attributed to the role of confinement and partly to the additional unsteadiness caused by the impingement. The decay in the mean centerline velocity also decreases with an increase in N_j (from 2 to 4), both for the case with the constant nozzle diameter (D_{pipe}) and that with the constant total nozzle area ($A_{pipe.tot}$). This is attributed to an increase in the number of jets inhibiting the lateral spread of the jet downstream from the impingement point. It also appears to inhibit the unsteadiness of the flow, although this was not quantified.
3. The resulting jet exhibits a high turbulence intensity due to the strong flow interaction between jets themselves and ambient fluids, while an increase in N_j was found to substantially reduce the turbulent fluctuations. A high degree of Reynolds stress anisotropy was also found in the resulting jet, particularly for the $N_j = 2$ cases.
4. Four dominant flow regimes (Regime I, II, III, IV) were found within the MIJCC configuration investigated here depending on the value of α_j, while an increase in N_j (2–8) decreases the α_j at which the flow transitions between each flow regime. For $N_j = 4$ configurations:
    - (a) Regime I ($0° \le \alpha_j < 10°$): the dominance of a central recirculation zone (CRZ) within the cylindrical chamber.
    - (b) Regime II ($10° \le \alpha_j < 35°$): the presence of jet impingement point and the dominance of an external recirculation zone (ERZ) within the cylindrical chamber.
    - (c) Regime III ($35° \le \alpha_j < 60°$): the presence of a reverse flow and vortex upstream from the impingement point.
    - (d) Regime IV ($60° \le \alpha_j \le 90°$): the presence of a secondary dominant ERZ within the secondary concentrator (SC) section.
5. The calculated recirculation rate ($K_v = \dot{m}_e/\dot{m}_{in}$) for $N_j = 4$ cases shows that Regime II ($\alpha_j = 25°$) provides the greatest total mass of recirculated fluid, which is also most uniform in the axial direction. This is important for combustion technologies, particularly for MILD (moderate or intense low-oxygen dilution) combustion, since the recirculation zone is associated with high rates of mixing, heat transfer, and quasi-homogeneous temperature within the chamber.
6. A critical inclination angle was found below which significant circulation between the throat and the secondary concentrator (SC) can be avoided, that is, $\alpha_{j.op} = 65°$ and $\alpha_{j.op} = 55°$ for $N_j = 2$ and $N_j = 4$ configurations, respectively. This finding is significant for combustion devices as the avoidance of upstream reverse flow is crucial for maintaining high reactor efficiency and thermal performance.

SUPPLEMENTARY MATERIAL

See supplementary material for the CFD model selection and validation.

ACKNOWLEDGMENTS

The authors would like to acknowledge the support of the Australian Research Council, FCT Combustion Pty. Ltd., and Vast Solar Pty. Ltd. through the ARC Linkage Grant No. LP110200060. The authors would also like to thank Mr. Xiao Chen for his useful contributions in CFD simulation. S.L. acknowledges the financial support of the Australian Government Research Training Program. Finally, the insightful observations and constructive feedback of the anonymous reviewers have strengthened the paper and are gratefully acknowledged.

[1] S. Pope, "An explanation of the turbulent round-jet/plane-jet anomaly," AIAA J. **16**, 279 (1978).

[2] B. Boersma, G. Brethouwer, and F. Nieuwstadt, "A numerical investigation on the effect of the inflow conditions on the self-similar region of a round jet," Phys. Fluids **10**, 899 (1998).

[3] F. Lockwood and A. Naguib, "The prediction of the fluctuations in the properties of free, round-jet, turbulent, diffusion flames," Combust. Flame **24**, 109 (1975).

[4] A. Yule, "Large-scale structure in the mixing layer of a round jet," J. Fluid Mech. **89**, 413 (1978).

[5] G. Cox, "Multiple jet correlations for gas turbine engine combustor design," J. Eng. Power **98**, 265 (1976).

[6] T. Boushaki, J. Sautet, L. Salentey, and B. Labegorre, "The behaviour of lifted oxy-fuel flames in burners with separated jets," Int. Commun. Heat Mass Transfer **34**, 8 (2007).

[7] Q. Li, H. Yoshino, A. Mochida, B. Lei, Q. Meng, L. Zhao, and Y. Lun, "CFD study of the thermal environment in an air-conditioned train station building," Build. Environ. **44**, 1452 (2009).

[8] B.v. d. Giesen, S. Penders, M. Loomans, P. Rutten, and J. Hensen, "Modelling and simulation of a jet fan for controlled air flow in large enclosures," Environ. Modell. Software **26**, 191 (2011).

[9] F. Colella, G. Rein, R. Borchiellini, R. Carvel, J. L. Torero, and V. Verda, "Calculation and design of tunnel ventilation systems using a two-scale modelling approach," Build. Environ. **44**, 2357 (2009).

[10] G. Nathan, D. Battye, and P. Ashman, "Economic evaluation of a novel fuel-saver hybrid combining a solar receiver with a combustor for a solar power tower," Appl. Energy **113**, 1235 (2014).

[11] J. H. Lim, G. J. Nathan, E. Hu, and B. B. Dally, "Analytical assessment of a novel hybrid solar tubular receiver and combustor," Appl. Energy **162**, 298 (2016).

[12] J. H. Lim, E. Hu, and G. J. Nathan, "Impact of start-up and shut-down losses on the economic benefit of an integrated hybrid solar cavity receiver and combustor," Appl. Energy **164**, 10 (2016).

[13] A. Chinnici, Z. F. Tian, J. H. Lim, G. J. Nathan, and B. B. Dally, "Comparison of system performance in a hybrid solar receiver combustor operating with MILD and conventional combustion. Part I: Solar-only and combustion-only employing conventional combustion," Sol. Energy **147**, 489 (2017).

[14] A. Chinnici, Z. F. Tian, J. H. Lim, G. J. Nathan, and B. B. Dally, "Comparison of system performance in a hybrid solar receiver combustor operating with MILD and conventional combustion. Part II: Effect of the combustion mode," Sol. Energy **147**, 479 (2017).

[15] J. A. Fitzgerald and S. V. Garimella, "A study of the flow field of a confined and submerged impinging jet," Int. J. Heat Mass Transfer **41**, 1025 (1998).

[16] A. Leite, M. Ferreira, and J. Carvalho, "An investigation of multiple jet acetylene flames," Int. Commun. Heat Mass Transfer **23**, 959 (1996).

[17] E. Tanaka, "The interference of two-dimensional parallel jets: 1st report, experiments on dual jet," Bull. JSME **13**, 272 (1970).

[18] E. Tanaka, "The interference of two-dimensional parallel jets: 2nd report, experiments on the combined flow of dual jet," Bull. JSME **17**, 920 (1974).

[19] E. Tanaka and S. Nakata, "The interference of two-dimensional parallel jets: 3rd report, the region near the nozzles in triple jets," Bull. JSME **18**, 1134 (1975).

[20] S. Raghunathan and I. Reid, "A study of multiple jets," AIAA J. **19**, 124 (1981).

[21] R. Menon and S. Gollahalli, "Combustion characteristics of interacting multiple jets in cross flow," Combust. Sci. Technol. **60**, 375 (1988).

[22] G. H. Moustafa, "Experimental investigation of high-speed twin jets," AIAA J. **32**, 2320 (1994).

[23] J. Yimer, H. Becker, and E. Grandmaison, "Development of flow from multiple-jet burners," Can. J. Chem. Eng. **74**, 840 (1996).

[24] E. Koepf, W. Villasmil, and A. Meier, "High temperature flow visualization and aerodynamic window protection of a 100-kW$_{\mathrm{th}}$ solar thermochemical receiver-reactor for ZnO dissociation," Energy Procedia **69**, 1780 (2015).

[25] R. C. Deo, J. Mi, and G. J. Nathan, "The influence of Reynolds number on a plane jet," Phys. Fluids **20**, 075108 (2008).

[26] T. Chammem, H. Mhiri, and O. Vauquelin, "Experimental and computational investigation of Reynolds number effect on the longitudinal ventilation in large enclosure of twin inclined jets," Build. Environ. **67**, 87 (2013).

[27] T. Chammem, O. Vauquelin, and H. Mhiri, "Performance evaluation of alternative tunnel longitudinal ventilation systems using two inclined jets," Tunnelling Underground Space Technol. **41**, 53 (2014).

[28] T. Boushaki and J.-C. Sautet, "Characteristics of flow from an oxy-fuel burner with separated jets: Influence of jet injection angle," Exp. Fluids **48**, 1095 (2010).

[29] J. Nikuradse, "Gesetzmäßigkeiten der turbulenten Strömung in glatten Rohren," Forsch. Geb. Ingenieurwes. **4**, 44 (1933).

[30] M. Angioletti, E. Nino, and G. Ruocco, "CFD turbulent modelling of jet impingement and its validation by particle image velocimetry and mass transfer measurements," Int. J. Therm. Sci. **44**, 349 (2005).

[31] J. Jiao, Z. Liu, and Y. Zheng, "Evaluations and modifications on Reynolds stress model in cyclone simulations," Chem. Eng. Technol. **30**, 15 (2007).

[32] Z. F. Tian, G. J. Nathan, and Y. Cao, "Numerical modelling of flows in a solar–enhanced vortex gasifier: Part 1, comparison of turbulence models," Prog. Comput. Fluid. Dyn., Int. J. **15**, 114 (2015).

[33] C. G. Speziale, S. Sarkar, and T. B. Gatski, "Modelling the pressure–strain correlation of turbulence: An invariant dynamical systems approach," J. Fluid Mech. **227**, 245 (1991).

[34] B. Launder, G. J. Reece, and W. Rodi, "Progress in the development of a Reynolds-stress turbulence closure," J. Fluid Mech. **68**, 537 (1975).

[35] M. Gibson and B. Launder, "Ground effects on pressure fluctuations in the atmospheric boundary layer," J. Fluid Mech. **86**, 491 (1978).

[36] J. Panda, H. Warrior, S. Maity, A. Mitra, and K. Sasmal, "An improved model including length scale anisotropy for the pressure strain correlation of turbulence," J. Fluids Eng. **139**, 044503 (2017).

[37] A. A. Mishra and S. S. Girimaji, "Toward approximating non-local dynamics in single-point pressure–strain correlation closures," J. Fluid Mech. **811**, 168 (2017).

[38] Y. Liu, M. G. Olsen, and R. O. Fox, "Turbulence in a microscale planar confined impinging-jets reactor," Lab Chip **9**, 1110 (2009).

[39] M. Icardi, E. Gavi, D. L. Marchisio, A. A. Barresi, M. G. Olsen, R. O. Fox, and D. Lakehal, "Investigation of the flow field in a three-dimensional confined impinging jets reactor by means of microPIV and DNS," Chem. Eng. J. **166**, 294 (2011).

[40] Z. Gao, J. Han, Y. Xu, Y. Bao, and Z. Li, "Particle image velocimetry (PIV) investigation of flow characteristics in confined impinging jet reactors," Ind. Eng. Chem. Res. **52**, 11779 (2013).

[41] C. X. Thong, P. A. Kalt, B. B. Dally, and C. H. Birzer, "Flow dynamics of multi-lateral jets injection into a round pipe flow," Exp. Fluids **56**, 15 (2015).

[42] D. L. Marchisio, "Large eddy simulation of mixing and reaction in a confined impinging jets reactor," Comput. Chem. Eng. **33**, 408 (2009).

[43] J. Mi, P. Kalt, G. Nathan, and C. Wong, "PIV measurements of a turbulent jet issuing from round sharp-edged plate," Exp. Fluids **42**, 625 (2007).

[44] G. Xu and R. Antonia, "Effect of different initial conditions on a turbulent round free jet," Exp. Fluids **33**, 677 (2002).

[45] T. C. Lau and G. J. Nathan, "The effect of Stokes number on particle velocity and concentration distributions in a well-characterised, turbulent, co-flowing two-phase jet," J. Fluid Mech. **809**, 72 (2016).

[46] M. Panao and J. Delgado, "Toward the design of low flow-rate multijet impingement spray atomizers," Exp. Therm. Fluid Sci. **58**, 170 (2014).

[47] N. Bremond and E. Villermaux, "Atomization by jet impact," J. Fluid Mech. **549**, 273 (2006).

[48] G. Morris, S. Garimella, and J. Fitzgerald, "Flow-field prediction in submerged and confined jet impingement using the Reynolds stress model," J. Electron. Packag. **121**, 255 (1999).

[49] M. K. Isman, P. J. Morris, and M. Can, "Investigation of laminar to turbulent transition phenomena effects on impingement heat transfer," Heat Mass Transfer **52**, 2027 (2016).

[50] E. Gavi, D. L. Marchisio, and A. A. Barresi, "CFD modelling and scale-up of confined impinging jet reactors," Chem. Eng. Sci. **62**, 2228 (2007).

[51] E. Faghani and S. N. Rogak, "A phenomenological model of two circular turbulent jets," Int. J. Engine Res. **14**, 293 (2013).

[52] A. Nasr and J. Lai, "Two parallel plane jets: Mean flow and effects of acoustic excitation," Exp. Fluids **22**, 251 (1997).

[53] N. Grosjean, L. Graftieaux, M. Michard, W. Hübner, C. Tropea, and J. Volkert, "Combining LDA and PIV for turbulence measurements in unsteady swirling flows," Meas. Sci. Technol. **8**, 1523 (1997).

[54] J. Volkert, C. Tropea, R. Domann, and W. Hübner, "Combined application of particle image velocimetry (PIV) and laser Doppler anemometry, (LDA) to swirling flows under compression," in *Proceedings of the 8th International Symposia on Applications of Laser Techniques to Fluid Mechanics* (Springer-Verlag, 1996), Vol. 19, pp. 1–19.

[55] G. Szegö, B. Dally, and G. Nathan, "Operational characteristics of a parallel jet MILD combustion burner system," Combust. Flame **156**, 429 (2009).

[56] J. Mi, F. Wang, P. Li, and B. Dally, "Modified vitiation in a moderate or intense low-oxygen dilution (MILD) combustion furnace," Energy Fuels **26**, 265 (2011).

Chapter 5

Iso-thermal Flow Characteristics of Rotationally Symmetric Jets generating a Swirl within a Cylindrical Chamber

Statement of Authorship

Title of Paper	Iso-thermal flow characteristics of rotationally symmetric jets generating a swirl within a cylindrical chamber
Publication Status	☑ Published ☐ Accepted for Publication ☐ Submitted for Publication ☐ Unpublished and Unsubmitted work written in manuscript style
Publication Details	Long, S., Lau, T.C., Chinnici, A., Tian, Z.F., Dally, B.B. and Nathan, G.J., 2018. Iso-thermal flow characteristics of rotationally symmetric jets generating a swirl within a cylindrical chamber. Physics of Fluids, vol. 30, no. 5, p.055110.

Principal Author

Name of Principal Author (Candidate)	Shen Long		
Contribution to the Paper	Conducted literature review, collected all experimental data, performed data processing and analysis, wrote manuscript and acted as corresponding author.		
Overall percentage (%)	65		
Certification:	This paper reports on original research I conducted during the period of my Higher Degree by Research candidature and is not subject to any obligations or contractual agreements with a third party that would constrain its inclusion in this thesis. I am the primary author of this paper.		
Signature		Date	07/01/2019

Co-Author Contributions

By signing the Statement of Authorship, each author certifies that:

i. the candidate's stated contribution to the publication is accurate (as detailed above);
ii. permission is granted for the candidate in include the publication in the thesis; and
iii. the sum of all co-author contributions is equal to 100% less the candidate's stated contribution.

Name of Co-Author	Timothy Lau		
Contribution to the Paper	Supervised the experiments, helped in data interpreting and edited manuscript.		
Signature		Date	7/01/2019

Name of Co-Author	Alfonso Chinnici		
Contribution to the Paper	Helped to develop the work and helped in data interpreting.		
Signature		Date	07/01/19

Name of Co-Author	Zhao Feng Tian		
Contribution to the Paper	Supervised the development of work and helped in data interpreting.		
Signature		Date	07/01/19

Name of Co-Author	Bassam Dally		
Contribution to the Paper	Supervised the development of work, provided comments and edited manuscript.		
Signature		Date	7-1-19

Name of Co-Author	Graham 'Gus' Nathan		
Contribution to the Paper	Supervised the development of work, helped in data interpreting, provided comments and edited manuscript.		
Signature		Date	7/1/19

PHYSICS OF FLUIDS **30**, 055110 (2018)

Iso-thermal flow characteristics of rotationally symmetric jets generating a swirl within a cylindrical chamber

Shen Long,[a)] Timothy C. W. Lau, Alfonso Chinnici, Zhao Feng Tian, Bassam B. Dally, and Graham J. Nathan
Centre for Energy Technology, School of Mechanical Engineering, The University of Adelaide, Adelaide, South Australia 5005, Australia

(Received 23 February 2018; accepted 8 May 2018; published online 31 May 2018)

We present a systematic experimental study of the interaction between four rotationally symmetric jets within a cylindrical chamber, under conditions relevant to a wide range of engineering applications, including the technology of a Hybrid Solar Receiver Combustor (HSRC). The HSRC geometry is simplified here to a cylindrical cavity with four inlet jets (representing four burners) which are configured in an annular arrangement and aligned at an inclination angle to the axis with a tangential component (azimuthal angle) to generate a swirl in the chamber. In this study, the jet inclination angle (α_j) was varied over the range of 25°–45°, while the jet azimuthal angle (θ_j) was varied from 5° to 15°. The inlet Reynolds number for each injected jet and the number of jets were fixed at $Re_D = 10\,500$ and 4, respectively. Measurements obtained with Particle Image Velocimetry were used to characterise the large-scale flow field within selected configurations. The results reveal a significant dependence of the mean and root-mean-square flow-fields on the jet azimuthal angle (θ_j) and the jet inclination angle (α_j). Three different flow regimes with distinctive flow characteristics were identified within the configurations investigated here. It was also found that θ_j can significantly influence (a) the position and strength of an external recirculation zone and a central recirculation zone, (b) the extent of turbulence fluctuation, and (c) the flow unsteadiness. Importantly, the effect of α_j on the flow characteristics was found to depend strongly on the value of θ_j. *Published by AIP Publishing.*
https://doi.org/10.1063/1.5026719

I. INTRODUCTION

Multiple symmetric jets are employed within confined spaces in a wide range of engineering applications which include solar receiver reactors,[1] gas turbine engines,[2] longitudinal ventilation systems,[3] and separated-jet combustors.[4] However, the greater complexity of these configurations over the single round jet issuing into a quiescent environment,[5] including the additional parameters and experimental challenges, means many gaps in understanding remain. Of particular interest here is a multiple-jet configuration featuring a rotationally symmetric arrangement of jets with a tangential component of relevance to the Hybrid Solar Receiver Combustor (HSRC) under development at the University of Adelaide.[6–11] The HSRC offers potential to reduce both the energy losses and total infrastructure requirements relative to a hybrid from stand-alone components, while providing a firm supply of energy for heat and power applications. The HSRC features a cavity that is operable as a combustion chamber, or as a cavity receiver with multiple burners to direct fuel and air into the chamber, and tubular heat exchangers to transfer the thermal energy to the heat transfer fluid. Importantly, the configuration of the combustion system in a solar cavity differs from that in a conventional combustor owing to the need to incorporate the aperture. This results in an annular ring of burners which can be configured in a rotationally symmetric arrangement and aligned at an inclination angle (α_j) relative to the axis of the chamber and/or at an azimuthal angle (θ_j) relative to the axis of the burner. The presence of walls (confinement), together with the α_j and θ_j of burners, has an additional influence on the pressure field, the jet interactions, and the entrainment rates so that the flow patterns within the cavity are complex.[6] The overall objective of the present paper is therefore to characterize for the first time the flow regimes that can be generated within a cylindrical chamber (i.e., as a confined flow) with multiple rotationally symmetric inlet-jets configured to generate a swirl in the chamber.

Previous investigations of flow-fields generated with multiple symmetric jets have been performed almost exclusively for either parallel-jets ($\alpha_j = 0°$)[12–15] or opposed-jets ($\alpha_j = 90°$).[16–18] However, the studies of inclined jets ($0° < \alpha_j < 90°$) revealed a strong dependence of the flow characteristics on the jet inclination angle (α_j).[3,4,6] The study of Chammem *et al.*[3] for inclined confined jets defined the "resulting jet" as a central, merged jet downstream from the jet impingement point. They also found that the reverse flow can only be generated within a certain range of α_j. The particle image velocimetry (PIV) measurements of Boushaki and Sautet[4] for a multi-jet combustor showed that an increase in α_j from 0° to 30° can significantly change the instantaneous velocity fields and the mixing characteristics of inclined confined jets. A detailed characterization of the flow-field generated with multiple planar-symmetric confined jets was also

---

[a)] Author to whom correspondence should be addressed: shen.long@adelaide.edu.au reported by Long *et al.*[6] They have conducted a computational fluid dynamics (CFD) study and PIV measurements to fully characterize the flow regimes within the range $0° \le \alpha_j \le 90°$, revealing a controlling influence of α_j on flow stability, turbulence intensity, and dominant recirculation regions. Nevertheless, to our knowledge, most of the previous multiple-jet studies considered only the influence of α_j so that little or no information is available of the influence of the azimuthal angle θ_j. This gap is significant because the combination of θ_j and α_j for multiple jets (rotational-symmetry) has a wide relevance to vortex combustors,[19–21] cyclone reactors,[22,23] and solar thermal devices.[24,25] More importantly, owing to the lack of sufficient reliable experimental data, the flow structure generated by multiple rotationally symmetric jets within a confined space is still poorly understood. This is a significant impediment to the continuous development of computational models for relevant configurations.[26] Hence, a more detailed characterization of the flow patterns within a confined chamber for a systematic range of well-defined, consistent inflow and boundary conditions is needed to provide new understanding of the flow generated with rotationally symmetric jets. The present paper aims to address this need.

The influence of the azimuthal angle on the flow-field has been widely investigated for the configuration with annular jets.[19,27–32] These previous studies showed that the value of θ_j, associated with a swirl number, S, can significantly influence the characterization of recirculation zones within a confined space. One of the major features is the presence of a central recirculation zone (CRZ) which is particularly important for the stabilization of a flame, notably by the recirculation of reactants during the combustion process.[19,32] However, while these studies provide useful insight, they are limited to a relatively few configurations since they have been performed almost exclusively for annular ($\alpha_j = 0°$ and $\theta_j = 0°$) or tangential jets ($\theta_j = 90°$ and $\alpha_j = 0°$). Importantly, although Long *et al.*[6] indicated that the inclination angle (α_j) significantly affects the strength and position of the external recirculation zone (ERZ) within a cylindrical chamber, the influence of θ_j on the transition and presence of dominant recirculation regions for multiple inclined jets' ($\alpha_j > 0°$) configurations remains unknown. Therefore, a more detailed and quantitative understanding is needed of the combined effects of θ_j and α_j on the dominant recirculation zones generated with multiple rotationally symmetric jets.

To meet the aforementioned needs, the current study reports an experimental investigation of the iso-thermal flow-fields generated by a cylindrical chamber with rotationally symmetric jets with the following aims: (a) to characterize the mean and RMS (root-mean-square) flow-fields and the integral length scale for a series of rotationally symmetric arrangements of Multiple Impinging Jets in a Cylindrical Chamber (MIJCC); (b) to identify the influence of the small azimuthal angle of jets (θ_j = 5°, 10°, and 15°) in addition to the inclination angle of jets α_j = 25°, 35°, and 45°, on the dominant recirculation zones within a cylindrical chamber; and (c) to characterize the dependence of flow regimes on rotationally symmetric arrangements of multiple jets within a cylindrical chamber.

II. METHODOLOGY

A. Configurations selected in the present study

The configuration of the Multiple Impinging Jets in a Cylindrical Chamber (MIJCC) investigated in the present study is presented schematically in Fig. 1. This can be related to more complex burner arrangements, such as those comprising a central fuel jet and a co-annular air jet, by considering the total momentum associated with the combined jet. The use of a simple jet configuration also makes these results relevant to other practical applications such as solar thermal devices, ventilation systems, and chemical reactors. The key features of the MIJCC are the main cavity, consisting of a cylindrical chamber with a conical expansion, and a secondary concentrator (SC), which is of conical shape. The SC was closed at the largest end with a flap (labeled with a yellow dashed line), preventing flow to the ambient environment, but open at the plane of the throat (labeled with a green line) to admit flow between these sections. This corresponds to the configuration of the HSRC within the combustion-only mode, where the aperture is closed with a flap to prevent heat loss. The MIJCC is also configured with four rotationally symmetric inlet jets distributed around the conical expansion of the main chamber

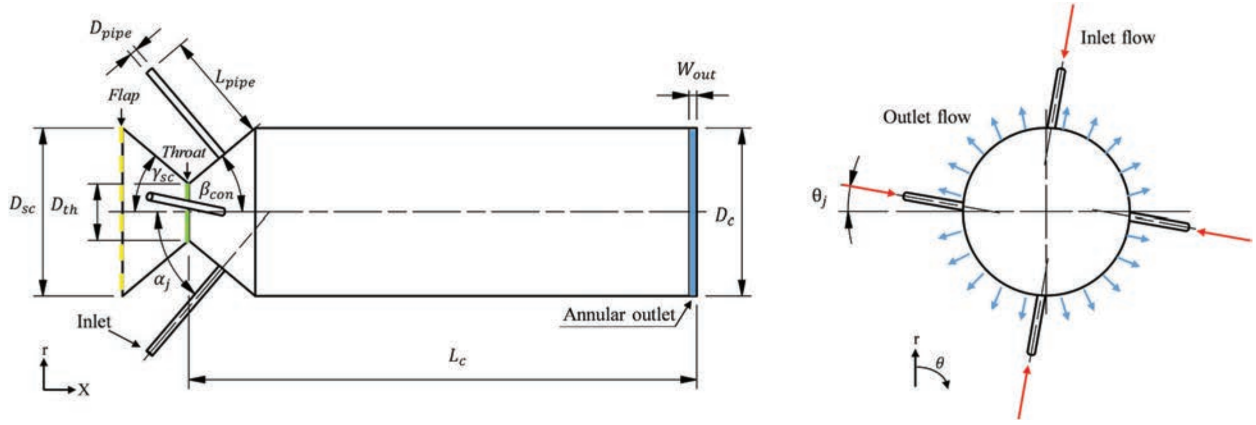

FIG. 1. Schematic diagram of the configurations of the Multiple Impinging Jets in a Cylindrical Chamber (MIJCC) investigated here, showing the key geometric features from the axial cross section (left) and a radial cross section (right). Here the flap plane, throat plane, and annular outlet are highlighted with yellow (dashed), green (solid), and blue lines, respectively.

with an inclination angle (α_j) to the axis of the chamber and/or at an azimuthal angle (θ_j) to the axis of the burner. The flow leaves the chamber in the radial direction through an annular gap around a bluff end wall of uniform thickness, W_{out}.

Nine laboratory-scale configurations were manufactured from acrylic to provide optical access and a close match between the refractive index of the cylindrical chamber and that of the working fluid (water). These have inclination angles of α_j = 25°, 35°, and 45° and azimuthal angles of θ_j = 5°, 10°, and 15°, together with a manufacturing tolerance of ±0.1 mm (linear) and ±0.5° (angular). The three values of α_j were selected to ensure that the jet interaction is within the cylindrical part of the chamber. This is necessary both for optical access and to provide the maximum relevance to related applications for establishing preferred flow regimes ($\alpha_j < 50°$), as discussed in our previous paper.[6] The increment of θ_j was selected to ensure that distinct flow-features can be generated and that the jets interact with each other. The dimensions of the key geometrical parameters of the MIJCC configurations investigated here are given in Table I.

B. Experimental arrangement

The present experimental arrangement is similar to our previous work.[6] Particle Image Velocimetry (PIV) was employed under iso-thermal conditions at ambient temperature, with water as the working fluid to avoid deposition of tracer particles onto confining walls. Importantly, the entire device was fully submerged into a rectangular water tank with dimensions of 500 mm (L) × 400 mm (W) × 390 mm (H) to minimize optical distortion. This water tank was also made from acrylic to enable optical access for laser sheet. The water from the outlets was discharged into the water tank which overflowed to a reservoir. The discharged fluid was reinjected through the jets using a variable-speed-drive enabled water pump (Pan World NH-200PS), a frequency converter (Danfoss VLT 2800), and flowmeters (ABB D10A11), resulting in a closed-loop system. All configurations employed equal flows to the four rotationally symmetric jets, as shown in Table II.

The bulk mean velocity at the nozzle exit (U_e) was fixed at 2.8 m/s for each inject pipe, leading to an inlet jet Reynolds number $Re_D = \rho_f U_e D_{pipe}/\mu_f$ = 10 500, where ρ_f is the fluid density and μ_f is the fluid dynamic viscosity. This ensures that the inlet flow is within the fully turbulent regime where the influence of Re_D is considered to be small.[33] The jets were generated with a supply system that was carefully designed to ensure both overall flow symmetry and fully developed pipe flow at the exit. A symmetrical manifolding system was employed to ensure equal flow distribution to each jet, which was generated by a perfectly straight pipe of 46 diameters in length and, in turn, by 150 diameters of gently curved flexible piping. The perfectly straight section exceeds the 40 diameters found by Nikuradse[34] to be the minimum needed to establish fully developed pipe flow. Hence, the combination of the long gently curved supply to the straight pipe is sufficient to ensure that the present configuration achieves or closely approximates fully developed pipe flow.

The seeding particles for PIV measurements are hollow glass spheres which have a specific gravity of 1.1 with a particle diameter (D_p) of 12 μm. The resultant Stokes number (Sk_D) based on the bulk mean velocity (U_e) and pipe diameter (D_{pipe}) of the inlet jet was $Sk_D = \rho_p {D_p}^2 U_e/18\mu_f D_{pipe} = 0.003$ (where ρ_p is the particle density). This is sufficiently low to enable the length scales of particle movements to be resolved with the PIV measurement.

The optical arrangement and the measurement region are shown schematically in Fig. 2. The source of illumination for the PIV measurements was a double-head, pulsed Nd:YAG laser (Quantel Brilliant B), operating at a fixed pulsing frequency of 10 Hz and a maximum power of approximately 400 mJ. The laser was operated in the frequency-doubled mode to provide a wavelength of 532 nm. The laser beam was formed into a sheet with a combination of three cylindrical lenses (Thorlabs) that were aligned with the centerline of the cylindrical chamber and positioned to illuminate the measurement region, as shown in Fig. 2. The thickness of the light sheet was estimated to be 1.5 mm at the focal line.

A Charged Coupled Device (CCD) camera (Kodak Megaplus ES2093) was used to capture raw images for each measurement, with an array of 1920 × 1080 pixels. The frame rate of the CCD camera for the PIV measurements was set to match that of the laser at 10 Hz. The x-r plane [see Fig. 2(b)], which provides the instantaneous information of axial (u) and radial (v) velocity components, was 125 mm (L_i) × 66 mm (W_i) in size. The planar PIV measurement was performed within the MIJCC configurations at two axial planes to provide flow-field information for multiple-locations, as presented in Fig. 2(c).

TABLE I. Values of the geometric parameters of the MIJCC configurations investigated in the present study.

Dimensions	Description	Value
D_c (mm)	Chamber diameter	74
D_{sc} (mm)	Diameter of the secondary concentrator	74
D_{th} (mm)	Throat diameter	24.6
D_{pipe} (mm)	Inlet pipe diameter	3.35
L_c (mm)	Chamber length	225
L_{pipe} (mm)	Inlet pipe length	150
W_{out} (mm)	Width of the outlet gap	3
α_j (deg)	Jet inclination angle	25, 35, and 45
θ_j (deg)	Jet azimuthal angle	5, 10, and 15
β_{con} (deg)	Conical expansion angle	40
γ_{sc} (deg)	Angle of the secondary concentrator	40

TABLE II. The notation for the configurations investigated experimentally in the present study.

Experiment case no.	Configurations	Jet inclination angles, α_j (deg)	Jet azimuthal angles, θ_j (deg)
1	MIJCC-25-05	25	5
2	MIJCC-25-10	25	10
3	MIJCC-25-15	25	15
4	MIJCC-35-05	35	5
5	MIJCC-35-10	35	10
6	MIJCC-35-15	35	15
7	MIJCC-45-05	45	5
8	MIJCC-45-10	45	10
9	MIJCC-45-15	45	15

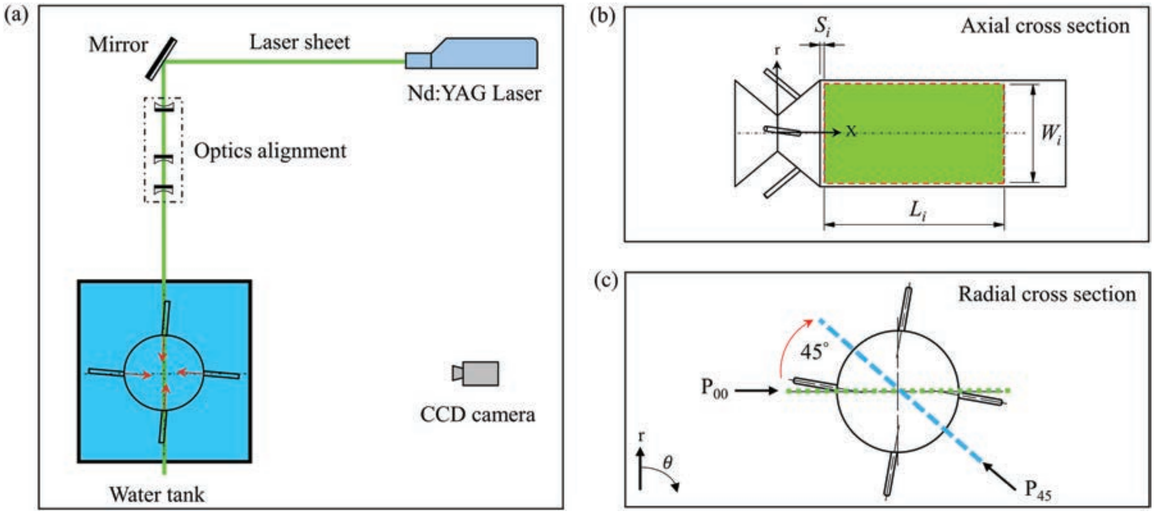

FIG. 2. (a) The optical arrangement, showing the laser, optics, light sheet, and camera, (b) measurement region (a green box enclosed by a red dashed line) relative to the chamber, and (c) measurement planes for "0°-plane" P_{00} and "45° offset-plane" P_{45}.

The measurement plane of P_{00} denotes the jet inlet plane (0° offset), while the P_{45} denotes the plane rotated 45° relative to P_{00} (45° offset). The shape of the conical component within the chamber prevented optical access there so that measurements were performed only within the cylindrical part of the chamber, downstream from the edge of the cylinder for approximately S_i = 1–3 mm [refer to Fig. 2(b)], depending on the configuration.

A minimum of 1500 PIV image pairs (12 bits) were recorded for each planar measurement. All images were processed using an in-house PIV code in MATLAB R2015a (Mathworks), with an interrogation window size of 32 × 32 pixels, resulting in a spatial resolution of 2 mm in each direction. A multi-grid correlation scheme with 50% overlap was applied to calculate the particle displacements and to minimize noise for all cases. Outliers (erroneous vectors) were detected in the post-processing using an in-house PIV code to compare the differences between absolute and relative velocities, and all erroneous vectors were removed from the ensemble.

A systematic study was employed to assess the overall uncertainty associated with the PIV measurements. The impact of slight variations between the flow-rate to different pipes was measured to be small (<2%) due to the care taken to ensure symmetry of the manifolding system. The measurement uncertainty derived from the flowmeter and water pump was measured to be ±1.6% of the desired flow rate, which results in an estimated uncertainty of the exit bulk velocity from the four pipes of less than 2%. The effect of optical distortion, which is associated with the spatial resolution of the PIV measurements, was assessed by calibration with a customized grid that was used before each measurement. On this basis, the uncertainty of position was estimated to be ±0.05 mm within the measurement region. The time delay between successive image pairs in the PIV measurements was varied between 100 μs and 200 μs (depends on the configuration). This yields an average particle displacement of approximately 8–10 pixels (1/3 of the interrogation window size) within the central region of images, where the highest mean axial velocity occurs. The experimental errors associated with the time separation between the laser pulses was estimated to be ±2%, while the uncertainty contributed from the image sample size was calculated to be ±1% for a sample size of 1500 image pairs. Based on the inaccuracies in calibration and observed scatter in present measurements, the overall uncertainty of the measured mean and RMS (root-mean-square) velocities for the present study is estimated to be less than 5%.

III. RESULTS AND DISCUSSION

A. Mean flow fields

Figure 3 presents the contours of measured mean axial velocity (U_x) normalized by the nozzle exit velocity (U_e), showing the velocity direction (black arrows) and magnitude (both the length of the arrows and the color map), for the cases (a) $\alpha_j = 25°$ and $\theta_j = 5°$, (b) $\alpha_j = 25°$ and $\theta_j = 10°$, (c) $\alpha_j = 25°$ and $\theta_j = 15°$, (d) $\alpha_j = 35°$ and $\theta_j = 5°$, (e) $\alpha_j = 35°$ and $\theta_j = 10°$, (f) $\alpha_j = 35°$ and $\theta_j = 15°$, (g) $\alpha_j = 45°$ and $\theta_j = 5°$, (h) $\alpha_j = 45°$ and $\theta_j = 10°$, and (i) $\alpha_j = 45°$ and $\theta_j = 15°$. Data are presented for both the P_{00} and P_{45} planes. It can be seen that an increase in azimuthal angle (θ_j) from 5° to 15° leads to a significant change to the mean velocity field within the range of $25° \leq \alpha_j \leq 45°$. For the configurations where $\alpha_j = 25°$ [Figs. 3(a)–3(c)] and for the smallest angles $\alpha_j = 25°$ and $\theta_j = 5°$, the inlet jets impinge at a point close to the chamber axis ($r/D_c = 0$) where they combine to form a resulting jet which then spreads and decays symmetrically. This is qualitatively similar to our previous study[6] for the same α_j, but with $\theta_j = 0°$. As the azimuthal angle is increased beyond $\theta_j \geq 10°$, the mean flow bifurcates into an axisymmetric divergent resulting jet downstream from a "stagnation point." This feature is most evident for the case of $\theta_j = 15°$, where the bifurcation is strong and slightly asymmetrical due to a relatively large θ_j, consistent with previous studies.[27,35] Also, for these larger azimuthal angles ($\theta_j \geq 10°$), a region of negative axial velocity is generated downstream from the stagnation point, indicating the presence of large-scale recirculation with a reverse flow in the chamber. The position of this recirculation progresses

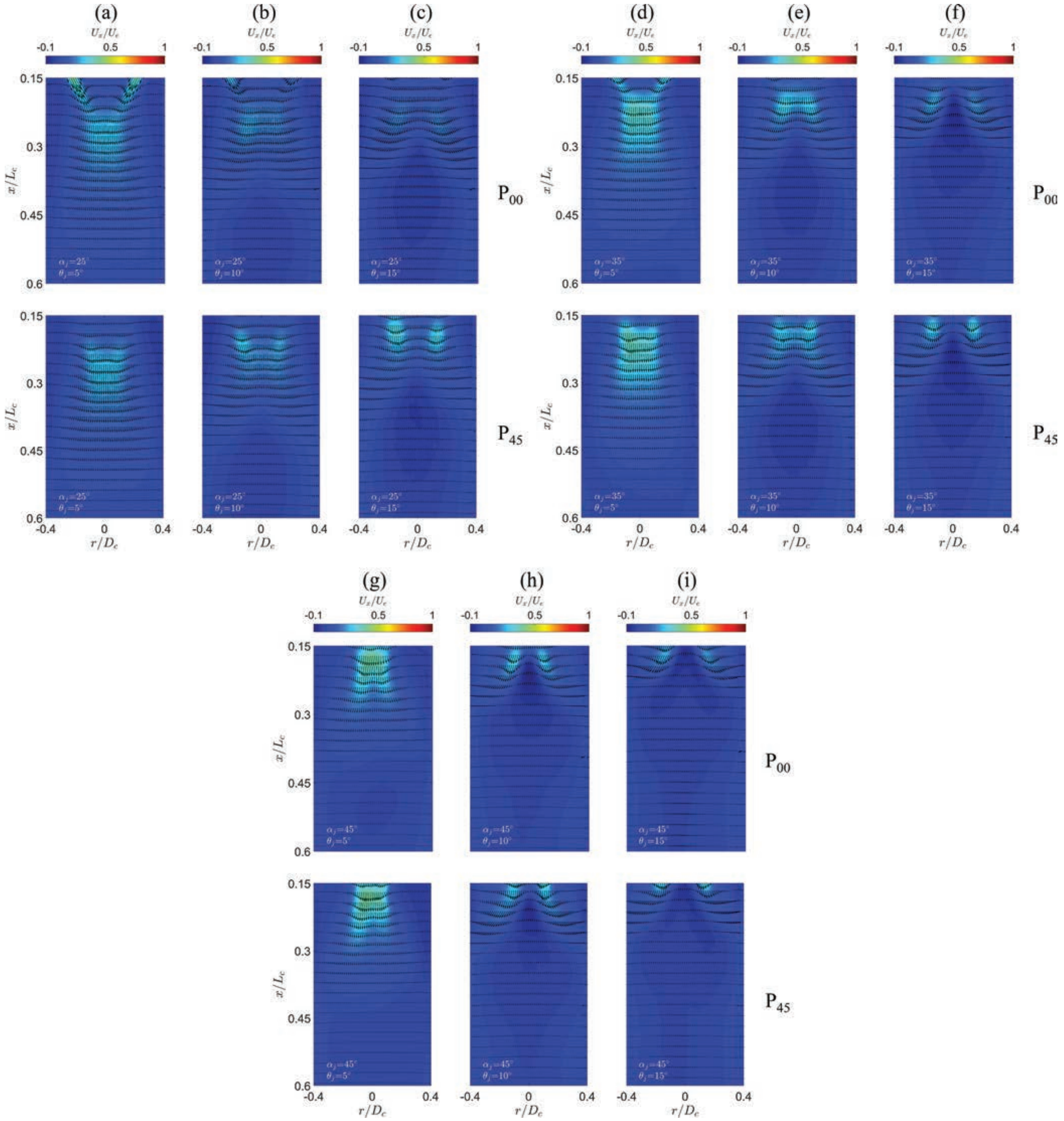

FIG. 3. Mean axial velocity (U_x) normalized by the bulk mean jet exit velocity (U_e), showing the velocity direction and magnitude (black arrows), overlaid with a color scale of magnitude (colored), for the cases (a) α_j = 25° and θ_j = 5°, (b) α_j = 25° and θ_j = 10°, (c) α_j = 25° and θ_j = 15°, (d) α_j = 35° and θ_j = 5°, (e) α_j = 35° and θ_j = 10°, (f) α_j = 35° and θ_j = 15°, (g) α_j = 45° and θ_j = 5°, (h) α_j = 45° and θ_j = 10°, and (i) α_j = 45° and θ_j = 15°. The data are measured from both the P$_{00}$ (0°-plane) and P$_{45}$ (45° offset-plane) between x/L_c = 0.15 and 0.6.

upstream from $x/L_c \approx 0.38$ to 0.28 as θ_j is increased from 10° to 15°, which can be deduced to be associated with the increased strength of the recirculation zone.

The results in Fig. 3 also show that the mean velocity field for $\alpha_j = 35°$ [Figs. 3(d)–3(f)] is qualitatively similar to $\alpha_j = 25°$. However, for the α_j = 35° cases, the large-scale recirculation zone is more prominent and the location of the negative velocity region is further upstream than in the α_j = 25° cases for all θ_j. For α_j = 45° [Figs. 3(g)–3(i)], the resulting divergent jet flow downstream from the stagnation point is even detected for the smallest θ_j = 5°, which reveals that α_j also influences the bifurcation of the resulting jets. More importantly, the negative axial velocity is found to extend further upstream to the conical section (above the measurement region $x/L_c < 0.15$) for the case with α_j = 45° and θ_j = 15°. This suggests that a portion of the flow is transported into the conical chamber section and, perhaps, even through the throat to the secondary concentrator. This data quantify the extent to which α_j influences the mean velocity field for a given value of θ_j.

It can also be seen from Fig. 3 that the magnitude of negative axial velocity typically increases with an increase in θ_j from 5° to 15° for a given value of α_j. This shows that the reverse flow is stronger for $\theta_j = 15°$ than that for $\theta_j = 5°$, consistent with highly swirled jets' configurations.[30,32] In addition, the mean velocity field can be seen to be slightly asymmetric for each case and for both planes P_{00} and P_{45}. This asymmetry

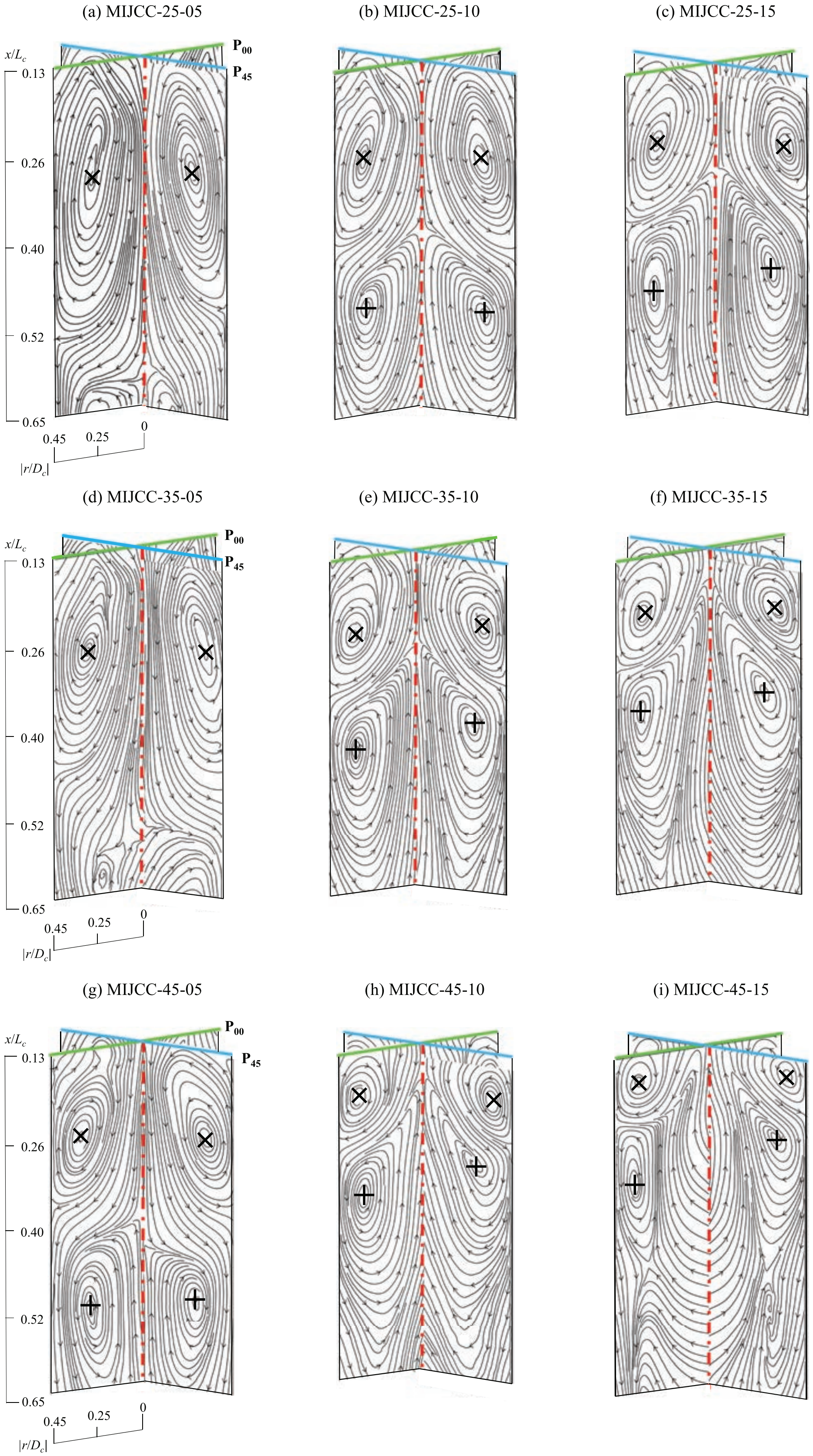

FIG. 4. Measured streamline, labeled with arrows to indicate the flow direction, for the cases (a) $\alpha_j = 25°$ and $\theta_j = 5°$, (b) $\alpha_j = 25°$ and $\theta_j = 10°$, (c) $\alpha_j = 25°$ and $\theta_j = 15°$, (d) $\alpha_j = 35°$ and $\theta_j = 5°$, (e) $\alpha_j = 35°$ and $\theta_j = 10°$, (f) $\alpha_j = 35°$ and $\theta_j = 15°$, (g) $\alpha_j = 45°$ and $\theta_j = 5°$, (h) $\alpha_j = 45°$ and $\theta_j = 10°$, and (i) $\alpha_j = 45°$ and $\theta_j = 15°$. The green line and the blue line denote the measurement plane P_{00} and P_{45}, respectively, while the red dash-dotted line refers to the centerline of the main cavity. The black cross and blackplus denote the vortex core of the external and central recirculation zones, respectively.

is also consistent with the previous finding for related configurations[36] that multi-jets configurations tend to amplify small asymmetries in the inflow conditions.

Figure 4 presents the measured streamlines, labeled with arrows to indicate the flow direction for all experimental cases (refer to Table II for a detailed description). The green line and the blue line denote the measurement plane P_{00} and P_{45}, respectively, while the red dash-dotted line refers to the centerline of the main cavity. It can be seen that, for all configurations, the flow-field is dominated by two distinctive vortex regions: a large-scale vortex with outward rotation, termed the external recirculation zone (ERZ), and a vortex with inward rotation, termed the central recirculation zone (CRZ).[37,38] The ERZ (whose vortex core is marked with a black "×") is typically generated in the upstream half of the chamber ($x/L_c \leq 0.5$) and is characterized by the interaction between the inclined inlet jets, while the CRZ (whose vortex core is marked with a black "+") is generated downstream from the negative bifurcation and is typically associated with the presence of swirling flows.[27] The position of ERZ corresponds well with the resulting jet, while the location of CRZ is associated with the downstream negative velocity region, consistent with Fig. 3. This shows that the large-scale mean flow structure (ERZ and CRZ) within the main cavity depends strongly on both α_j and θ_j.

Figure 4 also shows that, although the qualitative features of the mean flow field are present for all cases, their relative significance changes. For example, for the case where $\alpha_j = 25°$ and $\theta_j = 5°$ (MIJCC-25-05), the extent of ERZ spans the majority of the imaged region in the main cavity, while the CRZ is only observed in the most downstream region of it ($x/L_c \approx 0.65$). By contrast, for the case of $\alpha_j = 25°$ and $\theta_j = 15°$ (MIJCC-25-15), the ERZ and CRZ are of similar size. This trend is more notable for higher inclination angles' configurations ($\alpha_j \geq 35°$), although both α_j and θ_j influence the position of the dominant recirculation regions within the cylindrical chamber.

Another finding from Fig. 4 is that the structure of both the ERZ and CRZ is approximately axisymmetric for most cases. However, significant asymmetry can be seen in the CRZ for the cases of $\alpha_j = 35°$ and $\theta_j = 15°$ (MIJCC-35-15), $\alpha_j = 45°$ and $\theta_j = 10°$ (MIJCC-45-10), and $\alpha_j = 45°$ and $\theta_j = 15°$ (MIJCC-45-15), consistent with relevant previous studies.[27,39] This asymmetry can be seen to be associated with the largest angles of the jets which can also be deduced to generate the largest pressure gradients. This implies that the large pressure gradients amplify any small geometric asymmetry, for example: the misalignment of injection pipes. This also highlights the sensitivity of large α_j ($\geq 35°$) and θ_j ($\geq 10°$) to the axisymmetric flow features of rotationally symmetric confined jets.

Figure 5 presents the evolution of the dimensionless mean axial velocity (U_c/U_e) along the centerline of the Multiple Impinging Jets in a Cylindrical Chamber (MIJCC) for the cases of (a) $\alpha_j = 25°$ and $\theta_j = 5°$, (b) $\alpha_j = 25°$ and $\theta_j = 10°$, and (c) $\alpha_j = 25°$ and $\theta_j = 15°$. Here we define the jet impingement point, P_i, to be the location of the maximum mean axial velocity along the centerline of the chamber [$(U_c/U_e)_{max.cl}$], the stagnation point, P_s, as the zero velocity point at the crossover from positive to negative axial velocities ($U_c/U_e = 0$), and the point of minimum axial velocity, P_{min}, as the axial location of the minimum mean axial velocity [$(U_c/U_e)_{min.cl}$]. For comparison with the previous measurement of the non-swirling case ($\alpha_j = 25°$ and $\theta_j = 0°$), the PIV data from our previous work (Ref. 6) are also included. It can be seen that the evolution of U_c/U_e along the centerline of the chamber for all swirled-jets' cases is significantly smaller than that of non-swirling jets within $0.13 \leq x/L_c \leq 0.65$, although similar trends of velocity evolution were measured from all four cases. The magnitude of $(U_c/U_e)_{max.cl}$ for the cases of $\theta_j = 10°$ and 15° is approximately 35% and 60% lower than that of $\theta_j = 5°$, while the location of P_i progresses upstream from $x/L_c = 0.27$ for $\theta_j = 5°$ to $x/L_c = 0.21$ for $\theta_j = 15°$. This reveals that an increase in θ_j leads to a significant change in the location of P_i and the magnitude of $(U_c/U_e)_{max.cl}$ along the centerline of the chamber.

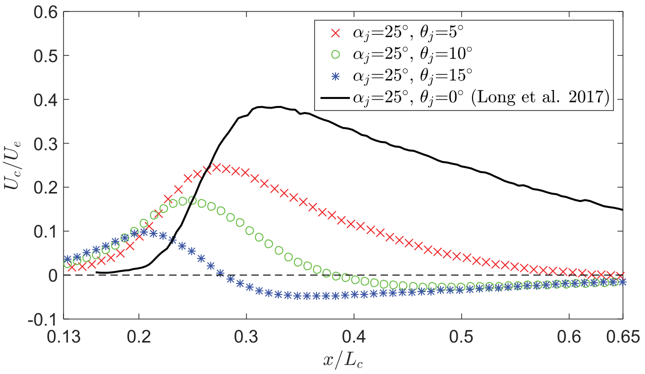

FIG. 5. Evolution of mean axial velocity along the centerline of the Multiple Impinging Jets in a Cylindrical Chamber (MIJCC), normalized by the bulk mean velocity (U_c/U_e), as functions of chamber length for the cases (a) $\alpha_j = 25°$ and $\theta_j = 5°$, (b) $\alpha_j = 25°$ and $\theta_j = 10°$, and (c) $\alpha_j = 25°$ and $\theta_j = 15°$. For clarity, the figure only presents one in two data points.

It can also be seen that a stagnation point P_s ($U_c/U_e = 0$) occurs on the axis for all cases, which is located at $x/L_c = 0.65$, 0.38, and 0.28 for $\theta_j = 5°$, 10°, and 15° cases, respectively. This marks the most upstream point of the region of the CRZ (Fig. 4). Taken together, it can be concluded that, for the configurations with the smallest α_j considered here ($\alpha_j = 25°$), the CRZ region is translated from the downstream half to the upstream half of the chamber as θ_j is increased from 5° to 15°. This is a further evidence of the influence of θ_j on the CRZ, for any given value of α_j.

Figure 5 also shows that a minimum axial velocity point P_{min} is detected at $x/L_c = 0.47$ and 0.34 for the cases of $\theta_j = 10°$ and 15°, respectively, and is outside of the measurement region for the case of $\theta_j = 5°$. This is upstream from the core of the annular vortex in the CRZ, which occurs at $x/L_c \approx 0.49$ ($\theta_j = 10°$) and 0.47 ($\theta_j = 15°$), respectively, and is consistent with the convergence of the streamlines toward the axis near to the position of P_{min} shown in Fig. 4. Importantly, the value of $(U_c/U_e)_{min.cl}$ increases with an increase in θ_j, also consistent with an increased strength of the reverse flow and CRZ for larger θ_j configurations.

Figure 6 presents the radial profiles of the mean axial (U_x) and radial (V_x) velocities, normalized by the nozzle exit velocity (U_e), at six axial distances along the chamber for the cases where $\alpha_j = 25°$ and $\theta_j = 5°$, 10°, and 15°. Data are presented only within the plane P_{00} because the results

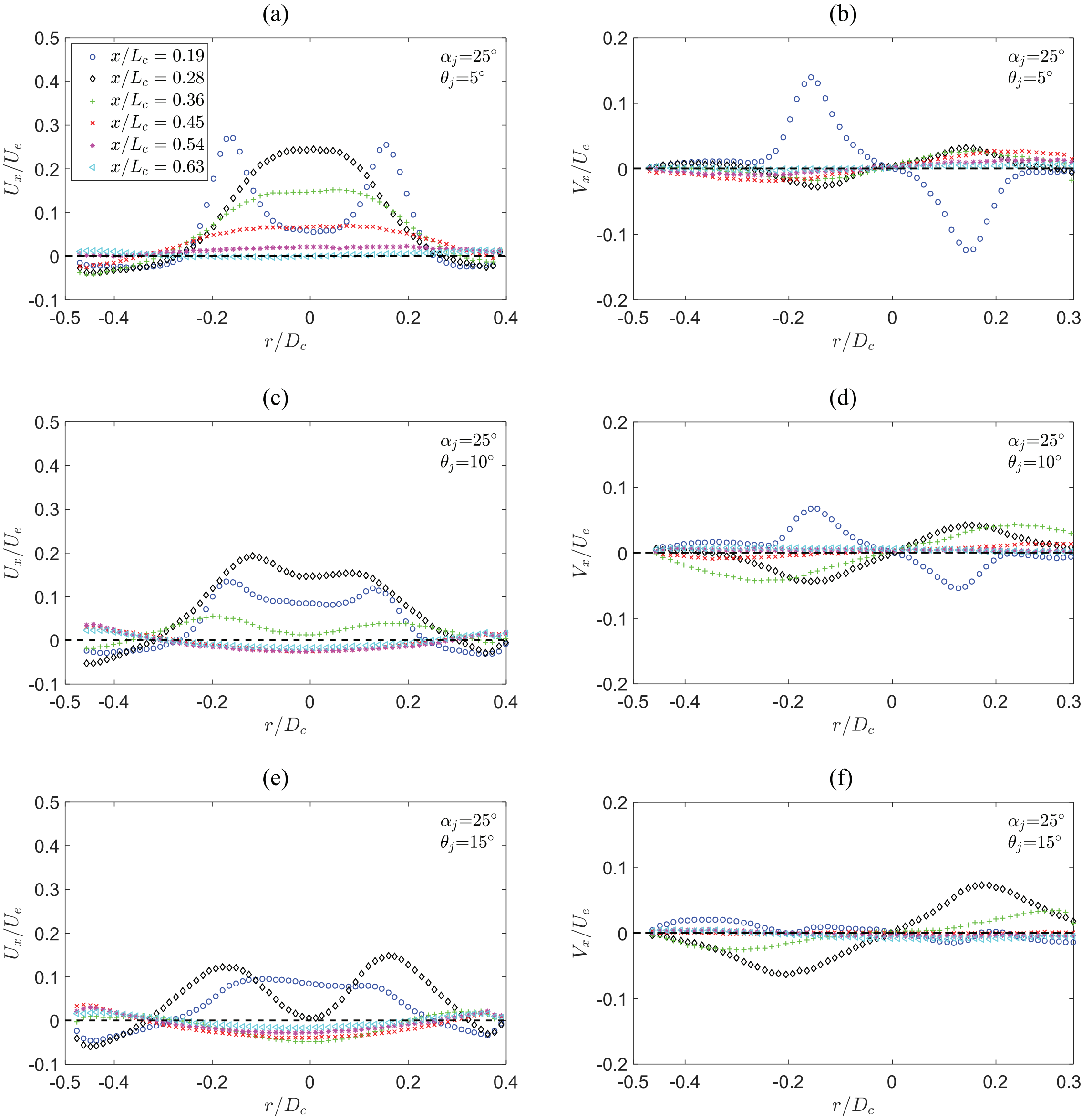

FIG. 6. Radial profiles of mean axial velocity, U_x, at six cross-sections through the Multiple Impinging Jets in a Cylindrical Chamber (MIJCC), for the cases of [(a) and (b)] α_j = 25° and θ_j = 5°, [(c) and (d)] α_j = 25° and θ_j = 10°, and [(e) and (f)] α_j = 25° and θ_j = 15°. Here D_c denotes the diameter of the MIJCC cylindrical chamber, and the dashed line denotes the location of $U_x/U_e = 0$.

in the P_{45} plane are qualitatively similar to them. The exact locations of P_i and P_s are presented in Fig. 5. In considering the mean axial velocity [Figs. 6(a), 6(c), and 6(e)], it can be seen that an increase in θ_j leads to a significant decrease in the magnitude of velocity peaks [$(U_x/U_e)_{max}$] throughout the chamber. For example, an approximately 40% reduction in the magnitude of $(U_x/U_e)_{max}$ is measured at $x/L_c = 0.19$ and 0.28, which is possibly attributed to the increased extent of offset in the inlet jets as θ_j is increased, consistent with the qualitative features in Fig. 3. Importantly, as θ_j is increased from 5° to 15°, the radial position of $(U_x/U_e)_{max}$ upstream from P_i ($x/L_c = 0.19$) remains the same ($|r/D_c| \approx 0.16$), while the location of $(U_x/U_e)_{max}$ downstream from P_i ($x/L_c = 0.28$) moves from the centerline ($|r/D_c| = 0$) to away from the axis ($|r/D_c| > 0$). This indicates that an increase in θ_j can significantly change the strength and position of the resulting jet flow.

It can also be seen from Figs. 6(a), 6(c), and 6(e) that an increase in θ_j leads to a significant increase in the magnitude of negative axial velocity within the CRZ region (downstream from P_s). For example, the negative peak velocity [$(U_x/U_e)_{min}$] along the centerline increases from $U_x/U_e \approx -0.001$ for the case of $\theta_j = 5°$ [Fig. 6(a)] to $U_x/U_e \approx -0.05$ for the case of $\theta_j = 15°$ [Fig. 6(e)]. This reveals an increased strength of downstream reverse flow within the CRZ for larger θ_j cases, consistent with the trend of $(U_c/U_e)_{min.cl}$ in Fig. 5. Nevertheless, the magnitude of $(U_x/U_e)_{min}$ within the ERZ region (upstream from P_s) does not significantly change with θ_j, although the strength of ERZ within the central region decays faster for the cases with a larger θ_j.

For the mean radial velocity [Figs. 6(b), 6(d), and 6(f)], an increase in θ_j leads to a significant change in both the magnitudes and profiles of V_x/U_e. For locations upstream from P_i ($x/L_c = 0.19$), the radial velocity peak [$(V_x/U_e)_{max}$]

is decreased from $V_x/U_e \approx 0.15$ for $\theta_j = 5°$ to $V_x/U_e \approx 0.02$ for $\theta_j = 15°$, which indicates a reduction in the magnitude of inlet velocity along the radial direction in the plane P_{00}. By contrast, for the location close to P_i ($x/L_c = 0.28$), the magnitude of $(V_x/U_e)_{max}$ increases from $V_x/U_e \approx 0.03$ [Fig. 6(b)] to $V_x/U_e \approx 0.06$ [Fig. 6(f)] with an increase in θ_j. This indicates an increase in the radial extent of the ERZ within the jet impingement region (where P_i occurs). Furthermore, for downstream locations where CRZ is dominated [$x/L_c > 0.36$ for Figs. 6(b) and 6(c)], the magnitude of V_x/U_e is further reduced with an increase in θ_j. This indicates that a reduction in the strength of V_x and also an increase in the swirling flow within the downstream CRZ region.

It is also worth noting that, for all cases shown in Fig. 6, the magnitude of the mean axial and radial velocities within the ERZ (for all locations upstream from P_s) is typically higher than that of the CRZ (for all locations downstream from P_s), which suggests that the strength of the ERZ is expected to be greater than that of the CRZ for all configurations. The reason for this is possibly due to the strong interaction between the jet flow and the ERZ within the fully turbulent flow regime, as expected for multiple-jet configurations.[6]

B. RMS of the turbulent flow fields

Figure 7 presents the evolution of normalized axial RMS (root-mean-square) velocity (u'/U_e) and the normalized radial

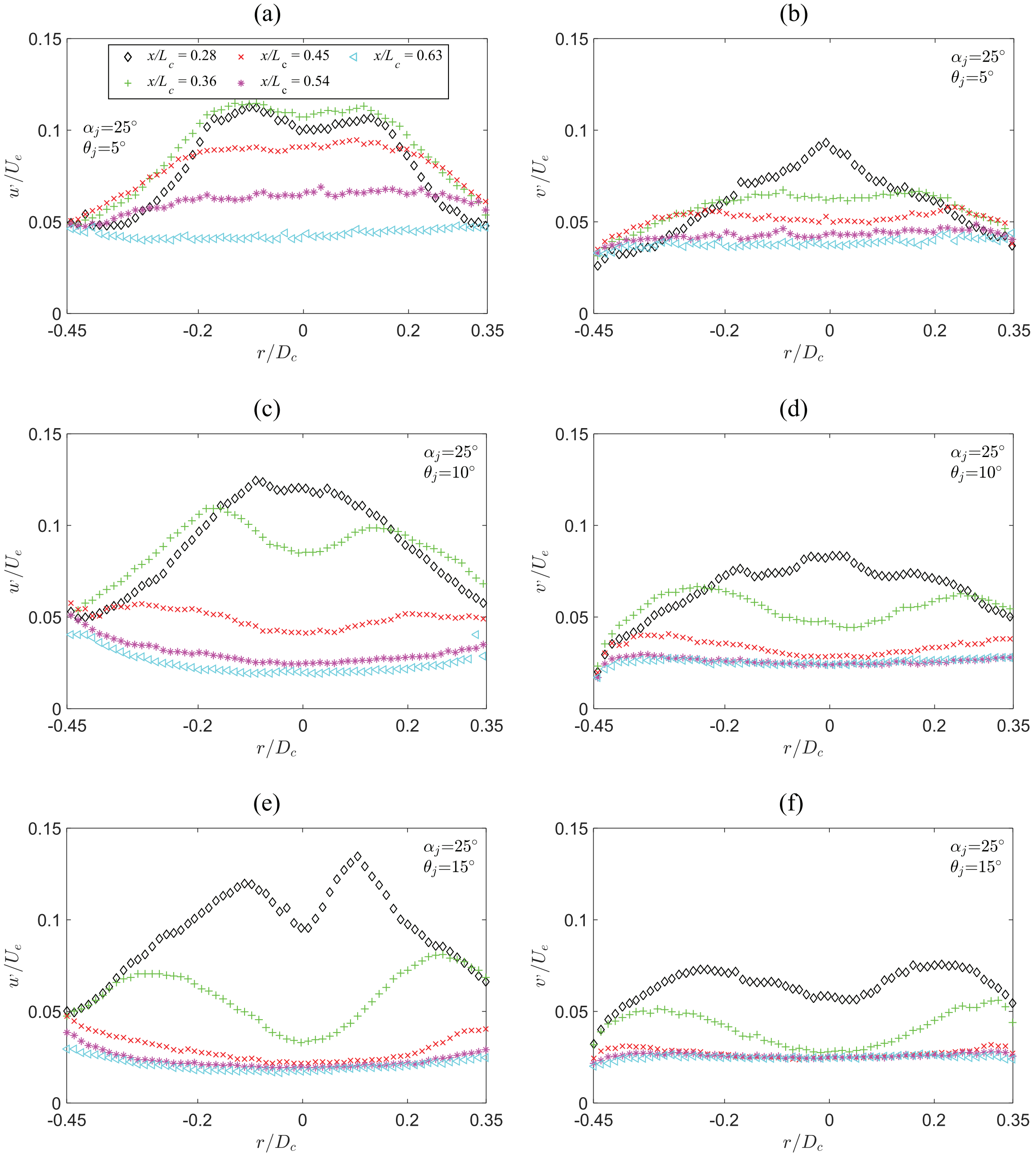

FIG. 7. Radial profiles of normalized axial RMS velocity (u'/U_e) and normalized radial RMS velocity (v'/U_e) downstream from the jet impingement point P_i for the cases [(a) and (b)] $\alpha_j = 25°$ and $\theta_j = 5°$, [(c) and (d)] $\alpha_j = 25°$ and $\theta_j = 10°$, and [(e) and (f)] $\alpha_j = 25°$ and $\theta_j = 15°$. Here D_c denotes the diameter of the MIJCC cylindrical chamber.

RMS velocity (v'/U_e) downstream from the jet impingement point (P_i) for the cases of [(a) and (b)] $\alpha_j = 25°$ and $\theta_j = 5°$, [(c) and (d)] $\alpha_j = 25°$ and $\theta_j = 10°$, and [(e) and (f)] $\alpha_j = 25°$ and $\theta_j = 15°$. Here $u' = \langle u^2\rangle^{0.5}$ and $v' = \langle v^2\rangle^{0.5}$, where u and v denote the fluctuating components of axial and radial velocities, respectively. All data reported are for the plane P_{00} since those for the plane P_{45} are qualitatively similar as above. It can be seen that the peak magnitude of the values of u'/U_e and v'/U_e are almost independent from θ_j, although the distributions change significantly. The peaks tend to be distributed in the shear layer at a different radial location from the peak in mean values.

For the axial RMS velocity [Figs. 7(a), 7(c), and 7(e)], it can be seen that, for all locations upstream from the stagnation point P_s (ERZ dominated region), the peak value of u'/U_e typically occurs within the central region of the main cavity ($|r/D_c| \leq 0.25$), featuring a double hump profile. The location of the peak u'/U_e corresponds well with the maximum mean velocity gradient presented in Fig. 6 and is therefore a good indicator of the maximum value in a shear layer. This coincides with the interaction between the high momentum jet flow and the dominant ERZ. Conversely, downstream from P_s where the CRZ is dominant, the maximum magnitude of u'/U_e is always measured from the outer region of the main cavity ($|r/D_c| > 0.25$), with a trend of increasing values toward the cavity wall. This indicates that the velocity fluctuations between the CRZ and the surrounding fluids are much higher than those that occur in the central reverse flow region, which is a common feature for configurations employing highly swirled jets.[27,30]

Figure 7 also shows that, for the radial RMS velocity [Figs. 7(b), 7(d), and 7(f)], a pronounced peak of v'/U_e along the centerline of the chamber occurs for $\theta_j = 5°$ case at $x/L_c = 0.28$, which is associated with the jet impingement point (P_i) in this case. That is, a high degree of radial velocity fluctuation is associated with this point. A large fluctuation in the radial velocity is commonly associated with a lateral (cross-stream) offset of the jet impingement point, such as a jet precession,[36] and has been widely documented for multiple-jet configurations.[16–18,36,40] In addition, the peak value of v'/U_e along the centerline of the chamber decreases with an increase in θ_j (from 5° to 15°), which also suggests a reduction in the extent of flow oscillation at P_i.

It is also important to note that, regardless of the value of α_j and θ_j, the magnitude of u'/U_e is typically higher than v'/U_e, inferring that a high degree of Reynolds stress anisotropy exists in the current MIJCC configurations. This is consistent with the findings from our previous work for non-azimuth jets' configurations[6] and it is of particular relevance to the development of computational modeling.[26] This implies that Reynolds-averaged Navier-Stokes (RANS) models which solve the Reynolds stress components individually (e.g., Reynolds stress model[26]) are likely to be more accurate than isotropic models.[41]

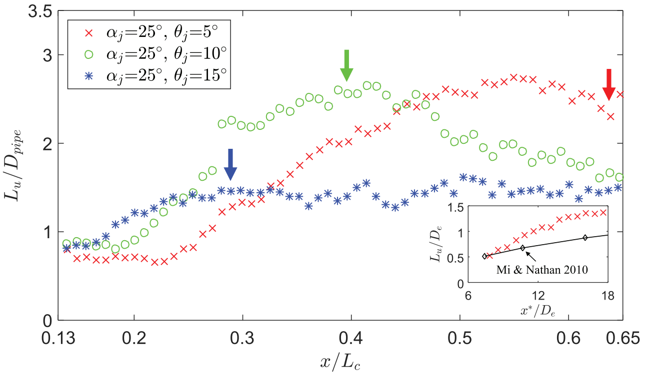

FIG. 8. Evolution of the integral length scale (L_u) along the centerline of the Multiple Impinging Jets in a Cylindrical Chamber (MIJCC) normalized by the inlet nozzle diameter (D_{pipe}), as functions of chamber length for (a) $\alpha_j = 25°$ and $\theta_j = 5°$, (b) $\alpha_j = 25°$ and $\theta_j = 10°$, and (c) $\alpha_j = 25°$ and $\theta_j = 15°$. Here the colored arrows denote the location of the stagnation point for each case. For the inset, the equivalent jet exit diameter, D_e, is the diameter of an equivalent circular pipe with the same exit area as the four inlet jets. The equivalent axial coordinate, x^*, along the axis of the central resulting jet can be approximated as being $x^* = x_0 + (x - x_i)$, where x_i denotes the distance between the throat and impingement point and x_0 denotes the distance along the local axis of each inlet jet between the pipe exit and jet impingement point. For clarity, the figure only presents one in two data points.

Figure 8 presents the normalized integral length scales (L_u/D_{pipe}) along the centerline of the MIJCC for the cases where $\alpha_j = 25°$ and $\theta_j = 5°$, 10°, and 15°. The integral length scale (L_u) is defined as $L_u = \int_0^{r_0} \langle u(x)u(x+r)\rangle\langle u^2\rangle^{-1} dr$, where $u(x)$ denotes the fluctuating component of the axial velocity and r_0 corresponds to the first zero crossing of the autocorrelation function $\langle u(x)u(x+r)\rangle\langle u^2\rangle^{-1}$, following Xu and Antonia.[42] It can be seen that the value of L_u/D_{pipe} increases along the centerline upstream from the stagnation point P_s (labeled with the corresponding colored arrows) for all three cases, with the slope of L_u/D_{pipe} increasing as θ_j is increased from 5° to 15°. The maximum value is $L_u/D_{pipe} \approx 2.7$ for the case where $\theta_j = 5°$. This trend indicates that the extent of large-scale motion increases both along the centerline and within the corresponding ERZ region. However, downstream from the P_s where the CRZ region is dominant, the value of L_u/D_{pipe} substantially decreases, with the minimum value of $L_u/D_{pipe} \approx 1.5$ occurring for the case of $\theta_j = 15°$. This decrease is possibly caused by the absence of the central jet flow for larger θ_j cases (as shown in Fig. 3), which reduces the large-scale motion in the CRZ region. Hence, it can be concluded that the large-scale flow motion, and hence the integral length scales, depends strongly on the position of the ERZ and CRZ within the chamber, which is also characterized by the value of θ_j.

For comparison with previous measurements of a single unconfined jet, the inset of Fig. 8 presents the integral length scale (L_u/D_e) of the central resulting jet (downstream from the jet impingement point P_i) for the case of $\alpha_j = 25°$ and $\theta_j = 5°$ together with the HWA (hot-wire anemometry) data of Mi and Nathan[43] for a round pipe. The equivalent jet exit diameter, D_e, can be expressed as $D_e = \sqrt{N_j}D_{pipe}$, where N_j denotes the number of jets. That is, D_e is the diameter of an equivalent circular pipe with the same exit area as the four inlet pipes. The equivalent axial coordinate, x^*, along the axis of the central resulting jet can be approximated as being $x^* = x_0 + (x - x_i)$, where x_i denotes the distance between the throat and impingement point and x_0 denotes the distance along the local axis of each inlet jet between the pipe exit and jet impingement point.[6] It can be seen that the evolution of L_u/D_e within

TABLE III. Dimensionless location of the jet impingement, stagnation, and minimum velocity points along the centerline of the MIJCC chamber.

Experiment case no.	Configurations	Jet impingement point, P_i, (x/L_c)	Stagnation point, P_s, (x/L_c)	Minimum velocity point, P_{min}, (x/L_c)
1	MIJCC-25-05	0.27	0.65	>0.65
2	MIJCC-25-10	0.25	0.38	0.47
3	MIJCC-25-15	0.21	0.28	0.34
4	MIJCC-35-05	0.23	0.59	>0.65
5	MIJCC-35-10	0.21	0.28	0.35
6	MIJCC-35-15	0.14	0.17	0.23
7	MIJCC-45-05	0.19	0.45	0.56
8	MIJCC-45-10	0.14	0.18	0.21
9	MIJCC-45-15	<0.13	<0.13	0.16

the central resulting jet for the case of $\theta_j = 5°$ is greater than a single unconfined jet within $7 \le x^*/D_e \le 18$, although the value of L_u/D_e at $x^*/D_e = 7$ coincides fairly well with each other. The maximum difference occurs at $x^*/D_e \approx 16$, with L_u/D_e for the current case of $\theta_j = 5°$ being 35% higher than that in the work of Mi and Nathan.[43] This result highlights that the combination of the presence of walls (confinement), the interaction of multiple-jets, and the swirling flow increases substantially the large-scale flow motion for the rotationally symmetric jets' configurations.

C. Effects of jet azimuthal and inclination angles

Table III presents a summary of the location of the jet impingement (P_i), stagnation (P_s) and minimum velocity (P_{min}) points along the centerline of the MIJCC chamber for all experimental cases. It can be seen that an increase in either angle tends to move these points closer to the inlet plane, as expected.

Figure 9 presents the normalized location of (a) the jet impingement point (P_i), (b) the stagnation point (P_s), and (c) the minimum velocity point (P_{min}) as a function of jet azimuthal angles (θ_j) for $\alpha_j = 25°$, 35°, and 45°. All measured data points are labeled with solid makers, while some "out of measurement region" points which are labeled with hollow markers are extrapolated from Table III. As noted from the table, it can be seen from Fig. 9(a) that the increase in either α_j or θ_j leads to an upstream progression of P_i. The location of P_i moves from $x/L_c = 0.27$ for the case of $\alpha_j = 25°$ and $\theta_j = 5°$ to $x/L_c < 0.13$ for the case of $\alpha_j = 45°$ and $\theta_j = 15°$, which is approximately 15% of the total chamber length. Hence, the influence of varying α_j between 25° and 45° or θ_j between 5° and 15° on the location of P_i is quantitatively similar.

Figure 9(b) shows that P_s moves upstream more significantly than does P_i with an increase in either α_j or θ_j. That is, the upstream progression of the CRZ depends on both the α_j and θ_j. However, the effect is non-linear so that, for a given value of α_j, the upstream movement of P_s is more significant from $\theta_j = 5°$ to 10° (≈27%) than that from $\theta_j = 10°$ to 15°

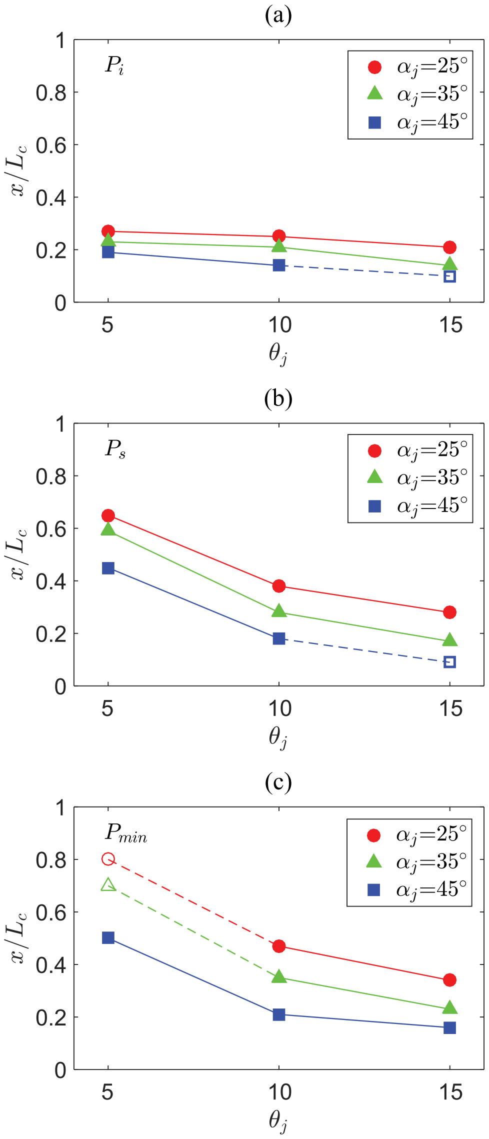

FIG. 9. Normalized location of the (a) jet impingement point (P_i), (b) stagnation point (P_s), and (c) minimum velocity point (P_{min}) along the centerline of the Multiple Impinging Jets in a Cylindrical Chamber (MIJCC), as a function of jet azimuthal angles (θ_j) for $\alpha_j = 25°$, 35°, and 45°.

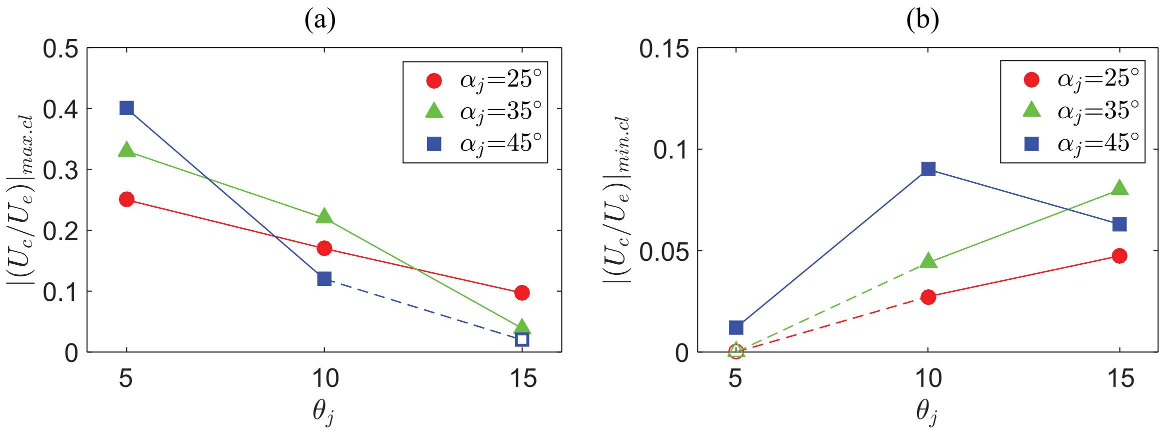

FIG. 10. (a) The normalized maximum mean axial velocity (absolute), $|(U_c/U_e)|_{max.cl}$, and (b) the normalized minimum mean axial velocity (absolute), $|(U_c/U_e)|_{min.cl}$, along the centerline of the chamber, as a function of jet azimuthal angles (θ_j) for α_j = 25°, 35°, and 45°.

(≈10%). By contrast, an increase in α_j from 25° to 45° results in a consistent 10% upstream progression between each point for a given value of θ_j. That is, θ_j has a greater influence on the CRZ than does α_j for these rotationally symmetric confined jets.

The results in Fig. 9 also show that, for the cases where θ_j is small (θ_j = 5°), an increase in α_j from 25° to 45° does not lead to the presence of P_s within the upstream half of the main cavity ($x/L_c < 0.45$), while for the cases where θ_j is relatively large (θ_j = 15°), P_s is even measured at $x/L_c = 0.28$ for the smallest α_j = 25° case. This indicates that the influence of the jet inclination angle (α_j) on the large-scale CRZ within the main chamber is expected to be greater for larger θ_j MIJCC configurations ($\theta_j \geq 10°$) than for smaller θ_j MIJCC configurations ($\theta_j < 10°$). In addition, the trend of upstream movement for the minimum velocity point P_{min} [Fig. 9(c)] is qualitatively similar to that of P_s which has maximum 35% and 10% progressions for constant α_j and constant θ_j, respectively. That is, an increase in either θ_j or α_j tends to move the central reverse flow further upstream, while the influence of θ_j is more significant.

Figure 10 presents (a) the normalized maximum mean axial velocity (absolute), $|(U_c/U_e)|_{max.cl}$, and (b) the normalized minimum mean axial velocity (absolute), $|(U_c/U_e)|_{min.cl}$, along the centerline of the chamber, as a function of jet azimuthal angles (θ_j) for α_j = 25°, 35°, and 45°. It can be seen that an increase in θ_j leads to a significant decrease of $|(U_c/U_e)|_{max.cl}$ for the cases of α_j = 25°, 35°, and 45°, although the decay rates for each α_j differ. For the α_j = 25° configurations, the rate at which $|(U_c/U_e)|_{max.cl}$ decreases with increasing θ_j is almost constant so that an overall 60% reduction in $|(U_c/U_e)|_{max.cl}$ occurs as θ_j is increased from 5° to 15°. However, the rate of $|(U_c/U_e)|_{max.cl}$ decays faster between θ_j = 10° and 15° than that between θ_j = 5° and 10° for α_j = 35° cases, with an overall 85% reduction as θ_j is increased from 5° to 15°. For α_j = 45° cases, the decay rate within the range of $10° \leq \theta_j \leq 15°$ is slightly lower than that in $5° \leq \theta_j < 10°$ and the total reduction in $|(U_c/U_e)|_{max.cl}$ achieves the highest (≈95%). Hence, the influence of θ_j on the magnitudes and decay rates of $|(U_c/U_e)|_{max.cl}$ is not linear and depends strongly on the value of α_j.

It can also be seen from Fig. 10(b) that a linear increase in $|(U_c/U_e)|_{min.cl}$ was measured as θ_j is increased from 5° to 15° for α_j = 25° and 35° cases. However, the dependence of $|(U_c/U_e)|_{min.cl}$ on θ_j increases between θ_j = 5° and 10° and then decreases between θ_j = 10° and 15° for α_j = 45° cases. The reduction in slope for θ_j = 15° is attributed to an increase in the significance of flow unsteadiness within in the CRZ region, which was observed in the planar images.

Figure 11 presents three radial profiles of the normalized radial RMS velocity (v'/U_e) within the CRZ region (downstream from P_s) for the cases of α_j = 45°, θ_j = 5° (solid markers) and α_j = 45°, θ_j = 15° (hollow markers). It can be seen that a pronounced peak of v'/U_e was observed at all three axial distances for the case of θ_j = 15°, with the profiles also being almost identical. By contrast, flat profiles of v'/U_e with low magnitudes were measured for θ_j = 5° case. This implies that the flow oscillation (radial direction) is much greater within the CRZ along the central axis for θ_j = 15° case than for θ_j = 5° case. The oscillations are key characteristics of flow unsteadiness such as the PVC (precessing vortex core) which is well known to be generated within a CRZ.[27,30,36] This also explains the trend of $|(U_c/U_e)|_{min.cl}$ for the cases of α_j = 45° in Fig. 10(b).

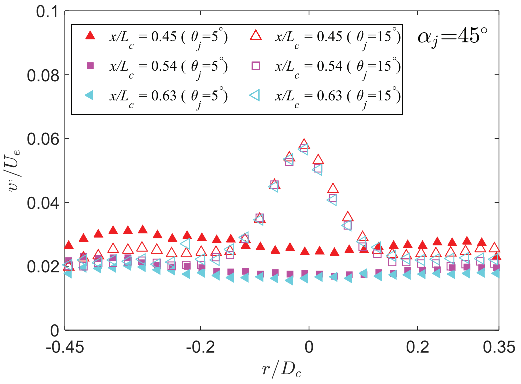

FIG. 11. Radial profiles of the normalized radial RMS velocity (v'/U_e) within the central recirculation zone (CRZ) for the cases where α_j = 45°, θ_j = 5° (solid markers), and θ_j = 15° (hollow markers). For clarity, the figure only presents one in two data points.

Overall, it can be concluded that, for a given value of α_j ($25° \le \alpha_j \le 45°$), an increase in θ_j from 5° to 15° leads to a decrease in $|(U_c/U_e)|_{max.cl}$ and an increase in $|(U_c/U_e)|_{min.cl}$ for most cases, which in turn suggests that the strength of the ERZ, corresponding to $|(U_c/U_e)|_{max.cl}$, is decreased, and the strength of CRZ [corresponding to $|(U_c/U_e)|_{min.cl}$] is increased for higher θ_j configurations.

Figure 12 presents the averaged radial RMS velocity within the CRZ region ($\overline{v'}_{CRZ.cl}/U_e$) along the centerline of the chamber, as a function of the length of the central recirculation zone (L_{CRZ}), for all experimental cases. The value of L_{CRZ} refers to the maximum axial length of the CRZ region, which can be calculated as $L_{CRZ} = L_c - L_s$. Here L_s denotes the distance between the throat and the stagnation point (shown in the inset of Fig. 12). Please note that the value of $\overline{v'}_{CRZ.cl}/U_e$ is calculated only within the range of $0.13 \le x/Lc \le 0.65$, while the value downstream from $x/Lc = 0.65$ is small for most cases and is estimated to have a negligible influence on the results in Fig. 12. The data for the case of $\alpha_j = 25°$ and $\theta_j = 5°$ are not included because P_s is located too close to the boundary of the PIV image. It can be seen that the slope of $\overline{v'}_{CRZ.cl}/U_e$ is relatively small and the value is within the range of $0.018 \le \overline{v'}_{CRZ.cl}/U_e \le 0.028$ for the cases where $0.4 \le L_{CRZ}/L_c \le 0.72$, while the slope of $\overline{v'}_{CRZ.cl}/U_e$ increases significantly for the cases where $L_{CRZ}/L_c > 0.72$ to achieve the highest value of $\overline{v'}_{CRZ.cl}/U_e = 0.057$ for the case of $\alpha_j = 45°$ and $\theta_j = 15°$. This trend is further evidence supporting the finding that the flow oscillation within the CRZ increases with azimuthal angles (Figs. 10 and 11), which in turns suggests that the increased dependence of $\overline{v'}_{CRZ.cl}/U_e$ on θ_j is strongest for the cases with large α_j ($\ge 35°$) and θ_j ($>10°$). In addition, this increase is most likely to be associated with the increased extent of flow unsteadiness (e.g., PVC) within the CRZ region, as previously discussed.

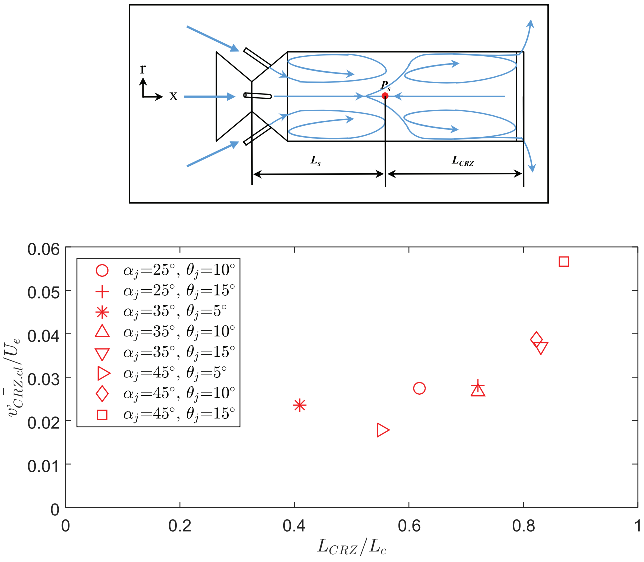

FIG. 12. Averaged radial RMS velocity ($\overline{v'}_{CRZ.cl}/U_e$) within the CRZ region as a function of the length of the central recirculation zone (L_{CRZ}). The value of L_{CRZ} refers to the maximum axial length of the CRZ region, $L_{CRZ} = L_c - L_s$, where L_s denotes the distance between the throat and the stagnation point (P_s).

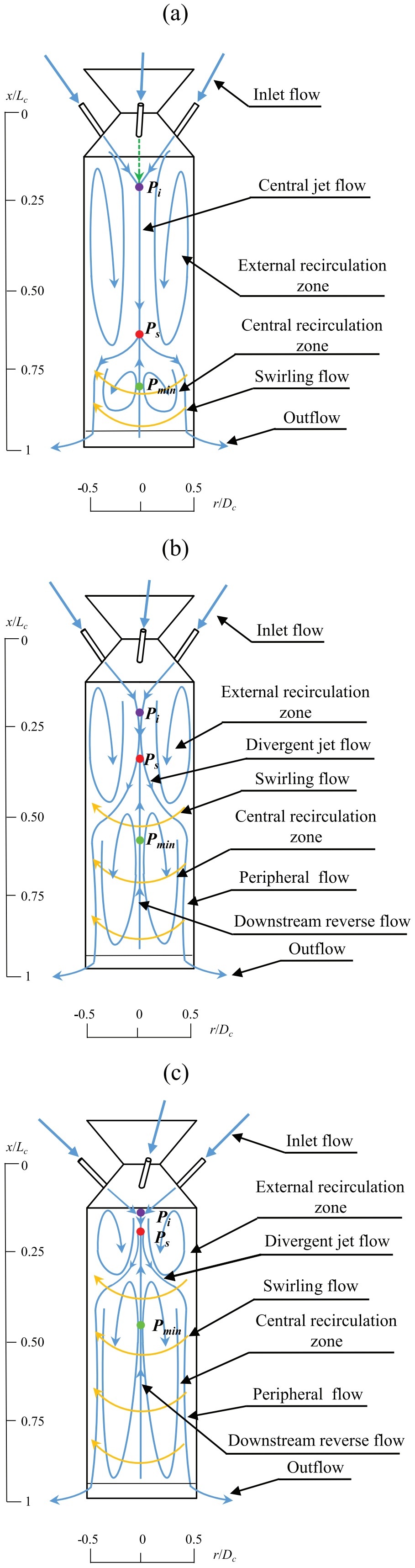

FIG. 13. Schematic diagrams of the three dominant flow regimes that have been identified within the rotationally symmetric MIJCC configurations. (a) Regime I: Dominant external recirculation zone with a downstream central recirculation zone. (b) Regime II: Dominant external and central recirculation zones. (c) Regime III: Dominant central recirculation zone with an upstream external recirculation zone.

TABLE IV. Definition of flow regimes in the Multiple Impinging Jets in a Cylindrical Chamber (MIJCC) configuration equipped rotationally symmetric jets.

Flow regime	Characteristics
Regime I	The dominance of an external recirculation zone (ERZ) within the cylindrical chamber so that its length exceeds half the chamber length, and a small central recirculation zone (CRZ) occurs downstream from the stagnation point. The location of the stagnation point at $x/L_c > 0.5$.
Regime II	The dominance of an ERZ within the upstream half of the chamber and a dominant CRZ downstream from the stagnation point. The location of the stagnation point at $0.25 < x/L_c < 0.5$.
Regime III	The dominance of CRZ within the majority of the cylindrical chamber and the presence of a high intensity ERZ at the upstream edge of the chamber. The location of the stagnation point at $x/L_c < 0.25$. The location of the jet impingement point at the conical section ($x/L_c < 0.15$).

D. Characterization of flow regimes

Figure 13 presents schematic diagrams of the three dominant flow regimes that have been identified within the rotationally symmetric MIJCC configurations. The key features of the three flow regimes are summarized in Table IV, using both the flow visualization and quantitative data. More details are presented in the following:

1. Regime I: Dominant external recirculation zone with downstream central recirculation zone

Regime I is characterized by a merged resulting jet within the upstream half of the chamber, together with an external recirculation zone (ERZ), which runs almost 2/3 of the cylindrical chamber. A jet impingement point (P_i) is observed downstream from the conical chamber. The ERZ is a dominant feature of this regime, which typically features a high vortex strength and a uniform distribution of the flow recirculation rate.[6] The central flow bifurcates into a small central recirculation zone (CRZ) downstream from the stagnation point at $x/L_c > 0.65$, although the strength of the CRZ is relatively low. This regime features a symmetric flow structure that is qualitatively similar to that identified for the MIJCC configuration[6] with $\alpha_j = 25°$ and $\theta_j = 0°$.

2. Regime II: Dominant external and central recirculation zones

Regime II is characterized by an upstream progression of the stagnation point (P_s) within the chamber from $x/L_c > 0.65$ to $x/L_c \approx 0.25$, which generates a dominant central recirculation zone (CRZ) within the downstream half of the chamber. An ERZ region is also observed within the upstream of the chamber, although its size is reduced relative to Regime I. Importantly, the strength of the ERZ in this regime is typically much greater than that for the CRZ. In addition, a low-velocity swirling flow is generated within the CRZ region.

3. Regime III: Dominant central recirculation zone with an upstream external recirculation zone

Regime III is qualitatively similar to Regime II, except that the CRZ is more dominant. It is also associated with a further reduction in the distribution of the ERZ and a significant upstream movement in the points of jet impingement (P_i), stagnation (P_s), and minimum velocity (P_{min}). As P_s approaches the upstream edge of the cylindrical chamber ($x/L_c \approx 0.13$), this regime will generate substantial transport of fluid from the main cavity toward the aperture and secondary concentrator, which is typically undesirable for solar thermal applications. The RMS velocity data also reveal that this regime tends to amplify the flow unsteadiness within the dominant CRZ region.

Figure 14 presents the geometric configurations for which the flow regimes are generated as a function of the jet azimuthal angle (θ_j) for the configurations of $\alpha_j = 25°$, 35°, and 45°. An additional case of $\alpha_j = 50°$ and $\theta_j = 5°$ is also included in this map, which was obtained under the same experimental condition described in Sec. II. Here the x-axis refers to the value of jet azimuthal angles (θ_j) while the y-axis refers to the value of jet inclination angles (α_j). The colored points denote the experimental cases and the contour maps denote the corresponding regimes of flow. It can be seen that, for a given value of α_j, an increase in θ_j leads to the transition from Regime I to Regime III, and vice versa. This implies that the transition and presence of each flow regime depend on both the α_j and θ_j investigated here. Nevertheless, the increment of α_j (~10°) in which the transition between each regime is greater than that for θ_j (~5°). This is distinctly different from the case in which $\theta_j = 0°$, for which an increase in α_j causes a significant reduction in the extent of the ERZ without a CRZ being generated further downstream from the ERZ.[6] This implies

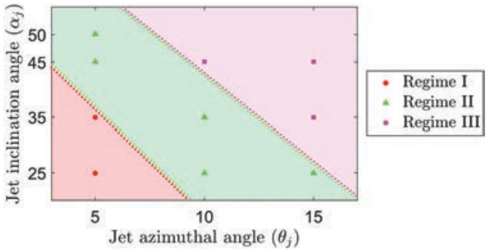

FIG. 14. Map of flow regimes as a function of the jet inclination angles (α_j) and the jet azimuthal angles (θ_j) for the Multiple Impinging Jets in a Cylindrical Chamber (MIJCC) equipped rotationally symmetric jets.

that the case of α_j is a singularity and that it is necessary for $\theta_j > 0°$ to generate a CRZ and also for α_j to have influence. Hence, taken together, it can be concluded that, for the rotationally symmetric jets within a confined space, the jet azimuthal angle (θ_j) is the dominant parameter that characterizes the presence of both the ERZ and CRZ regions, regardless of the value of α_j, while the jet inclination angle (α_j) can significantly influence the ERZ for which $\theta_j = 0°$ or both the ERZ and CRZ for which $\theta_j > 0°$.

Figure 14 also shows that Regime I occurs for the cases in which α_j and θ_j are both relatively small ($\alpha_j < 45°$, $\theta_j < 10°$), while Regimes II and III are favored for the cases of large α_j with a significant θ_j. This also suggests that the jet azimuthal angle for applications related to combustion and solar thermal technologies should be chosen sufficiently low (e.g., $\theta_j < 10°$) to minimize the risk of transporting fluid through the secondary concentrator or aperture.

IV. CONCLUSIONS

An experimental study of the iso-thermal flow field within a cylindrical chamber with rotationally symmetric jets has found that the characteristics of the mean and RMS (root-mean-square) flow-fields exhibit a primary dependence on the jet azimuthal angles (θ_j) and a secondary dependence on the jet inclination angles (α_j). The key outcomes of the study are as follows:

1. For a given value of α_j ($25° \leq \alpha_j \leq 45°$), an increase in θ_j from 5° to 15° leads to a decrease in the strength of the resulting jet flow and an increase in the strength of the downstream reverse flow, which changes the position and strength of the external recirculation zone (ERZ) and central recirculation zone (CRZ). It was also found that an increase in α_j from 25° to 45° causes a more significant upstream progression of the CRZ for configurations where $\theta_j \geq 10°$ than that of $\theta_j < 10°$, which indicates that the effect of α_j depends strongly on θ_j.
2. The presence of sufficient swirl was found to inhibit the large-scale oscillations (e.g., jet precession) that are otherwise associated with the jet impingement point (P_i). For example, an increase in θ_j from 5° to 15° avoids the large velocity fluctuations associated with large-scale jet oscillation and precession within the resulting jet flow downstream from P_i that do occur for the case of $\alpha_j = 25°$ and $\theta_j = 5°$. However, flow unsteadiness within the CRZ region (e.g., precessing vortex core) was found to be amplified for large θ_j cases that occur when $\alpha_j = 45°$ and $\theta_j = 15°$.
3. A high degree of Reynolds stress anisotropy was found in all experiment cases investigated here ($25° \leq \alpha_j \leq 45°$ and $5° \leq \theta_j \leq 15°$). Also, the large-scale flow motion corresponding to the integral length scale (L_u) depends strongly on the position of the ERZ and CRZ regions.
4. The magnitudes of mean and RMS velocities were found to be higher for the ERZ than those for the CRZ due to the strong interaction between inlet jets and the ERZ. This implies that the recirculation rate of the ERZ is greater than that for the CRZ. In addition, the velocity fluctuations were found to be stronger within the central region of the chamber for ERZ, in contrast to the CRZ for which the velocity fluctuations are greatest close to the wall region.
5. Three distinctive flow regimes were found within the Multiple Impinging Jet in a Cylindrical Chamber (MIJCC) investigated here depending on both α_j and θ_j, but most strongly on θ_j. The three flow regimes are as follows:
   a. Regime I: an upstream ERZ is dominant with a weak downstream CRZ.
   b. Regime II: an upstream ERZ is of similar extent to a downstream CRZ.
   c. Regime III: the downstream CRZ is dominant with a small ERZ upstream from the stagnation point.
6. For applications of combustion in a solar receiver, it is likely that some swirl will be desirable to avoid oscillations associated with jet precession. However, θ_j should also be sufficiently low (e.g., $\theta_j < 10°$) to minimize the risk of transporting fluid through the secondary concentrator or aperture.

ACKNOWLEDGMENTS

The authors would like to acknowledge the support of the Australian Research Council, FCT Combustion Pty. Ltd., and Vast Solar Pty. Ltd. through the ARC Linkage Grant No. LP110200060. Mr. Shen Long would like to acknowledge the financial support of the Australian Government Research Training Program. Finally, the insightful comments of the anonymous reviewers have strengthened the paper and are gratefully acknowledged.

[1] E. Koepf, W. Villasmil, and A. Meier, "High temperature flow visualization and aerodynamic window protection of a 100-kWth solar thermochemical receiver-reactor for ZnO dissociation," Energy Procedia **69**, 1780 (2015).

[2] G. Cox, "Multiple jet correlations for gas turbine engine combustor design," J. Eng. Power **98**, 265 (1976).

[3] T. Chammem, H. Mhiri, and O. Vauquelin, "Experimental and computational investigation of Reynolds number effect on the longitudinal ventilation in large enclosure of twin inclined jets," Build. Environ. **67**, 87 (2013).

[4] T. Boushaki and J.-C. Sautet, "Characteristics of flow from an oxy-fuel burner with separated jets: Influence of jet injection angle," Exp. Fluids **48**, 1095 (2010).

[5] H. J. Hussein, S. P. Capp, and W. K. George, "Velocity measurements in a high-Reynolds-number, momentum-conserving, axisymmetric, turbulent jet," J. Fluid Mech. **258**, 31 (1994).

[6] S. Long, T. C. W. Lau, A. Chinnici, Z. F. Tian, B. B. Dally, and G. J. Nathan, "Experimental and numerical investigation of the iso-thermal flow characteristics within a cylindrical chamber with multiple planar-symmetric impinging jets," Phys. Fluids **29**, 105111 (2017).

[7] G. J. Nathan, D. Battye, and P. Ashman, "Economic evaluation of a novel fuel-saver hybrid combining a solar receiver with a combustor for a solar power tower," Appl. Energy **113**, 1235 (2014).

[8] A. Chinnici, Z. F. Tian, J. H. Lim, G. J. Nathan, and B. B. Dally, "Comparison of system performance in a hybrid solar receiver combustor operating with MILD and conventional combustion. Part I: Solar-only and combustion-only employing conventional combustion," Sol. Energy **147**, 489 (2017).

[9] A. Chinnici, Z. F. Tian, J. H. Lim, G. J. Nathan, and B. B. Dally, "Comparison of system performance in a hybrid solar receiver combustor operating with MILD and conventional combustion. Part II: Effect of the combustion mode," Sol. Energy **147**, 479 (2017).

[10] J. H. Lim, G. J. Nathan, B. Dally, and A. Chinnici, "Techno-economic assessment of a hybrid solar receiver and combustor," AIP Conf. Proc. **1734**, 070020 (2016).

[11] J. H. Lim, A. Chinnici, B. B. Dally, and G. J. Nathan, "Assessment of the potential benefits and constraints of a hybrid solar receiver and combustor operated in the MILD combustion regime," Energy **116**(Part 1), 735 (2016).

[12] E. Tanaka, "The interference of two-dimensional parallel jets: 1st report, experiments on dual jet," Bull. JSME **13**, 272 (1970).

[13] E. Tanaka, "The interference of two-dimensional parallel jets: 2nd report, experiments on the combined flow of dual jet," Bull. JSME **17**, 920 (1974).

[14] E. Tanaka and S. Nakata, "The interference of two-dimensional parallel jets: 3rd report, the region near the nozzles in triple jets," Bull. JSME **18**, 1134 (1975).

[15] M. A. Mergheni, T. Boushaki, J. C. Sautet, and S. Ben Nasrallah, "Numerical study of oxy-flame characteristics in a burner with three separated jets," Appl. Therm. Eng. **111**, 1 (2017).

[16] Z. Gao, J. Han, Y. Xu, Y. Bao, and Z. Li, "Particle image velocimetry (PIV) investigation of flow characteristics in confined impinging jet reactors," Ind. Eng. Chem. Res. **52**, 11779 (2013).

[17] C. X. Thong, P. A. Kalt, B. B. Dally, and C. H. Birzer, "Flow dynamics of multi-lateral jets injection into a round pipe flow," Exp. Fluids **56**(1), 15 (2015).

[18] Y. Liu, M. G. Olsen, and R. O. Fox, "Turbulence in a microscale planar confined impinging-jets reactor," Lab Chip **9**, 1110 (2009).

[19] O. Lucca-Negro and T. O'Doherty, "Vortex breakdown: A review," Prog. Energy Combust. Sci. **27**, 431 (2001).

[20] A. Ridluan, S. Eiamsa-ard, and P. Promvonge, "Numerical simulation of 3D turbulent isothermal flow in a vortex combustor," Int. Commun. Heat Mass Transfer **34**, 860 (2007).

[21] A. Z'graggen, P. Haueter, D. Trommer, M. Romero, J. De Jesus, and A. Steinfeld, "Hydrogen production by steam-gasification of petroleum coke using concentrated solar power—II Reactor design, testing, and modeling," Int. J. Hydrogen Energy **31**, 797 (2006).

[22] C. Shephered and C. Lapple, "Flow pattern and pressure drop in cyclone dust collectors," Ind. Eng. Chem. **31**, 972 (1939).

[23] N. Ozalp, M.-H. Chien, and G. Morrison, "Computational fluid dynamics and particle image velocimetry characterization of a solar cyclone reactor," J. Sol. Energy Eng. **135**, 031003 (2013).

[24] L. O. Schunk, P. Haeberling, S. Wepf, D. Wuillemin, A. Meier, and A. Steinfeld, "A receiver-reactor for the solar thermal dissociation of zinc oxide," J. Sol. Energy Eng. **130**, 021009 (2008).

[25] D. Hirsch and A. Steinfeld, "Solar hydrogen production by thermal decomposition of natural gas using a vortex-flow reactor," Int. J. Hydrogen Energy **29**, 47 (2004).

[26] B. Launder, G. J. Reece, and W. Rodi, "Progress in the development of a Reynolds-stress turbulence closure," J. Fluid Mech. **68**, 537 (1975).

[27] M. Vanierschot and E. Van den Bulck, "Influence of swirl on the initial merging zone of a turbulent annular jet," Phys. Fluids **20**, 105104 (2008).

[28] P. Billant, J.-M. Chomaz, and P. Huerre, "Experimental study of vortex breakdown in swirling jets," J. Fluid Mech. **376**, 183 (1998).

[29] S. Roux, G. Lartigue, T. Poinsot, U. Meier, and C. Bérat, "Studies of mean and unsteady flow in a swirled combustor using experiments, acoustic analysis, and large eddy simulations," Combust. Flame **141**, 40 (2005).

[30] M. Vanierschot and E. Van den Bulck, "Hysteresis in flow patterns in annular swirling jets," Exp. Therm. Fluid Sci. **31**, 513 (2007).

[31] P. Wang, X.-S. Bai, M. Wessman, and J. Klingmann, "Large eddy simulation and experimental studies of a confined turbulent swirling flow," Phys. Fluids **16**, 3306 (2004).

[32] N. Syred and J. Beer, "Combustion in swirling flows: A review," Combust. Flame **23**, 143 (1974).

[33] R. C. Deo, J. Mi, and G. J. Nathan, "The influence of Reynolds number on a plane jet," Phys. Fluids **20**, 075108 (2008).

[34] J. Nikuradse, "Gesetzmäßigkeiten der turbulenten strömung in glatten rohren," Forsch. Geb. Ingenieurwes. **4**, 44 (1933).

[35] M. Escudier, A. Nickson, and R. Poole, "Influence of outlet geometry on strongly swirling turbulent flow through a circular tube," Phys. Fluids **18**, 125103 (2006).

[36] N. Syred, "A review of oscillation mechanisms and the role of the precessing vortex core (PVC) in swirl combustion systems," Prog. Energy Combust. Sci. **32**, 93 (2006).

[37] N. Syred and K. Dahman, "Effect of high levels of confinement upon the aerodynamics of swirl burners," Energy **2**, 8 (1978).

[38] A. K. Gupta, D. G. Lilley, and N. Syred, *Swirl Flows* (Abacus Press, Tunbridge Wells, Kent, England, 1984), p. 488.

[39] Y. M. Al-Abdeli and A. R. Masri, "Recirculation and flowfield regimes of unconfined non-reacting swirling flows," Exp. Therm. Fluid Sci. **27**, 655 (2003).

[40] D. L. Marchisio, "Large eddy simulation of mixing and reaction in a confined impinging jets reactor," Comput. Chem. Eng. **33**, 408 (2009).

[41] F. R. Menter, "Two-equation eddy-viscosity turbulence models for engineering applications," AIAA J. **32**, 1598 (1994).

[42] G. Xu and R. Antonia, "Effect of different initial conditions on a turbulent round free jet," Exp. Fluids **33**, 677 (2002).

[43] J. Mi and G. J. Nathan, "Statistical properties of turbulent free jets issuing from nine differently-shaped nozzles," Flow, Turbul. Combust. **84**, 583 (2010).

Chapter 6

The Influence of Aspect Ratio on the Isothermal Flow Characteristics of Multiple Confined Jets

Statement of Authorship

Title of Paper	The influence of aspect ratio on the iso-thermal flow characteristics of multiple confined jets
Publication Status	☑ Published ☐ Accepted for Publication ☐ Submitted for Publication ☐ Unpublished and Unsubmitted work written in manuscript style
Publication Details	Long, S., Lau, T.C., Chinnici, A., Tian, Z.F., Dally, B.B. and Nathan, G.J., 2018. The influence of aspect ratio on the iso-thermal flow characteristics of multiple confined jets. Physics of Fluids, vol. 30, no. 12, p.125108.

Principal Author

Name of Principal Author (Candidate)	Shen Long
Contribution to the Paper	Conducted literature review, collected all experimental data, performed data processing and analysis, wrote manuscript and acted as corresponding author.
Overall percentage (%)	65
Certification:	This paper reports on original research I conducted during the period of my Higher Degree by Research candidature and is not subject to any obligations or contractual agreements with a third party that would constrain its inclusion in this thesis. I am the primary author of this paper.

Signature		Date	07/01/2019

Co-Author Contributions

By signing the Statement of Authorship, each author certifies that:

i. the candidate's stated contribution to the publication is accurate (as detailed above);

ii. permission is granted for the candidate in include the publication in the thesis; and

iii. the sum of all co-author contributions is equal to 100% less the candidate's stated contribution.

Name of Co-Author	Timothy Lau
Contribution to the Paper	Supervised the experiments, helped in data interpreting and edited manuscript.

Signature		Date	7/01/2019

Name of Co-Author	Alfonso Chinnici
Contribution to the Paper	Helped to develop the work and helped in data interpreting.

Signature		Date	07/01/19

Name of Co-Author	Zhao Feng Tian		
Contribution to the Paper	Supervised the development of work and helped in data interpreting.		
Signature		Date	07/01/19

Name of Co-Author	Bassam Dally		
Contribution to the Paper	Supervised the development of work, provided comments and edited manuscript.		
Signature		Date	7-1-19

Name of Co-Author	Graham 'Gus' Nathan		
Contribution to the Paper	Supervised the development of work, helped in data interpreting, provided comments and edited manuscript.		
Signature		Date	7/1/19

PHYSICS OF FLUIDS **30**, 125108 (2018)

The influence of aspect ratio on the iso-thermal flow characteristics of multiple confined jets

Shen Long,[a)] Timothy C. W. Lau, Alfonso Chinnici, Zhao Feng Tian, Bassam B. Dally, and Graham J. Nathan
Centre for Energy Technology, School of Mechanical Engineering, The University of Adelaide, Adelaide, South Australia 5005, Australia

(Received 28 September 2018; accepted 23 November 2018; published online 20 December 2018)

We report a systematic study of the interaction between four rotationally symmetric jets within a cylindrical chamber obtained with particle image velocimetry, under conditions relevant to a wide range of practical applications including the hybrid solar receiver combustor. The geometry consists of a cylindrical cavity with four inlet jets (representing four burners), which are configured in an annular arrangement and aligned at an inclination angle (α_j) to the axis with a tangential component (azimuthal angle θ_j) to generate a swirl in the chamber. The configurations of $\alpha_j = 25°$ were assessed with two azimuthal angles $\theta_j = 5°$ and 15°, a range of chamber aspect ratios (L_c/D_c), and a fixed nozzle Reynolds number of $Re_D = 10\,500$. The experimental results reveal a significant dependence of the mean and turbulent flow-fields on the aspect ratio L_c/D_c for the values of α_j and θ_j considered here. Three different flow regimes and their controlling parameters were identified within the range $1 \leq L_c/D_c \leq 3$. The dependence of the flow characteristics on the chamber length L_c was weak within $1.5 < L_c/D_c \leq 3$, but significant for $1 \leq L_c/D_c \leq 1.5$. It was also found that the value of L_c/D_c has a controlling influence on the position and strength of large-scale recirculation regions, together with the extent of flow unsteadiness, although this influence is reduced as θ_j is increased. *Published by AIP Publishing.* https://doi.org/10.1063/1.5063500

I. INTRODUCTION

Multiple confined jets have been widely used in engineering applications such as solar receiver reactors,[1] gas turbine engines,[2] ventilation systems,[3] and multiple-burner combustors.[4] However, comprehensive understanding of the flow-field in these systems is still lacking owing to the large number of controlling parameters, such as jet angles,[5] the extent of confinement by walls,[6] and flow conditions.[7] Of particular interest here are those configurations featuring multiple jets of relevance to the Hybrid Solar Receiver Combustor (HSRC) under development at the University of Adelaide.[8–12] This device features a cavity that is operable as either a solar receiver or a combustion chamber equipped with multiple burners to direct fuel and air into the main cavity and tubular heat exchangers to transfer the thermal energy to the heat transfer fluid. The burners are configured in an annular ring and aligned at an inclination angle (α_j) relative to the axis of the cavity and/or at an azimuthal angle (θ_j) relative to the axis of the burner, resulting in a swirling flow within the main cavity. For conditions in which both $\alpha_j > 0°$ and $\theta_j > 0°$, this arrangement is termed "rotationally symmetric." Previous investigations of the flow-fields within the HSRC revealed a significant effect of the jet angles (α_j and θ_j) on the strength and position of the large-scale recirculation which is critical for achieving desirable flow regimes.[10,11] In addition, the aspect ratio of L_c/D_c has a strong influence on thermal efficiency and capital cost.[9,12] Nevertheless, the dependence of the important flow characteristics on the key geometrical parameters, such as the length (L_c) and diameter (D_c) of the chamber, remains unknown. Hence, the overall objective of the present paper is to provide new understanding of the flow characteristics generated with multiple rotationally symmetric inlet-jets within a cylindrical chamber for a range of chamber aspect ratios L_c/D_c.

Previous studies of flow-fields generated with multiple symmetric jets within a confined space revealed that the flow structure depends strongly on the arrangement and geometrical features of jets.[3,4,10,11,13–16] Chammem *et al.*[3] defined the flow structure downstream from the jet impingement point (P_i) as the "resulting jet flow" and that upstream as the "upstream reverse flow" noting that these flow features are significantly influenced by α_j. The experimental studies of Boushaki and Sautet[4] employing Particle Image Velocimetry (PIV) showed that an increase in α_j from 0° to 30° leads to a significant increase in the magnitude of mean and turbulent velocity fields within the jet merging region. Similarly, the PIV measurements of Long *et al.*[10,11] found a strong dependence on jet angles (α_j and θ_j) of the instantaneous and mean flow-fields generated with multiple symmetric jets. However, to the best of our knowledge, little or no information is available for the key geometrical parameters (e.g., L_c and D_c) of the confined space for multiple jet configurations, although the aspect ratio of geometry has been found to have a significant influence on the flow-fields of free jet impingement[17–19] and cavity flow.[20–22] Importantly, the existing experimental data provide insufficient information to

---

[a)] Author to whom correspondence should be addressed: shen.long@adelaide.edu.au adequately understand the effect of the aspect ratio on the multiple confined jets in which both α_j and θ_j are variables. Hence, there is a need to obtain reliable, comprehensive, and sufficient data to fully characterize the influence of the chamber aspect ratio L_c/D_c on the mean and RMS (root-mean-square) flow-fields generated with multiple inclined jets in a confined space.

The influence of confinement on the flow-fields has been investigated for a wide range of applications.[16,17,23–27] It has been found that the distance between the jet exit and an end plate, termed "confinement height" (H_c), can significantly influence the position and strength of the recirculation regions, wall jet development, and jet velocity.[17,23,24,26] It has also been found that the influence of the aspect ratio of a confined space is significant for near-field but negligible for far-field within a swirled jet chamber.[27] However, while these previous studies provide useful insight, they are of limited value for model validation due to the lack of information available for the inflow and boundary conditions. Another limit of these studies is that they have been performed almost exclusively for a single jet, which makes it difficult to directly apply to multiple confined jets. In our previous work, Long *et al.*[11] revealed the presence of both an external and internal recirculation zone (ERZ and CRZ) within these configurations. The ERZ and CRZ regions are associated with the entrainment rate (or the recirculation rate) within the chamber, which is important for combustion stabilization and thermal efficiency.[28–30] However, this was assessed for a fixed value of $L_c/D_c = 3$ so that the influence of L_c/D_c on large-scale recirculation regions is yet to be reported. Hence, additional measurements are needed to identify the influence of the chamber aspect ratio L_c/D_c on the dominant recirculation zones generated by multiple jets within a cylindrical chamber.

To meet the aforementioned needs, the present paper aims to provide new understanding of the iso-thermal flow-fields generated with a Multiple Impinging Jet in a Cylindrical Chamber, termed "MIJCC." More specifically, it aims: (a) to provide a detailed characterization of the flow generated with multiple rotationally symmetric inlet-jets within a cylindrical chamber for the aspect ratios L_c/D_c = 3, 2.5, 2, 1.5, and 1; (b) to identify the influence of the chamber aspect ratio L_c/D_c on both the mean and RMS flow-fields within a cylindrical chamber with multiple jets; and (c) to characterize the dependence of the large-scale recirculation zones (ERZ and CRZ) on the aspect ratio L_c/D_c for low-swirl ($\alpha_j = 25°$ and $\theta_j = 5°$) and high-swirl ($\alpha_j = 25°$ and $\theta_j = 15°$) jet configurations.

II. METHODOLOGY

A. Experimental configurations

The experimental MIJCC configuration is presented schematically in Fig. 1. The design principles have been reported in our previous work,[11] so here only the key geometrical features are discussed. The cavity of the MIJCC consists of a cylindrical chamber with a conical expansion, a secondary concentrator (SC), and four rotationally symmetric inlet jets ($N_j = 4$). The inlet jets were distributed around the main cavity with a combination of an inclination angle (α_j) and an azimuthal angle (θ_j). The flow leaves the device through an annular outlet around a bluff end-wall.

The values of the key geometrical parameters are listed in Table I. The diameter of the MIJCC was fixed at D_c = 74 mm, while the length of the chamber was set at either L_c = 185 mm, 148 mm, 111 mm, or 74 mm, resulting in aspect ratios of L_c/D_c = 2.5, 2, 1.5, or 1. These ratios were selected to span a sufficient range of flow-features and cover realistic geometrical dimensions for relevant applications. In addition, the chamber length of our previous work L_r = 225 mm ($L_r/D_c = 3$) was chosen as reference cases for comparison with the present study (labelled with an asterisk in Table II). Two azimuthal angles of θ_j = 5° and 15° were investigated at a fixed inclination angle of α_j = 25°, representing the "low-swirl" and "high-swirl" configurations, respectively. These angles were chosen to generate the two main classes of flow identified in our previous work,[11] which found that either a dominant ERZ or CRZ regime can be generated within the cylindrical chamber, depending on the geometry. All experimental cases are listed in Table II.

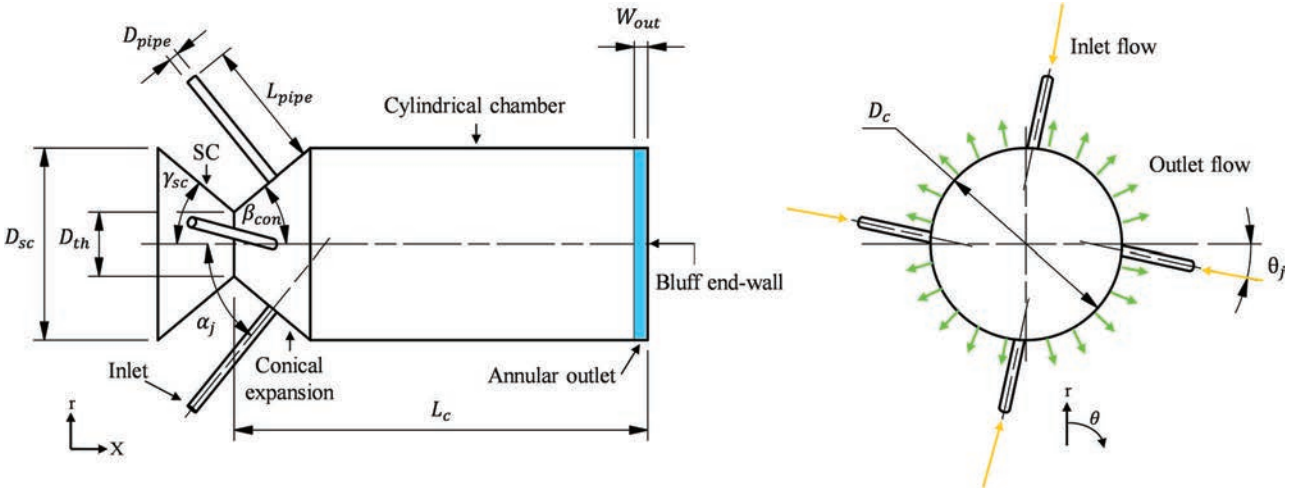

FIG. 1. Schematic diagram of the MIJCC configurations investigated in the present study, showing the key geometrical parameters from the axial cross section (left) and the radial cross section (right).

TABLE I. Values of the geometrical parameters of the MIJCC configurations investigated in the present study.

Dimensions	Description	Value
D_c	Chamber diameter (mm)	74
D_{sc}	Diameter of the SC (mm)	74
D_{th}	Throat diameter (mm)	24.6
D_{pipe}	Inlet pipe diameter (mm)	3.35
L_c	Chamber length (mm)	185, 148, 111, and 74
L_r	Reference chamber length (mm)	225
L_{pipe}	Inlet pipe length (mm)	150
W_{out}	Width of the outlet gap (mm)	3
β_{con}	Conical expansion angle (deg)	40
γ_{sc}	Angle of the SC (deg)	40
α_j	Jet inclination angle (deg)	25
θ_j	Jet azimuthal angle (deg)	5 and 15

TABLE II. The notation for the MIJCC configurations investigated in the present study.

Experiment case no.	Configurations	Jet angles, α_j and θ_j (deg)	Chamber aspect ratio, L_c/D_c
1	MIJCC-05-LD25	25 and 5	2.5
2	MIJCC-05-LD20	25 and 5	2
3	MIJCC-05-LD15	25 and 5	1.5
4	MIJCC-05-LD10	25 and 5	1
5	MIJCC-15-LD25	25 and 15	2.5
6	MIJCC-15-LD20	25 and 15	2
7	MIJCC-15-LD15	25 and 15	1.5
8	MIJCC-15-LD10	25 and 15	1
9*	MIJCC-05-LD30	25 and 5	3
10*	MIJCC-15-LD30	25 and 15	3

B. Experimental arrangement

The present experimental arrangement is similar to that reported previously,[10,11] so only the key experimental apparatus and parameters are described here. Planar Particle Image Velocimetry (PIV) was employed to investigate the mean and RMS flow-fields with the MIJCC configurations. The working fluid was water at ambient temperature, while a closed-loop system was used to recirculate the water from the outlets of the tank to the inlet-pipes. A symmetrical manifold system feeds fluid to four pipes with a length-to-diameter ratio of $L_{pipe}/D_{pipe} \approx 196$ (the straight pipe has a length of $46D_{pipe}$, and the gently curved flexible pipe has a length of $150D_{pipe}$), which ensures that a fully developed pipe flow is achieved at the pipe exit plane.[31] The flow was seeded with hollow glass spheres with a specific gravity of 1.1 and a particle diameter of 12 μm.

The optical arrangement, together with the axial measurement region, is presented schematically in Fig. 2, while the details of the key experimental parameters are listed in Table III. A Nd:YAG laser (Quantel Brilliant B) was used to generate a light sheet with a combination of three cylindrical lenses (Thorlabs). A Charged Coupled Device (CCD) camera (Kodak Megaplus ES2093) was used to capture the PIV images for each measurement.

A total of 1900 PIV image pairs was collected and processed for each experimental condition. An in-house PIV code in MATLAB R2015a (Mathworks) was employed to process the raw images. A multi-grid correlation algorithm with 50% overlap was applied to calculate the displacement of seeding particles and also to minimize noise. Outliers (erroneous vectors) were identified by using an in-house PIV code in the post-processing, which compares the value difference between

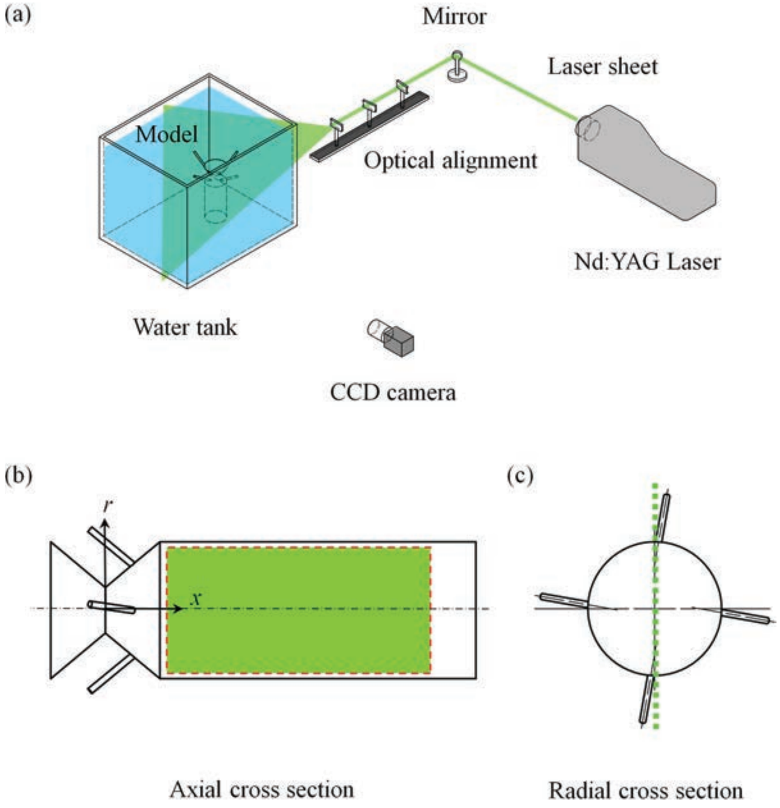

FIG. 2. (a) Schematic diagram of the PIV setup, showing the Nd:YAG laser, optical arrangement, water tank, and camera, (b) the axial measurement region (green box enclosed by a red dashed line) relative to the chamber (not to scale), and (c) the radial cross section, showing the laser sheet.

TABLE III. Details of the key experimental parameters for the present PIV measurements.

Experimental parameters	Value
Bulk mean velocity at the nozzle exit, U_e (m/s)	2.8
Inlet Reynolds number, Re_D	10 500
Laser wavelength (nm)	532
Laser thickness (mm)	1.5
Camera array size (pixels)	1920 × 1080
Measurement region (mm)	123 × 65
Image bit depth (bit)	12
Spatial resolution (mm)	2
Interrogation window (pixels)	32 × 32

the absolute and relative velocities. The average number of outliers was less than approximately 5% of the total vectors, and all outliers were removed from the ensemble.

The overall uncertainty ($\epsilon_{overall}$) associated with the PIV measurements was assessed via a series of systematic analyses, which accounted for the uncertainty derived from the experimental apparatus (2%), calibration (±0.05 mm), laser time-delay (2%), and the image sample size (1%). On these bases, the overall uncertainty for the present PIV measurements was calculated to be $\epsilon_{overall} \approx 5\%$.

III. RESULTS AND DISCUSSION

A. Mean flow fields

Figure 3 presents the contours of the mean axial velocity (U_x) normalized by the nozzle exit velocity (U_e), showing the streamlines, labelled with arrows to indicate the flow direction (white arrows), and magnitude (color map) for the configuration of α_j = 25° and θ_j = 5° with (a) L_c/D_c = 2.5, (b) L_c/D_c = 2, (c) L_c/D_c = 1.5, and (d) L_c/D_c = 1 and for

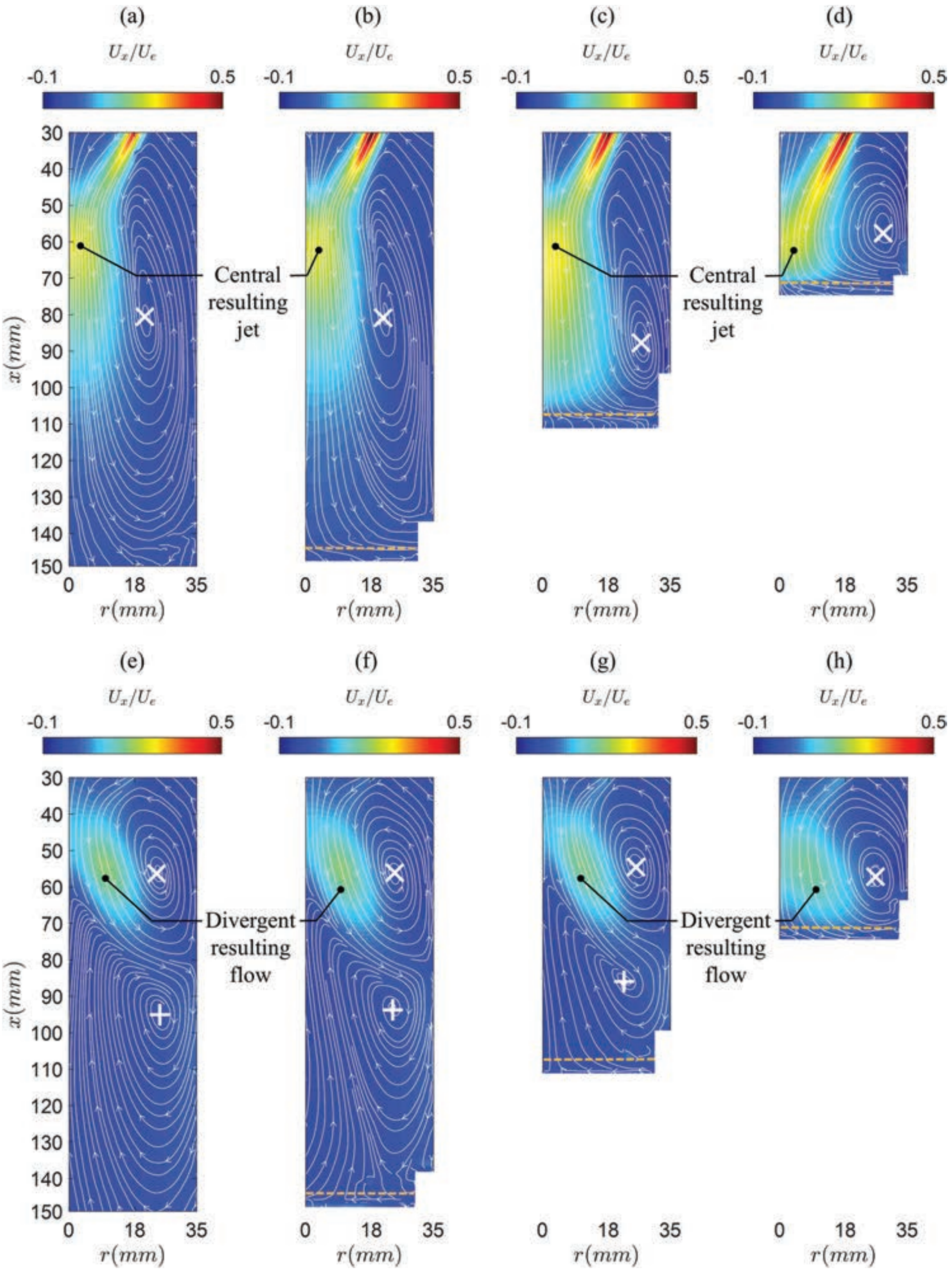

FIG. 3. Mean axial velocity normalized by the nozzle exit velocity (U_x/U_e), showing the streamlines, labelled with arrows to indicate the flow direction (white arrows), and magnitude (color map), for the configuration of α_j = 25° with θ_j = 5° and 15° for (a) and (e) L_c/D_c = 2.5, (b) and (f) L_c/D_c = 2, (c) and (g) L_c/D_c = 1.5, and (d) and (h) L_c/D_c = 1. Here x and r denote the axial and radial locations of the chamber, respectively. The orange dashed line denotes the upstream end of the annular outlet, while the region downstream from this line refers to the exit plane.

the configuration of $\alpha_j = 25°$ and $\theta_j = 15°$ with (e) $L_c/D_c = 2.5$, (f) $L_c/D_c = 2$, (g) $L_c/D_c = 1.5$, and (h) $L_c/D_c = 1$. Here x and r denote the axial and radial locations of the chamber, respectively. The orange dashed line denotes the upstream end of the annular outlet, while the region downstream from this line refers to the exit plane. The location of the vortex-core was determined by a combination of mathematical calculations described by Grosjean *et al.*[32] and visual observation. Owing to the symmetry of the flow in the MIJCC configurations,[11] which was reconfirmed in the preliminary measurements, only half of the measured region is presented here. For the configurations where $\theta_j = 5°$ [Figs. 3(a)–3(d)], it can be seen that a central resulting jet flow occurs for all cases downstream from the merging point (P_{mer}) of the four inlet jets. This resulting flow generates a large vortex (counter-clockwise in Fig. 3, with the vortex-core marked with a white "×") dubbed the external recirculation zone (ERZ). The secondary vortex that was found in the previous work of $L_c/D_c = 3$,[11] if present, must be outside of the imaged region for $L_c/D_c = 2.5$.

It can be seen that the position of the ERZ is almost independent of the chamber length for $L_c/D_c \geq 2$. For example, the axial location of the ERZ vortex-core relative to the throat location, x_{core}, remains constant at $x_{core} \approx 80$ mm as L_c/D_c is reduced from 2.5 to 2 [Figs. 3(a) and 3(b), respectively]. However, as L_c/D_c is further reduced from 2 to 1, x_{core} decreases to ≈60 mm, with the distance between the ERZ vortex-core and the bluff end-wall (Δx_{end}) reduces to $\Delta x_{end} \approx 20$ mm. In addition, this decrease in the aspect ratio also increases the radial location of the ERZ core (r_{core}) from $r_{core} \approx 21$ mm at $L_c/D_c = 2.5$ to $r_{core} \approx 29$ mm at $L_c/D_c = 1$. These findings are attributed to the effect of jet impingement on the bluff end-wall that influences the development of the resulting flow and are consistent with a previous study employing an unconfined single jet.[17] Hence, it can be concluded that the position of the ERZ exhibits a strong dependence on the aspect ratio L_c/D_c for low-swirl configurations ($\theta_j = 5°$), which is most significant for $L_c/D_c < 2$.

Figures 3(a)–3(d) also show that a reduction in the aspect ratio L_c/D_c leads to a significant increase in the velocity magnitude of the inlet-jets upstream from the merging point. For example, the velocity near the merging point increases by ≈35% from $L_c/D_c = 2.5$ [Fig. 3(a)] to $L_c/D_c = 1$ [Fig. 3(d)]. Since the inlet-jet parameters (α_j, θ_j, and U_e) are identical to all cases, the increased value in U_x/U_e is attributed primarily to a reduction in the flow oscillation at and upstream from the merging point as L_c is decreased. This reduction in flow unsteadiness, such as jet flapping or precessing, is addressed later in the paper and has also been widely reported previously for multiple-jet configurations.[16,33,34] For the current MIJCC configurations, a shorter length of the chamber tends to restrict both the "in-plane" and "out-of-plane" motions of the four inlet-jets, which therefore inhibits the flow oscillation that is associated with the interaction between inlet-jets. In addition, the reduction in the chamber length also increases the velocities in the ERZ, reducing the rate of decay in the jets upstream from the merging point.

For the higher-swirl cases with $\theta_j = 15°$ [Figs. 3(e)–3(h)], the ERZ is much shorter and a central recirculation zone (CRZ) also occurs within the measurement region so that no central resulting jet is generated. Instead the flow bifurcates to form a conically divergent resulting flow downstream from the merging point. The cores of the ERZ and CRZ are marked with a white "×" and a white "+," respectively. It can be seen that the axial and radial locations of the vortex-core within the ERZ region remain constant at $x_{core} \approx 56$ mm and $r_{core} = 25$ mm, respectively, regardless of L_c/D_c. By contrast, x_{core} within the CRZ moves upstream from $x_{core} \approx 95$ mm to $x_{core} \approx 86$ mm as L_c/D_c is reduced from 2.5 to 1.5. Importantly, as L_c/D_c is further reduced to 1, the downstream CRZ is no longer observed within the chamber due to insufficient space. The vortex-core of the ERZ at $L_c/D_c = 1$ moves slightly to further downstream ($x_{core} \approx 58$ mm), implying that L_c/D_c influences the ERZ for this case. This also suggests that the dependence of the ERZ on L_c/D_c will be increased if L_c/D_c is further reduced (e.g., $L_c/D < 1$). Hence, for the configurations with large azimuthal angle ($\theta_j = 15°$), the upstream ERZ region is almost independent of the value of L_c/D_c for $L_c/D_c \geq 1.5$ but becomes significant for $L_c/D_c < 1.5$, while the downstream CRZ region depends strongly on all values of L_c/D_c considered here.

Figure 4 presents the evolution of normalized mean axial velocity along the axis (U_c/U_e) for all MIJCC configurations investigated here. The PIV data from our previous work[11] of $L_c/D_c = 3$ are also included. Each mean velocity measurement has been performed from the time-average of the 1900 PIV image pairs. In each figure, the dashed line denotes the value of $U_c/U_e = 0$, while the dotted lines color-matched with data points refer to the locations of the bluff end-wall. The jet merging point, P_{mer}, refers to the location of the maximum velocity along the centerline of the chamber [$(U_c/U_e)_{max}$], the stagnation point, P_s, as the most upstream axial location of the velocity zero-crossing ($U_c/U_e = 0$), which also denotes the most downstream location of the resulting flow, and the point of the minimum axial velocity, P_{min}, as the axial location of the minimum velocity [$(U_c/U_e)_{min}$].

For the configurations of $\theta_j = 5°$ [Fig. 4(a)], it can be seen that a decrease in the aspect ratio L_c/D_c does not change the magnitude or location of U_c/U_e at the merging point, with $(U_c/U_e)_{max} \approx 0.26$ at $x/L_c = 0.27$ for all cases. However, downstream from the merging point, the evolution of U_c/U_e is strongly influenced by L_c/D_c. For example, as L_c/D_c reduces from 2.5 to 1.5, the location of the stagnation point moves upstream from $x/L_c = 0.65$ to 0.5, while the decay of U_c/U_e decreases significantly for $L_c/D_c = 1.5$. This is possibly caused by the effect of the end-wall on the development of central resulting jet flow that reduces the entrainment rate between the jet and surrounding fluids.[17,35] Importantly, large data fluctuations were found at $x/L_c \approx 0.48$, with RMS ≈ 0.037 for the case of $L_c/D_c = 1.5$, which is consistent with the strong gradients caused by the combined effects of a radial outlet flow, a bluff end-wall, and a cylindrical chamber. In addition, for $L_c/D_c = 1$ where the bluff end-wall closely approaches the location of the merging point, the central resulting flow is almost absent [see also Fig. 3(d)] due to the confinement effect from the cylindrical walls, while the decay of U_c/U_e is the highest for all cases. Hence, it can be concluded that, for the case of $\theta_j = 5°$, reducing the aspect ratio L_c/D_c significantly inhibits the axial development of the central resulting flow for $L_c/D_c < 2$.

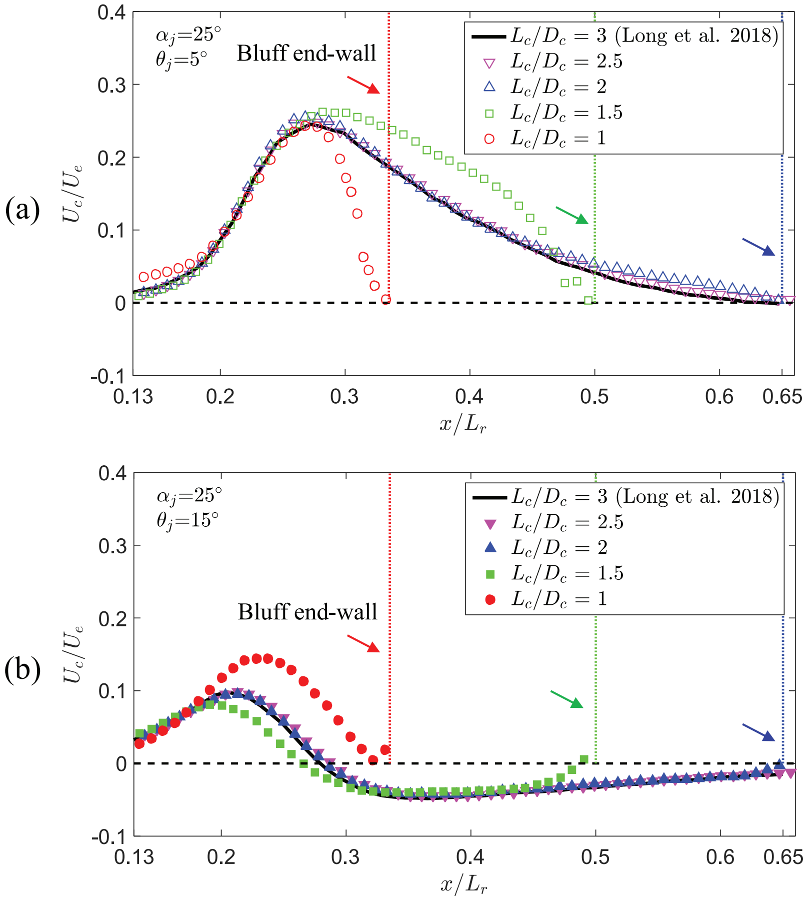

FIG. 4. Evolution of normalized mean axial velocity along the centerline of the MIJCC configurations (U_c/U_e), as a function of the reference chamber length (L_r) for the cases of (a) $\alpha_j = 25°$ and $\theta_j = 5°$, (b) $\alpha_j = 25°$ and $\theta_j = 15°$, and for aspect ratios of $L_c/D_c = 1$–3. The dotted lines color-matched with data points refer to the locations of the bluff end-wall. For clarity, only one in two data points is presented.

For the $\theta_j = 15°$ case [Fig. 4(b)], it can be seen that the evolution of U_c/U_e along the axis is almost independent from L_c/D_c for $L_c/D_c \geq 2$. The value of $(U_c/U_e)_{max}$ is approximately 0.1 at $x/L_c = 0.21$, while $(U_c/U_e)_{min}$ is approximately −0.05 at $x/L_c = 0.37$ for the cases of $L_c/D_c = 2$–3. This shows that the locations of both the merging and stagnation points are independent from L_c/D_c for these cases. However, as the value of L_c/D_c reduces to 1.5, the location of the merging point moves slightly upstream (from $x/L_c = 0.22$ to 0.19), while magnitude of $(U_c/U_e)_{max}$ reduces by 15%. The axial extent of the negative velocity flow ($U_c/U_e < 0$) was also found to be reduced due to a shorter L_c, although both the magnitude and location of $(U_c/U_e)_{min}$ remain the same. For the shortest L_c considered here ($L_c/D_c = 1$), no negative velocity region is present owing to the absence of the CRZ [see also Fig. 3(h)]. In addition, the location of the merging point progresses further downstream to $x/L_c = 0.24$, while the value of $(U_c/U_e)_{max}$ increases to 0.15 for $L_c/D_c = 1$. This indicates an increase in the size and intensity of the ERZ for $L_c/D_c = 1$, which also highlights the effect of the bluff end-wall on the development of divergent resulting flow. Hence, for the $\theta_j = 15°$ case, the aspect ratio of L_c/D_c can influence the flow characteristics within the CRZ for $L_c/D_c > 1$ or within the ERZ for $L_c/D_c < 2$.

Overall, the evolution of $U_c/U_e \geq 0$ is almost independent from the value of the chamber length L_c before the resulting flow approaches the bluff end-wall of the chamber, while this dependence increases significantly as L_c is further reduced. This is also consistent with the qualitative flow patterns in Fig. 3 as both the recirculation regions and resulting flow are changed for certain values of L_c depending on the configurations. Taken together, it can be concluded that the mean velocity field exhibits a strong dependence on the axial location of the resulting flow.

Figure 5 presents the evolution of the inverse mean axial velocity of the central resulting jet flow (U_e/U_c) as calculated on the equivalent axial coordinate from the jet origin

$$x^* = x_0 + (x - x_{mer}), \tag{1}$$

where x_{mer} denotes the distance between the throat and merging point and x_0 denotes the distance along the local axis of each jet between the pipe exit and merging point (see also the inset of Fig. 5). The cases with $\theta_j = 15°$ are not reported due to the absence of a resulting jet flow along the centerline of the chamber. However, the data for $L_c/D_c = 3$ and $\theta_j = 0°$ reported previously[10] for non-swirled jets are included as a reference, and also included are the free pipe jet data of Xu and Antonia[36] representing the unconfined single jet case. The axial coordinate is normalized by the equivalent jet exit diameter,

$$D_e = \sqrt{N_j} D_{pipe}, \tag{2}$$

where N_j denotes the number of jets and D_e is the diameter of an equivalent circular pipe with the same exit area as the four inlet pipes. Here the merging and stagnation points (P_{mer} and P_s) denote the most upstream and downstream of the resulting flow, respectively. It can be seen that, for all cases with a nonzero azimuthal angle ($\theta_j > 0°$), the decay of U_e/U_c along the

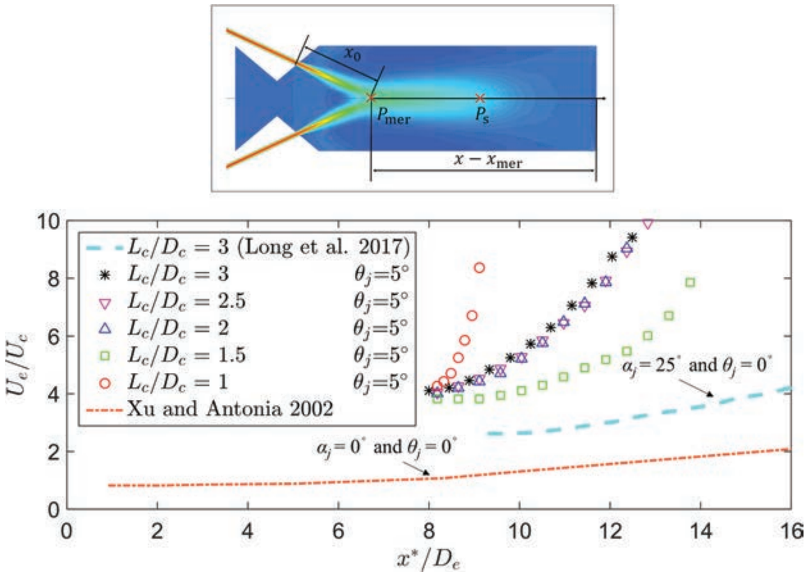

FIG. 5. Evolution of the inverse mean axial velocity of the central resulting jet flow (U_e/U_c) along the axis of the MIJCC for the case of $\alpha_j = 25°$ and $\theta_j = 5°$ for aspect ratios of L_c/D_c = 1–3. The equivalent axial coordinate, x^*, and the equivalent jet exit diameter, D_e, are expressed in Eqs. (1) and (2), respectively.

centerline of the chamber is significantly greater than the non-swirled jet ($\theta_j = 0°$) or single jet ($N_j = 1$) configurations within $8 \le x^*/D_e \le 16$, regardless of the value of L_c/D_c. This is due to the presence of θ_j that increases the "out-of-plane" motion from the inlet jets, which implies that the additional azimuthal angle of the multiple-jet configurations substantially increases the centerline velocity decay of the resulting flows.

Figure 5 also shows that, for the configurations with $\theta_j = 5°$, a decrease in L_c/D_c from 3 to 2 leads to a decrease of only 5% in the rate of decay, i.e., $\Delta(U_e/U_c)/\Delta(x^*/D_e)$, while a decrease in L_c/D_c from 2 to 1.5 leads to a decrease in the rate of decay by up to 40% at $x^*/D_e = 13$. The rate of centerline decay has long been used as a measure of rate at which the jet flow exchanges momentum with the surrounding flow.[37] Hence this step-change reduction at shorter chambers indicates a step change in the intensity of the ERZ. However, for the shortest chamber length considered here ($L_c/D_c = 1$), the rate of decay is the highest [$\Delta(U_e/U_c)/\Delta(x^*/D_e) \approx 4$], with $U_e/U_c \approx 8.5$ at $x^*/D_e \approx 9$. This is due to the insufficient space downstream from the merging point, which causes the distance between the merging and stagnation points to approach zero [$(x_{Ps} - x_{Pmer}) \approx 0$], implying that the resulting flow is almost absent. Hence, it can be concluded that the rate of decay of central resulting flow depends strongly on the distance between the merging and stagnation points—for the low-swirl configurations ($\alpha_j = 25°$ and $\theta_j = 5°$) considered here.

B. Turbulent flow fields

Figure 6 presents the evolution of the axial RMS (u') and radial RMS (v') velocities, normalized by the nozzle exit velocity (U_e), along the centerline of the MIJCC for all experimental cases. Note that the legends are identical to all cases with the same θ_j for all figures in the paper. For the $\theta_j = 5°$ cases [Figs. 6(a) and 6(b)], it can be seen that a decrease in L_c/D_c leads to a substantial decrease (≈20%) in both u'/U_e and v'/U_e, particularly where $L_c/D_c \le 1.5$. This suggests that the flow unsteadiness is substantially reduced as the chamber length is decreased. However, for the $\theta_j = 15°$ cases [Figs. 6(c) and 6(d)], both the magnitudes of u'/U_e and v'/U_e are almost independent from L_c for all aspect ratios investigated here, while the difference in the magnitude of u'/U_e and v'/U_e is typically within 10%. This weaker dependence of the centerline velocity fluctuations on L_c/D_c for $\theta_j = 15°$ than for $\theta_j = 5°$ provides further evidence of the reduced influence of the chamber aspect ratio on flow unsteadiness (e.g., precession) for higher azimuthal angles.

It is also worth noting that for both $\theta_j = 5°$ and $\theta_j = 15°$ configurations, a significant reduction in u'/Ue and an increase in v'/Ue were measured in the region where the resulting flow approaches the bluff end-wall (≈5% of the total length of L_c before the end-wall). This is most significant for the cases where $L_c/D_c \le 1.5$. That is, the impingement of the resulting flow on the bluff end-wall acts both to amplify the velocity fluctuations in the radial direction (v') and to inhibit the axial velocity fluctuations (u') within the impingement region.

The results in Figs. 4–6 show that both the mean and RMS flow-fields are typically independent from the value of L_c/D_c = 3. Hence, subsequent analyses are performed only for the range of $1 \le L_c/D_c \le 2.5$.

Figure 7 presents the radial profiles of the mean axial (U_x), axial RMS (u'), and radial RMS (v') velocities, normalized by the nozzle exit velocity (U_e), at the jet merging point for all experimental conditions. (The L_c/D_c = 3 case was not included here because the measurements are almost identical to the L_c/D_c = 2.5 case.) The results in Fig. 7(a) show that, for the $\theta_j = 5°$ cases, the value of U_x/U_e at the merging point is almost independent from the chamber length for $1 < L_c/D_c \le 2.5$. The peak mean velocity $(U_c/U_e)_{max}$ occurs on or near to the central axis, while the region of negative velocity is typically limited to $r/D_c \ge 0.3$ for all cases. This indicates that the radial extent of the ERZ does not change significantly with the value of L_c/D_c for $L_c/D_c > 1$. However, as L_c/D_c is decreased to 1, the magnitude of velocity within $r/D_c \ge 0.2$ increases by approximately 10% and the radial location of negative velocity extends to $r/D_c \ge 0.4$. This highlights the influence of the bluff end-wall on the flow field at and around the merging point for all cases.

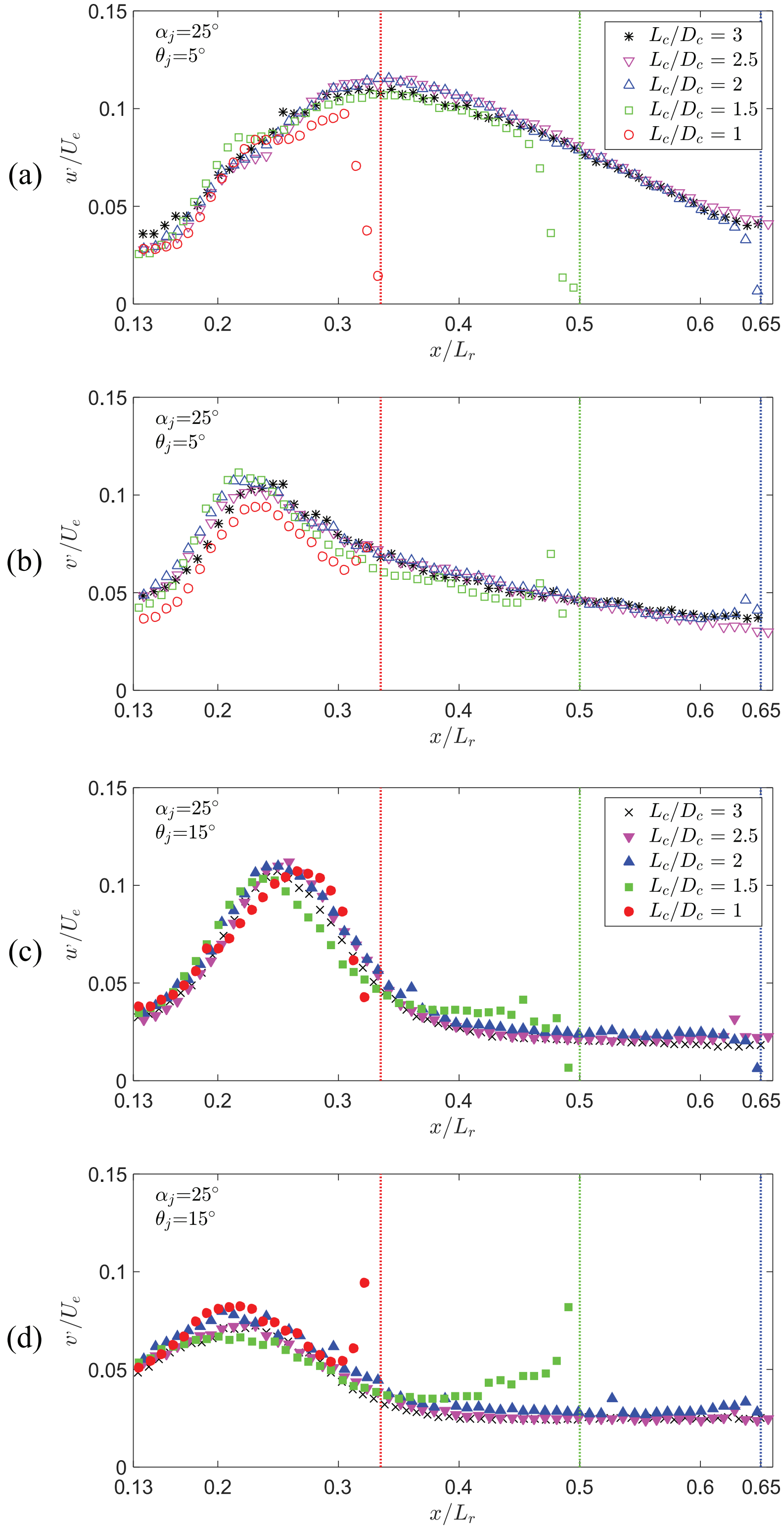

FIG. 6. Evolution of the axial RMS (u') and radial RMS (v') velocities, normalized by the nozzle exit velocity (U_e), along the centerline of the MIJCC for the cases of (a) and (b) α_j = 25° and θ_j = 5°, (c) and (d) α_j = 25° and θ_j = 15°, and for aspect ratios of L_c/D_c = 1–3. For clarity, only one in two data points is presented and the legends are identical to all cases with the same θ_j.

The results in Figs. 7(b) and 7(c) also show that a decrease in L_c/D_c leads to a maximum reduction of 20% in the value of u'/Ue, while the value of v'/Ue remains almost independent from the L_c/D_c. The location of $(u'/Ue)_{max}$, which corresponds well with the maximum value of the mean velocity gradient presented in Fig. 7(a), moves from $r/D_c \approx 0.16$ to $r/D_c \approx 0.09$ and its magnitude decreases from $(u'/Ue)_{max} \approx 0.12$ to ≈ 0.09 as L_c/D_c is decreased from 2.5 to 1. However, the value of $(v'/Ue)_{max}$ is approximately 0.08 at the central axis (r/D_c = 0) for all cases. This indicates that a decrease in L_c/D_c from 2.5 to 1 tends to inhibit the axial velocity fluctuation but not to influence significantly the radial velocity fluctuation at the merging point. As a large fluctuation of velocity is commonly associated with flow unsteadiness,[33] this provides further evidence that decreasing the aspect ratio tends to reduce the flow unsteadiness within the jet-interaction region for low-swirl configurations (α_j = 25° and θ_j = 5°).

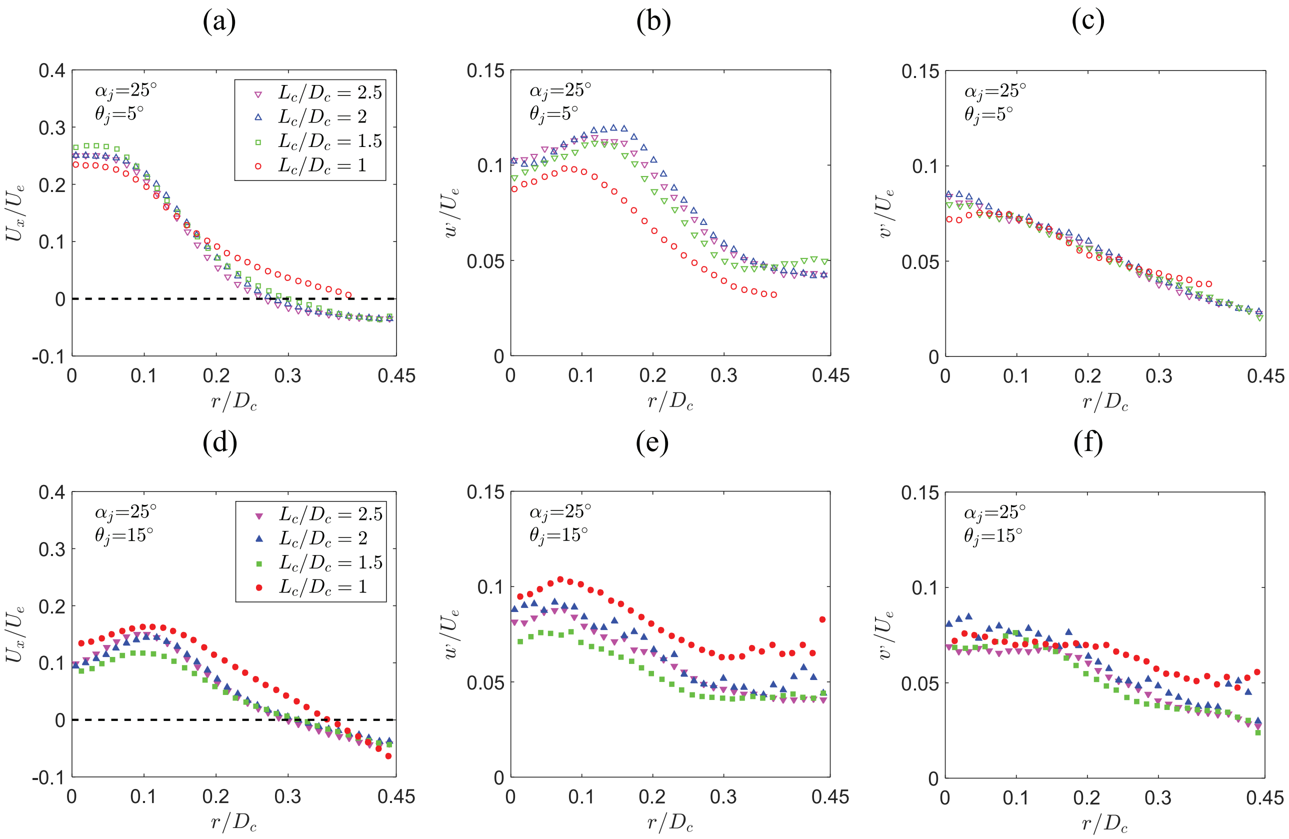

FIG. 7. Radial profiles of the mean axial (U_x), axial RMS (u'), and radial RMS (v') velocities, normalized by the nozzle exit velocity (U_e), at the jet merging point for the cases of (a)–(c) $\alpha_j = 25°$ and $\theta_j = 5°$, (d)–(f) $\alpha_j = 25°$ and $\theta_j = 15°$, and for aspect ratios of $L_c/D_c = 2.5$, 2, 1.5, and 1. Here D_c denotes the diameter of the MIJCC and the legends are identical to all cases with the same θ_j.

For the $\theta_j = 15°$ configurations, the velocity peak $(U_c/U_e)_{max}$ occurs at $r/D_c \approx 0.1$ for all cases [Fig. 7(d)]. It can also be seen that the mean axial velocity decreases slightly as L_c/D_c is decreased from 2.5 to 1.5, with a maximum 20% reduction in U_x/U_e at $r/D_c \approx 0.1$. However, the value of U_x/U_e increases significantly as L_c/D_c is further reduced to 1, and the maximum increase is around 70% within $r/D_c \geq 0.2$. The trend of an increased U_x/U_e for the case where L_c/D_c approaches 1 is possibly caused by the increased strength of the divergent resulting flow for $\theta_j = 15°$ cases, as shown qualitatively in Fig. 3.

The radial profiles of RMS velocities in Figs. 7(e) and 7(f) show that the effect of L_c/D_c on the velocity fluctuations is non-linear since both the values of u'/Ue and v'/Ue decrease as L_c/D_c is decreased from 2.5 to 1.5 and then increase as L_c/D_c is further decreased to 1. Interestingly, the CRZ is detected for $L_c/D_c \geq 1.5$, but not for $L_c/D_c = 1$ (see also Fig. 3). This suggests that the presence of a CRZ damps velocity fluctuations in the high-swirl configurations ($\theta_j = 15°$). Nevertheless, the case $L_c/D_c = 1$ has a different trend to the other cases in the mean and RMS velocity fields due to the absence of the central resulting jet flow for $\theta_j = 5°$ configurations or the CRZ region for $\theta_j = 15°$ configurations.

Overall, it can be concluded that a decrease in the aspect ratio L_c/D_c leads to a decrease in velocity fluctuations for most cases, although the effects are non-linear. That is, increasing L_c/D_c in this range tends to increase interaction with the wall, and hence the amplification of large-scale eddies in the flow.

Figure 8 presents the radial profiles of the ratio of axial and radial RMS velocities (u'/v') and the Reynolds shear stresses ($\langle uv\rangle/U^2{}_c$) at the merging point for all experimental conditions. For the configurations of $\theta_j = 5°$ [Fig. 8(a)], it can be seen that the value of u'/v' exhibits two peaks, one in the shear layer ($r/D_c \approx 0.15$), consistent with an unconfined single jet,[38] and the other in the near wall region ($r/D_c \approx 0.45$). These locally high values imply a high degree of anisotropy in these regions, consistent with an important role of large-scale turbulence. In addition, a decrease in L_c/D_c tends to reduce the value of u'/v' along the cylinder radius (r), with the most significant reduction occurring for $L_c/D_c = 1$. By contrast, for the configurations where $\theta_j = 15°$ [Fig. 8(b)], the value of u'/v' typically varies between 1.5 and 1 for all cases, so that the effect of L_c/D_c on u'/v' is relatively small. This indicates that, first, the variation of anisotropy at the merging point is more significant for $\theta_j = 5°$ than that for $\theta_j = 15°$, regardless of the value of L_c/D_c, and second, the influence of L_c/D_c on the anisotropy is more significant for the ERZ dominated regime ($\theta_j = 5°$) than that for the CRZ dominated regime ($\theta_j = 15°$).

Figures 8(c) and 8(d) also show that a decrease in L_c/D_c leads to a decrease in the Reynolds stresses at the merging point for both the $\theta_j = 5°$ and $\theta_j = 15°$ configurations, although it is most significant for $\theta_j = 5°$. This provides further evidence that reducing L_c/D_c reduces large-scale interactions between

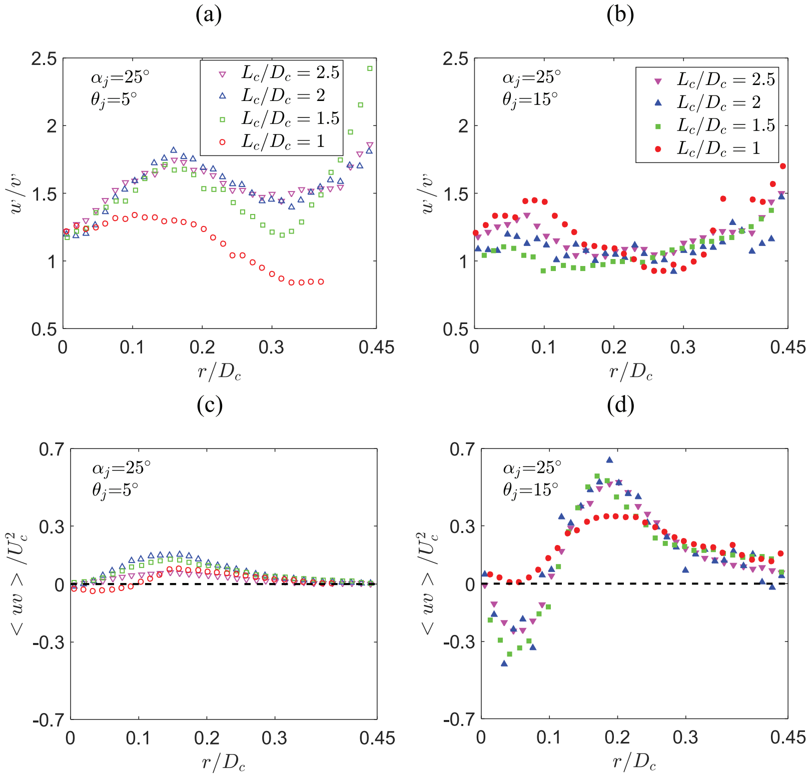

FIG. 8. Radial profiles of the ratio of axial and radial RMS velocities (u'/v') and the Reynolds shear stresses ($\langle uv\rangle/U^2{}_c$) at the merging point for the cases of (a) and (c) α_j = 25° and θ_j = 5°, (b) and (d) α_j = 25° and θ_j = 15°, and for aspect ratios of L_c/D_c = 2.5, 2, 1.5, and 1. Here D_c denotes the diameter of the MIJCC and the legends are identical to all cases with the same θ_j.

the jet and surrounding flow within the jet interaction region. However, the value of $\langle uv\rangle/U^2{}_c$ is typically greater for the higher-swirl cases than that for the low-swirl cases. That is, although the degree of anisotropy at the merging point is greater for $\theta_j = 5°$, the extent of large-scale flow motion at this point is greater for $\theta_j = 15°$ than that for $\theta_j = 5°$, regardless of the value of L_c/D_c. This evidence supports the finding that the interaction between multiple jets is stronger for high-swirl jet configurations.[39]

Figure 9 presents the integral length scale normalized by the nozzle diameter (L_u/D_{pipe}) along the centerline of the MIJCC for all experimental conditions. The integral length

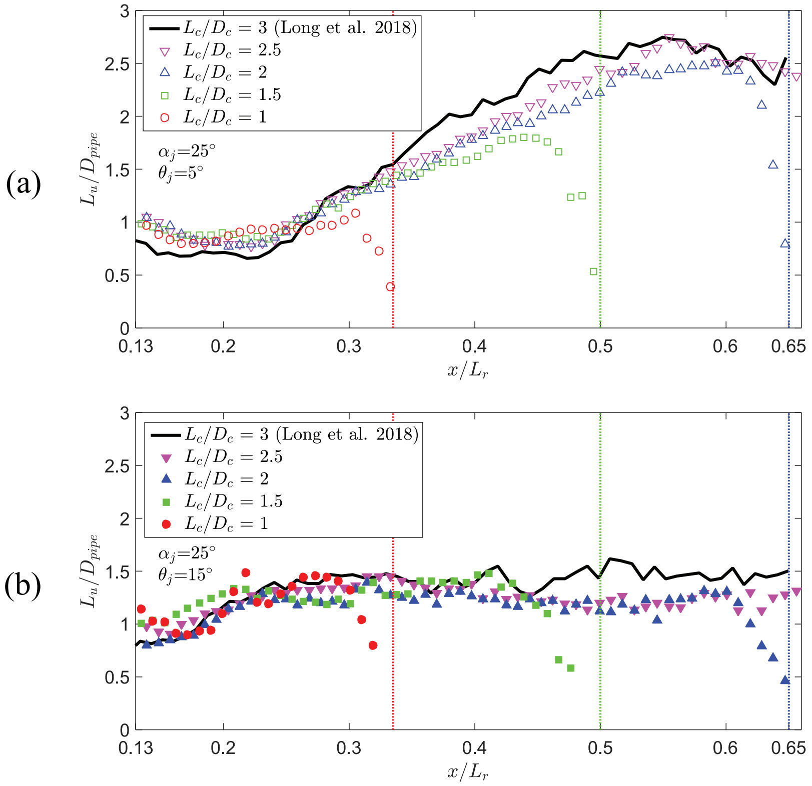

FIG. 9. Evolution of the integral length scale [see Eq. (3)] along the axis of the MIJCC device normalized by the nozzle diameter (D_{pipe}), as a function of the reference chamber length (L_r) for the cases of (a) α_j = 25° and θ_j = 5°, (b) α_j = 25° and θ_j = 15°, and for aspect ratios of L_c/D_c = 1–3. For clarity, only one in two data points is presented.

scale (L_u) is defined as

$$L_u = \int_0^{r_0} \langle u(x)u(x+r)\rangle \left\langle u^2 \right\rangle^{-1} dr, \tag{3}$$

where $u(x)$ denotes the fluctuating component of the axial velocity and r_0 corresponds to the first zero crossing of the cross-correlation function $\langle u(x)u(x+r)\rangle \left\langle u^2 \right\rangle^{-1}$, following Xu and Antonia.[36] The published data for the case of $L_c/D_c = 3$[11] are included for reference. The uncertainty associated with L_u was estimated to be less than 10% from a sensitivity study of the spatial resolution and literature data.[11,40] For the cases of $\theta_j = 5°$ [Fig. 9(a)], where the flow is characterized by a clear resulting central jet flow, it can be seen that, for all L_c/D_c, the value of L_u/D_{pipe} first decreases between $0.13 \leq x/L_r \leq 0.23$, which corresponds approximately to the region upstream from the merging point, before increasing approximately linearly for $x/L_r > 0.23$. This near linear increase in L_u/D_{pipe} with axial distance is consistent with free-jet measurements.[40] However, as L_c/D_c is decreased from 3 to 1, the slope and magnitude of L_u/D_{pipe} decrease so that a significant drop in L_u/D_{pipe} occurs at the end of the chamber (the bluff end-wall) for all cases. That is, a decrease in L_c/D_c tends to decrease the large-scale flow motion along the centerline of the chamber for $\theta_j = 5°$ configurations, consistent with the findings in Fig. 8. For the configurations of $\theta_j = 15°$ [Fig. 9(b)], the value of L_u/D_{pipe} increases linearly upstream from the stagnation point ($x/L_r \approx 0.3$) and then remains almost the same value along the axis of the chamber for all cases. However, the evolution of L_u/D_{pipe} is almost independent of L_c/D_c, although a drop in L_u/D_{pipe} is also observed at the end of the chamber due to the effect of the bluff end-wall. This finding, together with the evolution of u'/U_e and v'/U_e presented in Fig. 6, provides further evidence that the degree of large-scale flow oscillations tends to increase with L_c/D_c for cases where the swirl component is weak (here $\theta_j = 5°$).

C. Quantification of the recirculation rate

Figure 10 presents the effect of the chamber aspect ratio L_c/D_c on the recirculation rate (K_v) within the MIJCC configurations for all experimental conditions. The recirculation rate K_v is defined as

$$K_v = \dot{m}_{ent}/\dot{m}_{in}, \tag{4}$$

where

$$\dot{m}_{ent} = \int_0^{r} 2\pi r \rho U_{ent} dr \tag{5}$$

is the total mass flow rate of fluid entrained by all inlet jets transported upstream through a plane orthogonal to the axis at the plane x/L_c. Equation (5) was adapted from the calculation of the entrainment rate from the previous study of the jet,[41–43] where the entrainment velocity, U_{ent}, refers to the negative axial velocity ($U_x < 0$) within the chamber, while the positive axial velocity was excluded from the calculation. The symbol of $\dot{m}_{in}$ refers to the total inlet mass flow rate of fluid.

For the $\theta_j = 5°$ configurations [Fig. 10(a)], the results show that a single hump profile, approximately corresponding to the axial extent of the ERZ, occurs for all cases, while the location of peak K_v [$(K_v)_{max.ERZ}$] coincides well with the location of the vortex-core in the ERZ (x_{core} in Fig. 3). For $L_c/D_c = 2.5$–1.5, a decrease in L_c/D_c tends to decrease the value of K_v throughout the chamber, although $(K_v)_{max.ERZ}$ for all three cases remains approximately the same (occurring at $x/L_r = 0.38$). However, for $L_c/D_c = 1$, $(K_v)_{max.ERZ}$ increases significantly (by 25%) and its location moves further upstream to $x/L_r = 0.2$ due to the confinement effect caused by the chamber length. Hence, the axial profile of K_v is consistent for $L_c/D_c \geq 2$, while as L_c is further reduced to 1, both the value and distribution of K_v are strongly restricted by the reduced chamber length.

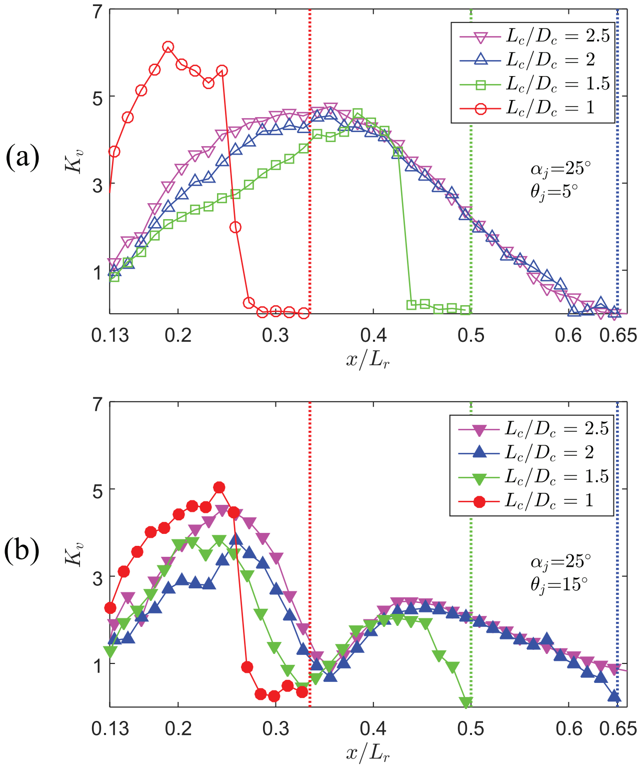

FIG. 10. Evolution of the recirculation rate ($K_v = \dot{m}_{ent}/\dot{m}_{in}$) along the axis of the MIJCC (x/L_r) for the configurations of (a) $\alpha_j = 25°$ and $\theta_j = 5°$, (b) $\alpha_j = 25°$ and $\theta_j = 15°$, and for aspect ratios of $L_c/D_c = 2.5$, 2, 1.5, and 1. For clarity, only one in three data points is presented.

For the $\theta_j = 15°$ configurations [Fig. 10(b)], it can be seen that a double-hump profile occurs for all cases in which both ERZ and CRZ are present (see Fig. 3). Furthermore, for each given case of L_c/D_c, the maximum value of K_v in ERZ [$(K_v)_{max.ERZ}$] is approximately 50% higher than that in CRZ [$(K_v)_{max.CRZ}$]. This implies that the circulation strength in ERZ is similarly stronger.[11] In addition, the maximum value of K_v is almost independent of L_c/D_c for both the ERZ and CRZ regions, although the axial extent where $K_v > 0$ is reduced by 50% for a decreased L_c/D_c.

The results in Fig. 10 also show that the value of $(K_v)_{max.ERZ} > 3$ for all cases considered here, regardless of L_c/D_c. This is an important finding for the development of practical combustion applications, particularly those employing combustion in the MILD (moderate or intense low-oxygen dilution) regime because it implies the presence of a large and uniform recirculation zone, which is important for the MILD combustion regime, suggesting strong potential for a quasi-homogeneous temperature.[28,30]

D. Effects of the chamber aspect ratio

Table IV presents a summary of the location of the jet merging point (x_{mer}/L_r), stagnation point (x_s/L_r), and the CRZ axial extent (x_{CRZ}/L_r) along the axis of the MIJCC for all chamber aspect ratios investigated in the present study. Here x_{CRZ} denotes the maximum axial location of the CRZ region. It can be seen from the table that all critical locations change significantly as the L_c/D_c is reduced.

Figure 11 presents the characteristic centerline length of (a) the stagnation point (Δx_s), (b) the CRZ region (Δx_{CRZ}), and (c) the ERZ region (Δx_{ERZ}), normalized by the diameter of the chamber (D_c), as a function of the aspect ratio L_c/D_c. As shown in the inset, we define $\Delta x_s = (L_c - x_s)$ as the distance between the stagnation point and the bluff end-wall, $\Delta x_{ERZ} = (x_s - x_{mer})$ refers to the distance between the merging and stagnation points, and $\Delta x_{CRZ} = (x_{CRZ} - x_s)$ denotes the distance between the stagnation and CRZ points. The data points for $L_c/D_c = 3$, which were measured from our previous study but not previously published, are also included. All measured data points are labelled with solid makers, while some "extrapolated" points, which are labelled with hollow markers, are extrapolated from the values in Table IV.

For Fig. 11(a), it can be seen that Δx_s increases linearly with the aspect ratio L_c/D_c in the range $1 \leq L_c/D_c \leq 3$ for the high-swirl cases ($\theta_j = 15°$) and $2 \leq L_c/D_c \leq 3$ for the low-swirl cases ($\theta_j = 5°$). For the latter case, the value of $\Delta x_s \approx 0$ occurs for $L_c/D_c \leq 2$, which suggests that $L_{c.crit}/D_c = 2$ is the critical chamber length where the bluff end-wall starts to significantly impact the ERZ and the resulting flow. Conversely, it can also be inferred that for $L_c > L_{c,crit}$, the chamber length does not significantly influence the ERZ within the cylindrical chamber. For the higher-swirl cases ($\theta_j = 15°$), the values of Δx_s are larger than the low-swirl cases due to the decreased axial extent of the ERZ. Hence, the value of $L_{c.crit}$ is approximately equal to D_c for these configurations ($L_{c.crit}/D_c = 1$).

The trends for Δx_{CRZ} in Fig. 11(b) are qualitatively similar to those for Δx_s. That is, a decrease in the aspect ratio L_c/D_c significantly decreases the value of $\Delta x_{CRZ}/D_c$ for both the $\theta_j = 5°$ and $\theta_j = 15°$ configurations. The value of $\Delta x_{CRZ}/D_c$ reduces from 0.45 at $L_c/D_c = 3$ to 0 at $L_c/D_c = 2$ for $\theta_j = 5°$ configurations, while for $\theta_j = 15°$ cases, the value of $\Delta x_{CRZ}/D_c$ decreases from 1.55 at $L_c/D_c = 3$ to 0 at $L_c/D_c = 1$. The value of $\Delta x_{CRZ}/D_c$ is important for quantifying the effect of L_c/D_c on the CRZ region since the critical value of $\Delta x_{CRZ.crit}/D_c = 0$ indicates the absence of the CRZ within the cylindrical chamber. Hence, a decrease in the value of L_c/D_c from 3 to 1 leads to a reduction in the size of the CRZ for both configurations,

TABLE IV. Normalized axial location of the jet merging and stagnation points, and the CRZ axial extent along the centerline of the MIJCC.

Experiment case no.	Configurations	Jet merging point (x_{mer}/L_r)	Stagnation point (x_s/L_r)	CRZ point (x_{CRZ}/L_r)
1	MIJCC-05-LD25	0.27	0.65	>0.65
2	MIJCC-05-LD20	0.27	0.65	N/A
3	MIJCC-05-LD15	0.27	0.50	N/A
4	MIJCC-05-LD10	0.27	0.33	N/A
5	MIJCC-15-LD25	0.21	0.29	>0.65
6	MIJCC-15-LD20	0.21	0.29	0.65
7	MIJCC-15-LD15	0.19	0.27	0.48
8	MIJCC-15-LD10	0.24	0.32	N/A
9*	MIJCC-05-LD30	0.27	0.65	>0.65
10*	MIJCC-15-LD30	0.21	0.28	>0.65

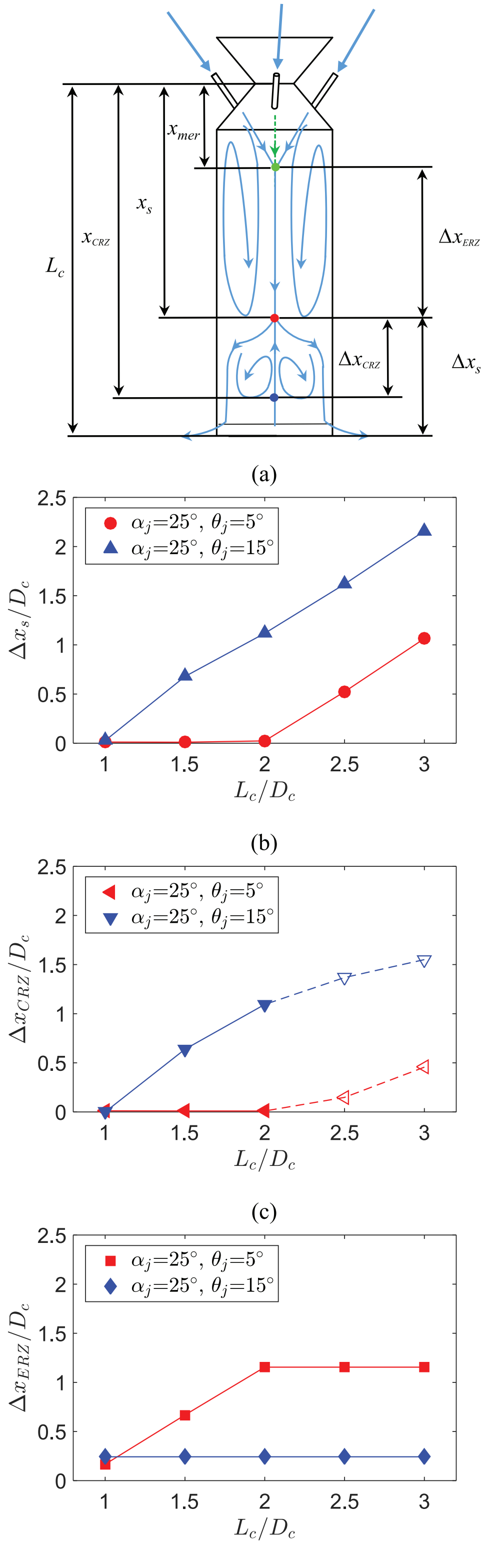

FIG. 11. Characteristic length of (a) the stagnation point (Δx_s), (b) the CRZ region (Δx_{CRZ}), and (c) the ERZ region (Δx_{ERZ}), normalized by the diameter of the chamber (D_c), as a function of the chamber aspect ratio L_c/D_c.

TABLE V. Definition of flow regimes and their key controlling parameters in the MIJCC configurations equipped with multiple jets for α_j = 25° and θ_j = 5°, 15°.

Flow regime		Controlling parameters	Resulting parameters	ERZ	CRZ	Resulting flow
Regime I	Decreasing L_c/D_c ↓	α_j and θ_j	$\Delta x_s/D_c > 0$ $\Delta x_{CRZ}/D_c > 0$ $\Delta x_{ERZ}/D_c > 0$	Yes	Yes	Yes
Regime II		α_j and θ_j L_c/D_c	$\Delta x_s/D_c = 0$ $\Delta x_{CRZ}/D_c = 0$ $\Delta x_{ERZ}/D_c > 0.2$	Yes	No	Yes
Regime III		α_j and θ_j L_c/D_c x_{mer}	$\Delta x_s/D_c = 0$ $\Delta x_{CRZ}/D_c = 0$ $\Delta x_{ERZ}/D_c \leq 0.2$	Yes	No	No

while the absence of the CRZ region occurs for $L_c/D_c \leq 2$ and 1 for θ_j = 5° and 15° configurations, respectively.

It can also be seen from Fig. 11(c) that for θ_j = 5° configurations, the value of $\Delta x_{ERZ}/D_c = 1.2$ for all cases where $L_c/D_c \geq 2$. This means that the bluff-end wall only impacts the CRZ and does not influence the ERZ. This, in turn, implies that the CRZ vortex is somewhat decoupled from the ERZ vortex for $L_c/D_c \geq 2$. In addition, the value of $\Delta x_{ERZ}/D_c$ significantly decreases from 1.2 to 0.1 as L_c/D_c is further decreased to 1. By contrast, the value of $\Delta x_{ERZ}/D_c \approx 0.3$ is almost independent of L_c/D_c within the range of $1 \leq L_c/D_c \leq 3$ for θ_j = 15° configurations. This is because the bluff end-wall only impacts the upstream ERZ for $L_c/D_c \leq 1$ due to the shorter axial extent of the ERZ for θ_j = 15°. The parameter of $\Delta x_{ERZ}/D_c$ quantifies the effect of the aspect ratio L_c/D_c on both the ERZ and the jet merging point, which means that for the cases where $\Delta x_{ERZ}/D_c$ approaches 0, the inlet-jets impinge on the bluff end-wall instead of generating a resulting flow. Hence, the value of L_c/D_c significantly influences the interaction of multiple jets for $L_c/D_c \leq 1$, for all values of θ_j.

It is also worth noting that, for the values of L_c/D_c considered here, a reduction in L_c/D_c leads to a significant decrease in the difference between the values of $\Delta x_s/D_c$, $\Delta x_{ERZ}/D_c$, and $\Delta x_{CRZ}/D_c$ for both the θ_j = 5° and θ_j = 15° configurations. For example, the difference in $\Delta x_s/D_c$ between θ_j = 5° and θ_j = 15° reduces from $\Delta(\Delta x_s/D_c) = 1.1$ at $L_c/D_c = 3$ to $\Delta(\Delta x_s/D_c) = 0$ at $L_c/D_c = 1$. This, in turn, suggests that as the aspect ratio L_c/D_c is reduced from 3 to 1, the significance of L_c/D_c on the larger-scale recirculation zones within the MIJCC increases, while the significance of θ_j decreases substantially.

E. Identification of the key controlling parameters for flow regimes

Table V summarizes the key parameters for controlling the three distinctive flow regimes that have been identified within the rotationally symmetric MIJCC configurations for a fixed value of α_j = 25° but with θ_j = 5° and 15°, and a decrease value of the chamber aspect ratio L_c/D_c from 3 to 1, using both the flow visualization and quantitative data. The three flow regimes are shown schematically in Fig. 12, and the detailed description are presented in Secs. III E 1–III E 3.

1. Regime I: External and central recirculation zones

Regime I is characterized by the presence of both external and central recirculation zones [ERZ (red dashed box) and CRZ (purple dotted box)] within the MIJCC. The relative significance of the ERZ and CRZ depends strongly on the value of jet angles (α_j and θ_j), which is consistent with our previous work,[10,11] while the aspect ratio L_c/D_c has a negligible influence on the large-scale flow structure in this regime.

2. Regime II: External recirculation zone with a resulting flow

Regime II is characterized by the presence of a dominant ERZ generated from the resulting flow within the MIJCC. The effect of the aspect ratio L_c/D_c significantly reduces the position and strength of the ERZ due to the increased confinement

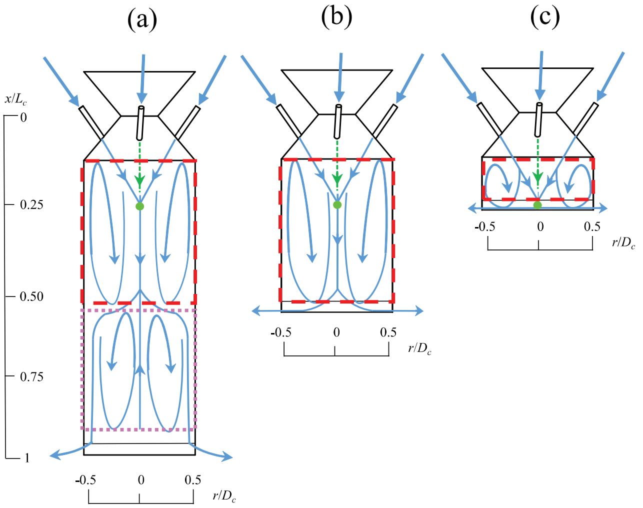

FIG. 12. Schematic diagrams of the three distinctive flow regimes that have been identified within the MIJCC configurations for aspect ratios of L_c/D_c = 1–3. (a) Regime I: External and central recirculation zones. (b) Regime II: External recirculation zone with a resulting flow. (c) Regime III: External recirculation zone with no resulting flow.

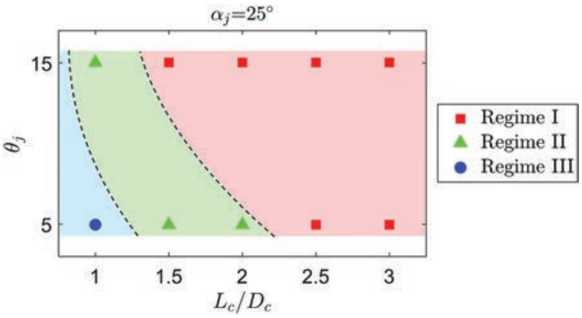

FIG. 13. Map of the three dominant flow regimes that have been identified within the MIJCC configurations for the jet inclination angle α_j = 25° and two jet azimuthal angles θ_j = 5° and 15°, and for chamber aspect ratios L_c/D_c = 1–3.

caused by the bluff end-wall. The influence of jet angles (α_j and θ_j) remains significant in this regime, although it is not as prominent as that in Regime I.

3. *Regime III: External recirculation zone with no resulting flow*

Regime III is characterized by the presence of dominant ERZ generated from the multiple inlet-jets, which runs the entire chamber of the MIJCC. Owing to the significantly reduced value in L_c/D_c, the inlet-jets have insufficient space to generate a resulting flow downstream from the merging point. Therefore, the size of the ERZ is further reduced and the strength of the ERZ is the strongest.

Figure 13 presents a regime map as a function of the chamber aspect ratio L_c/D_c and jet azimuthal angles (θ_j) for the MIJCC configurations of α_j = 25°. It can be seen that the transition between each regime occurs for $L_c/D_c \approx 2$ and 1 for θ_j = 5° configurations, and $L_c/D_c \approx 1$ and <1 for θ_j = 15° configurations. This implies that a higher value of θ_j reduces the critical value of L_c/D_c. This is because a higher value in θ_j results in less impingement among inlet-jets, a weaker resulting flow, and a higher swirl, which in turn decreases the axial extent of the ERZ and CRZ. Hence, it can be concluded that, for both the low-swirl (θ_j = 5°) and high-swirl (θ_j = 15°) configurations, the flow patterns are strongly controlled by the combination of the jet azimuthal angle (θ_j) and the chamber aspect ratio (L_c/D_c), with the significance of L_c/D_c increases as L_c/D_c decreases.

IV. CONCLUSIONS

New quantitative information has been provided on the iso-thermal flow field within a cylindrical chamber featuring multiple jets with an inclination angle α_j = 25° and two azimuthal angles θ_j = 5° and 15° for a range of chamber aspect ratios (L_c/D_c). Three distinctive flow regimes were identified within the Multiple Impinging Jet in a Cylindrical Chamber (MIJCC) as follows:

a. Regime I ($L_c/D_c > 2$ for θ_j = 5° or $L_c/D_c > 1$ for θ_j = 15°): External and central recirculation zones.
b. Regime II ($L_c/D_c > 1$ for θ_j = 5° or $L_c/D_c = 1$ for θ_j = 15°): External recirculation zone with a distinctive resulting flow.
c. Regime III ($L_c/D_c \leq 1$ for θ_j = 5° or $L_c/D_c < 1$ for θ_j = 15°): External recirculation zone with no resulting flow.

The key findings of the study are as follows:

1. The presence of each flow regime is strongly controlled by the combination of the jet angles (α_j and θ_j) and the chamber aspect ratio (L_c/D_c), with the significance of L_c/D_c increases as the value of L_c/D_c is decreased from 3 to 1.
2. The flow field within the ERZ immediately downstream from the jet merging point in Regime I is approximately independent of the length of the cavity L_c. However, in Regimes II and III, the characteristics of the ERZ depend strongly on L_c.
3. For $\theta_j > 0°$ cases, the decay of the central resulting flow downstream from the jet merging point is significantly greater than for $\theta_j = 0°$ (single jet or multiple jets). The value of mean axial velocity (U_c) along the axis of the chamber was found to increase by approximately 40% from Regime I to Regime II, while it decreases significantly (by 50%) for Regime III. This indicates that the effect of the aspect ratio L_c/D_c depends strongly on the presence or absence of the resulting flow downstream from the merging point.
4. The significance of the large-scale oscillations (e.g., jet precession) and the velocity fluctuations (u' and v') was found to increase with the chamber aspect ratio L_c/D_c for those configurations where the ERZ is dominant (θ_j = 5°). However, the influence of L_c/D_c on flow unsteadiness was found to be relatively small for those configurations generating a dominant CRZ (θ_j = 15°). This is evidenced by a higher value of Reynolds shear stress ($\langle uv \rangle / U^2{}_c$) for all L_c/D_c cases at the merging point for θ_j = 15° than for θ_j = 5°.
5. The large-scale flow motion corresponding to the integral length scale (L_u) was found to be inhibited as L_c/D_c is decreased for the case where a swirl is relatively weak (θ_j = 5°), while it is almost independent from L_c/D_c for higher-swirl cases (θ_j = 15°). This indicates a reduced influence of the chamber aspect ratio on the turbulent velocity field for θ_j = 15° cases.
6. The value of the recirculation rate (K_v) was found to increase by 25% as L_c/D_c is reduced from 3 to 1 (Regime I to Regime III), although the axial extent of K_v reduces by 50%. The value of K_v exceeds 3 for all cases, which has been found by others to be an important indicator for the avoidance of combustion reactants impinging on the walls and also maintaining a relatively high recirculation rate ($K_v \geq 3$).

ACKNOWLEDGMENTS

We acknowledge the support of the Australian Research Council, FCT Combustion Pty. Ltd., and Vast Solar Pty. Ltd. through the ARC Linkage Grant No. LP110200060. Mr. Shen Long acknowledges the financial support of the Australian Government Research Training Program. Finally, we gratefully acknowledge the anonymous reviewers who provided constructive feedback to strengthen the paper.

[1] E. Koepf, W. Villasmil, and A. Meier, "High temperature flow visualization and aerodynamic window protection of a 100-kWth solar thermochemical receiver-reactor for ZnO dissociation," Energy Procedia **69**, 1780 (2015).

[2] G. Cox, "Multiple jet correlations for gas turbine engine combustor design," J. Eng. Power **98**, 265 (1976).

[3] T. Chammem, H. Mhiri, and O. Vauquelin, "Experimental and computational investigation of Reynolds number effect on the longitudinal ventilation in large enclosure of twin inclined jets," Build. Environ. **67**, 87 (2013).

[4] T. Boushaki and J.-C. Sautet, "Characteristics of flow from an oxy-fuel burner with separated jets: Influence of jet injection angle," Exp. Fluids **48**, 1095 (2010).

[5] H. Becker and B. Booth, "Mixing in the interaction zone of two free jets," AIChE J. **21**, 949 (1975).

[6] J. A. Fitzgerald and S. V. Garimella, "A study of the flow field of a confined and submerged impinging jet," Int. J. Heat Mass Transfer **41**, 1025 (1998).

[7] R. C. Deo, J. Mi, and G. J. Nathan, "The influence of Reynolds number on a plane jet," Phys. Fluids **20**, 075108 (2008).

[8] G. J. Nathan, D. Battye, and P. Ashman, "Economic evaluation of a novel fuel-saver hybrid combining a solar receiver with a combustor for a solar power tower," Appl. Energy **113**, 1235 (2014).

[9] J. H. Lim, A. Chinnici, B. B. Dally, and G. J. Nathan, "Assessment of the potential benefits and constraints of a hybrid solar receiver and combustor operated in the MILD combustion regime," Energy **116**(Part 1), 735 (2016).

[10] S. Long, T. C. W. Lau, A. Chinnici, Z. F. Tian, B. B. Dally, and G. J. Nathan, "Experimental and numerical investigation of the iso-thermal flow characteristics within a cylindrical chamber with multiple planar-symmetric impinging jets," Phys. Fluids **29**, 105111 (2017).

[11] S. Long, T. C. W. Lau, A. Chinnici, Z. F. Tian, B. B. Dally, and G. J. Nathan, "Iso-thermal flow characteristics of rotationally symmetric jets generating a swirl within a cylindrical chamber," Phys. Fluids **30**, 055110 (2018).

[12] J. H. Lim, G. J. Nathan, E. Hu, and B. B. Dally, "Analytical assessment of a novel hybrid solar tubular receiver and combustor," Appl. Energy **162**, 298 (2016).

[13] E. Tanaka, "The interference of two-dimensional parallel jets: 1st report, experiments on dual jet," Bull. JSME **13**, 272 (1970).

[14] E. Tanaka, "The interference of two-dimensional parallel jets: 2nd report, experiments on the combined flow of dual jet," Bull. JSME **17**, 920 (1974).

[15] E. Tanaka and S. Nakata, "The interference of two-dimensional parallel jets: 3rd report, the region near the nozzles in triple jets," Bull. JSME **18**, 1134 (1975).

[16] Z. Gao, J. Han, Y. Xu, Y. Bao, and Z. Li, "Particle image velocimetry (PIV) investigation of flow characteristics in confined impinging jet reactors," Ind. Eng. Chem. Res. **52**, 11779 (2013).

[17] T. Guo, M. J. Rau, P. P. Vlachos, and S. V. Garimella, "Axisymmetric wall jet development in confined jet impingement," Phys. Fluids **29**, 025102 (2017).

[18] S. Beltaos and N. Rajaratnam, "Impingement of axisymmetric developing jets," J. Hydraul. Res. **15**, 311 (1977).

[19] G. M. Carlomagno and A. Ianiro, "Thermo-fluid-dynamics of submerged jets impinging at short nozzle-to-plate distance: A review," Exp. Therm. Fluid Sci. **58**, 15 (2014).

[20] Y. Varol and H. F. Oztop, "Buoyancy induced heat transfer and fluid flow inside a tilted wavy solar collector," Build. Environ. **42**, 2062 (2007).

[21] D. Rockwell and E. Naudascher, "Self-sustaining oscillations of flow past cavities," J. Fluids Eng. **100**, 152 (1978).

[22] V. Prasad and F. A. Kulacki, "Convective heat transfer in a rectangular porous cavity—Effect of aspect ratio on flow structure and heat transfer," J. Heat Transfer **106**, 158 (1984).

[23] G. K. Morris and S. V. Garimella, "Orifice and impingement flow fields in confined jet impingement," J. Electron. Packag. **120**, 68 (1998).

[24] G. Morris, S. Garimella, and J. Fitzgerald, "Flow-field prediction in submerged and confined jet impingement using the Reynolds stress model," J. Electron. Packag. **121**, 255 (1999).

[25] S. V. Garimella and R. Rice, "Confined and submerged liquid jet impingement heat transfer," J. Heat Transfer **117**, 871 (1995).

[26] S. A. Al-Sanea, M. F. Zedan, and M. B. Al-Harbi, "Effect of supply Reynolds number and room aspect ratio on flow and ceiling heat-transfer coefficient for mixing ventilation," Int. J. Therm. Sci. **54**, 176 (2012).

[27] Y.-H. Kao, S. B. Tambe, and S.-M. Jeng, "Effect of chamber length with converging exhaust on swirling flow field characteristics of a counter-rotating radial-radial swirler," in *ASME Turbo Expo 2013: Turbine Technical Conference and Exposition* (American Society of Mechanical Engineers, 2013), p. V01BT04A026.

[28] J. Wünning and J. Wünning, "Flameless oxidation to reduce thermal NO-formation," Prog. Energy Combust. Sci. **23**, 81 (1997).

[29] J. Mi, F. Wang, P. Li, and B. Dally, "Modified vitiation in a moderate or intense low-oxygen dilution (MILD) combustion furnace," Energy Fuels **26**, 265 (2011).

[30] G. Szegö, B. Dally, and G. Nathan, "Operational characteristics of a parallel jet MILD combustion burner system," Combust. Flame **156**, 429 (2009).

[31] J. Nikuradse, "Gesetzmäßigkeiten der turbulenten Strömung in glatten Rohren," Forsch. Geb. Ingenieurwes. **4**, 44 (1933).

[32] N. Grosjean, L. Graftieaux, M. Michard, W. Hübner, C. Tropea, and J. Volkert, "Combining LDA and PIV for turbulence measurements in unsteady swirling flows," Meas. Sci. Technol. **8**, 1523 (1997).

[33] N. Syred, "A review of oscillation mechanisms and the role of the precessing vortex core (PVC) in swirl combustion systems," Prog. Energy Combust. Sci. **32**, 93 (2006).

[34] Y. Liu, M. G. Olsen, and R. O. Fox, "Turbulence in a microscale planar confined impinging-jets reactor," Lab Chip **9**, 1110 (2009).

[35] L. Chua and A. Lua, "Measurements of a confined jet," Phys. Fluids **10**, 3137 (1998).

[36] G. Xu and R. Antonia, "Effect of different initial conditions on a turbulent round free jet," Exp. Fluids **33**, 677 (2002).

[37] G. J. Nathan, J. Mi, Z. T. Alwahabi, G. J. R. Newbold, and D. S. Nobes, "Impacts of a jet's exit flow pattern on mixing and combustion performance," Prog. Energy Combust. Sci. **32**, 496 (2006).

[38] T. C. Lau and G. J. Nathan, "The effect of Stokes number on particle velocity and concentration distributions in a well-characterised, turbulent, co-flowing two-phase jet," J. Fluid Mech. **809**, 72 (2016).

[39] M. Vanierschot and E. Van den Bulck, "Influence of swirl on the initial merging zone of a turbulent annular jet," Phys. Fluids **20**, 105104 (2008).

[40] J. Mi and G. J. Nathan, "Statistical properties of turbulent free jets issuing from nine differently-shaped nozzles," Flow, Turbul. Combust. **84**, 583 (2010).

[41] S. Park and H. Shin, "Measurements of entrainment characteristics of swirling jets," Int. J. Heat Mass Transfer **36**, 4009 (1993).

[42] J. Panda and D. McLaughlin, "Experiments on the instabilities of a swirling jet," Phys. Fluids **6**, 263 (1994).

[43] M. Amielh, T. Djeridane, F. Anselmet, and L. Fulachier, "Velocity near-field of variable density turbulent jets," Int. J. Heat Mass Transfer **39**, 2149 (1996).

Chapter 7

Characteristics of Swirling and Precessing Flows generated by Multiple Confined Jets

Statement of Authorship

Title of Paper	Characteristics of swirling and precessing flows generated by multiple confined jets
Publication Status	☐ Published ☐ Accepted for Publication ☑ Submitted for Publication ☐ Unpublished and Unsubmitted work written in manuscript style
Publication Details	Long, S., Lau, T.C., Chinnici, A., Tian, Z.F., Dally, B.B. and Nathan, G.J., 2019. Characteristics of swirling and precessing flows generated by multiple confined jets. Physics of Fluids, (submitted January 2019).

Principal Author

Name of Principal Author (Candidate)	Shen Long		
Contribution to the Paper	Conducted literature review, collected all experimental data, performed data processing and analysis, wrote manuscript and acted as corresponding author.		
Overall percentage (%)	65		
Certification:	This paper reports on original research I conducted during the period of my Higher Degree by Research candidature and is not subject to any obligations or contractual agreements with a third party that would constrain its inclusion in this thesis. I am the primary author of this paper.		
Signature		Date	07/01/2019

Co-Author Contributions

By signing the Statement of Authorship, each author certifies that:

i. the candidate's stated contribution to the publication is accurate (as detailed above);

ii. permission is granted for the candidate in include the publication in the thesis; and

iii. the sum of all co-author contributions is equal to 100% less the candidate's stated contribution.

Name of Co-Author	Timothy Lau		
Contribution to the Paper	Supervised the experiments, helped in data interpreting and edited manuscript.		
Signature		Date	7/01/2019

Name of Co-Author	Alfonso Chinnici		
Contribution to the Paper	Helped to develop the work and helped in data interpreting.		
Signature		Date	07/01/19

Name of Co-Author	Zhao Feng Tian		
Contribution to the Paper	Supervised the development of work and helped in data interpreting.		
Signature	[redacted]	Date	07/01/2019

Name of Co-Author	Bassam Dally		
Contribution to the Paper	Supervised the development of work, provided comments and edited manuscript.		
Signature	[redacted]	Date	7-1-19

Name of Co-Author	Graham 'Gus' Nathan		
Contribution to the Paper	Supervised the development of work, helped in data interpreting, provided comments and edited manuscript.		
Signature	[redacted]	Date	7/1/19.

Physics of Fluids ARTICLE scitation.org/journal/phf

Characteristics of swirling and precessing flows generated by multiple confined jets

Cite as: Phys. Fluids 31, 055102 (2019); doi: 10.1063/1.5089904
Submitted: 23 January 2019 • Accepted: 13 April 2019 •
Published Online: 3 May 2019

Shen Long,[a] Timothy C. W. Lau, Alfonso Chinnici, Zhao Feng Tian, Bassam B. Dally, and Graham J. Nathan

AFFILIATIONS

Centre for Energy Technology, School of Mechanical Engineering, The University of Adelaide, Adelaide, South Australia 5005, Australia

[a] Author to whom correspondence should be addressed: shen.long@adelaide.edu.au

ABSTRACT

An experimental study is reported of the interaction between multiple isothermal jets within a cylindrical chamber under conditions relevant to a wide range of engineering applications, including the confined swirl combustors, industrial mixers, and concentrated solar thermal devices. The particle image velocimetry technique was used to investigate the swirling and precessing flows generated with four rotationally symmetric inlet pipes at a fixed nozzle Reynolds number of $Re_D = 10\,500$ for two configurations of swirl angle (5° and 15°) and two alternative tilt angles (25° and 45°). The measurements reveal three distinctive rotational flow patterns within the external recirculation zone (ERZ) and the central recirculation zone (CRZ) for these configurations. It was found that the mean and root-mean-square flow characteristics of the swirl within the chamber depend strongly on the relative significance of the ERZ and CRZ, with the swirling velocity being higher in the CRZ than that in the ERZ. A precessing vortex core was identified for all experimental conditions considered here, although its significance was less for the cases with a dominant CRZ.

I. INTRODUCTION

Devices that utilize multiple-jets within a confined environment are commonly used in a wide range of scientific and industrial applications, such as gas turbine engines,[1] solar cavity receivers,[2] separated-jet combustors,[3] and ventilation systems.[4] Furthermore, the details of the flow-field within them can have a significant influence on their system performance and thermal efficiency. However, despite their importance, the internal flow within these systems has not been well characterized due to their greater complexity relative to a single round free jet.[5] Recently, a series of investigations has provided new details of these flows,[6–8] such as their large-scale flow regimes and recirculation rates. Nevertheless, some important characteristics of the swirling flow configurations, notably of the presence of any precessing vortex core (PVC)[9] within them, are still not fully understood. Hence, the present investigation aims to address key gaps in understanding of these classes of flow through detailed measurements of the flow velocity within a Multiple Impinging Jets in a Cylindrical Chamber (MIJCC), which has geometrical relevance to the Hybrid Solar Receiver Combustor (HSRC) under development at the University of Adelaide.[6–8,10–12]

While a range of configurations of the MIJCC are available, one of the most common is that which employs rotationally symmetric nozzles configured in an annular ring aligned with an inclination angle (α_j) relative to the axis of the cavity and/or at an azimuthal angle (θ_j) to the axis of the burner. This configuration generates a swirling flow within the main cavity. Previous studies of the flow-field within the MIJCC found that the two angles that characterize the jet's orientation (α_j and θ_j) and the chamber aspect ratio (L_c/D_c, where L_c refers to the chamber length and D_c is the chamber diameter) have a controlling influence on the mean and turbulent flow-fields.[6,7] However, while these studies provide useful information, they are limited to the velocity data within the axial plane of the main chamber (across the chamber axis). That is, no quantitative data are available of the tangential velocity (U_θ) within the radial planes (orthogonal to the chamber axis) despite the swirling component typically having the largest magnitude in high-swirl flows.[13–15] Additionally, no comprehensive data set of velocity measurements suitable for the development of computational models is presently available for the MIJCC and relevant configurations.[16] Hence, the overall aim of the present study is to provide new quantitative

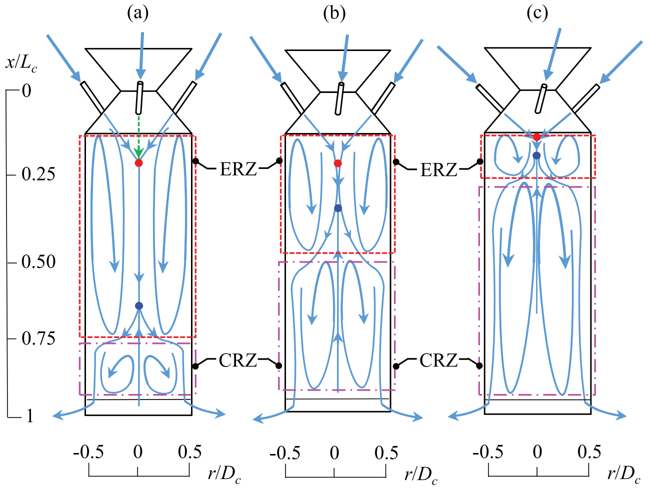

FIG. 1. Schematic diagrams of the three dominant flow regimes within the rotationally symmetric MIJCC configurations, showing the eternal and central recirculation zones (CRZ and ERZ). (a) Regime I, (b) Regime II, and (c) Regime III. Adapted from Ref. 7.

understanding of the flow regimes within a cylindrical chamber with multiple interacting jets through detailed planar measurements of the flow velocity in both the axial and tangential directions.

Previous investigations revealed a strong influence of the nozzle angles on the flow characteristics of multiple confined jets.[3,4,6,7,14,15,17,18] It has been found that the impingement of inclined jets ($\alpha_j > 0^{\circ}$) generates a merged flow downstream from the jet merging point (P_{mer}), termed the "resulting jet," together with a reverse flow upstream from this, termed the "upstream reverse flow."[4] It has also been found that an increase in nozzle inclination angle α_j can significantly increase the turbulence intensity and mixing efficiency within the jet merging region.[3] Importantly, the Particle Image Velocimetry (PIV) measurements of Long *et al.*[7] identified three distinctive flow regimes generated with the combination of α_j and θ_j for multiple confined jets (see Fig. 1), which are as follows:

- Regime I: a dominant external recirculation zone (ERZ) surrounding a small central recirculation zone (CRZ),
- Regime II: an upstream ERZ that is of similar extent to the downstream CRZ, and
- Regime III: a dominant CRZ downstream from a small upstream ERZ.

Long *et al.*[7] characterized the flow regimes by the relative size and position of the ERZ and CRZ within a cylindrical chamber and assessed their dependence on the geometric configuration of the nozzle and chamber. They found that for a given value of α_j ($25^{\circ} \leq \alpha_j \leq 45^{\circ}$), an increase in θ_j from 5° to 15° significantly increases the axial extent of the CRZ and reduces the size of the ERZ, leading to the transition from Regime I to Regime III. However, since that study only measured the velocity data in the axial plane, the tangential velocity and its corresponding swirling flow within the ERZ and CRZ remain unknown. This gap is significant because the strength of swirl within the large-scale recirculation zone is crucial for achieving desirable mixing and flow stabilization for relevant configurations such as vortex combustors,[19,20] cyclone reactors,[21] and solar thermal devices.[22,23] Hence, there is a need for reliable, comprehensive, and sufficient data under well-defined, consistent inflow and boundary conditions to fully characterize the swirl within the ERZ and CRZ generated by a range of α_j and θ_j.

Flow unsteadiness has been widely investigated for swirling annular jet configurations.[9,18,24–31] One of the key flow features is the precessing vortex core (PVC) within the recirculation zone, which has been identified for a wide range of vortex applications.[27,29,30,32] The PVC is a large-scale coherent and time-dependent flow structure embedded within a vortex, which is defined as the precession of the vortex-core relative to the geometric axis of an axisymmetric device, as described in the detailed review by Syred.[9] Their study showed that the PVC can significantly influence flow behavior, mixing performance, and combustion efficiency for vortex devices such as cyclones and swirl burners. Previous investigations revealed that

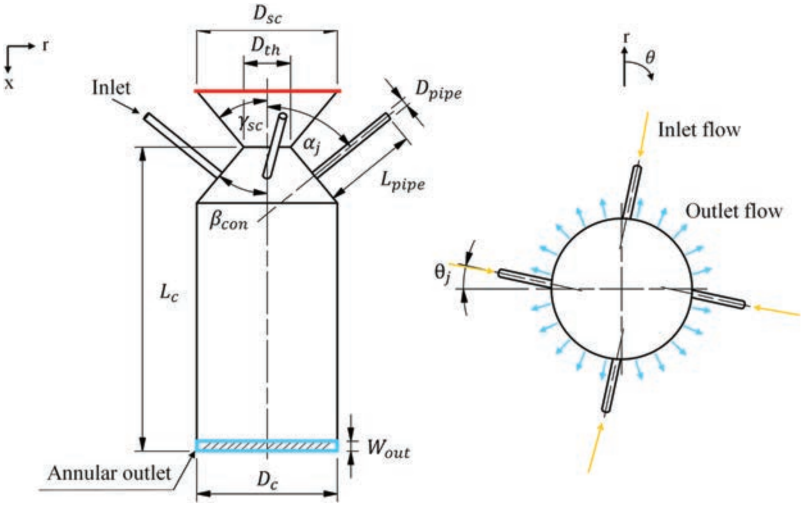

FIG. 2. Schematic diagram of the Multiple Impinging Jets in a Cylindrical Chamber (MIJCC) configurations investigated here, showing the key geometric features from the axial cross section (left) and a radial cross section (right). Here, the plane of the movable flap and that of the annular outlet are highlighted with the red line and blue enclosure, respectively.

TABLE I. Values of the geometric parameters of the MIJCC (see Fig. 2) that have been investigated in the present study.

Dimensions	Description	Value
D_c	Chamber diameter (mm)	74
D_{sc}	Diameter of the secondary concentrator (mm)	74
D_{th}	Throat diameter (mm)	24.6
D_{pipe}	Inlet pipe diameter (mm)	3.35
L_c	Chamber length (mm)	225
L_{pipe}	Inlet pipe length (mm)	150
W_{out}	Annular outlet gap (mm)	3
β_{con}	Conical expansion angle (deg)	40
γ_{sc}	Angle of the secondary concentrator (deg)	40

the presence of the PVC depends strongly on the geometric confinement,[33] recirculation zone,[34] and thermal conditions.[28,35] Consistent with this, our previous PIV measurements showed that the strong interaction between multiple-jets tends to amplify flow precession and oscillation,[6,7] although this has not yet been quantified. However, while the dynamics of the PVC in a swirling or single jet has been widely documented,[9] none of the previous investigations provided a comprehensive understanding of the influence of the multiple confined jets on the PVC so that the dependence of the PVC on large-scale recirculation zones generated by multiple-jets remains unclear. Hence, there is also a need to better understand the characteristics of the PVC generated by multiple jets within a confined environment.

In light of the needs identified above, the overall objective of the present study is to provide new understanding of the swirling and precessing flows generated within the MIJCC. The specific aims are as follows: (a) to provide a quantitative description of the mean and root-mean-square (rms) flow-fields in both the axial and tangential directions for multiple confined jets, (b) to identify the characteristics of swirl within the ERZ and CRZ generated by a confined chamber with multiple-jets, and (c) to characterize the dependence of the precessing vortex core (PVC) on the configuration of the four confined jets.

II. METHODOLOGY

A. Configurations selected in the present study

A schematic diagram of the MIJCC device, which has been described in detail in our previous work,[7] is presented in Fig. 2. Briefly, the MIJCC consists of a cylindrical chamber with a conical expansion, a secondary concentrator (SC), and a number $N_j = 4$ of rotationally symmetric inlet jets. The inlet jets were distributed around the conical expansion of the main cavity with a combination of α_j and θ_j. The SC was closed at the largest end to prevent flow to or from the ambient environment (labeled with a red line), while the flow leaves the device through an annular outlet around a bluff end-wall (labeled with a blue enclosure). In addition, the cylindrical section of the MIJCC was manufactured from transparent acrylic to enable optical access into the chamber. The key geometric parameters of the MIJCC investigated in the present experiment are given in Table I.

Two azimuthal ($\theta_j = 5°$ and $15°$) and inclination angles ($\alpha_j = 25°$ and $45°$) were chosen to generate three experimental configurations of the MIJCC representing Regimes I, II, and III in Fig. 1. These angles have been selected to ensure that each distinctive class of flow-feature (i.e., each flow regime) is represented, based on our previous work.[6–8] A detailed description of the experimental cases is presented in Table II.

B. Measurements

The optical arrangements were similar to those reported previously[6,7] so that only the key details are described here. The flow-field was measured using PIV. The working fluid was water at ambient temperature, which avoids the deposition of seeding particles onto the confining walls. The jet Reynolds number $Re_D = \rho_f U_e D_{pipe}/\mu_f = 10\,500$ (where ρ_f is the fluid density and μ_f is the fluid dynamic viscosity) ensures that the flow at the nozzle exit is in the fully turbulent regime. The flow was seeded with hollow glass spheres with a specific gravity of 1.1 and a particle diameter of 12 μm. A closed-loop system, including a water pump (Pan World NH-200PS), a frequency converter (Danfoss VLT 2800), and flowmeters (ABB D10A11), was used to recirculate the water from the outlets of the tank to the inlet-pipes. Importantly, a symmetrical manifold system which consists of two straight pipes and four gently curved flexible pipes ($L_{pipe}/D_{pipe} \approx 196$) ensures a fully developed pipe flow is achieved at the exit plane of the supply pipes.[36]

Figure 3 presents the optical arrangement and the measurement regions for the present study. A double-head Nd:YAG laser (Quantel Brilliant B) was used to generate a light sheet of 1.5 mm thickness with a combination of three cylindrical lenses (Thorlabs). A Charged Coupled Device (CCD) camera (Kodak Megaplus ES2093) was used to capture the PIV images for each measurement. The image size was selected so that it spans the entire radial cross section of the cylinder ($D_c = 74$ mm).

The measurement planes for the present study are listed in Table III. Five radial planes (orthogonal to the axis) and one axial plane (across the axis) within the cylindrical chamber of the MIJCC

TABLE II. The notation for the MIJCC configurations investigated in the present study.

Experiment case No.	Configurations	Inclination angles, α_j (deg)	Azimuthal angles, θ_j (deg)	Flow Regime
1	MIJCC-25-05	25	5	I
2	MIJCC-25-15	25	15	II
3	MIJCC-45-15	45	15	III

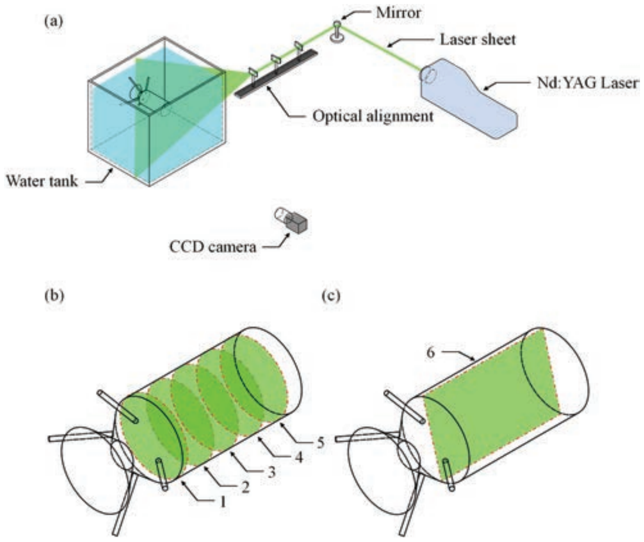

FIG. 3. (a) Schematic diagram of the optical arrangement, showing the laser, optics, light sheet, and water tank; (b) the five radial measurement planes, undertaken separately, along the axis of the MIJCC; and (c) the axial measurement plane relative to the chamber.

were assessed. It should be noted that the results for planes 1 and 6 are only reported for selected figures for conciseness because they are qualitatively similar to those from other planes. The selection of these measurement planes ensures that the velocity data can be obtained from all three classes of flow (see Table III for details).

A minimum of 1500 PIV image pairs were recorded by using the CCD camera for each measurement. The raw images were processed utilizing an in-house PIV code in MATLAB R2015a (Mathworks), employing a multigrid correlation algorithm with 50% overlap to calculate the displacement of tracer particles and also to minimize noise. In addition, an in-house post-processing PIV code was used to identify the outliers (erroneous vectors) for all experimental conditions. As a result, the average number of outliers was less than approximately 5% of the total vectors, and all outliers were removed from the ensemble. The details of the key experimental parameters are listed in Table IV.

TABLE IV. Details of the key experimental parameters for the present PIV measurements.

Experimental parameters	Value
Bulk mean velocity at nozzle exit, U_e (m/s)	2.8
Inlet Reynolds number, Re_D	10500
Laser wavelength (nm)	532
Laser thickness (mm)	1.5
Laser frequency (Hz)	10
Camera array size (pixels)	1920 × 1080
Measurement region (mm)	134 × 77
Particle Stokes number, Sk_D	0.003
Image bit depth (bit)	12
Spatial resolution (mm)	2 × 2 × 1.5
Interrogation window (pixels)	32 × 32

The overall uncertainty associated with the PIV measurements was assessed via a series of systematic analysis steps. The estimated uncertainty derived from the experimental apparatus (i.e., flowmeter, water pump, and frequency converter) was measured to be less than 2%, while the uncertainty of a given measurement position was estimated to be ±0.05 mm within the measurement region. The experimental errors associated with the laser system (e.g., time-delay) were estimated to be less than 2%. Also, the uncertainty contributed from the image sample size was calculated to be less than 1%. On this basis, the overall uncertainty of the measured mean and rms velocities for the present PIV measurements was estimated to be approximately 5%.

III. RESULTS AND DISCUSSION

A. Mean velocity fields

Figure 4 presents the contours of mean tangential velocity (U_θ), normalized by the nozzle exit velocity (U_e), labeled with arrows to indicate the flow direction (black arrows), and magnitude (both the length of the arrows and the color map) at four radial planes x/L_c = 0.36, 0.45, 0.63, and 0.80 for the configurations of [Figs. 4(a)–4(d)] Regime I (α_j = 25° and θ_j = 5°), [Figs. 4(e)–4(h)] Regime II (α_j = 25° and θ_j = 15°), and [Figs. 4(i)–4(l)] Regime III (α_j = 45° and θ_j = 15°). The locations of the CRZ and ERZ for each plane are also presented.

For the case of Regime I (dominant ERZ and small CRZ), the mean flow spirals outward from the center to the near-wall region in each case (except for the most downstream one), with a

TABLE III. Axial positions of the measurement profiles for which data are reported. The circumferential plane is shown in Fig. 3. Note that plane 6 denotes the axial plane illustrated in Fig. 3(c).

Measurement plane	Location, x/L_c	Regime I	Regime II	Regime III
1	0.27	ERZ	ERZ	CRZ
2	0.36	ERZ	ERZ	CRZ
3	0.45	ERZ	CRZ	CRZ
4	0.63	ERZ	CRZ	CRZ
5	0.80	CRZ	CRZ	CRZ
6	N/A	ERZ and CRZ	ERZ and CRZ	ERZ and CRZ

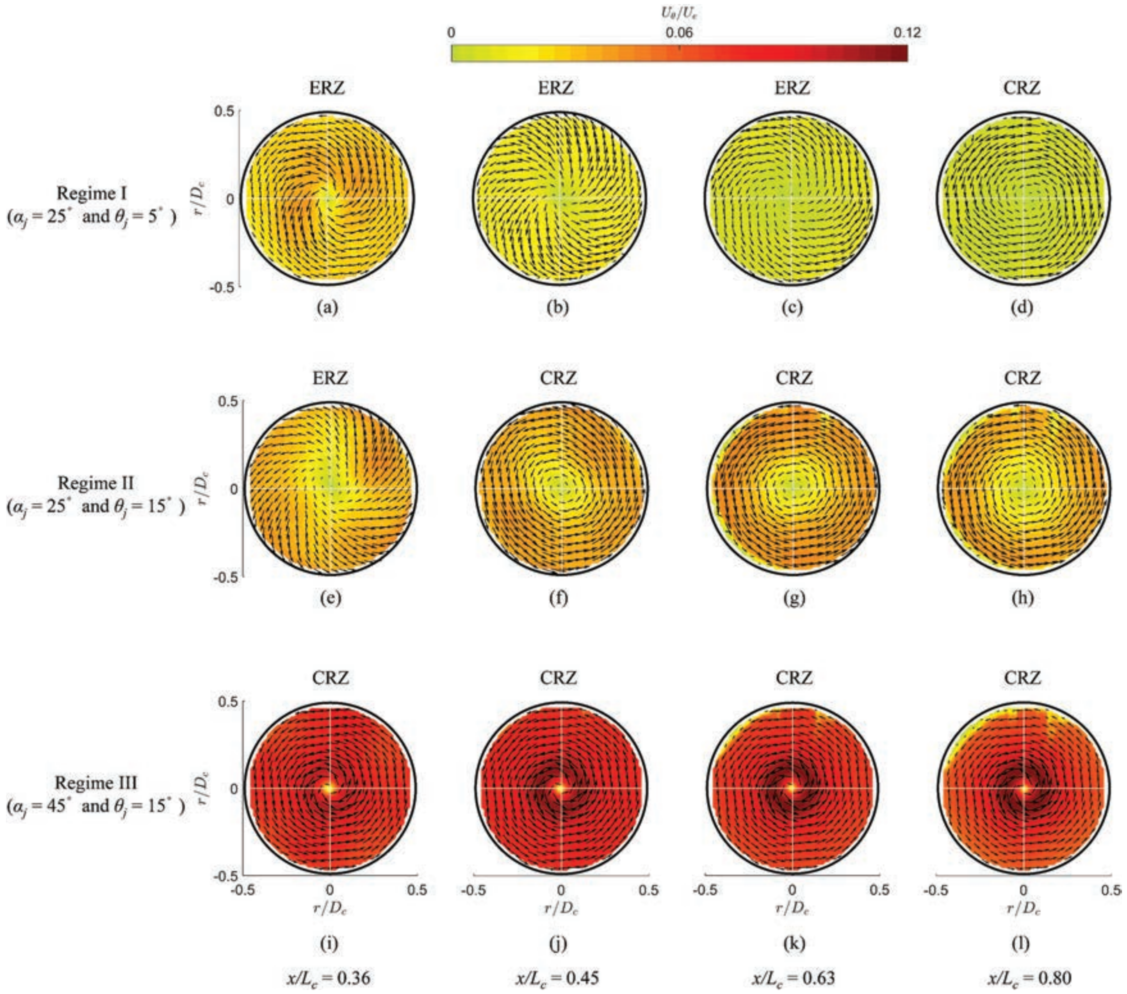

FIG. 4. Mean tangential velocity (U_θ) normalized by the nozzle exit velocity (U_e), labeled with arrows to indicate the flow direction (black arrows) and magnitude (color map) at four axial planes x/L_c = 0.36, 0.45, 0.63, and 0.80 within the MIJCC for the configurations of [(a)–(d)] Regime I (α_j = 25° and θ_j = 5°), [(e)–(h)] Regime II (α_j = 25° and θ_j = 15°), and [(i)-(l)] Regime III (α_j = 45° and θ_j = 15°). Note that the axes and pseudo-color scales are identical for all cases.

magnitude that is greatest at $x/L_c = 0.36$ and decreases with axial distance $x/L_c \geq 0.45$. It can also be seen from the color scale that there is a trend for the magnitude of U_θ within the outer regions of the chamber (i.e., within the ERZ) to decrease with axial distance from $x/L_c = 0.36$ to $x/L_c = 0.63$. By contrast, the magnitude of U_θ near to the axis (i.e., within the CRZ) remains almost independent of axial distance. This is qualitatively similar to the velocity field generated by annular swirling jets.[37] Taken together, it can be concluded that the swirl intensity within the ERZ decreases with an increase in x/L_c within this regime.

For Regime II (where the ERZ and CRZ are of similar size), the velocity contours show that the distribution of U_θ is almost independent of axial distance so that it is higher than that of Regime I for all cases of x/L_c. This confirms that the axial extent of the swirl zone is greater in Regime II than in Regime I. The contours also show that the distribution of U_θ does not change significantly from the upstream ERZ (x/L_c = 0.36) to the downstream CRZ planes ($x/L_c \geq 0.45$). This confirms that the decay of swirl within the chamber reduces as the size of the CRZ is increased, as expected. In addition, it should also be noted that at each axial position, the value of U_θ is fairly uniform, except for a lower velocity component near to the axis. This also suggests that the symmetry of the tangential velocity tends to be approximately achieved in this regime.

Regime III is characterized by a generally significantly higher magnitude of U_θ than the other regimes, as can be seen from the redder color, consistent with the greater swirl angle of the inlet jets. Indeed, the flow direction approaches a tangential direction except for the very core. In addition, the distribution of U_θ is relatively uniform for all locations considered here. That is, the swirl generated with the multiple inlet-jets is almost independent from the location of radial plane for Regime III. This is consistent with the dominance of the CRZ throughout all measured planes. It can also be seen that a high velocity region ($U_\theta/U_e \approx 0.12$) occurs within the range $-0.15 \le r/D_c \le 0.15$ for all measured locations except the central point ($r/D_c \approx 0$). This, in turn, suggests that a higher degree of swirl occurs close to the axis of the cylindrical chamber,[29] while this pronounced swirl region is not observed in the other two regimes. Hence, it can be concluded that the significance of the swirl within the central region tends to increase significantly as the dominant flow feature changes from the ERZ (Regime I) to the CRZ (Regime III).

It is also worth noting that for a given radial plane x/L_c, the magnitude of tangential velocity U_θ typically increases from Regime I to Regime III, with the highest value of U_θ for each plane is measured from Regime III. For example, the swirl at $x/L_c = 0.80$ in Regime III [Fig. 4(l)] is an order of magnitude higher than that in Regime I [Fig. 4(d)]. This also indicates that the combination of high inclination and azimuthal angles ($\alpha_j = 45°$ and $\theta_j = 15°$) tends to significantly increase the degree of swirl at any given location for multiple confined jets.

Figure 5 presents the measured streamlines, labeled with arrows to indicate the flow direction at four radial planes $x/L_c = 0.36$, 0.45, 0.63, and 0.80 for all experimental conditions. Clear differences can be seen. For the case of Regime I [Figs. 5(a)–5(d)], it can be seen that the flow exhibits an outwardly spiraling flow pattern from a point source at the cylinder axis within three planes in the ERZ, i.e., $x/L_c = 0.36$, 0.45, and 0.63. This flow is generated by the central resulting jet formed by the merging of the inlet jets, superimposed onto the swirl generated by the tangential component of the inlet-jets ($\theta_j = 5°$). This flow pattern is consistent with conventional swirling jets[38,39] and also with our previous paper.[7] However, further downstream at $x/L_c = 0.80$, the flow exhibits an internally spiraling flow toward the axis within the CRZ (i.e., the source becomes a sink), while the swirling direction is unchanged. This flow pattern is caused by the low-pressure core with the CRZ, which also generates the reverse flow zone.

For the case of Regime II [Figs. 5(e)–5(h)], the trends are similar although the axial extent of each region changes. The spiraling out from the source on the axis is only present at location $x/L_c = 0.36$, which corresponds well with the presence of the ERZ. The other two positions exhibit a sink at the axis $x/L_c = 0.45$ and 0.63, corresponding well with the CRZ. Importantly, as the radial component becomes weaker for $x/L_c = 0.80$, the flow approaches being tangential. This indicates that a strongly swirled flow is present in which

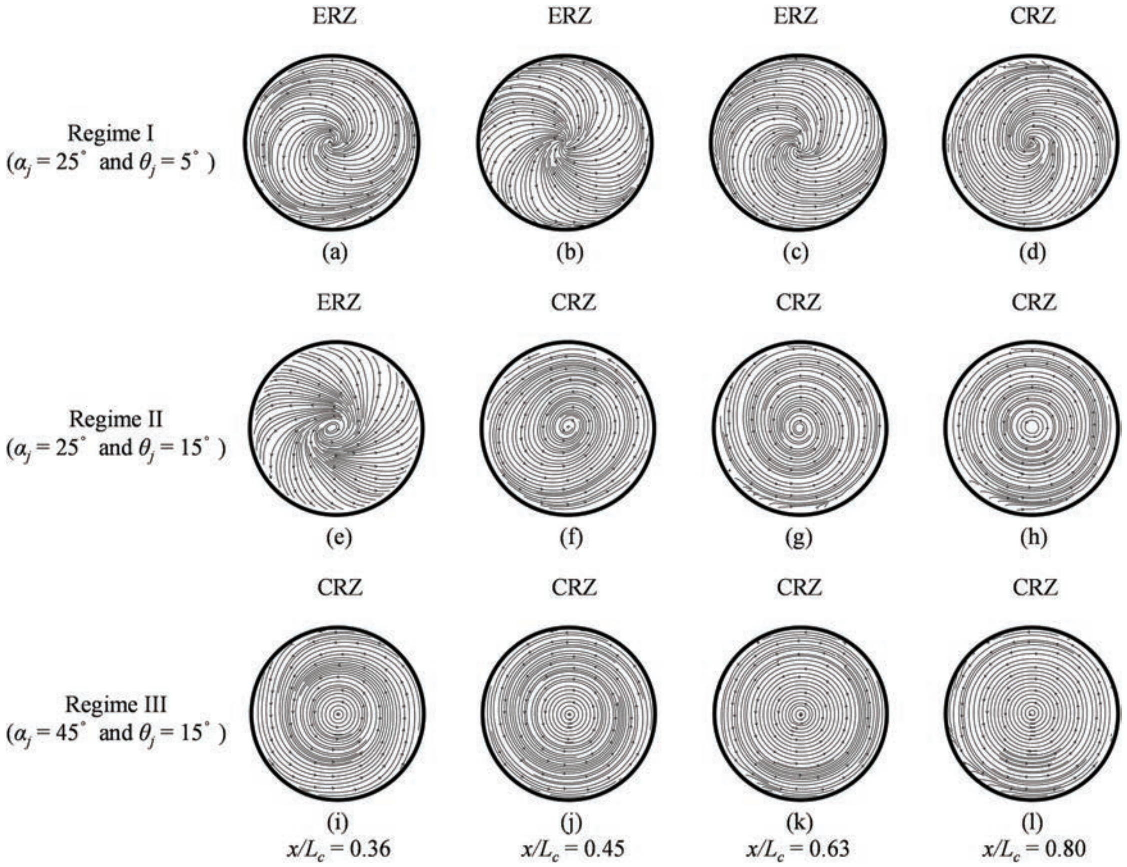

FIG. 5. Measured streamlines, labeled with arrows to indicate the flow direction at four axial planes $x/L_c = 0.36$, 0.45, 0.63, and 0.80 within the MIJCC for the configurations of [(a)–(d)] Regime I, [(e)–(h)] Regime II, and [(i)–(l)] Regime III.

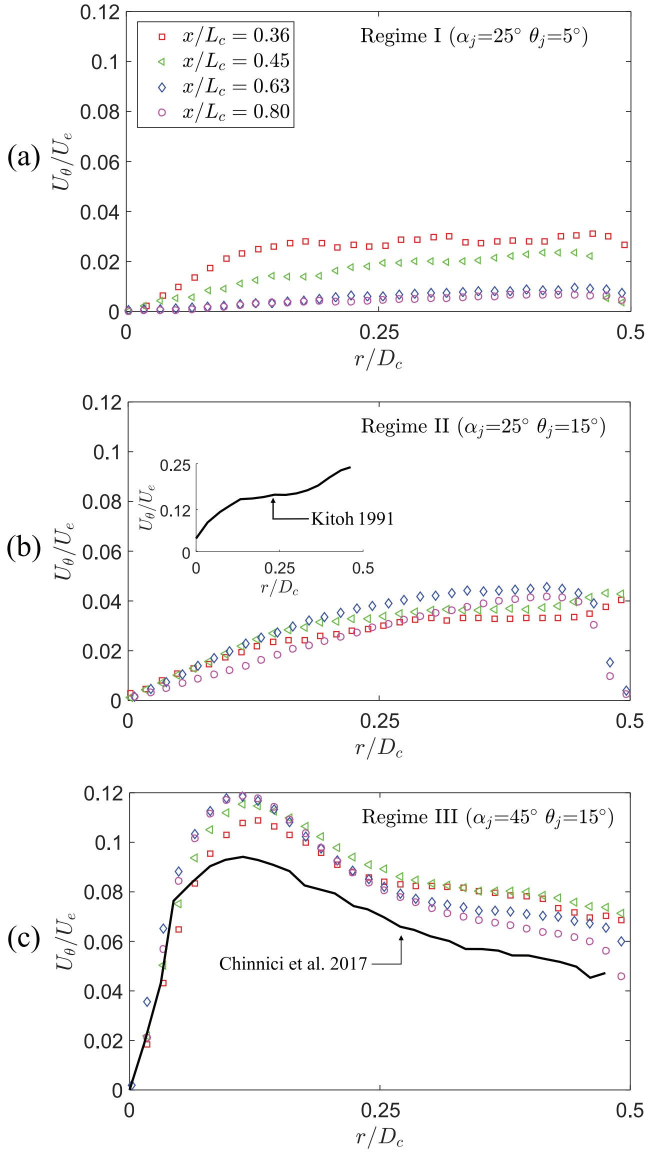

FIG. 6. Radial profiles of the normalized mean tangential velocities (U_θ/U_e) at four radial planes x/L_c = 0.36, 0.45, 0.63, and 0.80 within the MIJCC for cases of (a) Regime I, (b) Regime II, and (c) Regime III. Note that the axes and symbols are identical for all cases.

the tangential velocity U_θ is much greater than the radial velocity component (U_r).

For the case of Regime III [Figs. 5(i)–5(l)], the flow-field everywhere is characterized by a very weak radial inflow so that it approaches an almost purely rotational flow for all radial planes investigated here. This is consistent with the presence of highly swirled flow for Regime III together with a dominant CRZ.

Overall, the results show that a source within the rotational flow is associated with the presence of an ERZ, while a sink within the rotational flow represents the occurrence of a CRZ. This is consistent with expectation. Importantly, as the source or sink is absent and a flow of pure rotation occurs, the region tends to be dominated by a high-swirled flow within the CRZ (for which $U_\theta > U_r$). That is, the value of swirl angles (α_j and θ_j) and their corresponding large-scale recirculation zones (ERZ and CRZ) have a controlling influence on the presence of rotational flow patterns for multiple confined jets.

Figure 6 presents the radial profiles of the normalized mean tangential velocities (U_θ/U_e) at four radial planes x/L_c = 0.36, 0.45, 0.63, and 0.80 within the MIJCC for all experimental conditions. Note that the axes and symbols are identical for all of these subfigures. The measurements for Regime I [Fig. 6(a)] show that the magnitude of U_θ/U_e decreases by approximately 70% as x/L_c is increased from 0.36 to 0.8. For example, the peak velocity, $(U_\theta/U_e)_{max}$, decreases from 0.03 at x/L_c = 0.36 to 0.01 at x/L_c = 0.8. Furthermore, the value of U_θ/U_e decreases faster within the ERZ than that in CRZ plane. For example, it decreases by 70% from x/L_c = 0.36 to 0.63 (ERZ) and only by 10% from x/L_c = 0.63 to 0.80 (CRZ). It should also be noted that the magnitude of the tangential velocity $U_\theta \approx 0.01U_e$–$0.03U_e$ for all measured planes in Regime I. This is an order of magnitude lower than that of the axial velocity ($U_x \approx 0.15U_e$) as we reported previously.[7] Hence, the swirl in Regime I is weak.

For Regime II [Fig. 6(b)], it can be seen that the tangential velocity does not change as significantly with x/L_c as it does in Regime I but only decays by about 30% from upstream (x/L_c = 0.36) to downstream (x/L_c = 0.80). The decay of the tangential velocity is noticeably lower than that of Regime I as $(U_\theta/U_e)_{max}$ at x/L_c = 0.80 is approximately 40% higher than that for the case of θ_j = 5° (within the CRZ). This reveals that the swirl increases as θ_j is increased, as expected. It can also be seen that the radial profile of U_θ/U_e increases monotonically with the radial distance (r) from the axis to $r/D_c \approx 0.25$ for x/L_c = 0.36 and 0.45 plateaus and then increases slightly toward the wall. This is qualitatively consistent with a turbulent swirling pipe flow measured by Kitoh[40] [see the inset of Fig. 6(b)], which indicates that the flow is characterized by a forced vortex within these planes. However, the magnitude of the forced vortex in Regime II is approximately 80% lower than that of Kitoh,[40] indicating that the swirl is weaker in this case. For further downstream planes (x/L_c = 0.63 and 0.80), a significant reduction of U_θ/U_e was measured at the near-wall region of $r/D_c \geq 0.46$ (≈10% of the total radius). This implies the transition between a forced and a free vortex, corresponding well with the ERZ and CRZ regions of Regime II.

For Regime III [Fig. 6(c)], the tangential velocity is the highest [$(U_\theta/U_e)_{max} \approx 0.12$]. For all radial profiles, the value of U_θ/U_e increases from 0 to 0.12 within $0 \leq r/D_c \leq 0.15$ and then decreases to 0.07 for $r/D_c > 0.15$. This is qualitatively similar to the PIV data reported by Chinnici *et al.*[29] for multiple swirling jets, which shows the presence of a forced vortex near to the central region, surrounded by a free vortex, i.e., a "Rankine" vortex (a forced and free combined vortex). This vortex has also been widely documented for high-swirled jet configurations.[41–44] Importantly, the combination of a forced and free vortex (Rankine vortex) is typically associated with the presence of a high degree of flow oscillations within the CRZ, such as a PVC.[9,34]

The results in Fig. 6(c) also show that U_θ/U_e in Regime III is around 20% higher than the data of Chinnici *et al.*[29] This indicates the presence of a highly swirled flow for this regime.

However, as x/L_c is increased from 0.36 to 0.8, the tangential velocity increases by 10% within the forced vortex ($|r/D_c| \leq 0.15$) while it decreases by 15% within the free vortex ($|r/D_c| > 0.15$). This reveals that the intensity of "Rankine" vortex is not consistent throughout the chamber, although the difference of U_θ/U_e is typically small (≤15%).

It is also worth noting that for the cases where the inclination and azimuthal angles (α_j and θ_j) are both small and an ERZ dominates the chamber (Regime I), the magnitude of tangential velocity decreases significantly (by 40%) with x/L_c, while for the cases in which both α_j and θ_j are sufficiently large to generate a dominant CRZ (Regime III), the decay in the tangential velocity is relatively small (by up to 15%) and the magnitude remains the highest. This suggests that the strength of the swirl persists further within a CRZ than within an ERZ.

B. rms of the turbulent flow fields

Figure 7 presents the radial profiles of normalized tangential rms (root-mean-square) velocity (u'_θ/U_e) within the MIJCC at four radial planes $x/L_c = 0.36$, 0.45, 0.63, and 0.80 for the configurations of (a) Regime I ($\alpha_j = 25°$ and $\theta_j = 5°$), (b) Regime II ($\alpha_j = 25°$ and $\theta_j = 15°$), and (c) Regime III ($\alpha_j = 45°$ and $\theta_j = 15°$).

For Regime I [Fig. 7(a)], the location of the peak rms velocity, $(u'_\theta/U_e)_{max}$, at $x/L_c = 0.36$ and 0.45 is found at, or close to, the center of the chamber and then decreases approximately linearly toward the wall region. A maximum in turbulent fluctuation within the central region is associated with the unsteady merging point of the multiple inlet-jets,[7] resulting in a precessing jet flow.[9] At $x/L_c = 0.63$, the rms velocity is 70% lower than at $x/L_c = 0.45$, while the radial profile of the rms velocity remains approximately constant ($u'_\theta/U_e \approx 0.025$) across the chamber's radius. The value of u'_θ/U_e continues to decrease with axial distance to a value of $u'_\theta/U_e \approx 0.02$ at $x/L_c = 0.80$, which is very close to uniform throughout the radial profile. Taken together, it can be concluded that the fluctuations in the tangential velocity for Regime I reduce significantly with axial distance from the nozzle exit, consistent with trends in conventional annular jets.[14,37]

It can be seen from Fig. 7(b) that the tangential rms velocity in Regime II is significantly lower than that of Regime I at $x/L_c = 0.36$ and 0.45. However, u'_θ/U_e is quite similar in the two regimes at $x/L_c = 0.63$ and 0.80. This gives some evidence that the fluctuation in tangential velocity tends to reduce as θ_j is increased. The shapes of the upstream profiles are also different. At the two upstream locations, $x/L_c = 0.36$ and 0.45, the rms peaks on the axis for Regime I but peaks away from the axis for Regime II. However, further downstream they are flatter. This indicates that the axial extent of the zone with relatively low fluctuation of swirl in the downstream region grows from Regime I to Regime II. Hence, it can be concluded that the radial profile of the rms of tangential velocity is small and relatively flat for the CRZ region but significantly higher for the ERZ.

For Regime III [Fig. 7(c)] where the flow is characterized by a dominant CRZ, it can be seen that a pronounced peak in u'_θ/U_e occurs at the central region $-0.15 \leq r/D_c \leq 0.15$ for all radial profiles, with the peak value of $u'_\theta/U_e \approx 0.06$ occurring at the centerline of the chamber. This corresponds well with the maximum gradient of the mean tangential velocity (U_θ) shown in Fig. 6(c). That is, a high value of u'_θ/U_e is associated with the central region for Regime III. Such a large fluctuation in the tangential velocity is commonly associated with a high degree of flow unsteadiness, which may be evidence of the presence of a PVC within the central region, consistent with previous studies in swirled burners and reactors.[9,13,37,45] Importantly, this pronounced peak only occurs at Regime III, which suggests that this regime is most likely to generate a PVC at, or close to, the axis of the chamber.

Overall, it can be concluded that, first, for a given value of nozzle angle (α_j and θ_j), the degree of fluctuation in the tangential velocity decreases along the axis of the chamber for both the ERZ and CRZ, although the reduction is most significant for the smallest jet angles considered here (Regime I) and, second, an increase in α_j and θ_j (Regime III) leads to a significant increase in the velocity

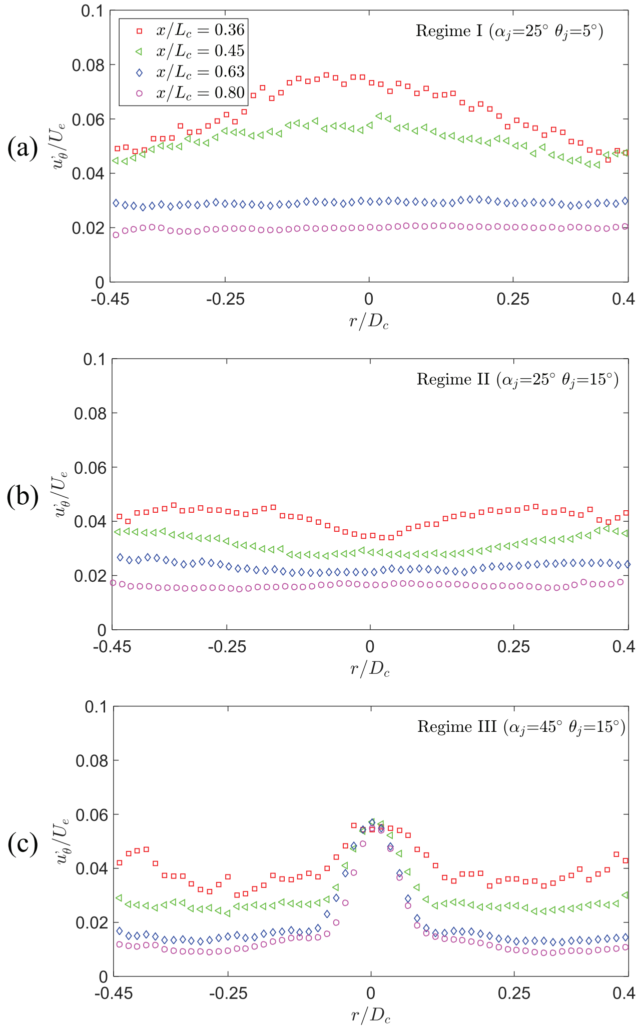

FIG. 7. Radial profiles of tangential rms (root-mean-square) velocity normalized by the nozzle mean exit velocity (u'_θ/U_e) at four radial planes $x/L_c = 0.36$, 0.45, 0.63, and 0.80 within the MIJCC for configurations of (a) Regime I, (b) Regime II, and (c) Regime III. Note that the axes and symbols are identical for all cases.

fluctuation of the central region ($r/D_c \approx 0$) for a given radial plane (x/L_c). This also highlights the influence of the CRZ on the amplification of flow unsteadiness along the axis of the chamber, as discussed in the previous study.[7]

Figure 8 presents axial profiles of the evolution of normalized axial (u_x'/U_e) and radial rms velocities (u_r'/U_e) along the centerline of the MIJCC for representative configurations that generate Regimes I, II, and III. The data for Regimes I and II are reproduced from our previous paper (Long *et al.*[8]) to complete the data set, while red solid lines denote Regime I and blue dashed lines refer to Regime II. For Fig. 8(a), the results show that the transition from Regime I to Regime III leads to a significant decrease in axial rms velocity u_x' along the axis of the chamber. The magnitude of the peak $(u_x'/U_e)_{max}$ remains almost constant ($u_x'/U_e \approx 0.1$) from Regime I to Regime II and decreases by 40% from Regime II to Regime III. The position of the peak also moves upstream from $x/L_c \approx 0.32$ (Regime I) to 0.15 (Regime III). This is consistent with the upstream movement of the jet merging point for each case, as reported previously.[7] The axial extent of the region with low u_x'/U_e therefore increases commensurately from Regime I, where it is negligible, to Regime III, where it is the dominant phenomena in the measured region. Hence, it can be concluded that Regime III is associated with a lower fluctuation in the axial velocity component along the centerline of the chamber.

The axial profile of u_r'/U_e is presented in Fig. 8(b). It can be seen that for Regime I and II, the position of the peak tends to be further upstream than for u_x'/U_e and the corresponding axial extent is shorter. Hence, the average value of u_r'/U_e in Regime II is typically 30% lower than that in Regime I. However, the peak for Regime III is found further upstream and asymptotes to a higher value of $u_r'/U_e \approx 0.06$ than for the other regimes. This value of $u_r'/U_e \approx 0.06$ is similar to that of the pronounced peak in u_θ' within the central region of the radial planes reported above. Taken together, it can be concluded that Regime III is associated with strong fluctuation in the radial and tangential velocity components but weaker fluctuations in the axial direction which is also consistent with the presence of precessing flows for the configurations with high nozzle angles ($\alpha_j = 45°$ and $\theta_j = 15°$).

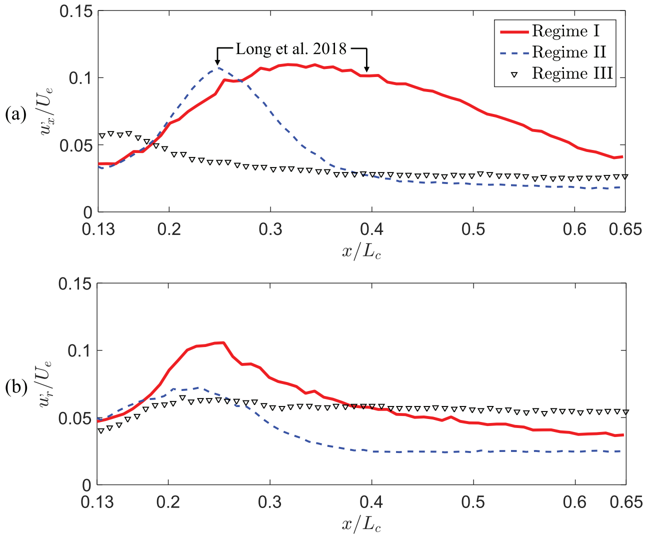

FIG. 8. Evolution of (a) normalized axial rms (u_x'/U_e) and (b) normalized radial rms velocity (u_r'/U_e) along the centerline of the MIJCC for all experimental cases. The red and blue lines denote the data published in our previous work.[8] For clarity, only every second data point is presented and both cases use identical axes and symbols.

C. Characterization of the precessing vortex core

Figure 9 presents (a) two typical instantaneous streamlines, labeled with arrows to indicate the flow direction, and (b) the angular displacement of the vortex-core relative to the center of the cylinder (θ_{core}), as a function of time (t) for the case of Regime III ($\alpha_j = 45°$ and $\theta_j = 15°$). Note that the data are presented only at $x/L_c = 0.8$ here for consistency. The location of the vortex-core was determined by a combination of mathematical calculations and visual observation. Mathematically, the position of the vortex-core is defined as the crossing point where the tangential velocity U_θ and the radial velocity U_r equals or approaches zero on the θ-r coordinate system, following Grosjean *et al.*[26] and Volkert *et al.*[46] The results were calibrated with the visualization from the raw PIV images to obtain the final location of the vortex-cores. On this basis, the uncertainty of the vortex-core location was estimated to be less than 10%.

For the instantaneous velocity field [Fig. 9(a)], it can be seen that the vortex-core (labeled with a red cross) moves from the bottom-half [Fig. 9(a) left] to the top-half [Fig. 9(a) right] section

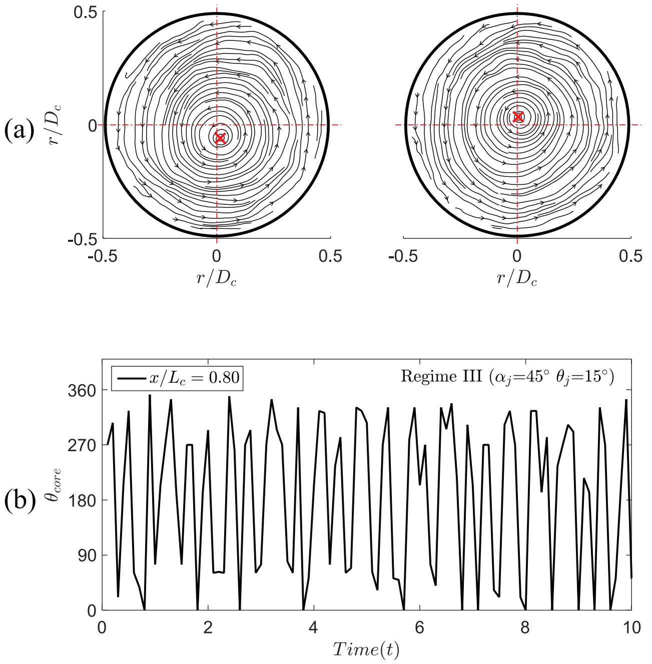

FIG. 9. (a) Typical instantaneous streamlines, labeled with arrows to indicate the flow direction for the case of $\alpha_j = 45°$ and $\theta_j = 15°$ (Regime III) at the plane $x/L_c = 0.8$, and (b) the angular displacement of the vortex-core (θ_{core}) as a function of the time (t).

of the cylindrical chamber, with a significant displacement relative to the axis of the chamber (labeled with the red lines). That is, the location of vortex-core changes significantly with time. The temporal displacement of the vortex-core is presented in a time-series in Fig. 9(b) for some 25 cycles. This shows that θ_{core} moves periodically around the axis of the chamber with a regular frequency. This is a typical of previous descriptions of a PVC,[9,29] which confirms its presence within the cylindrical chamber.

Figure 10 presents the probability density function (PDF) of the radial displacement of the vortex-core relative to the axis of the chamber (r_{core}), normalized by the chamber diameter (D_c) for the cases of Regimes I, II, and III. All of these data are measured in the CRZ at the radial plane $x/L_c = 0.8$ (refer to Table III). The results show that the most probable displacement of the vortex-core is $r_{core}/D_c \approx 0.11$–$0.13$ for Regimes I and II, while it is smaller at $r_{core}/D_c \approx 0.03$ for Regime III. However, the peak in probability is much sharper for Regime III, showing that the fluctuations are more regular. The finding that the transition between Regime I and Regime II does not significantly influence the radial displacement of the PVC is consistent with them both being associated with a dominant ERZ upstream from $x/L_c = 0.8$, while Regime III is associated with a CRZ that fills almost the entire cylindrical chamber. Hence, the presence of a dominant CRZ tends to inhibit the precession of vortex-core and to generate a coherent PVC for the configurations of multiple confined jets.

It can also be seen from Fig. 10 that the higher peak in the PDF for Regime III is consistent with the higher values of rms velocities along the centerline of the chamber for Regime III (see also Figs. 7 and 8). Taken together, it can be concluded that the PVC is present in all of these flows, regardless the types of vortex (i.e., free, forced, or Rankine), although it is more coherent in the CRZ of Regime III but with a smaller displacement than it is for Regime I.

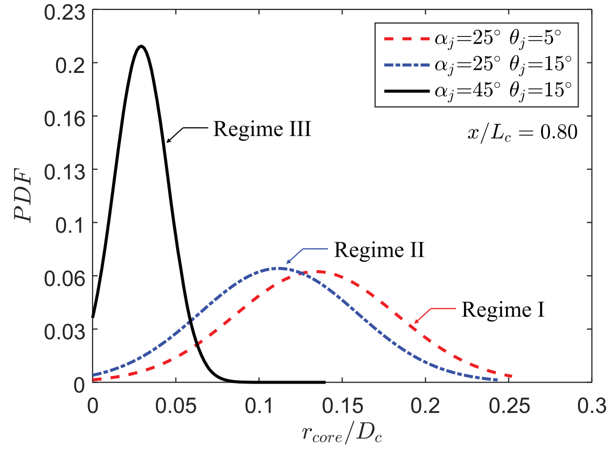

FIG. 10. Probability distribution of the radial displacements of the vortex core relative to the axis of the chamber, normalized by the chamber diameter, for the configurations of Regime I (α_j = 25° and θ_j = 5°), Regime II (α_j = 25° and θ_j = 15°), and Regime III (α_j = 45° and θ_j = 15°).

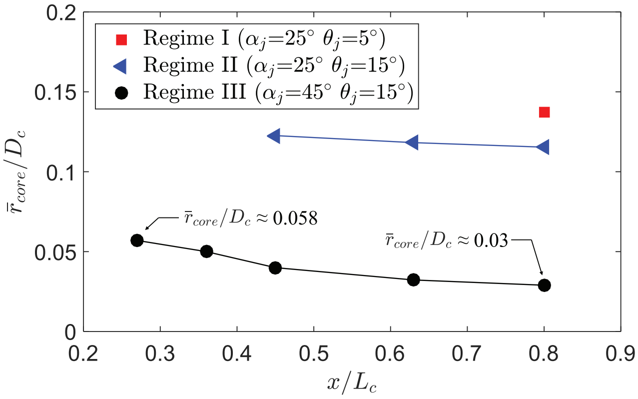

FIG. 11. Averaged vortex-core displacement, normalized by the diameter of the chamber (**$\bar{r}_{core}/D_c$**) along the axis of the MIJCC for the configurations of Regime I, Regime II, and Regime III.

Figure 11 presents the averaged radial displacement of the vortex-core ($\bar{r}_{core}$) normalized by the chamber diameter (D_c) at five radial planes (x/L_c = 0.27, 0.36, 0.45, 0.63, and 0.80) for the configurations generating Regimes I, II, and III. Data are only presented for those cases where a vortex-core can be identified from the method illustrated in Fig. 9. It can be seen that the axial extent of the regions in which a PVC can be identified is the greatest for Regime III (x/L_c = 0.27, 0.36, 0.45, 0.63, and 0.80) and the least for Regime I (x/L_c = 0.80). This is consistent with the increase in the magnitude of the tangential velocity for Regime III. Furthermore, these regions correspond to radial planes where a CRZ is present (see also Table III for details), which is consistent with a previous study,[9] indicating that the position of the PVC corresponds well with that of the CRZ.

Figure 11 also shows that the value of $\bar{r}_{core}/D_c$ typically decreases from Regime I to Regime III, although the extent of the reduction is small for Regime II. For example, at x/L_c = 0.80, the value of $\bar{r}_{core}/D_c$ in Regime II is 20% lower than that in Regime I, while it is approximately 80% lower for Regime III. This is consistent with the PDF of the position of the vortex-core (Fig. 10), showing that a more coherent PVC has a smaller displacement. However, the extent of the reduction in the position of the PVC for each regime is not consistent. For example, the value of $\bar{r}_{core}/D_c$ for Regime III decreases by ≈50% from 0.058 at x/L_c = 0.27 to 0.03 at x/L_c = 0.80. However, for the case of Regime II, the extent of the reduction in $\bar{r}_{core}/D_c$ is relatively small (≈10%) from x/L_c = 0.46 to 0.80 where a PVC is identified. This suggests that the presence of jet precession in the upstream ERZ in Regime II is associated with a substantially lower reduction in the position of the PVC in the downstream CRZ.

Overall, it can be concluded that for the cases in which the size of the ERZ is larger than, or similar to, that of the CRZ (Regimes I and II), the displacement of the PVC remains high throughout the CRZ region, while for the cases with higher swirl angles and a dominant CRZ (Regime III), the displacement of the PVC is smaller and the movement is more regular.

D. Identification of the three-dimensional flow regimes

Figure 12 presents a schematic diagram of the three rotational flow patterns that have been identified for Regime I (α_j = 25° and

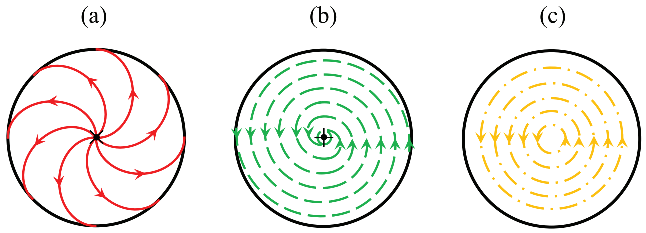

FIG. 12. Schematic diagram of the three rotational flow patterns that have been identified within the MIJCC configurations: (a) Pattern A: rotation + source, (b) Pattern B: rotation + sink, (c) Pattern C: pure rotation. Here, the "×" denotes the source and "+" is the sink.

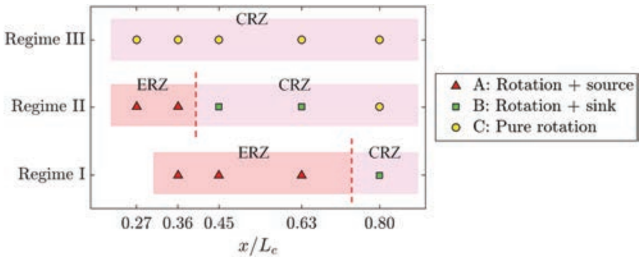

FIG. 13. Map of the key rotational flow patterns as a function of the Regimes I, II, and III within the rotationally symmetric MIJCC configurations. The ERZ and CRZ are highlighted with red and purple colors, respectively.

$\theta_j = 5°$), Regime II ($\alpha_j = 25°$ and $\theta_j = 15°$), and Regime III ($\alpha_j = 45°$ and $\theta_j = 15°$), using both the measured streamlines and quantitative information from Secs. III A–III C. A brief summary of the key flow features generated by the MIJCC configurations is listed in Table V and presented below:

1. Pattern A: Rotation + source

Pattern A is characterized by a rotational flow superimposed on a point source at the cylinder axis. The source is associated with the central resulting jet generated by the interaction of multiple inlet-jets. Hence, this flow pattern typically occurs in the ERZ where the magnitude of the axial velocity is significantly greater than that of the tangential velocity ($U_x > U_\theta$).

2. Pattern B: Rotation + sink

Pattern B is characterized by a rotational flow superimposed on a sink at the axis of the chamber. The sink is generated by the combination of a central reverse flow along the axis and a downstream peripheral flow near to the wall region. This flow pattern is present within a CRZ where the magnitude of the tangential velocity is similar to that of the radial velocity ($U_\theta \approx U_r$).

3. Pattern C: Pure rotation

Pattern C is characterized by a purely rotational flow dominating the radial planes, which is generated by the high magnitude of tangential component from the swirl angle of the multiple inlet-jets. This flow pattern occurs within the CRZ where the tangential velocity is significantly higher than the radial velocity ($U_\theta > U_r$).

Figure 13 presents the three distinctive rotational flow patterns within the chamber of the MIJCC for the geometric configurations of Regimes I, II, and III that have been identified using both the flow visualization and quantitative data. The axial extent of the ERZ and CRZ regions within the MIJCC is also identified by the use of highlighting with red and purple colors, respectively. The results show that the presence of Pattern A corresponds well with the ERZ, while Patterns B and C are typically associated with a CRZ, as expected. However, it should be noted that Pattern B occurs at regions for which the downstream end of the ERZ is located at $x/L_c \geq 0.36$, labeled with a red dashed line (i.e., $0.63 \leq x/L_c \leq 0.80$ for Regime I and $0.36 \leq x/L_c \leq 0.45$ for Regime II), while Pattern B is totally absent for Regime III where the ERZ is expected to be located at further upstream ($x/L_c < 0.27$). This finding indicates that the position and size of the ERZ have a controlling influence on the presence of Pattern B (rotational flow with a sink), which in turn suggests that Pattern B tends to be only generated within the transition region between the ERZ and the CRZ. This is also consistent with the transition from a forced to a Rankine vortex as discussed in Fig. 6. Taken together, it can be concluded that a change from Regimes I to III eliminates Pattern A and leads to the dominance of Pattern C, consistent with the change in the relative significance of the ERZ and CRZ from Regime I to III.

Figure 14 presents a schematic diagram of the three flow regimes that have been identified within the MIJCC configurations. The data for the *x*-*r* plane (axial) have been adapted from our previously published work,[7] while those for the r–θ plane (tangential) were obtained from Patterns A, B, and C reported in Fig. 12. The detailed description of the key flow features for the x–r plane is discussed by Long *et al.*[7]

a. Regime I: Dominant ERZ + weak CRZ + low swirl flow. Regime I is characterized by the presence of a dominant ERZ and a small downstream CRZ within the cylindrical chamber of the MIJCC. The rotational flows with a source (Pattern A) and a sink (Pattern B) are associated with the main ERZ and the weak CRZ regions, respectively. The swirl strength in this regime is weak, with the majority of the flow being in the axial direction of the chamber.

TABLE V. Definition of rotational flow patterns within the MIJCC configurations equipped with rotationally symmetric multiple-jets.

Rotational flow	Flow direction	Recirculation zone	Source	Sink	Swirl strength
Pattern A (rotation + source)	Outwardly spiraling	ERZ	Yes	No	Weak ($U_\theta \approx 0.02U_e$)
Pattern B (rotation + sink)	Inwardly spiraling	CRZ	No	Yes	Medium ($U_\theta \approx 0.04U_e$)
Pattern C (pure rotation)	Purely tangential	CRZ	No	No	Strong ($U_\theta \approx 0.12U_e$)

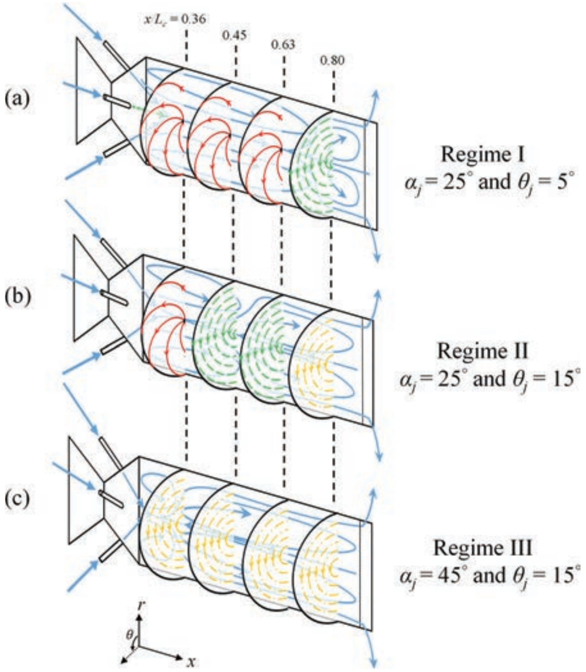

FIG. 14. Schematic diagrams showing the major flow features for the axial plane (across the axis) and four radial planes (orthogonal to the axis) within the rotationally symmetric MIJCC configurations. (a) Regime I: Dominant ERZ + weak CRZ + low swirl flow, (b) Regime II: ERZ + CRZ + medium swirl flow, and (c) Regime III: Weak ERZ + dominant CRZ + high swirl flow.

The displacement of the PVC in this regime is the greatest of all cases investigated here.

b. Regime II: ERZ + CRZ + medium swirl flow. Regime II is characterized by a strong ERZ and CRZ within the cylindrical chamber, with the axial extent of the ERZ and CRZ is relatively similar. The extent of Pattern B is greater than that for Regime I, while a purely rotational flow (Pattern C) occurs at the downstream region of the chamber. Hence, the swirl strength for this regime is significantly greater than that for Regime I, although the displacement of the core of the PVC is smaller than that for Regime I.

c. Regime III: Weak ERZ + dominant CRZ + high swirl flow. Regime III is characterized by the dominance of a CRZ within the chamber, while the ERZ is limited to the conical section of the chamber. Pattern C is recorded for all radial planes downstream from the jet merging point. This regime is also characterized by a significant swirling flow (the most significant among the three identified regimes). Importantly, the PVC in this regime is mostly regular and stable.

IV. CONCLUSIONS

In conclusion, new qualitative and quantitative information has been provided to the swirling and precessing flows generated by the Multiple Impinging Jets in a Cylindrical Chamber (MIJCC) with the inclination ($\alpha_j = 25^\circ$ and 45°) and azimuthal angles ($\theta_j = 5^\circ$ and 15°):

1. The new findings of the three distinctive flow regimes (Regimes I, II, and III) are as follows:
   (a) The magnitude of tangential velocity U_θ is the strongest $[(U_\theta/U_e)_{max} \approx 0.12]$ and is almost independent from the axial locations throughout the chamber for Regime III ($\alpha_j = 45^\circ$ and $\theta_j = 15^\circ$) where a dominant central recirculation zone (CRZ) occurs, while the value of U_θ is relatively weak $[(U_\theta/U_e)_{max} \approx 0.04]$ and decays much faster along the axis for the cases where a dominant external recirculation zone (ERZ) is present (e.g., Regime I, $\alpha_j = 25^\circ$ and $\theta_j = 5^\circ$). This indicates that the swirl strength is much stronger and remains higher value for the CRZ than that for the ERZ.
   (b) The transition from Regime I to Regime III is associated with an increase by 60%–90% in the magnitude of tangential velocity for a given cross section (x/L_c) within the chamber, resulting in the absence of a free vortex and the presence of a Rankine (forced and free combined) vortex. This corresponds well with the increase in the size of the CRZ, which is caused by the combined effects of large α_j and θ_j increasing the tangential velocity.
   (c) The rms (root-mean-square) of tangential velocity (u'_θ) was found to be small and relatively flat for the CRZ but typically higher for the ERZ. This is associated with the unsteady merging point of the multiple inlet-jets within the ERZ. It was also found that a pronounced peak of the rms velocities for axial, radial, and tangential directions (u'_x, u'_r, and u'_θ) occurs within the central region for Regime III. This indicates that a dominant CRZ in Regime III amplifies significantly the level of turbulent fluctuations within the central region of a cylindrical chamber.
   (d) Three rotational flow patterns were identified within Regimes I, II, and III, depending on the relative significance of the ERZ and CRZ:
      - Pattern A: rotational flow superimposed on a source (for the ERZ with a weak swirl $U_x > U_\theta$);
      - Pattern B: rotational flow superimposed on a sink (for the CRZ with a medium swirl $U_\theta \approx U_r$);
      - Pattern C: pure rotation (for the CRZ with a high-swirled flow $U_\theta > U_r$).
2. A precessing vortex core (PVC) was found to occur for all cases investigated here. The key findings of the PVC are as follows:
   (a) The axial extent of the regions in which a PVC can be identified is the greatest for Regime III and the least for Regime I. This corresponds well with the axial extent of the CRZ for Regimes I, II, and III, indicating that the position of the PVC depends strongly on the size of the CRZ.
   (b) The significance of the PVC tends to be amplified for small swirl angles (e.g., $\theta_j = 5^\circ$) but to be inhibited for higher swirl angles (e.g., $\theta_j = 15^\circ$). This is evidenced by up to 80% smaller displacement of the vortex-core (r_{core}) relative to the center of the chamber for Regime III than that for Regime I.

(c) The value of r_{core} was found to be reduced along the axis of the chamber for all three flow regimes. However, the value of r_{core} is reduced by up to 50% for Regime III but only 10% for Regime II. This indicates that a strong interaction of inlet-jets within the upstream ERZ for Regime II tends to retain the displacement of the PVC within the CRZ.

ACKNOWLEDGMENTS

The authors acknowledge the support of the Australian Research Council, FCT Combustion Pty. Ltd., and Vast Solar Pty. Ltd. through the ARC Linkage Grant No. LP110200060. Mr. Shen Long acknowledges the financial support of the Australian Government Research Training Program. In addition, the constructive comments from the anonymous reviewers have significantly strengthened the paper and are gratefully acknowledged.

REFERENCES

[1] G. Cox, "Multiple jet correlations for gas turbine engine combustor design," J. Eng. Power **98**, 265 (1976).

[2] E. Koepf, W. Villasmil, and A. Meier, "High temperature flow visualization and aerodynamic window protection of a 100-kW th solar thermochemical receiver-reactor for ZnO dissociation," Energy Procedia **69**, 1780 (2015).

[3] T. Boushaki and J.-C. Sautet, "Characteristics of flow from an oxy-fuel burner with separated jets: Influence of jet injection angle," Exp. Fluids **48**, 1095 (2010).

[4] T. Chammem, H. Mhiri, and O. Vauquelin, "Experimental and computational investigation of Reynolds number effect on the longitudinal ventilation in large enclosure of twin inclined jets," Build. Environ. **67**, 87 (2013).

[5] H. J. Hussein, S. P. Capp, and W. K. George, "Velocity measurements in a high-Reynolds-number, momentum-conserving, axisymmetric, turbulent jet," J. Fluid Mech. **258**, 31 (1994).

[6] S. Long, T. C. W. Lau, A. Chinnici, Z. F. Tian, B. B. Dally, and G. J. Nathan, "Experimental and numerical investigation of the iso-thermal flow characteristics within a cylindrical chamber with multiple planar-symmetric impinging jets," Phys. Fluids **29**, 105111 (2017).

[7] S. Long, T. C. W. Lau, A. Chinnici, Z. F. Tian, B. B. Dally, and G. J. Nathan, "Iso-thermal flow characteristics of rotationally symmetric jets generating a swirl within a cylindrical chamber," Phys. Fluids **30**, 055110 (2018).

[8] S. Long, T. C. W. Lau, A. Chinnici, Z. F. Tian, B. B. Dally, and G. J. Nathan, "The influence of aspect ratio on the iso-thermal flow characteristics of multiple confined jets," Phys. Fluids **30**, 125108 (2018).

[9] N. Syred, "A review of oscillation mechanisms and the role of the precessing vortex core (PVC) in swirl combustion systems," Prog. Energy Combust. Sci. **32**, 93 (2006).

[10] G. Nathan, D. Battye, and P. Ashman, "Economic evaluation of a novel fuel-saver hybrid combining a solar receiver with a combustor for a solar power tower," Appl. Energy **113**, 1235 (2014).

[11] A. Chinnici, Z. F. Tian, J. H. Lim, G. J. Nathan, and B. B. Dally, "Comparison of system performance in a hybrid solar receiver combustor operating with MILD and conventional combustion. Part I: Solar-only and combustion-only employing conventional combustion," Sol. Energy **147**, 489 (2017).

[12] A. Chinnici, Z. F. Tian, J. H. Lim, G. J. Nathan, and B. B. Dally, "Comparison of system performance in a hybrid solar receiver combustor operating with MILD and conventional combustion. Part II: Effect of the combustion mode," Sol. Energy **147**, 479 (2017).

[13] M. Escudier, A. Nickson, and R. Poole, "Influence of outlet geometry on strongly swirling turbulent flow through a circular tube," Phys. Fluids **18**, 125103 (2006).

[14] P. Wang, X.-S. Bai, M. Wessman, and J. Klingmann, "Large eddy simulation and experimental studies of a confined turbulent swirling flow," Phys. Fluids **16**, 3306 (2004).

[15] Y. Wang, X. Wang, and V. Yang, "Evolution and transition mechanisms of internal swirling flows with tangential entry," Phys. Fluids **30**, 013601 (2018).

[16] J. Jiao, Z. Liu, and Y. Zheng, "Evaluations and modifications on Reynolds stress model in cyclone simulations," Chem. Eng. Technol. **30**, 15 (2007).

[17] T. Chammem, O. Vauquelin, and H. Mhiri, "Performance evaluation of alternative tunnel longitudinal ventilation systems using two inclined jets," Tunnelling Underground Space Technol. **41**, 53 (2014).

[18] Y. Wang and V. Yang, "Central recirculation zones and instability waves in internal swirling flows with an annular entry," Phys. Fluids **30**, 013602 (2018).

[19] A. Ridluan, S. Eiamsa-ard, and P. Promvonge, "Numerical simulation of 3D turbulent isothermal flow in a vortex combustor," Int. Commun. Heat Mass Transfer **34**, 860 (2007).

[20] A. Z'graggen, P. Haueter, D. Trommer, M. Romero, J. De Jesus, and A. Steinfeld, "Hydrogen production by steam-gasification of petroleum coke using concentrated solar power—II Reactor design, testing, and modeling," Int. J. Hydrogen Energy **31**, 797 (2006).

[21] N. Ozalp, M.-H. Chien, and G. Morrison, "Computational fluid dynamics and particle image velocimetry characterization of a solar cyclone reactor," J. Sol. Energy Eng. **135**, 031003 (2013).

[22] L. O. Schunk, P. Haeberling, S. Wepf, D. Wuillemin, A. Meier, and A. Steinfeld, "A receiver-reactor for the solar thermal dissociation of zinc oxide," J. Sol. Energy Eng. **130**, 021009 (2008).

[23] D. Hirsch and A. Steinfeld, "Solar hydrogen production by thermal decomposition of natural gas using a vortex-flow reactor," Int. J. Hydrogen Energy **29**, 47 (2004).

[24] G. Nathan, S. Hill, and R. Luxton, "An axisymmetric 'fluidic' nozzle to generate jet precession," J. Fluid Mech. **370**, 347 (1998).

[25] G. Schneider, D. Froud, N. Syred, G. Nathan, and R. Luxton, "Velocity measurements in a precessing jet flow using a three dimensional LDA system," Exp. Fluids **23**, 89 (1997).

[26] N. Grosjean, L. Graftieaux, M. Michard, W. Hübner, C. Tropea, and J. Volkert, "Combining LDA and PIV for turbulence measurements in unsteady swirling flows," Meas. Sci. Technol. **8**, 1523 (1997).

[27] F. Martinelli, A. Olivani, and A. Coghe, "Experimental analysis of the precessing vortex core in a free swirling jet," Exp. Fluids **42**, 827 (2007).

[28] N. Syred and J. Beer, "Combustion in swirling flows: A review," Combust. Flame **23**, 143 (1974).

[29] A. Chinnici, Y. Xue, T. C. Lau, M. Arjomandi, and G. J. Nathan, "Experimental and numerical investigation of the flow characteristics within a solar expanding-vortex particle receiver-reactor," Sol. Energy **141**, 25 (2017).

[30] A. Valera-Medina, N. Syred, and A. Griffiths, "Visualisation of isothermal large coherent structures in a swirl burner," Combust. Flame **156**, 1723 (2009).

[31] M. Bauerheim, F. Nicoud, and T. Poinsot, "Progress in analytical methods to predict and control azimuthal combustion instability modes in annular chambers," Phys. Fluids **28**, 021303 (2016).

[32] S. I. Voropayev, X. Sanchez, C. Nath, S. Webb, and H. J. S. Fernando, "Evolution of a confined turbulent jet in a long cylindrical cavity: Homogeneous fluids," Phys. Fluids **23**, 115106 (2011).

[33] N. Syred and K. Dahman, "Effect of high levels of confinement upon the aerodynamics of swirl burners," J. Energy **2**, 8 (1978).

[34] A. K. Gupta, D. G. Lilley, and N. Syred, "Swirl flows," in *Tunbridge Wells* (Abacus Press, Kent, England, 1984), p. 488.

[35] D. M. Markovich, S. S. Abdurakipov, L. M. Chikishev, V. M. Dulin, and K. Hanjalić, "Comparative analysis of low- and high-swirl confined flames and jets by proper orthogonal and dynamic mode decompositions," Phys. Fluids **26**, 065109 (2014).

[36] J. Nikuradse, "Gesetzmäßigkeiten der turbulenten strömung in glatten rohren," Forsch. Geb. Ingenieurwes. **4**, 44 (1933).

[37] M. Vanierschot and E. Van den Bulck, "Hysteresis in flow patterns in annular swirling jets," Exp. Therm. Fluid Sci. **31**, 513 (2007).

[38] M. S. Chong, A. E. Perry, and B. J. Cantwell, "A general classification of three-dimensional flow fields," Phys. Fluids **2**, 765 (1990).

[39] A. E. Perry and M. S. Chong, "A description of eddying motions and flow patterns using critical-point concepts," Annu. Rev. Fluid Mech. **19**, 125 (1987).

[40] O. Kitoh, "Experimental study of turbulent swirling flow in a straight pipe," J. Fluid Mech. **225**, 445 (1991).

[41] F. Chang and V. Dhir, "Turbulent flow field in tangentially injected swirl flows in tubes," Int. J. Heat Fluid Flow **15**, 346 (1994).

[42] A. Hoekstra, J. Derksen, and H. Van Den Akker, "An experimental and numerical study of turbulent swirling flow in gas cyclones," Chem. Eng. Sci. **54**, 2055 (1999).

[43] P. Billant, J.-M. Chomaz, and P. Huerre, "Experimental study of vortex breakdown in swirling jets," J. Fluid Mech. **376**, 183 (1998).

[44] F. Gallaire and J.-M. Chomaz, "Instability mechanisms in swirling flows," Phys. Fluids **15**, 2622 (2003).

[45] M. Vanierschot and E. Van den Bulck, "Influence of swirl on the initial merging zone of a turbulent annular jet," Phys. Fluids **20**, 105104 (2008).

[46] J. Volkert, C. Tropea, R. Domann, and W. Hübner, "Combined application of particle image velocimetry (PIV) and laser Doppler anemometry, (LDA) to swirling flows under compression," in *Proceedings of the 8th International Symposia on Applications of Laser Techniques to Fluid Mechanics* (Springer-Verlag, 1996), Vol. 19, pp. 1–19.

Chapter 8

8 Conclusions and Future Work

8.1 Conclusions

The thesis provides a new understanding of the large-scale flow dynamics generated by multiple-jets confined in a cylindrical chamber. It was found that the annular arrangement of multiple impinging jets forms a resulting jet flow downstream from the jet merging point, generating an external recirculation zone (ERZ) and a central recirculation zone (CRZ). The flow-field downstream from the merging point reveals strong qualitative similarity to single-jet, parallel-jets and swirling-jets flow but retains significant quantitative differences. New qualitative and quantitative information has been added to the flow-field of multiple confined jets for model development and validation.

The key findings of the present study are as follows:

1. An increase in the inclination angle α_j from 0° to 90° was found to move the jet merging point further upstream by up to 60%, while an increase in the number of jets N_j from 2 to 4 only changes the location of this point by 5%. The velocity decay within the region of the resulting jet generated by α_j (planar-symmetric) was found to be at least 60% greater than a single unconfined free jet, but 20% lower than that generated by the combination of α_j and azimuthal angle θ_j (rotationally-symmetric). This is due to the combined effects of the cylindrical-wall confinement and the strong interaction between inlet-jets. However, a decrease in the chamber aspect ratio L_c/D_c from 3 to 2 was also found to increase the velocity field of the resulting jet by up to 40%, while its strength decreases by up to 50% as L_c/D_c is further reduced to 1 due to the confinement effect from the bluff end-wall.

2. The velocity fluctuation within the region of the resulting jet generated by either multiple swirling or non-swirling confined jets was found to be at least 50% higher than a single unconfined free jet. This is partly attributed to the role of confinement and partly to the additional unsteadiness caused by the jet impingement. An increase in N_j was also found to reduce the fluctuation of velocity by up to 50%, due to the reduction in the lateral spread of the resulting jet. The presence of a relatively large θ_j (e.g., $\theta_j \geq 10^\circ$), or a short chamber length (e.g., $L_c/D_c = 1$) inhibits the large-scale oscillations (e.g., jet precession) that are otherwise associated with the jet merging point, although the degree of velocity fluctuations within the ERZ is typically up to 60% higher than that in the CRZ for all investigated conditions.

3. For configurations of multiple swirling jets (rotationally-symmetric), the value of swirling velocity U_θ is the strongest (up to 12% of the nozzle exit velocity U_e) and is almost independent of the axial locations within the CRZ, while U_θ is relatively weak ($U_\theta \approx 0.01 \sim 0.03U_e$) and decays much faster within the ERZ. For a given location within a cylindrical chamber, a higher value of both α_j and θ_j (e.g., $\alpha_j = 45^\circ$ and $\theta_j = 15^\circ$) leads to an approximately 60% increase in the strength of swirl, resulting in the presence of a Rankine (the combination of forced and free) vortex.

4. Precessing flows such as the precessing vortex core (PVC) has been identified for all configurations of multiple confined jets in this study. The significance of the PVC tends to be amplified for the cases with a dominant ERZ (e.g., $\alpha_j = 25^\circ$ and $\theta_j = 5^\circ$), but to be inhibited for the dominant CRZ cases (e.g., $\alpha_j = 45^\circ$ and $\theta_j = 15^\circ$). This is evidenced by up to 80% smaller displacement of the vortex-core relative to the centre of the chamber (r_{core}) for the dominant CRZ regime.

5. The present study has identified all of the major flow regimes that can be generated by the combination of α_j, θ_j and L_c/D_c within a cylindrical chamber. It was found that an increase in α_j from 0° to 90° leads to the presence of an ERZ and the absence of a CRZ, while a larger α_j (e.g., $\alpha_j \geq 35^\circ$) also generates a secondary ERZ upstream from the jet merging point. It was also found that an increase in θ_j from 0° to 15° increases the size of the CRZ and decreases the size of the ERZ. However, a decrease in chamber length from $L_c/D_c = 3$ to 1 reduces both the size of the ERZ and CRZ significantly.

6. For applications of combustion and solar thermal devices, it was found that the value of θ_j should be sufficiently low (e.g., $\theta_j < 10^\circ$) and the value of α_j should not exceed approximately 65° for $N_j = 2$ and 55° for $N_j = 4$ configurations to minimize the risk of transporting fluid from the chamber to the aperture. This finding is crucial for relevant configurations (such as the HSRC) to maintain high reactor efficiency and thermal performance. In addition, it was also found that the value of α_j should be approximately $10^\circ \sim 35^\circ$ to provide the greatest total mass of recirculated fluid and a uniform recirculation zone. This is important for combustion technologies, particularly for MILD (Moderate or Intense Low-oxygen Dilution) combustion regime, since the recirculation zone is associated with high rates of mixing, heat transfer, and quasi-homogeneous temperature within the chamber.

8.2 Recommendations for further work

It is recommended that new systematic investigations should be conducted to extend the current study of multiple annular jets from iso-thermal to reacting flow conditions. For example, to further investigate the thermal performance of configurations that avoid the transport of flow from chamber to the aperture (e.g., $\alpha_j < 55^\circ$ and $\theta_j > 10^\circ$). This study extends the finding from the present study to more complex flow conditions, which can quantify the important parameters such as recirculation rate and heat transfer efficiency for reacting flow and provide benefit to the future development and refinement of combustion technologies. Further numerical study of the PVCs and precession-jet should also be included for both the iso-thermal and reacting flow conditions to motivate the continuous development of the most accurate modelling approaches for multiple confined jets.

In addition, it is also recommended that further extension work should be proposed to investigate the influence of the wind effects on the internal flow-field generated by multiple annular jets within a cylindrical chamber. This is because that the majority of solar thermal devices is designed to be operated on top of the tower (≈ 100 m in height) where the wind (e.g., wind speed and direction) tends to significantly change the flow patterns and convective heat losses within the cavity. However, to my best knowledge, no previous study has fully characterised the effects of external wind on the flow-field generated by multiple confined jets. Hence, a better understanding of the external flow could potentially benefit the improvement of heat transfer and thermal efficiency for practical combustion and solar thermal devices such as the HSRC technology.

The final recommendation for future work is to develop a cost-effective solution to mitigate the potential negative effects of the wind on the flow-field generated by multiple confined jets within a cylindrical chamber. For example, to identify the potential arrangement of aerodynamic curtains to reduce the convective heat loss of the HSRC within the solar and mixed modes (aperture shutter is open). It has been found that the majority of the investigations of the aerodynamic curtains was performed almost exclusively for numerical simulation, while no reliable experimental data is yet available for multiple annular jets in an axisymmetric chamber. Hence, it is recommended to conduct a systematic study with well-defined inflow and boundary conditions to optimise the performance of aerodynamic curtains for multiple annular jets within a cylindrical chamber.

References

1. Pope, S., *An explanation of the turbulent round-jet/plane-jet anomaly.* AIAA journal, 1978. **16**(3): p. 279-281.

2. Boersma, B., Brethouwer, G., and Nieuwstadt, F., *A numerical investigation on the effect of the inflow conditions on the self-similar region of a round jet.* Physics of Fluids, 1998. **10**(4): p. 899-909.

3. Lockwood, F. and Naguib, A., *The prediction of the fluctuations in the properties of free, round-jet, turbulent, diffusion flames.* Combustion and Flame, 1975. **24**: p. 109-124.

4. Yule, A., *Large-scale structure in the mixing layer of a round jet.* Journal of Fluid Mechanics, 1978. **89**(03): p. 413-432.

5. Jambunathan, K., Lai, E., Moss, M., and Button, B., *A review of heat transfer data for single circular jet impingement.* International Journal of Heat and Fluid Flow, 1992. **13**(2): p. 106-115.

6. Koepf, E., Villasmil, W., and Meier, A., *High Temperature Flow Visualization and Aerodynamic Window Protection of a 100-kW th Solar Thermochemical Receiver-reactor for ZnO Dissociation.* Energy Procedia, 2015. **69**: p. 1780-1789.

7. Cox, G., *Multiple jet correlations for gas turbine engine combustor design.* Journal of Engineering for Power, 1976. **98**(2): p. 265-272.

8. Chammem, T., Mhiri, H., and Vauquelin, O., *Experimental and computational investigation of Reynolds number effect on the longitudinal ventilation in large enclosure of twin inclined jets.* Building and Environment, 2013. **67**: p. 87-96.

9. Boushaki, T. and Sautet, J.-C., *Characteristics of flow from an oxy-fuel burner with separated jets: influence of jet injection angle.* Experiments in Fluids, 2010. **48**(6): p. 1095-1108.

10. Moore, J. and Apt, J., *Can hybrid solar-fossil power plants mitigate CO2 at lower cost than PV or CSP?* Environmental Science & Technology, 2013. **47**(6): p. 2487-2493.

11. Jin, H.G. and Hong, H., *12 - Hybridization of concentrating solar power (CSP) with fossil fuel power plants*, in *Concentrating Solar Power Technology*, K. Lovegrove and W. Stein, Editors. 2012, Woodhead Publishing. p. 395-420.

12. Wright, M. and Hearps, P., 2010. *Zero Carbon Australia Stationary Energy Plan: Australian Sustainable Energy*. Melbourne Energy Institute, University of Melbourne.

13. Cavaliere, A. and de Joannon, M., *Mild Combustion.* Progress in Energy and Combustion Science, 2004. **30**(4): p. 329-366.

14. Nathan, G.J., Jafarian, M., Dally, B.B., Saw, W.L., Ashman, P.J., Hu, E., and Steinfeld, A., *Solar thermal hybrids for combustion power plant: A growing opportunity.* Progress in Energy and Combustion Science, 2018. **64**: p. 4-28.

15. Nathan, G., Dally, B., Alwahabi, Z., van Eyk, P., Jafarian, M., and Ashman, P., *Research challenges in combustion and gasification arising from emerging technologies employing directly irradiated concentrating solar thermal radiation.* Proceedings of the Combustion Institute, 2017. **36**(2): p. 2055-2074.

16. Mehos, M.S., Anselmo, K.M., Moreno, J.B., Andraka, C.E., Rawlinson, K.S., Corey, J., and Bohn, M.S., *Combustion system for hybrid solar fossil fuel receiver*. 2004. (No. 6,739,136). National Renewable Energy Lab.(NREL), Golden, CO (United States).

17. Nathan, G., Battye, D., and Ashman, P., *Economic evaluation of a novel fuel-saver hybrid combining a solar receiver with a combustor for a solar power tower.* Applied Energy, 2014. **113**: p. 1235-1243.

18. Lim, J.H., Chinnici, A., Dally, B.B., and Nathan, G.J., *Assessment of the potential benefits and constraints of a hybrid solar receiver and combustor operated in the MILD combustion regime.* Energy, 2016. **116, Part 1**: p. 735-745.

19. Chinnici, A., Tian, Z.F., Lim, J.H., Nathan, G.J., and Dally, B.B., *Comparison of system performance in a hybrid solar receiver combustor operating with MILD and conventional combustion. Part I: Solar-only and combustion-only employing conventional combustion.* Solar Energy, 2017. **147**: p. 489-503.

20. Chinnici, A., Tian, Z.F., Lim, J.H., Nathan, G.J., and Dally, B.B., *Comparison of system performance in a hybrid solar receiver combustor operating with MILD and conventional combustion. Part II: Effect of the combustion mode.* Solar Energy, 2017. **147**: p. 479-488.

21. Chinnici, A., Nathan, G., and Dally, B., *Experimental demonstration of the hybrid solar receiver combustor.* Applied Energy, 2018. **224**: p. 426-437.

22. Chinnici, A., Nathan, G., and Dally, B., *An experimental study of the stability and performance characteristics of a Hybrid Solar Receiver Combustor operated in the MILD combustion regime.* Proceedings of the Combustion Institute, 2018. **37**(4): p. 5687-5695.

23. Lim, J.H., Nathan, G.J., Hu, E., and Dally, B.B., *Analytical assessment of a novel hybrid solar tubular receiver and combustor.* Applied Energy, 2016. **162**: p. 298-307.

24. Nathan, G., Dally, B., Ashman, P., and Steinfeld, A., *A hybrid receiver-combustor*. 2013, Provisional Patent Application No. 2012/901258., Adelaide Research and Innovation Pty. Ltd.; 2012 [Priority Date: 29.03.2].

25. Z'Graggen, A., 2008. *Solar Gasification of Carbonaceous Materials: Reactor Design, Modeling and Experimentation*. (Doctoral dissertation, ETH Zurich).

26. Tan, T., Chen, Y., Chen, Z., Siegel, N., and Kolb, G.J., Wind effect on the performance of solid particle solar receivers with and without the protection of an aerowindow. Solar Energy, 2009. 83(10): p. 1815-1827.

27. Z’graggen, A., Haueter, P., Trommer, D., Romero, M., De Jesus, J., and Steinfeld, A., *Hydrogen production by steam-gasification of petroleum coke using concentrated solar power—II Reactor design, testing, and modeling.* International Journal of Hydrogen Energy, 2006. **31**(6): p. 797-811.

28. Hussein, H.J., Capp, S.P., and George, W.K., *Velocity measurements in a high-Reynolds-number, momentum-conserving, axisymmetric, turbulent jet.* Journal of Fluid Mechanics, 1994. **258**: p. 31-75.

29. Becker, H. and Booth, B., *Mixing in the interaction zone of two free jets.* AIChE Journal, 1975. **21**(5): p. 949-958.

30. Fitzgerald, J.A. and Garimella, S.V., *A study of the flow field of a confined and submerged impinging jet.* International Journal of Heat and Mass Transfer, 1998. **41**(8-9): p. 1025-1034.

31. Deo, R.C., Mi, J., and Nathan, G.J., *The influence of Reynolds number on a plane jet.* Physics of Fluids, 2008. **20**(7): p. 075108.

32. Boushaki, T., Sautet, J., Salentey, L., and Labegorre, B., *The behaviour of lifted oxy-fuel flames in burners with separated jets.* International Communications in Heat and Mass Transfer, 2007. **34**(1): p. 8-18.

33. Chinnici, A., Xue, Y., Lau, T.C., Arjomandi, M., and Nathan, G.J., *Experimental and numerical investigation of the flow characteristics within a Solar Expanding-Vortex Particle Receiver-Reactor.* Solar Energy, 2017. **141**: p. 25-37.

34. Vanierschot, M. and Van den Bulck, E., *Influence of swirl on the initial merging zone of a turbulent annular jet.* Physics of Fluids, 2008. **20**(10): p. 105104.

35. Thong, C.X., Kalt, P.A., Dally, B.B., and Birzer, C.H., *Flow dynamics of multi-lateral jets injection into a round pipe flow.* Experiments in Fluids, 2015. **56**(1): p. 1-16.

36. Tanaka, E., *The interference of two-dimensional parallel jets: 1st report, experiments on dual jet.* Bulletin of JSME, 1970. **13**(56): p. 272-280.

37. Syred, N., *A review of oscillation mechanisms and the role of the precessing vortex core (PVC) in swirl combustion systems.* Progress in Energy and Combustion Science, 2006. **32**(2): p. 93-161.

38. Worth, N.A., Dawson, J.R., Sidey, J.A.M., and Mastorakos, E., *Azimuthally forced flames in an annular combustor.* Proceedings of the Combustion Institute, 2017. **36**(3): p. 3783-3790.

39. Worth, N.A. and Dawson, J.R., *Effect of equivalence ratio on the modal dynamics of azimuthal combustion instabilities.* Proceedings of the Combustion Institute, 2017. **36**(3): p. 3743-3751.

40. Prieur, K., Durox, D., Schuller, T., and Candel, S., *A hysteresis phenomenon leading to spinning or standing azimuthal instabilities in an annular combustor.* Combustion and Flame, 2017. **175**: p. 283-291.

41. Chen, H.J., Moshfegh, B., and Cehlin, M., *Numerical investigation of the flow behavior of an isothermal impinging jet in a room.* Building and Environment, 2012. **49**: p. 154-166.

42. Al-Sanea, S.A., Zedan, M.F., and Al-Harbi, M.B., *Effect of supply Reynolds number and room aspect ratio on flow and ceiling heat-transfer coefficient for mixing ventilation.* International Journal of Thermal Sciences, 2012. **54**: p. 176-187.

43. Deo, R.C., Mi, J., and Nathan, G.J., *The influence of nozzle aspect ratio on plane jets.* Experimental Thermal and Fluid Science, 2007. **31**(8): p. 825-838.

44. Nasr, A. and Lai, J., *Two parallel plane jets: mean flow and effects of acoustic excitation.* Experiments in Fluids, 1997. **22**(3): p. 251-260.

45. Faghani, E. and Rogak, S.N., *A phenomenological model of two circular turbulent jets.* International Journal of Engine Research, 2013. **14**(3): p. 293-304.

46. Faghani, E. and Rogak, S.N., *Application of CFD and Phenomenological Models in Studying Interaction of Two Turbulent Plane Jets.* Journal ISSN, 2012. **1929**: p. 2724.

47. Leite, A., Ferreira, M., and Carvalho, J., *An investigation of multiple jet acetylene flames.* International Communications in Heat and Mass Transfer, 1996. **23**(7): p. 959-970.

48. Tanaka, E., *The interference of two-dimensional parallel jets: 2nd report, experiments on the combined flow of dual jet.* Bulletin of JSME, 1974. **17**(109): p. 920-927.

49. Tanaka, E. and Nakata, S., *The Interference of Two-Dimensional Parallel Jets: 3rd Report, The Region near the Nozzles in Triple Jets.* Bulletin of JSME, 1975. **18**(124): p. 1134-1141.

50. Raghunathan, S. and Reid, I., *A study of multiple jets.* AIAA Journal, 1981. **19**(1): p. 124-127.

51. Menon, R. and Gollahalli, S., *Combustion characteristics of interacting multiple jets in cross flow.* Combustion Science and Technology, 1988. **60**(4-6): p. 375-389.

52. Moustafa, G.H., *Experimental investigation of high-speed twin jets.* AIAA Journal, 1994. **32**(11): p. 2320-2322.

53. Yimer, J., Becker, H., and Grandmaison, E., *Development of flow from multiple-jet burners.* The Canadian Journal of Chemical Engineering, 1996. **74**(6): p. 840-851.

54. Gao, Z., Han, J., Xu, Y., Bao, Y., and Li, Z., *Particle image velocimetry (PIV) investigation of flow characteristics in confined impinging jet reactors.* Industrial & Engineering Chemistry Research, 2013. **52**(33): p. 11779-11786.

55. Gavi, E., Marchisio, D.L., and Barresi, A.A., *CFD modelling and scale-up of Confined Impinging Jet Reactors.* Chemical Engineering Science, 2007. **62**(8): p. 2228-2241.

56. Klein, M., Sadiki, A., and Janicka, J., *Investigation of the influence of the Reynolds number on a plane jet using direct numerical simulation.* International Journal of Heat and Fluid Flow, 2003. **24**(6): p. 785-794.

57. Dimotakis, P.E., *The mixing transition in turbulent flows.* Journal of Fluid Mechanics, 2000. **409**: p. 69-98.

58. Nathan, G.J., Mi, J., Alwahabi, Z.T., Newbold, G.J.R., and Nobes, D.S., *Impacts of a jet's exit flow pattern on mixing and combustion performance.* Progress in Energy and Combustion Science, 2006. **32**(5–6): p. 496-538.

59. Mi, J., Nobes, D., and Nathan, G., *Influence of jet exit conditions on the passive scalar field of an axisymmetric free jet.* Journal of Fluid Mechanics, 2001. **432**: p. 91-125.

60. Chammem, T., Vauquelin, O., and Mhiri, H., *Performance evaluation of alternative tunnel longitudinal ventilation systems using two inclined jets.* Tunnelling and Underground Space Technology, 2014. **41**: p. 53-61.

61. Boushaki, T., Mergheni, M., Sautet, J., and Labegorre, B., *Effects of inclined jets on turbulent oxy-flame characteristics in a triple jet burner.* Experimental Thermal and Fluid Science, 2008. **32**(7): p. 1363-1370.

62. Li, C.C., Chen, J.W., and Yang, J.T., *Stabilization of double flames interacting with the intersecting flow on a V-shaped burner.* Combustion Science and Technology, 2012. **184**(12): p. 2117-2135.

63. Radhouane, A., Mahjoub Saïd, N., Mhiri, H., Bournot, P., and Le Palec, G., *Twin inclined jets in crossflow: experimental investigation of different flow regimes and jet elevations.* Environmental Fluid Mechanics, 2016. **16**(1): p. 45-67.

64. Billant, P., Chomaz, J.-M., and Huerre, P., *Experimental study of vortex breakdown in swirling jets.* Journal of Fluid Mechanics, 1998. **376**: p. 183-219.

65. Lucca-Negro, O. and O'doherty, T., *Vortex breakdown: a review.* Progress in Energy and Combustion Science, 2001. **27**(4): p. 431-481.

66. Roux, S., Lartigue, G., Poinsot, T., Meier, U., and Bérat, C., *Studies of mean and unsteady flow in a swirled combustor using experiments, acoustic analysis, and large eddy simulations.* Combustion and Flame, 2005. **141**(1): p. 40-54.

67. Vanierschot, M. and Van den Bulck, E., *Hysteresis in flow patterns in annular swirling jets.* Experimental Thermal and Fluid Science, 2007. **31**(6): p. 513-524.

68. Wang, P., Bai, X.-S., Wessman, M., and Klingmann, J., *Large eddy simulation and experimental studies of a confined turbulent swirling flow.* Physics of Fluids, 2004. **16**(9): p. 3306-3324.

69. Vashahi, F., Lee, S., and Lee, J., *Experimental analysis of the swirling flow in a model rectangular gas turbine combustor.* Experimental Thermal and Fluid Science, 2016. **76**(Supplement C): p. 287-295.

70. Khalil, A.E., Brooks, J.M., and Gupta, A.K., *Impact of confinement on flowfield of swirl flow burners.* Fuel, 2016. **184**: p. 1-9.

71. Beér, J.M. and Chigier, N.A., *Combustion aerodynamics.* New York, 1972.

72. Gupta, A.K., Lilley, D.G., and Syred, N., *Swirl flows.* Tunbridge Wells, Kent, England, Abacus Press, 1984, 488 p., 1984.

73. Syred, N. and Beer, J., *Combustion in swirling flows: a review.* Combustion and Flame, 1974. **23**(2): p. 143-201.

74. Sheen, H., Chen, W., and Jeng, S., *Recirculation zones of unconfined and confined annular swirling jets.* AIAA Journal, 1996. **34**(3): p. 572-579.

75. Ridluan, A., Eiamsa-ard, S., and Promvonge, P., *Numerical simulation of 3D turbulent isothermal flow in a vortex combustor.* International Communications in Heat and Mass Transfer, 2007. **34**(7): p. 860-869.

76. Chinnici, A., Arjomandi, M., Tian, Z., and Nathan, G., *A Novel Solar Expanding-Vortex Particle Reactor: Experimental and Numerical Investigation of the Iso-thermal Flow Field and Particle Deposition.* Solar Energy, 2016. **133**: p. 451-464.

77. Tian, Z.F., Nathan, G.J., and Cao, Y., *Numerical modelling of flows in a solar–enhanced vortex gasifier: Part 1, comparison of turbulence models.* Progress in Computational Fluid Dynamics, an International Journal, 2015. **15**(2): p. 114-122.

78. Ozalp, N., Chien, M.-H., and Morrison, G., *Computational fluid dynamics and particle image velocimetry characterization of a solar cyclone reactor.* Journal of Solar Energy Engineering, 2013. **135**(3): p. 031003.

79. Krishna, D.J. and Ozalp, N., *Numerical investigation of particle deposition inside aero-shielded solar cyclone reactor: A promising solution for reactor clogging.* International Journal of Heat and Fluid Flow, 2013. **40**: p. 198-209.

80. Shephered, C. and Lapple, C., *Flow pattern and pressure drop in cyclone dust collectors.* Industrial & Engineering Chemistry, 1939. **31**(8): p. 972-984.

81. Schunk, L.O., Haeberling, P., Wepf, S., Wuillemin, D., Meier, A., and Steinfeld, A., *A receiver-reactor for the solar thermal dissociation of zinc oxide.* Journal of Solar Energy Engineering, 2008. **130**(2): p. 021009.

82. Hirsch, D. and Steinfeld, A., *Solar hydrogen production by thermal decomposition of natural gas using a vortex-flow reactor.* International Journal of Hydrogen Energy, 2004. **29**(1): p. 47-55.

83. Launder, B., Reece, G.J., and Rodi, W., *Progress in the development of a Reynolds-stress turbulence closure.* Journal of Fluid Mechanics, 1975. **68**(3): p. 537-566.

84. Morris, G.K. and Garimella, S.V., *Orifice and impingement flow fields in confined jet impingement.* Journal of Electronic Packaging, 1998. **120**(1): p. 68-72.

85. Morris, G., Garimella, S., and Fitzgerald, J., *Flow-field prediction in submerged and confined jet impingement using the Reynolds stress model.* Journal of Electronic Packaging, 1999. **121**(4): p. 255-262.

86. Garimella, S.V. and Rice, R., *Confined and submerged liquid jet impingement heat transfer.* Journal of Heat Transfer, 1995. **117**(4): p. 871-877.

87. Guo, T., Rau, M.J., Vlachos, P.P., and Garimella, S.V., *Axisymmetric wall jet development in confined jet impingement.* Physics of Fluids, 2017. **29**(2): p. 025102.

88. Kao, Y.-H., Tambe, S.B., and Jeng, S.-M., *Effect of chamber length with converging exhaust on swirling flow field characteristics of a counter-rotating radial-radial swirler.* in ASME Turbo Expo 2013: Turbine Technical Conference and Exposition (American Society of Mechanical Engineers, 2013), p. V01BT04A026.

89. Khelil, A., Naji, H., Loukarfi, L., Meliani, M.H., and Braikia, M., *Numerical simulation of the interactions among multiple turbulent swirling jets mounted in unbalanced positions.* Applied Mathematical Modelling, 2016. **40**(5): p. 3749-3763.

90. Wünning, J. and Wünning, J., *Flameless oxidation to reduce thermal NO-formation.* Progress in Energy and Combustion Science, 1997. **23**(1): p. 81-94.

91. Mi, J., Wang, F., Li, P., and Dally, B., *Modified vitiation in a moderate or intense low-oxygen dilution (MILD) combustion furnace.* Energy & Fuels, 2011. **26**(1): p. 265-277.

92. Szegö, G., Dally, B., and Nathan, G., *Operational characteristics of a parallel jet MILD combustion burner system.* Combustion and Flame, 2009. **156**(2): p. 429-438.

93. Nathan, G., Hill, S., and Luxton, R., *An axisymmetric 'fluidic'nozzle to generate jet precession.* Journal of Fluid Mechanics, 1998. **370**: p. 347-380.

94. Schneider, G., Froud, D., Syred, N., Nathan, G., and Luxton, R., *Velocity measurements in a precessing jet flow using a three dimensional LDA system.* Experiments in Fluids, 1997. **23**(2): p. 89-98.

95. Grosjean, N., Graftieaux, L., Michard, M., Hübner, W., Tropea, C., and Volkert, J., *Combining LDA and PIV for turbulence measurements in unsteady swirling flows.* Measurement Science and Technology, 1997. **8**(12): p. 1523.

96. Martinelli, F., Olivani, A., and Coghe, A., *Experimental analysis of the precessing vortex core in a free swirling jet.* Experiments in Fluids, 2007. **42**(6): p. 827-839.

97. Valera-Medina, A., Syred, N., and Griffiths, A., *Visualisation of isothermal large coherent structures in a swirl burner.* Combustion and Flame, 2009. **156**(9): p. 1723-1734.

98. Syred, N. and Dahman, K., *Effect of high levels of confinement upon the aerodynamics of swirl burners.* Journal of Energy, 1978. **2**(1): p. 8-15.

99. Liu, Y., Olsen, M.G., and Fox, R.O., *Turbulence in a microscale planar confined impinging-jets reactor.* Lab on a Chip, 2009. **9**(8): p. 1110-1118.

100. Adrian, R.J., *Twenty years of particle image velocimetry.* Experiments in Fluids, 2005. **39**(2): p. 159-169.

101. Mi, J., Kalt, P., Nathan, G., and Wong, C., *PIV measurements of a turbulent jet issuing from round sharp-edged plate.* Experiments in Fluids, 2007. **42**(4): p. 625-637.

102. Nikuradse, J., *Gesetzmäßigkeiten der turbulenten Strömung in glatten Rohren (Nachtrag).* Forschung im Ingenieurwesen, 1933. **4**(1): p. 44-44.

103. Angioletti, M., Nino, E., and Ruocco, G., *CFD turbulent modelling of jet impingement and its validation by particle image velocimetry and mass transfer measurements.* International Journal of Thermal Sciences, 2005. **44**(4): p. 349-356.

104. Jiao, J., Liu, Z., and Zheng, Y., *Evaluations and modifications on Reynolds stress model in cyclone simulations.* Chemical Engineering & Technology, 2007. **30**(1): p. 15-20.

105. Speziale, C.G., Sarkar, S., and Gatski, T.B., *Modelling the pressure–strain correlation of turbulence: an invariant dynamical systems approach.* Journal of Fluid Mechanics, 1991. **227**: p. 245-272.

106. Gibson, M. and Launder, B., *Ground effects on pressure fluctuations in the atmospheric boundary layer.* Journal of Fluid Mechanics, 1978. **86**(3): p. 491-511.

107. Panda, J., Warrior, H., Maity, S., Mitra, A., and Sasmal, K., *An improved model including length scale anisotropy for the pressure strain correlation of turbulence.* Journal of Fluids Engineering, 2017. **139**(4): p. 044503.

108. Mishra, A.A. and Girimaji, S.S., *Toward approximating non-local dynamics in single-point pressure–strain correlation closures.* Journal of Fluid Mechanics, 2017. **811**: p. 168-188.

Appendix A: CFD Modelling of Isothermal Multiple Jets in a Combustor

Eleventh International Conference on CFD in the Minerals and Process Industries
CSIRO, Melbourne, Australia
7-9 December 2015

CFD MODELLING OF ISOTHERMAL MULTIPLE JETS IN A COMBUSTOR

Shen LONG[1*], Zhao Feng TIAN, Graham NATHAN, Alfonso CHINNICI, Bassam DALLY

[1] School of Mechanical Engineering, The University of Adelaide, South Australia 5005, Australia
*Corresponding author, E-mail address: shen.long@adelaide.edu.au

ABSTRACT

This paper assesses the performance of three turbulence models on the simulation of an isothermal flow from a burner with three separated-jet inlets. This burner has key flow features of a novel hybrid solar receiver combustor (HSRC) that is under development in the Centre for Energy Technology (CET) at the University of Adelaide. Three turbulence models, namely, the Baseline Reynolds Stress (BSL RSM), the Shear-Stress-Transport (SST) and the Standard k-ε (SKE) models were chosen. The paper reports numerical results from two cases of the separated-jet flows. In these two cases, the angle between the side jet and the centre jet is 0° and 20°. The predicted mean velocity profiles at six positions of this burner are compared against experimental results from the literature. It is found that the best prediction is provided by the BSL RSM model, which predicts well the velocity peaks and reproduces the trend of velocity profiles in different axial positions. Importantly, the BSL RSM model has the advantage of predicting anisotropic Reynolds stresses in interacting jet flows. This opens the way to use these models to inform the development of the combustion system within the HSRC.

INTRODUCTION

The concept of integrating Concentrating Solar Thermal (CST) technology and traditional combustion energy is gaining prominence globally due to the complementary nature of these two thermal energy sources (Ordorica-Garcia, Delgado & Garcia 2011). CST can reduce the emission of greenhouse gas and provide a cost-effective way to incorporate solar with thermal energy storage (Steinmann 2012) to overcome the challenge of the intermittent nature of solar radiation (Jin & Hong 2012). The integration of combustion energy source with CST offers a relatively low cost solution which minimises the need for costly long term energy storage and provides certainty for baseload power.

A Hybrid Solar Receiver Combustor (HSRC) has been proposed by the Centre for Energy Technology (CET) at the University of Adelaide, which is a combination of a solar cavity receiver and a gaseous fuel combustor. The HSRC reduces heat losses relative to equivalent hybrids by integrating CST and combustion energy source into a single device (Nathan et al. 2013; Nathan et al. 2009). The HSRC is designed to operate in any of three modes: the ‘combustion only mode’, the ‘solar only mode’ and the ‘mixed mode’. For the ‘solar only mode’, the shutter of Compound Parabolic Concentrator (CPC) is open to allow the entry of concentrated solar radiation into the receiver, so that the heat source for the HSRC is only solar energy. In contrast, the heat source in the ‘combustion only mode’ is derived only from the burning of injected fuel. In the ‘mixed mode’, the heat source for the HSRC is derived from both solar radiation and combustion, with the percentage of each being dependent on the solar intensity available at the time. A schematic diagram of the HSRC is presented in Figure 1.

The HSRC is still in the early stages of development. Owing to the range of operational modes, it can be expected that different flow regimes, flame structures and dominant heat transfer mechanisms will occur at different times inside the HSRC. Hence there is a need to understand the flow dynamics of this unique geometry to design burners that can work effectively. Based on the proposed configurations of the HSRC, multiple burners are distributed within the conical configuration of the chamber with an angle of inclination (β_{jet}) that causes the jets to interact within the chamber (Figure 1). According to Chinnici (2015), by changing the inclination angle of the jet from 30° to 90°, the flow features and combustion behaviours inside the HSRC change dramatically. Therefore, a comprehensive understanding of the influence of interacting jets on flow dynamics inside the HSRC is desirable.

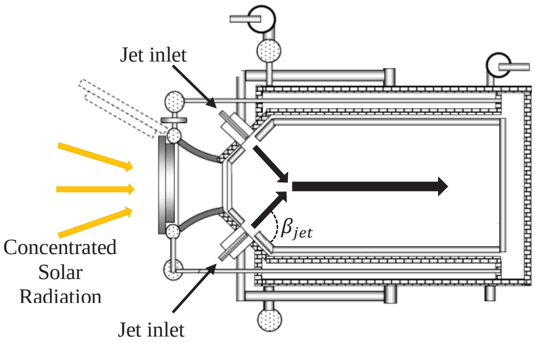

Figure 1: Schematic diagram of the Hybrid Solar Receiver Combustor (Nathan et al. 2013).

Prior to building experimental facilities with which to directly assess the performance of the HSRC, CFD models have been developed using other experimental data from related configurations. Of these, the investigation of interacting jets of an oxy-fuel combustion separated-jet burner developed by Boushaki and Sautet (2010) was chosen for CFD model validation. This burner consists of a central jet of natural gas placed between two oxygen jets, the orientation of which is adjustable (Boushaki et al. 2008; Boushaki et al. 2007). Hence this system has similar features to the multiple-jet configuration of the HSRC. A schematic diagram of this system is shown in Figure 2. Importantly, the work of Boushaki and Sautet (2010) provides sufficient details of the geometry and flow velocity measurement for reliable model development and validation.

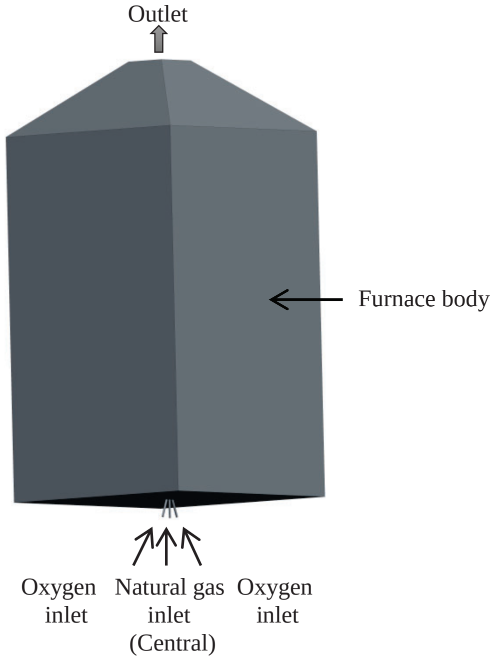

Figure 2: Schematic diagram of the separated-jet burner of Boushaki and Sautet (2010).

In light of the needs mentioned above, the aim of the present paper is to conduct a CFD study to better understand the flow behaviour of inclined jets and to test the performance of different turbulence models in predicting the flow behaviour of a separated-jet burner. The performance of three turbulence models, namely, the Baseline Reynolds Stress (BSL RSM) model, Standard k-ε (SKE) model and Shear-Stress-Transport (SST) model, is evaluated in this study. The selection of these models was based on our previous CFD modelling studies of flows in a solar-enhanced vortex gasifier (Tian, Nathan & Cao 2015). Particularly, this study compares the simulated results against the experimental data of axial velocity profiles at six positions from the burner exit, in non-reacting conditions.

MODEL DESCRIPTION

The computational model of the separated-jet burner shown in Figure 3 was generated with a commercial CAD package Creo 2.0. Two models of the burner have been constructed for the case of $\alpha_{jet} = 0^{\circ}$ and $\alpha_{jet} = 20^{\circ}$. The dimensions of the burner are shown in Table 1.

The ANSYS/ICEM CFD code was used to generate the structural mesh of this computational model. In order to accelerate the process of mesh generation and refinement, the shape of the burner has been simplified by replacing the conical structure of the exhaust duct (Figure 2) with a square structure (Figure 3). While this change will inevitably influence the secondary flows in the chamber, here our primary interest is the first order recirculation flow patterns. Additionally, due to the symmetric configuration of this burner, only a quarter of the full domain was analysed and a symmetric boundary was employed. This results in an efficient use the number of mesh nodes. The mesh quality was checked for expansion factor, aspect ratio, skewness and orthogonality. The influence of the number of mesh nodes on the CFD results was evaluated through a mesh independence test, which is reported in the next section.

The flow field measurements reported by Boushaki and Sautet (2010) were undertaken by replacing natural gas with an inert mixture of 65.38% of nitrogen and 34.63% of helium (by volume) to achieve a similar density to natural gas. Hence in this paper the designation of ‘central jet’ is used to denote the mixed gases in this jet. The mass flow rate of the central jet and oxygen jet were held constant for all simulation cases to match the inlet conditions in the reference paper of Boushaki and Sautet (2010). The detailed boundary conditions are given in Table 2 and 3, and the complete boundary settings and experimental configurations are reported by Boushaki and Sautet (2010).

The CFD calculations were carried out with the commercial Finite Volume code ANSYS CFX 16.1. The convergence criterion for all simulations was set to be 1×10^{-5} (RMS).

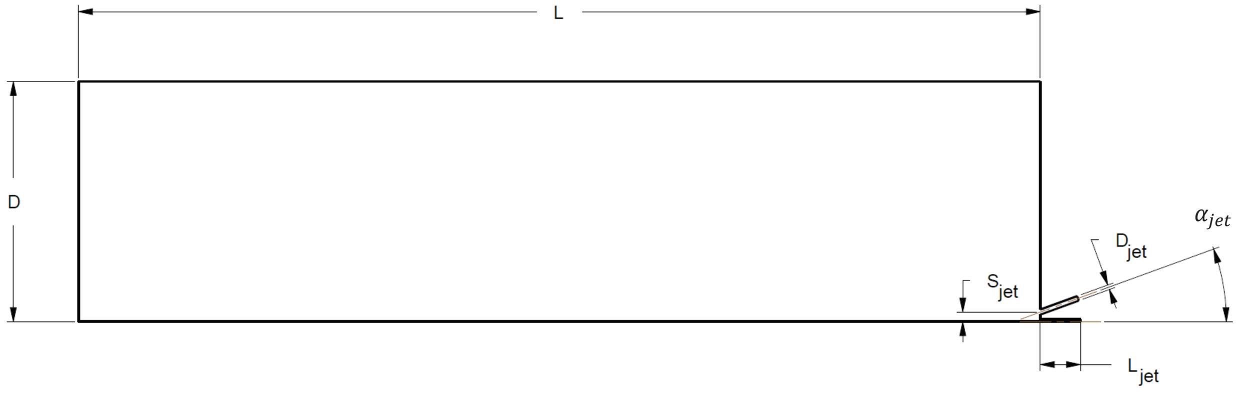

Figure 3: Geometry of the CFD domain.

Dimension	Description	Value (mm)
D	Furnace width (half)	300
L	Furnace length	1200
L_{jet}	Jet inlet length	50
S_{jet}	Distance between jets	12
D_{jet}	Jet diameter	6
α_{jet}	Jet inclination angle	0° and 20°

Table 1: Geometric parameters.

Boundary Type	Mass Flow Rate (kg/s)
Central Inlet	0.000556
Oxygen Inlet	0.001964

Table 2: Inlet boundary details.

Boundary Name	Boundary Type
1,2	Mass flow inlet
3	Opening
4	Symmetric planes
Other	No slip wall

Table 3: Boundary conditions.

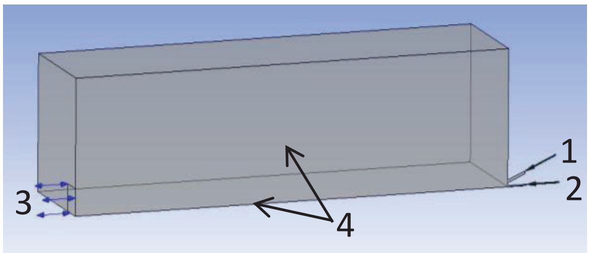

Figure 4: CFD Domain

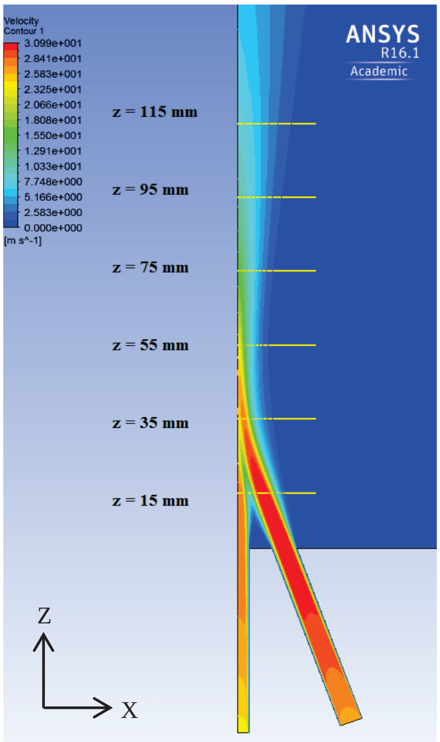

Figure 5: The six measurement planes, together with the mean velocity profile simulated by 4 million mesh nodes with $\boldsymbol{\alpha_{jet} = 20^\circ}$.

RESULTS

Mesh independence test

A series of mesh refinements was carried out for four different grid sizes of 1 million, 2 million, 4 million and 8 million mesh nodes, respectively. The BSL RSM model was chosen to investigate the influence of the number of mesh nodes on the results, for the case with $\alpha_{jet} = 20^\circ$. In the work of Boushaki and Sautet (2010), the mean axial velocity profiles were obtained at six radial traverses at the axial locations of z = 15 mm, 35 mm, 55 mm, 75 mm, 95 mm, 115 mm, as is illustrated in Figure 5. The comparison between the numerical results and experimental data at z = 15 mm and 115 mm is shown in Figure 6. At z = 15 mm (Figure 6 a), it can be seen that there is only a slight difference between the results predicted using these four mesh sizes, and all simulated results are similar to experimental data. At z = 115 mm (Figure 6 b), the prediction also changes little with an increase in the number of mesh nodes, although all models under-predict the velocity profile. This under-prediction may be caused by the inaccurate reproduction of an out-of-plane motion as the mass flow and momentum are conserved. Therefore, 4 million mesh size was chosen to evaluate the performance of turbulence models in this study.

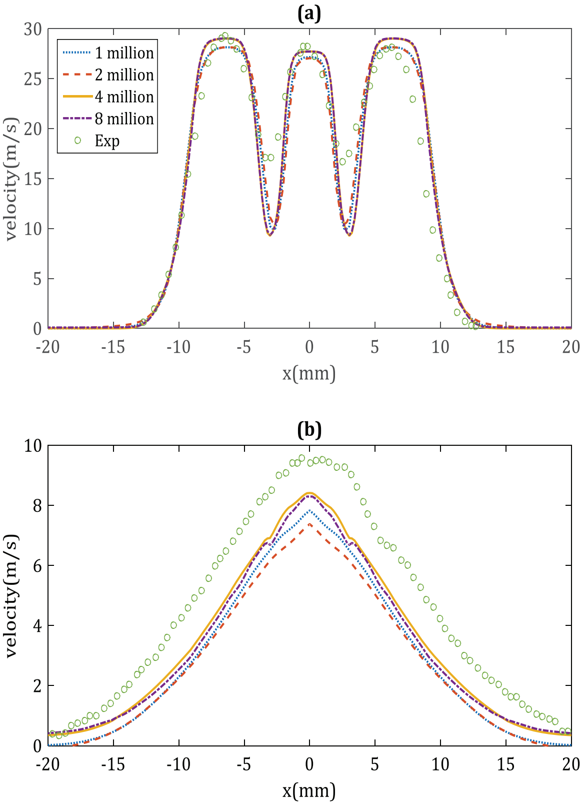

Figure 6: Comparison between the CFD simulations and the epxeriments for four different mesh sizes at (a) z = 15 mm and (b) z = 115 mm.

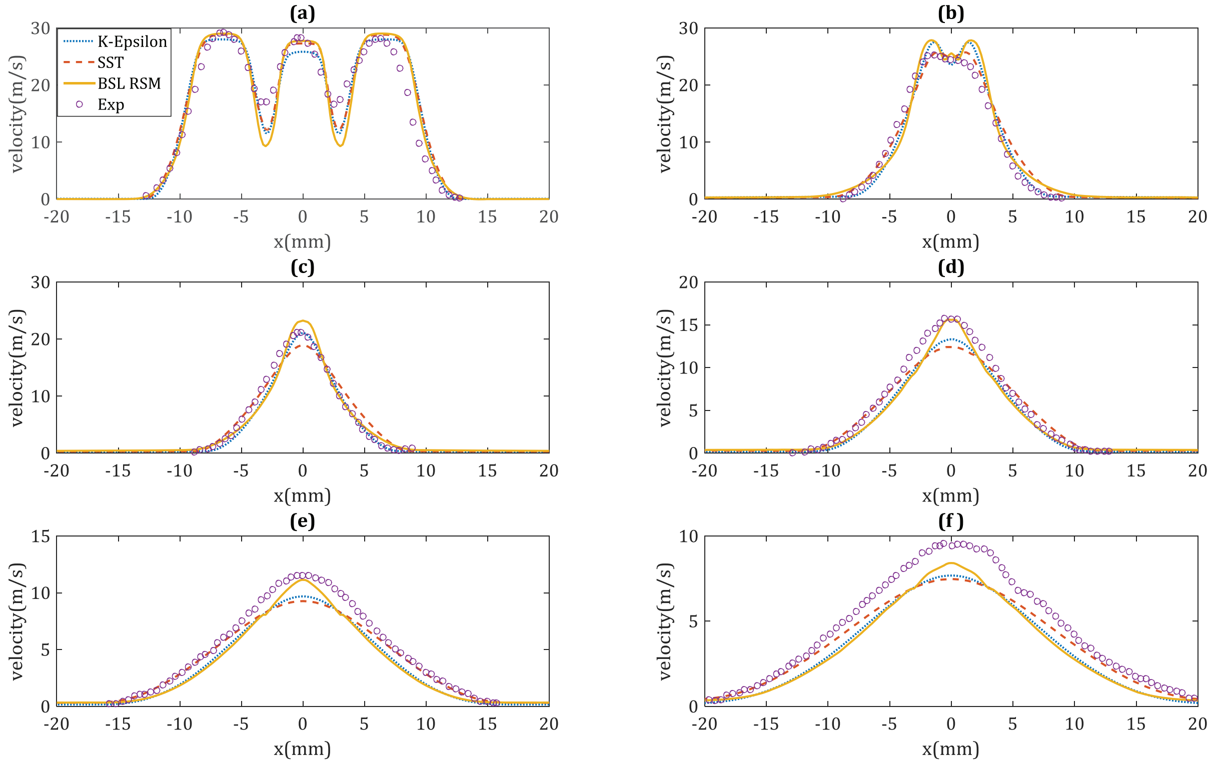

Figure 7: Comparison of calculated radial profile of mean axial velocity using three turbulence models with experimental data $\boldsymbol{\alpha_{jet} = 20^{\circ}}$ (Boushaki & Sautet 2010) at axial positions (a) z = 15 mm, (b) z = 35 mm, (c) z = 55 mm, (d) z = 75 mm, (e) z = 95 mm, (f) z = 115 mm.

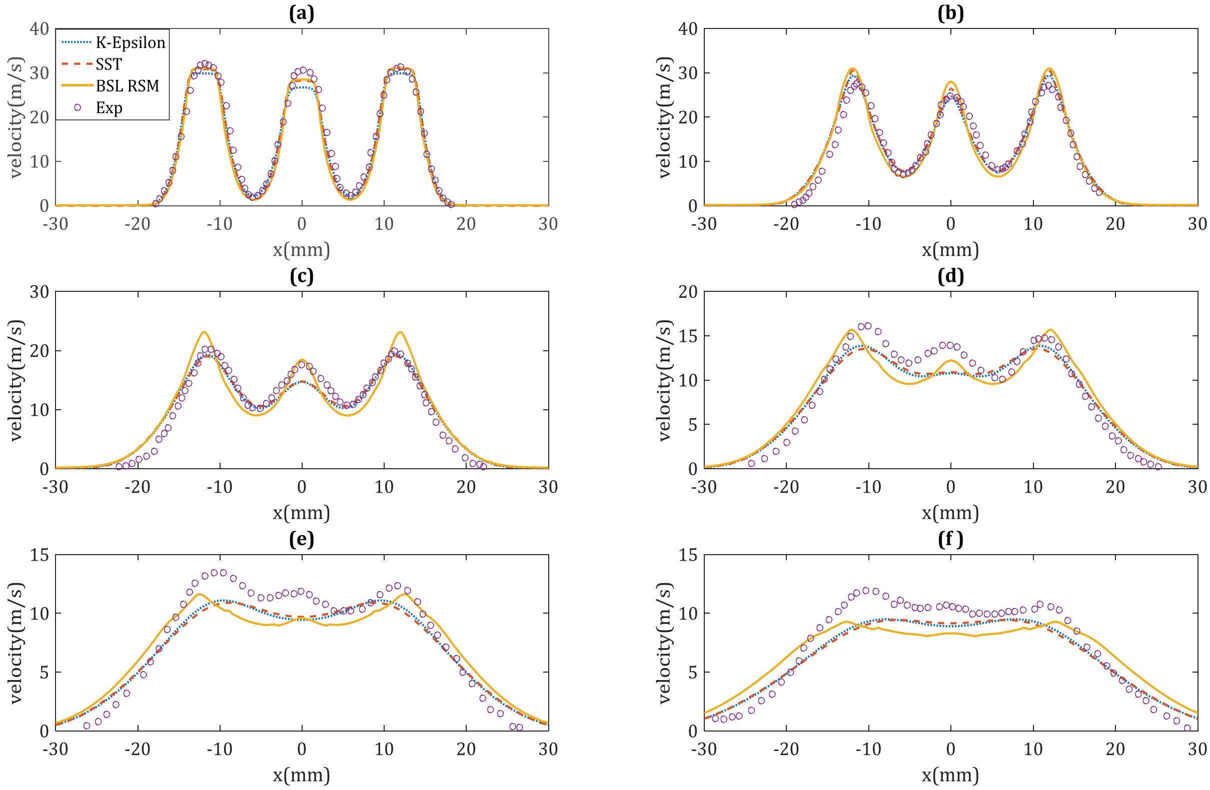

Figure 8: Comparison of calculated radial profile of mean axial velocity using three turbulence models with experimental data $\boldsymbol{\alpha_{jet} = 0^{\circ}}$ (Boushaki & Sautet 2010) at axial positions (a) z = 15 mm, (b) z = 35 mm, (c) z = 55 mm, (d) z = 75 mm, (e) z = 95 mm, (f) z = 115 mm.

Comparison of different turbulence models

Figure 7 shows the comparison of mean axial velocity profiles at six positions downstream from the burner exit (z = 15 mm, 35 mm, 55 mm, 75 mm, 95 mm and 115 mm) to illustrate the performance of different turbulence models for the case of $\alpha_{jet} = 20^\circ$. At z = 15 mm (Figure 7 a), all turbulence models provide good agreement with the experimental data for the side jets (oxygen jets shown in Figure 2), while they under-predict the velocity at the central jets (maximum difference 5%). Similarly, at z = 35 mm (Figure 7 b), all three models slightly over-predict the peak value of velocity by about 5% (x = ± 12 mm, 0 mm), and results of the SKE model are in relatively good agreement with the experimental data. However, at z = 55 mm (Figure 7 c), the predictions based on BSL RSM model have a similar trend to the SKE model, while they over-predict the velocity magnitude around the central jet region (maximum difference 8% at x = 0 mm). At z = 75 mm (Figure 7 d), the jet velocity predicted by the BSL RSM model is quite similar to that of the measurement, which reproduces the peak velocity at x = 0 mm. Also, at z = 95 mm (Figure 7 e), the maximum value of under-prediction is found to be 19.5% at x = 0 mm, which is provided by the SST model. The jet velocity predicted by the BSL RSM model at the centre of the jet (x = 0 mm) has the best agreement with the experimental data. In addition, at z = 115 mm (Figure 7 f), all models under-predict the velocity value at all jet regions, while the results from BSL RSM model agree best with the measured data at x = 0 mm, where there is 10% difference between the measured and calculated velocity.

Figure 8 presents a comparison of the mean axial velocity profiles at the same six positions from the burner exit for the case of $\alpha_{jet} = 0^\circ$. At z = 15 mm (Figure 8 a), the maximum difference occurs at x = 0 mm, the SKE model under-predicts the velocity by about 11.5%, the SST model by 6.5% and the BSL RSM model by 5.5%. Also, at z = 35 mm (Figure 8 b), all models slightly over-predict the velocity magnitude in the three jet regions. At z = 55 mm (Figure 8 c), the BSL RSM model offers a good match with the central velocity peak, but an obvious difference to the side velocity peaks (around 10%). At z = 75 mm (Figure 8 d), the results based on all three models are slightly different from the experimental data. The SKE model and the SST model can only reproduce the trends in the velocity of the two side jets, while the predictions of the central jet velocity profile differ significantly from the data. A closer observation indicates that the simulated velocity profile from the BSL RSM model agrees best with the experimental data since it reproduces all three peak velocity regions. At z = 95 mm (Figure 8 e) and z = 115 mm (Figure 8 f), there are significant differences between the numerical results and the experimental data for all tested turbulence models. Notably, the results of BSL RSM model under-predict most of the measured locations between z = 95 mm and 115 mm. However, this model still reproduces the velocity trend for all three velocity peaks, and the overall trend is in reasonable agreement with that of the experiment.

Discussion

Generally, reasonable agreement with the measured data can be obtained using all three turbulence models for the case of $\alpha_{jet} = 0^\circ$ and 20°. Both SKE and SST models under-predict the jets downstream the location z = 75 mm (maximum difference 20.5%). This under-prediction is consistent with their performance in modelling a single round free jet. For instance, Figure 9 shows the centreline velocity decay of the central jet for the case of $\alpha_{jet} = 20^\circ$. It can be seen that the velocity decay of SKE and SST models is much higher than that of BSL RSM model, and BSL RSM model provides good agreement with the experimental data at z = 15 mm, 75 mm, 95 mm and 115 mm.

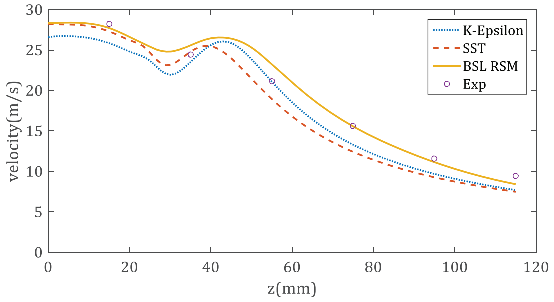

Figure 9: Comparison of centreline velocity decay of the central jet using three turbulence models with experimental data $\alpha_{jet} = 20^\circ$ (Boushaki & Sautet 2010) along the z axis.

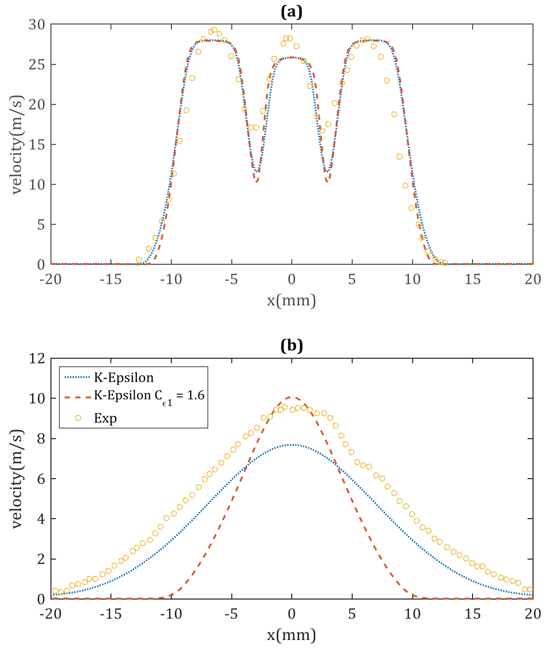

Figure 10: Comparison of calculated radial profile of mean axial velocity from two different $C_{\varepsilon 1}$ at axial positions (a) z = 15 mm, (b) z = 115 mm with experimental data (Boushaki & Sautet 2010).

Specifically, it is well known that the SKE model over-predicts the velocity decay of a round free jet. Morse (1980) and Pope (1978) suggested to change the constant $C_{\varepsilon 1}$ (Epsilon coefficient) in the turbulence dissipation rate, ε, equation of the SKE model from 1.44 to 1.6, to overcome the under-prediction of a round free jet. Figure 10 illustrates the simulated mean axial velocity profile from two different $C_{\varepsilon 1}$ values at z = 15 mm and z = 115 mm. It can be seen that at the upstream region (z = 15 mm), there is no significant difference between the results from the two $C_{\varepsilon 1}$ values. However, in the far-field region (z = 115 mm), changing the value of $C_{\varepsilon 1}$ to 1.6 only provides a good prediction for central jet, but under-predicts the side jets compared with the default value of $C_{\varepsilon1}$ (1.44). Hence, this change does not improve the simulated results in these cases.

The performance of the BSL RSM model is slightly better than that of SST and SKE models. According to Tian, Nathan and Cao (2015), the normal Reynolds stress in both SKE model and SST model are assumed to be isotropic, which reduces the prediction accuracy of a turbulence model when dealing with turbulence flow conditions such as jet interaction. By resolving turbulence intensity and additional transport equations, the BSL RSM model considers the anisotropic Reynolds stresses. Figure 11 shows the predicted normal Reynolds stress of BSL RSM model at z = 115 mm, $\alpha_{jet} = 20^\circ$. The normal Reynolds stress τ_{ww} (ww in the figure) is predicted to be much higher than the normal Reynolds stress τ_{vv} and τ_{uu}. This may explain why the BSL RSM model has a better performance of predicting interacting jet flow than the other two models.

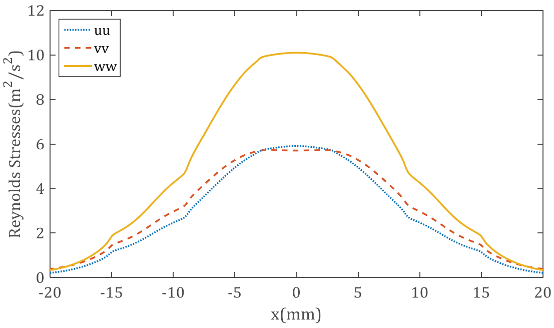

Figure 11: Predicted Reynolds stresses of BSL RSM model at z = 115 mm with $\boldsymbol{\alpha_{jet} = 20^\circ}$.

CONCLUSION

The simulated results of the Baseline Reynolds Stress (BSL RSM), the Standard k-ε (SKE) and the Shear-Stress-Transport (SST) models were found to predict the experimental data reasonably well at upstream locations of z = 15 mm to z = 55 mm in Boushaki and Sautet (2010), where z is the downstream distance from the burner exit. However, all three models under-predict the measured velocity for locations z = 75 mm to 115 mm. The best model is the BSL RSM model, which predicts the peak velocity magnitude (z = 75 mm) and reproduces the trend of velocity profiles in different axial positions. Owing to the advantage of predicting the anisotropic Reynolds stresses, the BSL RSM model mitigates the deficiency found in SKE and SST models. Therefore, the BSL RSM model is expected to provide good prediction to interacting jet flows, and it is deduced to be the preferred type of RANS model for the turbulent flows inside the HSRC.

ACKNOWLEDGEMENTS

The authors will acknowledge the financial support from the Australian Research Council.

REFERENCES

BOUSHAKI, T., MERGHENI, M.A., SAUTET, J.C., LABEGORRE, B (2008), "Effects of inclined jets on turbulent oxy-flame characteristics in a triple jet burner", *Exp. Therm. Flu. Sci.*, **32**, 1363-1370.

BOUSHAKI, T., SAUTET, J., SALENTEY, L., LABEGORRE, B (2007), "The behaviour of lifted oxy-fuel flames in burners with separated jets", *Int. Commun. Heat Mass*, **34**, 8-18.

BOUSHAKI, T. and SAUTET, J.C. (2010), "Characteristics of flow from an oxy-fuel burner with separated jets: influence of jet injection angle", *Exp. Fluids*, **48**, 1095-1108.

CHINNICI, A. (2015), Internal Report. The University of Adelaide, School of Mechanical Engineering.

JIN, H.G., HONG, H. (2012), "12 - Hybridization of concentrating solar power (CSP) with fossil fuel power plants", in K Lovegrove & W Stein (eds), *Concentrating Solar Power Technology*, Woodhead Publishing, 395-420.

MORSE, A.P. (1980), "Axisymmetric Turbulent Shear Flows with and Without Swirl", *Thesis*, University of London.

NATHAN, G.J., DALLY, B., ASHMAN, P., STEINFELD, A., (2013), "A hybrid receiver-combustor", Provisional Patent Application No. 2012/901258., Adelaide Research and Innovation Pty. Ltd.; 2012 [Priority Date: 29.03.2].

NATHAN, G.J., HU, E.J., DALLY, B., ALWAHABI, Z., BATTYE, D.L., ASHMAN, P. (2009), 'A boiler system receiving multiple energy sources'., Provisional Patent Application No.2009/905065 [Priority Date: 19.10.09].

ORDORICA-GARCIA, G., DELGADO, A.V., GARCIA, A.F. (2011), "Novel integration options of concentrating solar thermal technology with fossil-fuelled and CO_2 capture processes", *Energy Procedia*, **4**, 809-816.

POPE, S.B. (1978), "An explanation of the turbulent round-jet/plane-jet anomaly", *AIAA. J.*, **16**, 279-281.

STEINMANN, W.D. (2012), "11 - Thermal energy storage systems for concentrating solar power (CSP) plants", in K Lovegrove & W Stein (eds), *Concentrating Solar Power Technology*, Woodhead Publishing, 362-394.

TIAN, Z.F., NATHAN, G.J., CAO, Y. (2015), "Numerical modelling of flows in a solar–enhanced vortex gasifier: Part 1, comparison of turbulence models", *Prog. Comput. Fluid Dy.*, **15**, 114-122.

Appendix B：　Effect of Jet Inclination Angle on the Flow Field within a Hybrid Solar Receiver Combustor

20th Australasian Fluid Mechanics Conference
Perth, Australia
5-8 December 2016

Effect of Jet Inclination Angle on the Flow Field within a Hybrid Solar Receiver Combustor

S. Long[1], Z.F. Tian[1], A. Chinnici[1], T.C.W. Lau[1], B.B. Dally[1], G.J. Nathan[1]

[1]School of Mechanical Engineering, Centre for Energy Technology
The University of Adelaide, Adelaide, South Australia 5005, Australia

Abstract

This paper reports on a systematic numerical study that investigates the interaction of four isothermal jets within an annular chamber under conditions relevant to a Hybrid Solar Receiver Combustor (HSRC). The HSRC features a cavity that is operable as a combustion chamber, an aperture to admit concentrated solar radiation into the chamber, multiple burners to direct a flame into the chamber, and a heat exchanger within it to absorb the heat from both energy sources (depending on the mode of operation). The HSRC geometry is simplified in this study to include a cylindrical cavity with four jets, representing the burners, which are configured in an annular arrangement and aligned at an angle to the axis. The aperture to the cavity is closed while the four jets interact with each other and with the cavity wall. The jet inclination angle (α_{jet}) was varied from 0° to 90°, while the jet Reynolds number and the number of jets were fixed at $Re_j = 15{,}000$ and 4, respectively. The numerical study utilised the commercial Computational Fluid Dynamics (CFD) code ANSYS CFX. The results show that the α_{jet} significantly influences the flow field with smaller α_{jet} $(0^{\circ} \le \alpha_{jet} < 10^{\circ})$ leading to a strong inward annular recirculation while larger α_{jet} $(10^{\circ} \le \alpha_{jet} < 90^{\circ})$ generates an outward annular recirculation with a strong back-flow through the aperture plane. Four flow regimes were identified, namely: inward recirculation dominant flow $(0^{\circ} \le \alpha_{jet} < 10^{\circ})$; outward recirculation dominant flow $(10^{\circ} \le \alpha_{jet} < 40^{\circ})$; outward recirculation with back-flow $(40^{\circ} \le \alpha_{jet} < 60^{\circ})$; and jet impinging flow $(60^{\circ} \le \alpha_{jet} < 90^{\circ})$. The findings are presented and discussed with relevance to heat transfer within the HSRC.

Introduction

With the growing need for a more sustainable living, clean energy generation has received increasing interest globally. Within the context of renewable energy, solar energy has received particular attention because it is both clean and abundant [7]. In recent years, Concentrating Solar Thermal (CST) systems have been developed because it offers opportunities to utilise energy at high temperatures, to allow the storage of thermal energy and to allow hybridisation with combustion devices [10]. However, a key barrier for developing CST technologies is the intermittent nature of the solar source.

The concept of integrating CST and traditional combustion systems is gaining prominence globally due to the complementary nature of these two thermal energy sources [12]. It offers a relatively low cost solution that minimises the need for costly large energy storage and also provides continuous power supply. While a number of hybrid systems have been proposed to date [9], none of them combine a solar receiver and a combustor directly within a cavity.

The concept of a Hybrid Solar Receiver Combustor (HSRC) has been recently proposed by the Centre for Energy Technology (CET) at the University of Adelaide. The HSRC configuration has the potential to reduce heat losses relative to equivalent hybrids by integrating CST and combustion energy sources into a single device [11]. The HSRC features a cavity operable as a combustion chamber, an aperture to admit concentrated solar radiation into the chamber, multiple burners to direct a flame into the chamber and a heat exchanger within it to absorb the heat from both energy sources. The burners are configured in an annular arrangement and aligned at an angle to the axis of chamber. This causes the jets to interact with each other as well as with the wall and the aperture. The HSRC design allows the device to operate in any of three operational modes, namely, the ‘combustion only mode’, the ‘solar only mode’ and the ‘mixed mode’. For the ‘solar only mode’, the shutter of secondary concentrator (SC) is open to allow the concentrated solar radiation to enter the chamber. Under this mode, the only heat source for the HSRC is solar energy. In contrast, the heat source in the ‘combustion only mode’ is derived only from the burning of injected fuel and the shutter is closed. In the ‘mixed mode’, the power of the HSRC is derived from both solar energy and combustion, with the percentage of each being dependent on the solar intensity available at the time. A schematic diagram of the HSRC is presented in Figure 1. Owing to the annular arrangement of jets and the range of operational modes, it can be expected that different flow regimes, flame structures and dominant heat transfer mechanisms will occur inside the HSRC depending on the mode of operation. Ideally, the optimised flow patterns would lead to an enhanced mixing while preventing fluid to escape through the aperture plane. A larger flow through the aperture would lead to a larger convective heat losses in the mixed mode of operation. More importantly, an optimised flow field would be characterised by a reduced in-flow since this would alter the equivalence ratio of the flame, and therefore altering the heat transfer, fuel conversion and pollutant emissions. Hence, a comprehensive understanding of the influence of interacting jets on the overall flow-field within the HSRC is needed.

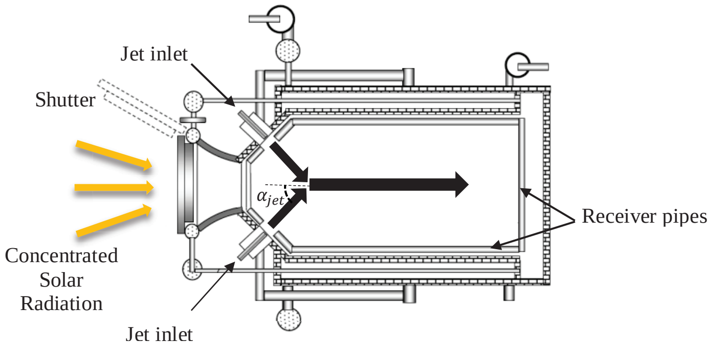

Figure 1. Hybrid Solar Receiver Combustor [11].

A number of researchers have studied the behaviour of interacting jets using experimental techniques [1,2,3], numerical techniques

[4], or a combination of both experimental and numerical techniques [5, 6]. However, there are only limited investigations with regard to multiple inclined annular jets inside a cylinder. The relationship between the variation of inclination angle and flow regimes is still not fully understood, and the fundamentals of these variations in the flow-field have not been fully quantified. Also, previous studies have only provided a detailed understanding of the flow-field for collinear inclined jets configurations $(\text{number of jets} \leq 3)$ [1,2,3,4,5,6], while the impact of other configurations such as annular jets $(\text{number of jets} \geq 4)$ on the overall flow-field within a confined space is still not well understood.

In light of the needs above, the aim of the present paper is to conduct a Computational Fluid Dynamics (CFD) study to a) investigate the iso-thermal flow-field of interacting jets within the HSRC configuration, b) identify potential flow regimes as a function of jet inclination angles within a circular chamber, and c) select the preferred flow regimes for ‘combustion only mode’ (closed-shutter) of the HSRC.

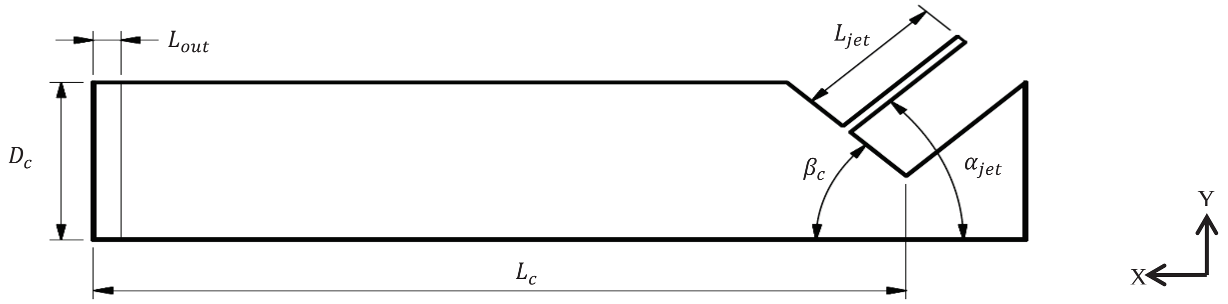

Figure 2. Geometry of the CFD domain (not to scale).

Methodology

A computational study was conducted using a commercial CFD code ANSYS CFX. The computational model of the HSRC shown in Figure 2 was generated with a commercial CAD package PTC Creo. 19 models of the HSRC were constructed for the cases from $\alpha_{jet} = 0^\circ$ to 90°, with an increment of 5° for each case. The dimensions of the HSRC are shown in Table 1.

Due to the symmetric nature of the geometry and to reduce computational cost, only a quarter of the full domain (Figure 2) was modelled utilising the symmetry boundary option in the code. The ANSYS Meshing code was used to generate the mesh of this computational model. The mesh quality was checked for expansion factor, aspect ratio, skewness and orthogonality. The influence of the number of mesh nodes on the CFD results was evaluated through a mesh independence test, which showed that 8 million mesh nodes represents a compromise between the accuracy of the calculated results and the simulation time. The convergence criterion for all cases was set to be 1×10^{-5}(RMS).

Shen et al. [8] reported a numerical investigation of an isothermal flow from a burner with three separated-jet inlets. This burner has similar features to the multiple-jet configuration of the HSRC. Shen et al. [8] found that the Baseline Reynolds Stress model (BSL RSM) is able to reproduce the velocity peaks and trends for interacting jets, due to the capability of the BSL RSM to calculate the anisotropic Reynolds stresses in different directions. Hence, the BSL RSM model was used for the current CFD study.

It is necessary to understand the isothermal flow-field before moving to the more complex cases of non-isothermal, therefore, the working fluid in the current CFD model was defined as isothermal water at $25^\circ C$. Water can provide a relatively high Reynolds number at a lower flow velocity. The Reynolds number in all cases was fixed at Re_j = 15,000 (Re_j is the jet Reynolds number), which ensured all calculated cases were performed in the fully-turbulent regime. The detailed boundary and inlet conditions are given in Table 2 and Figure 3.

Dimensions	Description	Value (mm)
$\boldsymbol{D_c}$	Chamber width (half)	37
$\boldsymbol{L_c}$	Chamber length	225
$\boldsymbol{L_{jet}}$	Jet inlet length	150
$\boldsymbol{\alpha_{jet}}$	Jet inclination angle	0° to 90°
$\boldsymbol{\beta_c}$	Conical chamber angle	45°
$\boldsymbol{L_{out}}$	Outlet length	3

Table 1. Geometric parameters.

Boundary Name	Boundary Type
1,2	Mass flow inlet
3	Opening outlet
4	Symmetric planes
Other	No slip wall

Table 2. Boundary conditions.

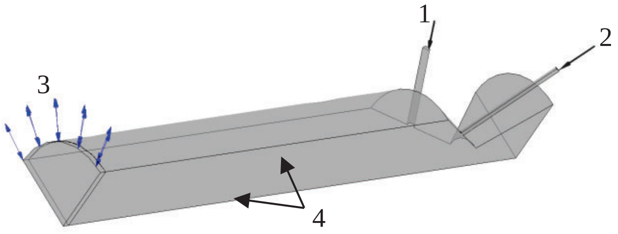

Figure 3. CFD domain.

Results and discussion

Figure 4 presents the calculated flow-patterns within the HSRC under ‘combustion only mode’ for four different α_{jet}. Four classes of flow can be identified from these CFD results. Figure 5 to Figure 8 present the key features of the different flow regimes:

Regime 1: Inward recirculation dominant flow regime. For an inclination angle of $0^\circ \leq \alpha_{jet} < 10^\circ$, an annular inward recirculation dominates the flow-field within the chamber, and a small annular outward recirculation is observed near the downstream wall ('outward' means from the axis towards the chamber wall, while 'inward' means from the wall to the axis).

Regime 2: Outward recirculation dominant flow regime. For an inclination angle of $10^{\circ} \leq \alpha_{jet} < 40^{\circ}$, the jets start to interact with each other and also with the cavity wall. An annular outward recirculation zone is found to dominate the flow-field inside the chamber. The recirculation length L_{re} in Regime 2 is much longer than that in Regime 1.

Regime 3: Outward recirculation with backflows regime. For an inclination angle of $40^{\circ} \leq \alpha_{jet} < 60^{\circ}$, the annular outward recirculation is still the dominating flow feature within the chamber. The recirculation length L_{re} is similar to Regime 2. However, annular outward backflows are observed around the impinging point (merging point) of multiple jets ('backflow' means the flow reversing into the SC).

Regime 4: Jet impingement regime. For an inclination angle $60^{\circ} \leq \alpha_{jet} < 90^{\circ}$, large annular outward backflows can be found within the secondary concentrator section, while the area of annular outward recirculation inside the chamber becomes smaller. Also, L_{re} has a significant decrease compared with Regime 3. Hence, annular outward recirculation zones are identified in both chamber and secondary concentrator sections.

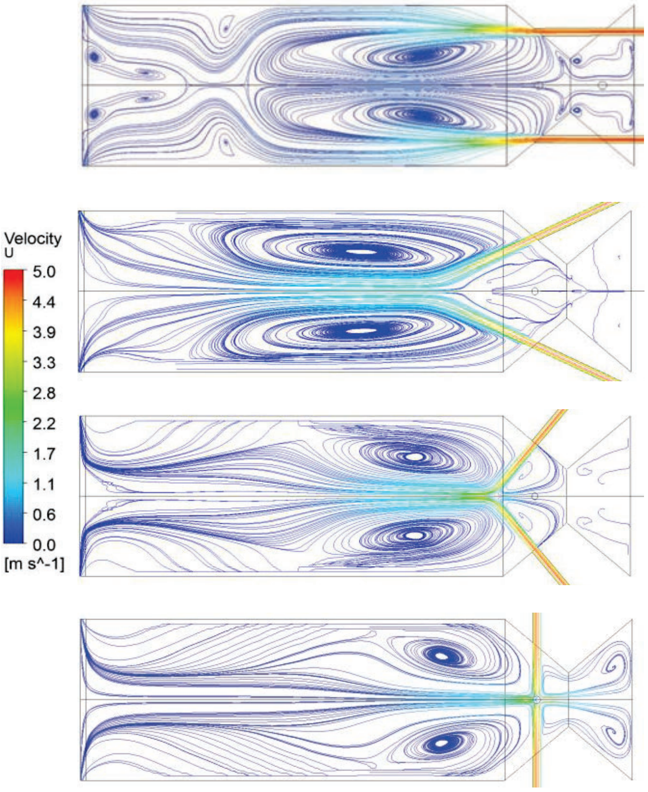

Figure 4. Calculated streamline for the case of $\alpha_{jet} = 0^{\circ}, 25^{\circ}, 50^{\circ}, 90^{\circ}$.

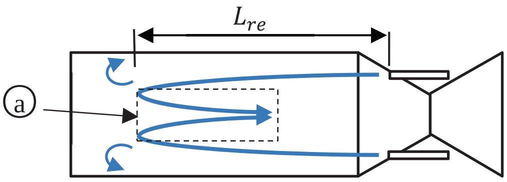

Figure 5. Flow regime 1 (a = annular inward recirculation, L_{re} = recirculation length).

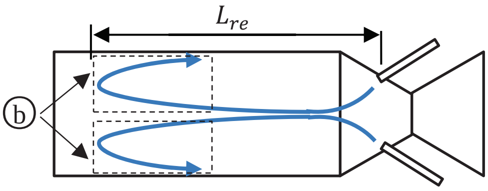

Figure 6. Flow regime 2 (b = annular outward recirculation).

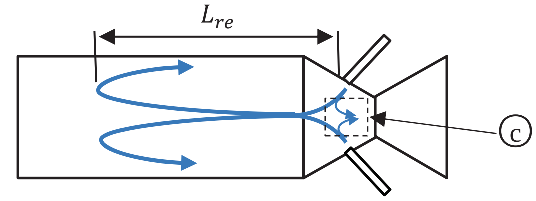

Figure 7. Flow regime 3 (c = outward backflows).

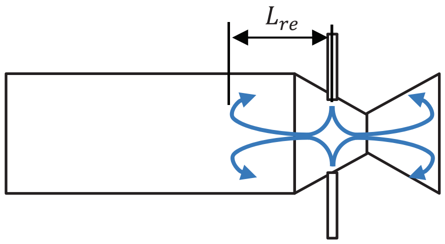

Figure 8. Flow regime 4.

This section would present the quantitative analysis for five distinct angles ($\alpha_{jet} = 0^{\circ}, 25^{\circ}, 50^{\circ}, 75, 90^{\circ}$). Figure 9 presents the dependence of the mean centreline velocity profile along the centreline on the inclination angles. It can be seen that the inclination angles 50°, 75° and 90° generate significant negative velocity profiles ($u_c/U_j < 0$) upstream of the impinging region ($x \leq 0.03\,m$). However, for small inclination angles (0° and 25°), the negative velocity profile was found to disappear. This indicates that the significant back-flow is likely to be found at larger inclination angles (Regime 3 and Regime 4). In addition, it can also be seen that with an increase of α_{jet} from 25° to 90°, the location of the positive velocity peak in the chamber varies from downstream (0.07 m) to the upstream (0.02 m) region, which indicates that the impinging point is moving from downstream to upstream. However, the impinging point does not depart significantly from the axis of the chamber.

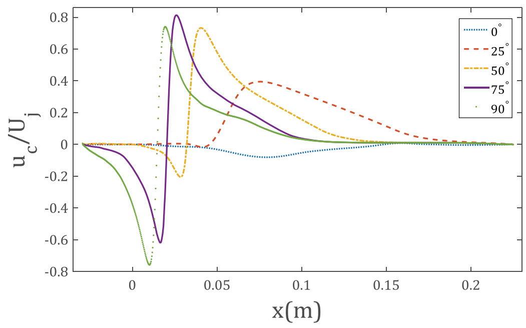

Figure 9. Calculated evolution of the axial velocity u_c along the HSRC centreline normalised by injection velocity U_j as a function of the HSRC length for five inclination angles, x = 0 m refers to the location of the aperture plane. The range of x < 0 m refers to the secondary concentrator.

Figure 10 presents the effects of the inclination angles ($\alpha_{jet} = 0^{\circ}, 25^{\circ}, 50^{\circ}, 75, 90^{\circ}$) on the normalised recirculation length (L_{re}/L_c), and mass flow rate through the secondary concentrator (M_{ap} refers to the mass flow rate through SC, and M_{in} refers to the injected mass flow rate). It can be seen that the recirculation zone increases significantly (L_{re}/L_c = 64% to 76%) varying α_{jet} from 0° to 25°, while it decreases in the range $25^{\circ} \leq \alpha_{jet} \leq 90^{\circ}$. The case of $\alpha_{jet} = 25^{\circ}$ provides the largest annular recirculation zone ($L_{re}/L_c = 76\%$) and very small back-flow rate ($M_{ap}/M_{in} \approx 0.3\%$) compared with the other four cases, which is able to enhance the mixing of reactants and heat transfer in 'combustion only' mode. It can also be seen that for $\alpha_{jet} < 50^{\circ}$, there is almost not injected flow entering the secondary concentrator ($M_{ap}/M_{in} \approx 0.3\%$). However, as the inclination angle is further increased ($\alpha_{jet} \geq 50^{\circ}$), the percentage of mass flow rate (M_{ap}/M_{in}) increases significantly from 0.3 % (at $\alpha_{jet} = 50^{\circ}$) to 66 % (at $\alpha_{jet} = 90^{\circ}$), which means more fluids will escape to the SC (closed-shutter mode) or even outside (open-shutter mode). The loss of hot reactants from the cavity through the aperture may lead to significant decreases in reactor efficiency.

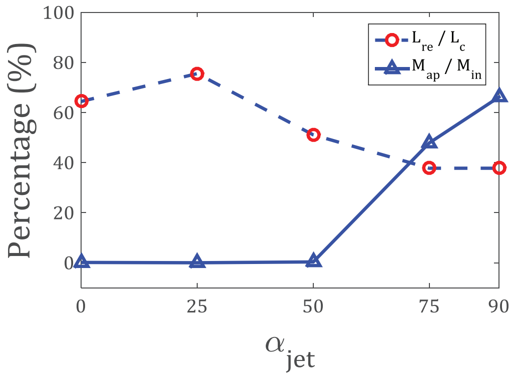

Figure 10. Calculated recirculation length normalised by chamber length, and calculated mass flow rate through the secondary concentrator normalised by inlet mass flow rate as a function of the inclination angle

Conclusions

A CFD study was conducted to better understand the flow patterns inside a cylindrical geometry equipped with four annular jets inclined at several different angles (α_{jet}). This iso-thermal study aimed at emulating the flow regimes for 'combustion only mode' of the Hybrid Solar Receiver Combustor (HSRC). The key outcomes are as follows:

- Significant back-flow through the secondary concentrator is likely to be identified in $\alpha_{jet} \geq 50^{\circ}$.
- About 0.3% of the injected flow would enter the secondary concentrator when $\alpha_{jet} < 50^{\circ}$. This indicates that the angle range $\alpha_{jet} < 50^{\circ}$ may limit the decrease of reactor efficiency.
- The α_{jet} could significantly influence the flow field within the HSRC with smaller α_{jet} ($0^{\circ} \leq \alpha_{jet} < 10^{\circ}$) leading to an inward annular recirculation while larger α_{jet} ($10^{\circ} \leq \alpha_{jet} < 90^{\circ}$) generates an outward annular recirculation with a back-flow ($\alpha_{jet} \geq 50^{\circ}$) through the aperture plane.
- The 'inward recirculation dominant flow' ($0^{\circ} \leq \alpha_{jet} < 10^{\circ}$) and 'outward recirculation dominant flow' ($10^{\circ} \leq \alpha_{jet} < 40^{\circ}$) are deduced to be the preferred classes of flow for the 'combustion only mode' HSRC because a long recirculation and a small backflow occur in these two flow regimes.

Acknowledgements

The authors will acknowledge the financial support from the Australian Research Council.

References

[1] Boushaki, T., et al., Effects of inclined jets on turbulent oxy-flame characteristics in a triple jet burner. *Exp. Therm. Fluid Sci.*, **32**, 2008, 1363-1370.

[2] Boushaki, T., et al., The behaviour of lifted oxy-fuel flames in burners with separated jets. *Int. Commun. Heat Mass*, **34**, 2007, 8-18.

[3] Boushaki, T. & Sautet, J.C., Characteristics of flow from an oxy-fuel burner with separated jets: influence of jet injection angle. *Exp. Fluids*, **48**, 2010, 1095-1108.

[4] Chammem, T., Vauquelin, O., & Mhiri, H., Performance evaluation of alternative tunnel longitudinal ventilation systems using two inclined jets. *Tunn. Undergr. Sp. Tech.*, **41**, 2014, 53-61.

[5] Chammem, T., Mhiri, H. & Vauquelin, O., Dominant Flow Features of Two Inclined Impinging Jets Confined in Large Enclosure. in *Proceedings of World Academy of Science, Engineering and Technology*. 2013.

[6] Chammem, T., Mhiri, H. & Vauquelin, O., Experimental and computational investigation of Reynolds number effect on the longitudinal ventilation in large enclosure of twin inclined jets. *Build. Environ.*, **67**, 2013, 87-96.

[7] Desideri, U. & Campana, P.E., Analysis and comparison between a concentrating solar and a photovoltaic power plant. *Appl. Energ.*, **113**, 2014, 422-433.

[8] Long, S., et al., CFD Modelling of Isothermal Multiple Jets in A Combustor, in *International Conference on CFD in the Minerals and Process Industries (11th: 2015: Melbourne, Australia)*, 2015.

[9] Mehos, M.S., et al., Combustion system for hybrid solar fossil fuel receiver, Midwest Research Institute, 2004.

[10] Moore, J. & Apt, J., Can hybrid solar-fossil power plants mitigate CO2 at lower cost than PV or CSP? *Environ. Sci. Tech.*, **47**, 2013, 2487-2493.

[11] Nathan, G., et al., A hybrid receiver-combustor. 2013, *Provisional Patent Application No. 2012/901258.*, Adelaide Research and Innovation Pty. Ltd, 2012.

[12] Ordorica-Garcia, G., Delgado, A.V. & Garcia, A.F., Novel integration options of concentrating solar thermal technology with fossil-fuelled and CO 2 capture processes. *Energy Procedia*, **4**, 2011, 809-816.

Appendix C： Effect of Jet Azimuthal Angle on the Flow Field within a Hybrid Solar Receiver Combustor

ASIA-PACIFIC
SOLAR RESEARCH
CONFERENCE

Peer Reviewed
2017 Solar Research Conference

Effect of Jet Azimuthal Angle on the Flow Field within a Hybrid Solar Receiver Combustor

S. Long, T.C.W. Lau, A. Chinnici, Z.F. Tian, B.B. Dally and G.J. Nathan

Centre for Energy Technology, School of Mechanical Engineering,
The University of Adelaide, Adelaide, South Australia 5005, Australia
E-mail: shen.long@adelaide.edu.au

Abstract

This paper reports on a systematic experimental and numerical study that investigates the interaction between four isothermal jets within a cylindrical chamber under conditions relevant to a Hybrid Solar Receiver Combustor (HSRC). The HSRC features a cavity that is operable as a combustion chamber, or as a cavity receiver with an aperture to admit the concentrated solar radiation, multiple burners to direct fuel and air into the chamber and tubular heat exchangers to transfer the heat to the heat transfer fluid. The HSRC geometry is simplified here to the cylindrical cavity with four jets, representing the burners, which are configured in an annular arrangement and aligned at an angle to the axis with a swirling component. The aperture to the cavity is closed while the four jets interact with each other and with the cavity wall. The jet inclination angle (α_j) was fixed at 25°, while the jet azimuthal angle (θ_j) was varied from 5° to 15°. The inlet Reynolds number for each injected jet and the number of jets were fixed at Re_D = 10500 and 4, respectively. Measurements obtained with Particle Image Velocimetry (PIV) were used together with numerical modelling employing Reynolds-Averaged Navier-Stokes (RANS) methods to characterise the large-scale flow field within the HSRC device. The results reveal a significant dependence of the mean flow-field on the jet azimuthal angle (θ_j) and have implications on the heat transfer within the HSRC.

1. Introduction

Renewable energy generation is gaining interest globally due to the growing need for a more sustainable society (Christoff 2016). Solar energy has received particular attention because it is both clean and abundant (Desideri & Campana 2014). In recent years, there is growing interest in Concentrating Solar Thermal (CST) system because it offers opportunities to utilise energy at high temperatures, to allow the storage of thermal energy and to allow hybridisation with combustion devices (Moore & Apt 2013). Nevertheless, the intermittent nature of the solar source is a barrier to the penetration of all solar and wind energy technologies. In contrast, the combustion of fuels offers high availability. In the near term, fossil fuels have low cost but high emissions of CO_2 and other pollutants (Cavaliere & de Joannon 2004). However, the cost of more sustainable fuels such as hydrogen and syngas are expected to decrease in the future. Thus, the complementary nature of these two thermal energy sources means that their integration is gaining prominence globally (Nathan et al. 2017).

A Hybrid Solar Receiver Combustor (HSRC) has been recently proposed by the Centre for Energy Technology (CET) at the University of Adelaide, which offers potential to reduce both the energy losses and total infrastructure requirements relative to a hybrid from stand-alone components, while providing a firm supply of energy for heat and power applications (Nathan et al. 2014). It features a cavity operable as a combustion chamber, an aperture to admit concentrated solar radiation into the chamber, multiple burners to direct fuel and air into the chamber and a heat exchanger within it to absorb the heat from both energy sources (Figure 1). In addition, the HSRC can be operated in any of three modes, namely, the 'combustion only mode', the 'solar only mode' and the 'mixed mode'. For the 'solar only mode', the shutter of the secondary concentrator (SC) is open to allow the entrance of concentrated solar radiation, while the only heat source for the HSRC is solar energy. For the 'combustion only mode', the heat source is derived only from the burning of injected fuel and the shutter is closed. In the 'mixed mode', the power of the HSRC is derived from both solar energy and combustion, with the percentage of each being dependent on the solar intensity available at the time. Importantly, the configuration of the combustion system in a solar cavity differs from that in a conventional combustor owing to the need to incorporate the aperture. This results in an annular ring of burners, which can be configured with an inclination angle (α_j) relative to the axis of the chamber, and/or as well as an azimuthal angle (θ_j) to the axis of the burner. The azimuthal angle generates swirling flows within the chamber, which causes the jets to interact with each other as well as with the wall and the aperture. Owing to the swirling burner arrangement and the range of operational modes, it can be expected that different flow regimes, flame structures and dominant heat transfer mechanisms will occur with changes to these angles. Hence, a more detailed characterisation of the flow field within the HSRC for a well-defined and consistent inflow conditions is needed to better understand the flow generated by the swirled burner arrangement.

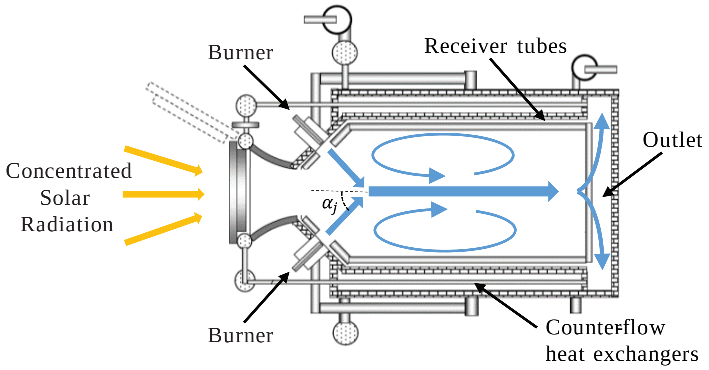

Figure 1. Schematic diagram of Hybrid Solar Receiver Combustor (Nathan et al. 2013).

To meet the aforementioned needs, the current investigation aims to conduct an experimental and numerical study to a) investigate the iso-thermal flow-field of interacting jets with swirling component within the HSRC configuration, b) identify potential flow regimes as a function of jet azimuthal angles (θ_j) within a circular chamber, and c) analyse the effect of different flow regimes on the 'combustion only' (closed-aperture) and 'mixed' modes of operation. In particular the aim of the CFD work is to provide a qualitative understanding of the flow patterns in the regions for which experimental data is not available (i.e. out-of-plane motion).

2. Methodology

A schematic diagram of the experimental HSRC configuration is shown in Figure 2. The cavity of the experimental model consists of a cylindrical chamber with a conical expansion, connected with a secondary concentrator (SC). An aperture shutter is employed at the end of the SC. Particularly, the current study investigates the HSRC within the 'combustion-only' mode, where the aperture is closed to prevent heat loss. The geometric parameters are given in Table 1.

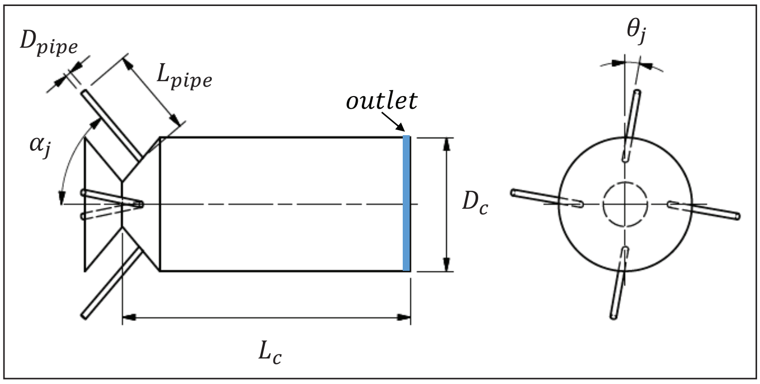

Figure 2. Schematic diagram of cold flow device used for the experimental investigation.

Table 1. Values of the geometric parameters of the experimental models.

Dimensions	Description	Value (mm)
D_c	Chamber diameter	37
L_c	Chamber length	225
D_{pipe}	Pipe diameter	3.35
L_{pipe}	Pipe length	150
α_j	Jet inclination angle	25°
θ_j	Jet azimuthal angle	5°, 10° and 15°

2.1. *Experiment arrangement*

Planar Particle Image Velocimetry (PIV) was employed to investigate the mean flow-fields within experimental models under iso-thermal conditions at ambient temperature. Three laboratory-scale devices were manufactured with inclination angles of $\alpha_j = 25^{\circ}$ and azimuthal angles of $\theta_j = 5^{\circ}$, 10° and 15°. Acrylic was chosen as the material to provide optical access and a close match between the refractive index of the chamber and that of the working fluid. The entire experimental model was fully submerged into a rectangular water tank with dimensions of 500 mm (L) × 400 mm (W) × 390 mm (H) to prevent optical distortion.

Water was chosen as the working fluid to avoid deposition of tracer particles onto confining walls. The water from the outlets was discharged into the water tank, which overflowed to a reservoir. The inlet jet bulk injection velocity (U_b) was fixed at 2.8 m/s for each nozzle, leading to an inlet jet Reynolds number $Re_D = 10{,}500$. This ensures that the inlet flow is within the fully turbulent regime. The flow was seeded with hollow glass spheres of 12 μm in diameter and with a specific gravity of 1.1.

The optical arrangement and the measurement region are shown schematically in Figure 3. The illumination for the PIV measurements was sourced from a double-head, pulsed Nd:YAG laser (Quantel Brilliant B), frequency doubled to provide a wavelength of 532 nm at a fixed pulsing frequency of 10 Hz. The thickness of the light sheet was estimated to be 1.5 mm at the focal line.

The images were captured with a Charged Coupled Device (CCD) camera (Kodak Megaplus ES2093) with an array of 1920 × 1080 pixels, which provides the axial (u) and radial (v) instantaneous velocity components with an image size of 118 mm (L_i) × 66 mm (W_i). A minimum of 3000 PIV images (12 bits) was recorded for each measurement. The image-processing was performed with an in-house PIV code in MATLAB (Mathworks), with an interrogation window size of 32 × 32 pixels, leading to a spatial resolution of 2 mm in each direction. A multi-grid correlation algorithm with 50% overlap was applied to all cases. All erroneous vectors were removed from the ensemble.

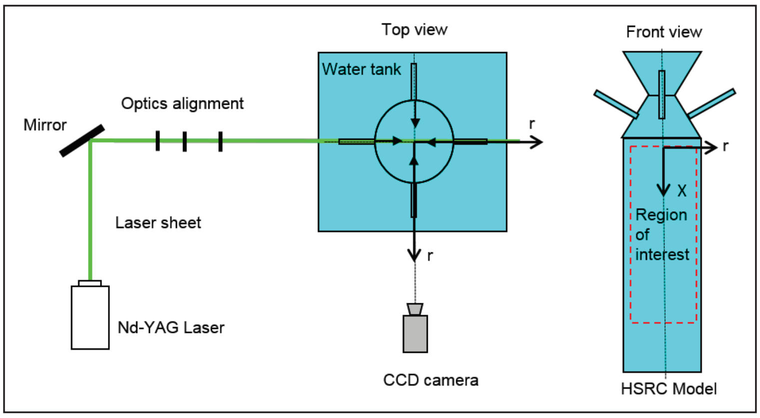

Figure 3. Experiment layout for the PIV measurements, together with the optical arrangement.

2.2. Computational modelling

The commercial computational fluid dynamics (CFD) code ANSYS/CFX 17.0 was employed to simulate the flow-field, utilising the Reynolds-Averaged Navier-Stokes (RANS) method. The 3-dimensional computational model of the device, shown in Figure 4, was generated with a commercial CAD package PTC Creo. To reduce computational cost, only a quarter of the full domain was modelled utilising the periodic boundary option in the code. The ANSYS/Meshing 17.0 CFD code was used to generate the computational mesh. The mesh quality was checked for expansion factor, aspect ratio, skewness and orthogonality. The influence of the number of mesh nodes on the CFD results was evaluated through a mesh independence test, which showed that approximately 8 million mesh nodes yield a good compromise between the accuracy of the calculated results and the simulation time. The convergence criterion for all cases was set to be 1×10^{-5} (RMS). The working fluid and the inflow conditions assessed in the CFD simulations were chosen to match those of the PIV measurements (i.e., water as working fluid and Re_D = 10500). The Shear Stress Transport (SST) model was selected as the turbulence closure model, owing to the reasonable prediction of the mean flow-field in related configurations (Chen et al. 2012; Tian et al. 2015).

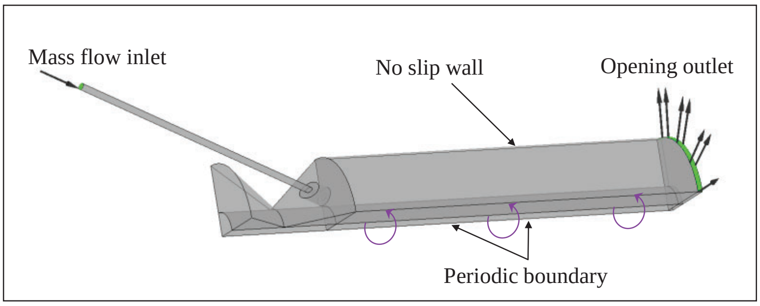

Figure 4. The CFD domain of the Hybrid Solar Receiver Combustor.

3. Results and Discussion

Figure 5 presents the contours of measured mean axial velocity (U_x) normalised by the inlet velocity (U_b) for the cases (a) $\alpha_j = 25^\circ$ and $\theta_j = 5^\circ$ (HSRC-25-5), (b) $\alpha_j = 25^\circ$ and $\theta_j = 10^\circ$ (HSRC-25-10) and (c) $\alpha_j = 25^\circ$ and $\theta_j = 15^\circ$ (HSRC-25-15). It can be seen that an increase in azimuthal angle (θ_j) from 5° to 15° leads to a significant change of the mean flow field for a given value of α_j. For the case of HSRC-25-5, the mean flow of the resulting jet (merged jet downstream from the impingement point) spreads out gradually and symmetrically beyond the impingement point, qualitatively similar to non-swirling jets configurations ($\theta_j = 0^\circ$). By increasing θ_j to 10° (HSRC-25-10), the mean flow bifurcates into two resulting jets downstream from the interacting region (Vanierschot & Van den Bulck 2008). This is most evident for the case of HSRC-25-15, with a higher value of θ_j for which the bifurcation is strong and slightly asymmetrical. Indeed, slight asymmetry can be seen for each flow, which is consistent with such a configuration tending to amplify small asymmetries in the inflow conditions.

It is also worth noting that a region of significant central recirculation zone, CRZ (i.e. negative axial velocity) is generated in the region downstream from the bifurcation point for the cases of HSRC-25-10 and HSRC-25-15. The position of this CRZ progresses upstream with an increase in θ_j, from $0.38 < x/L_c < 0.6$ for HSRC-25-10, to $0.27 < x/L_c < 0.53$ for HSRC-25-15. This is consistent with previous investigations of swirling flows for other configurations, in which an increase in swirl increases the strength of the CRZ (Vanierschot & Van den Bulck 2008).

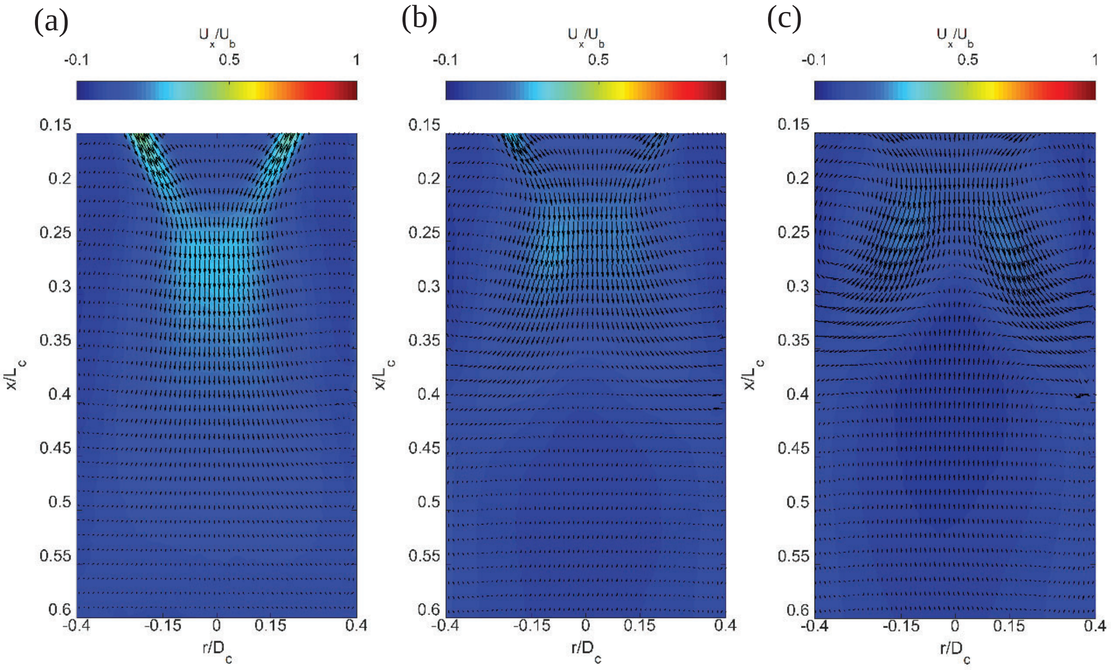

Figure 5. Measured normalised mean velocity (U_x/U_b) contours for the cases of (a) $\alpha_j = 25^\circ$ and $\theta_j = 5^\circ$ (HSRC-25-5), (b) $\alpha_j = 25^\circ$ and $\theta_j = 10^\circ$ (HSRC-25-10) and (c) $\alpha_j = 25^\circ$ and $\theta_j = 15^\circ$ (HSRC-25-15).

Figure 6 presents the evolution of measured dimensionless mean axial velocity (U_c/U_b) along the centreline of the HSRC chamber for the cases of (a) HSRC-25-5, (b) HSRC-25-10 and (c) HSRC-25-15. For comparison with previous measurements of non-swirling ($\theta_j = 0^\circ$) jets, the PIV data of Long et al. (2017) for multiple-impinging jets in a cylindrical chamber, namely HSRC-25-0, is also included. It can be seen that all cases feature similar trends in the mean axial centreline velocity decay, although the locations and magnitudes of their peak values differ. The velocity peak for HSRC-25-5, HSRC-25-10 and HSRC-25-15 is approximately 27%, 50% and 70% lower than that of HSRC-25-0, and the location of velocity peak progresses upstream from $x/L_c = 0.28$ for HSRC-25_5 to $x/L_c = 0.20$ for HSRC-25-15. This reveals that an increase in θ_j leads to a significant decrease in the velocity peak along the centreline of the chamber.

It can also be seen that a significant saddle point occurs on the axis for the cases of HSRC-25-10 and HSRC-25-15, which is located at $x/L_c = 0.38$ and 0.27 for HSRC-25-10 and HSRC-25-15, respectively. This marks the most upstream point of the region of the CRZ described in Figure 5. Taking together, it can be concluded that a CRZ is established for the configurations where in which $\theta_j \geq 10^\circ$.

It is also worth noting that an increase in θ_j from 10° to 15° causes a significant upstream movement of saddle point for a given value of α_j. This progression is important because where the saddle point to move too far upstream, it would risk transporting hot gases through the aperture and even into the secondary concentrator, which would lead to large convective heat losses. Importantly, the present configurations avoid this condition although some differences may occur between the reacting and non-reacting cases.

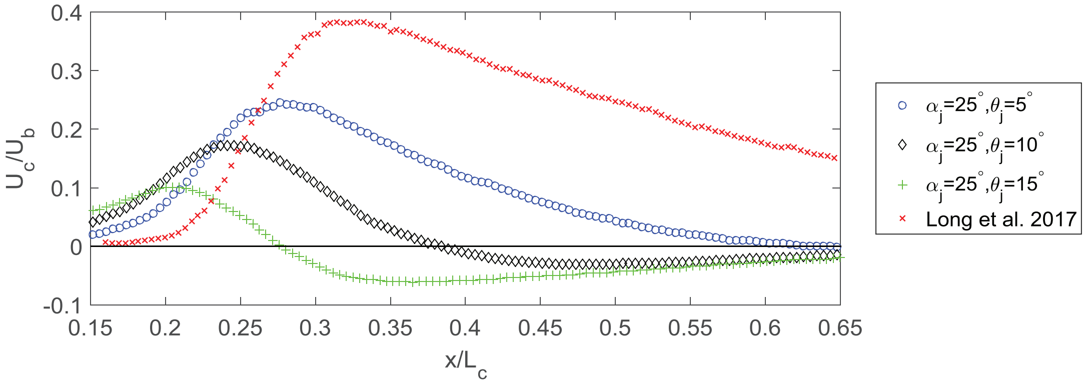

Figure 6. Evolution of the mean axial velocity (U_c/U_b) along the centreline of the experimental models normalised by the inlet velocity, as a function of the axial distance through the chamber for the cases (a) $\alpha_j = 25^{\circ}$ and $\theta_j = 5^{\circ}$ (HSRC-25-5), (b) $\alpha_j = 25^{\circ}$ and $\theta_j = 10^{\circ}$ (HSRC-25-10) and (c) $\alpha_j = 25^{\circ}$ and $\theta_j = 15^{\circ}$ (HSRC-25-15).

Figure 7 presents the radial profiles of the measured mean axial velocity, normalised by the inlet velocity (U_x/U_b) at four axial distances along the chamber for the cases (a) HSRC-25-5, (b) HSRC-25-10 and (c) HSRC-25-15. It can be seen that, for HSRC-25-5, significant positive velocity peak is found upstream from the impingement point (x/L_c = 0.19), while a central resulting jet with single velocity peak occurs downstream from the impingement point. The positive velocity peak at x/L_c = 0.19 for the case of HSRC-25-10 is less significant than that of HSRC-25-05, while the magnitude is reduced by 40%. For the case of HSRC-25-15, the velocity peak at x/L_c = 0.19 is no longer exist, which indicates that the extent of asymmetry increased with an increase of θ_j.

Figure 7 also shows that there are regions of negative axial velocity in the outer region of the chamber ($|r/D_c| > 0.3$) for all cases. This implies the presence of a large-scale external recirculation zone (ERZ) within the main cavity. In addition, the profiles of negative axial velocity in the inner region ($|r/D_c| < 0.3$) are only measured for the cases of HSRC-25-10 and HSRC-25-15, which in turn suggests that a CRZ exists for higher θ_j configurations ($\theta_j \geq 10^{\circ}$) of the HSRC, consistent with qualitative features in Figure 5.

It is also important to note that, for the case of HSRC-25-15, the CRZ region occurs from x/L_c = 0.28 to downstream locations, which indicates that an upstream progression of negative velocity profiles occurs with an increase in θ_j, consistent with Figure 5 and Figure 6.

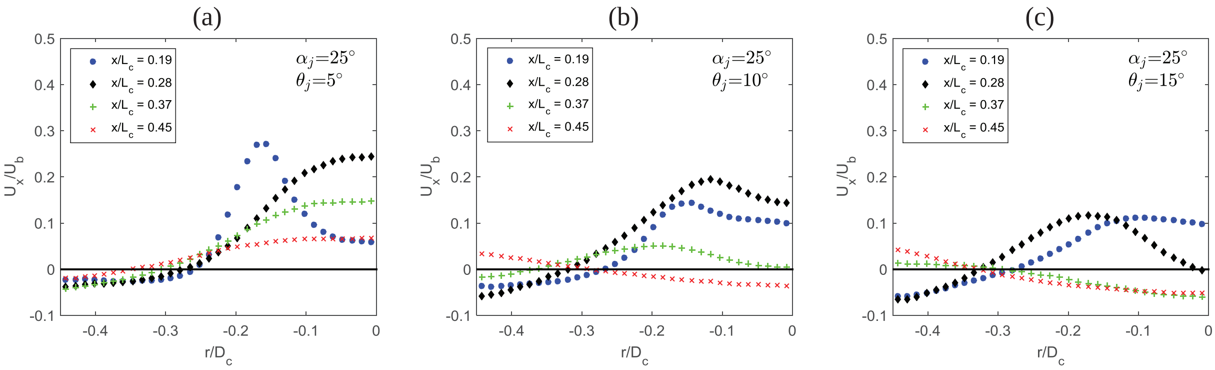

Figure 7. Radial profiles of measured mean axial velocity (U_x/U_b) at four cross-sections through the experimental models for (a) $\alpha_j = 25^\circ$ and $\theta_j = 5^\circ$ (HSRC-25-5), (b) $\alpha_j = 25^\circ$ and $\theta_j = 10^\circ$ (HSRC-25-10) and (c) $\alpha_j = 25^\circ$ and $\theta_j = 15^\circ$ (HSRC-25-15).

Figure 8 presents schematic diagrams of the measured and calculated streamlines for the dominant flow regimes that have been identified within the HSRC configuration for the cases (a) HSRC-25-5, (b) HSRC-25-10 and (c) HSRC-25-15.

For the case $\alpha_j = 25^\circ$ and $\theta_j = 5^\circ$ (HSRC-25-5), it can be seen that the flow regime is characterised by a merged central jet within the upstream half of the chamber, together with a dominant external recirculation zone (ERZ), which runs almost the full length of the chamber. Importantly, the ERZ also extends upstream from the burners, so may present a potential risk for convective heat losses through the aperture. The impingement point is observed downstream from the conical chamber, consistent with the non-swirling case. At the downstream end of the chamber, close to the centerline of the chamber, a negative bifurcation is observed in the modelled flow, although its presence still needs to be confirmed with experiments. This leads to the generation of a central vortex region at the end of the chamber. A low-velocity swirling flow region is also observed downstream from the negative bifurcation. This swirling flow has potential to augment mixing and heat transfer within the chamber.

For the case $\alpha_j = 25^\circ$ and $\theta_j = 10^\circ$ (HSRC-25-10), it can be seen that a saddle point can be seen in the central region of the chamber, which is attributed to slight asymmetry of the jets. An ERZ is also observed within the chamber, although its size is reduced relative to the HSRC-25-5. Downstream from the saddle point, a significant reverse flow is observed, while the downstream CRZ and swirling flow are larger than for HSRC-25-5.

For the further increase in the value of θ_j to 15°(HSRC-25-15), the key flow features within the HSRC remain the same, although their relative significance changes. The ERZ is now confined to the upstream region of the chamber, while CRZ dominates, together with the subsequent swirling flow region dominates 2/3 of the total HSRC chamber. This suggests that this configuration will generate substantial transport of gases from downstream to upstream and perhaps, even through the aperture to the secondary concentrator. Therefore, the heat losses from this system may increase significantly for the case in which the HSRC is operated with an 'open-aperture' in the mixed mode regime.

(a)

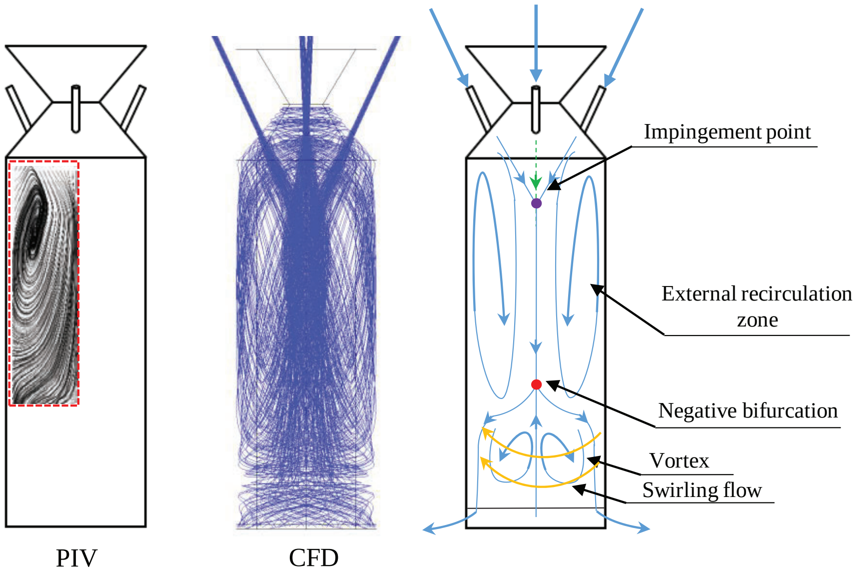
Impingement point
External recirculation zone
Negative bifurcation
Vortex
Swirling flow
PIV
CFD

(b)

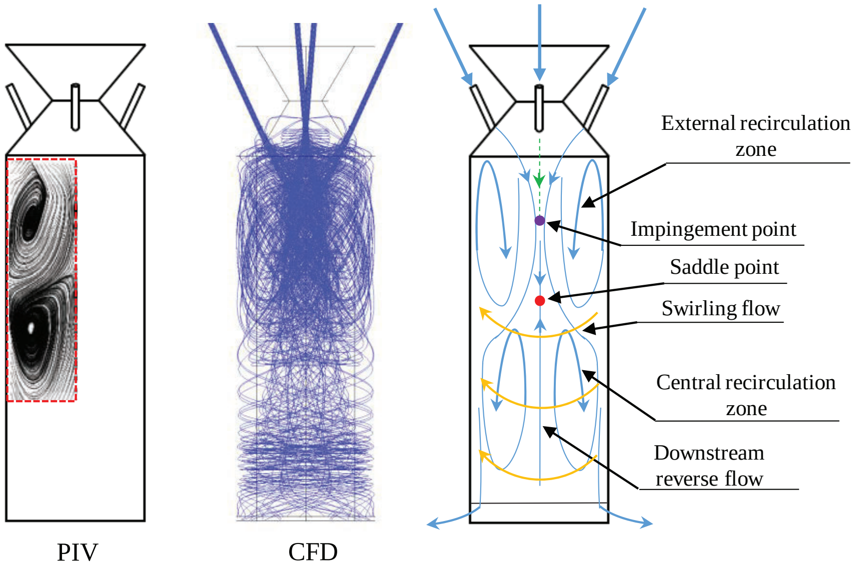
External recirculation zone
Impingement point
Saddle point
Swirling flow
Central recirculation zone
Downstream reverse flow
PIV
CFD

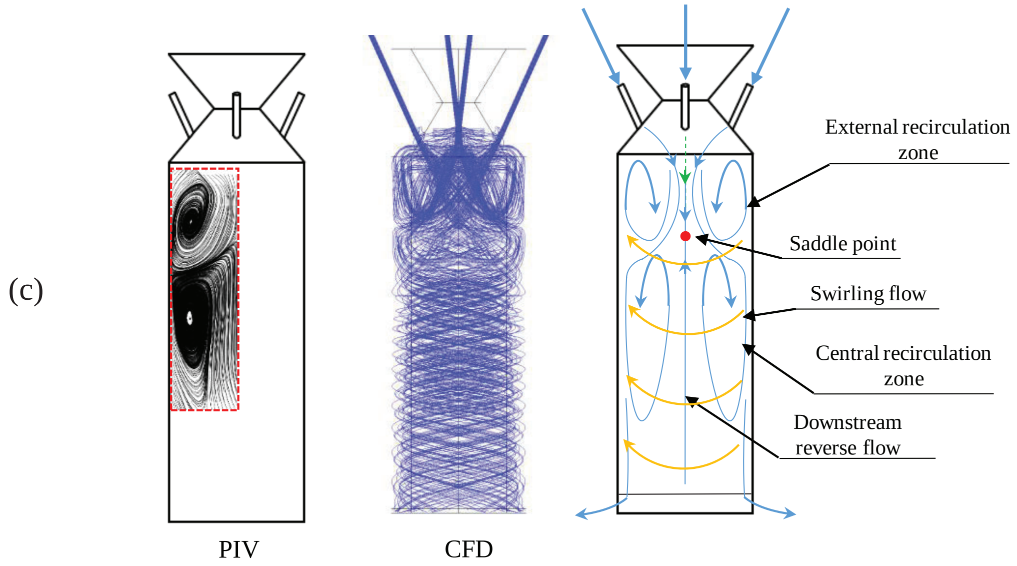

Figure 8. Simplified diagrams showing the main flow features within the Hybrid Solar Receiver Combustor (HSRC) for (a) $\alpha_j = 25^{\circ}$ and $\theta_j = 5^{\circ}$ (HSRC-25-5), (b) $\alpha_j = 25^{\circ}$ and $\theta_j = 10^{\circ}$ (HSRC-25-10) and (c) $\alpha_j = 25^{\circ}$ and $\theta_j = 15^{\circ}$ (HSRC-25-15), as generated with the CFD and PIV results.

4. Conclusions

A joint experimental and numerical study was carried out to characterise the iso-thermal flow behaviour within a Hybrid Solar Receiver Combustor configured with four jets, inclined at $\alpha_j = 25^{\circ}$ and swirling components ($\theta_j = 5^{\circ}, 10^{\circ}, 15^{\circ}$). The key outcomes of the study are as follows:

1. The characteristics of the flow field for the current HSRC configuration exhibit a primary dependence on the azimuthal angles (θ_j). An increase in azimuthal angle (θ_j) from 5° to 15° leads to the increase of the swirl intensity within the chamber, which changes the position and strength of external recirculation zone (ERZ) and central recirculation zone (CRZ).
2. An increase in azimuthal angle (θ_j) from 5° to 15° generates a low-velocity swirling flow region downstream from the bifurcation (saddle point), which is typically sought after for applications such as MILD (Moderate or intense low-oxygen dilution) combustion.
3. For $\theta_j = 15^{\circ}$, the flow field is dominated with central recirculation zone (CRZ), reverse flow and swirling flow. The strength of the CRZ in this region is significant, and has potential to risk transporting fluid through the aperture. The significance needs further analysis.

References

Cavaliere, A & de Joannon, M 2004, 'Mild Combustion', *Progress in Energy and Combustion Science*, vol. 30, no. 4, //, pp. 329-366.

Chen, HJ, Moshfegh, B & Cehlin, M 2012, 'Numerical investigation of the flow behavior of an isothermal impinging jet in a room', *Building and Environment*, vol. 49, 3//, pp. 154-166.

Christoff, P 2016, 'The promissory note: COP 21 and the Paris Climate Agreement', *Environmental Politics*, vol. 25, no. 5, pp. 765-787.

Desideri, U & Campana, PE 2014, 'Analysis and comparison between a concentrating solar and a photovoltaic power plant', *Applied Energy*, vol. 113, pp. 422-433.

Long, S, Lau, TCW, Chinnici, A, Tian, ZF, Dally, BB & Nathan, GJ 2017, 'Experimental and numerical investigation of the iso-thermal flow characteristics within a cylindrical chamber with multiple planar-symmetric impinging jets', *Physics of Fluids*, vol. 29, no. 10, p. 105111.

Moore, J & Apt, J 2013, 'Can hybrid solar-fossil power plants mitigate CO2 at lower cost than PV or CSP?', *Environmental Science & Technology*, vol. 47, no. 6, pp. 2487-2493.

Nathan, GJ, Battye, D & Ashman, P 2014, 'Economic evaluation of a novel fuel-saver hybrid combining a solar receiver with a combustor for a solar power tower', *Applied Energy*, vol. 113, pp. 1235-1243.

Nathan, GJ, Dally, BB, Ashman, P & Steinfeld, A 2013, 'A hybrid receiver-combustor', Provisional Patent Application No. 2012/901258., Adelaide Research and Innovation Pty. Ltd.; 2012 [Priority Date: 29.03.2].

Nathan, GJ, Jafarian, M, Dally, BB, Saw, WL, Ashman, PJ, Hu, E & Steinfeld, A 2017, 'Solar thermal hybrids for combustion power plant: A growing opportunity', *Progress in Energy and Combustion Science*, 2017/10/04/.

Tian, ZF, Nathan, GJ & Cao, Y 2015, 'Numerical modelling of flows in a solar–enhanced vortex gasifier: Part 1, comparison of turbulence models', *Progress in Computational Fluid Dynamics, an International Journal*, vol. 15, no. 2, pp. 114-122.

Vanierschot, M & Van den Bulck, E 2008, 'Influence of swirl on the initial merging zone of a turbulent annular jet', *Physics of Fluids*, vol. 20, no. 10, p. 105104.

Acknowledgements

The authors would like to acknowledge the support of the Australian Research Council, FCT Combustion Pty. Ltd. and Vast Solar Pty. Ltd. through the ARC Linkage grant LP110200060. The first author would like to thank the financial support of Australian Government Research Training Program.

Appendix D：The Effect of Aspect Ratio on the Flow Characteristics of a Hybrid Solar Receiver Combustor

21st Australasian Fluid Mechanics Conference
Adelaide, Australia
10-13 December 2018

The effect of aspect ratio on the flow characteristics of a Hybrid Solar Receiver Combustor

S. Long[1], T.C.W. Lau[1], A. Chinnici[1], Z.F. Tian[1], B.B. Dally[1], G.J. Nathan[1]

[1] Centre for Energy Technology, School of Mechanical Engineering
The University of Adelaide, Adelaide, South Australia 5005, Australia.

Abstract

We present a systematic experimental study of the interaction between four rotationally-symmetric jets within a cylindrical chamber, under conditions relevant to a wide range of practical applications, including the Hybrid Solar Receiver Combustor (HSRC). The HSRC geometry is simplified here to a cylindrical cavity with four inlet jets (representing four burners), which are configured in an annular arrangement and aligned at an inclination angle (α_j) to the axis with a tangential component (azimuthal angle θ_j) to generate a swirl in the chamber. In this study, we assess the configurations of $\alpha_j = 25^\circ$ and $\theta_j = 5^\circ$. The length of the chamber was varied from $L_c = 148$ mm to 74 mm and the diameter of the chamber was $D_c = 74$ mm, resulting in an aspect ratio of $L_c/D_c = 2$, 1.5 and 1. The inlet Reynolds number for each injected jet and the number of jets were fixed at $Re_D = 10{,}500$ and 4, respectively. Velocity data obtained with Particle Image Velocimetry (PIV) were used to characterise the large-scale flow field within the selected experimental configurations. The results reveal a significant dependence of the mean flow-field on the aspect ratio L_c/D_c for the value of α_j and θ_j considered here. More specifically, it was found that L_c/D_c can influence the position of the external recirculation zone (ERZ), the strength of the central resulting jet, and the recirculation rate (K_v).

Introduction

Multiple jets have been widely used in many practical applications as solar receiver reactors [9], gas turbine engines [5], longitudinal ventilation systems [3] and separated-jet combustors [1]. However, the greater complexity of these configurations over the single round jet issuing into a quiescent environment [8], including the additional parameters and experimental challenges, means many gaps in understanding remain. Of particular interest here are the configurations featuring multiple-jets relevant to the Hybrid Solar Receiver Combustor (HSRC) under development at the University of Adelaide [3,4,10,11,12,13]. The HSRC offers potential to reduce both the energy losses and total infrastructure requirements relative to a hybrid from stand-alone components, while providing a firm supply of energy for heat and power applications. The geometry of a typical HSRC (Figure 1) features a cavity that is operable as either a cavity receiver or a combustion chamber equipped multiple burners to direct fuel and air into the main cavity, and tubular heat exchangers to transfer the thermal energy to the heat transfer fluid. The burners are configured in an annular ring arrangement and aligned at an inclination angle (α_j) relative to the axis of the cavity, and/or at an azimuthal angle (θ_j) to the axis of the burner, resulting in a swirling flow within the main cavity. This burner arrangement, referring to the conditions where both $\alpha_j > 0^\circ$ and $\theta_j > 0^\circ$, is termed "rotationally-symmetric". Previous investigations of the flow-fields within the HSRC revealed a significant dependence of the jet angles (α_j and θ_j) on the strength and position of the large-scale recirculation which is critical for achieving flow conditions conducive for efficient receiver operation [11,12]. Nevertheless, the dependence of the geometrical parameters, such as the length (L_c) and diameter (D_c) of the chamber, on important flow characteristics remains unknown, although relevant studies have found that the aspect ratio of L_c/D_c is critical for maintaining high thermal efficiency with low infrastructure costs [10, 13]. Hence, a comprehensive understanding of the effect of aspect ratio L_c/D_c is needed to characterize the flow-fields of multiple jets.

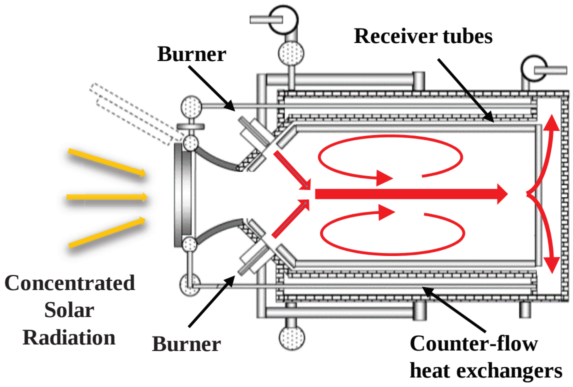

Figure 1. Hybrid Solar Receiver Combustor

Previous studies of flow-fields generated with multiple symmetric jets within a confined space revealed that the flow structure depends strongly on the arrangement and geometric features of jets [1,2,6,11,15,16,17]. However, to our knowledge, little or no information is available for the key geometrical parameters (e.g., L_c and D_c) of the confined space for multiple jets configurations. In addition, our previous work Long et al [12] revealed the presence of an external recirculation zone (ERZ) within a cylindrical chamber. The ERZ is typically associated with the recirculation rate (K_v) within the chamber, which is particularly critical for combustion stabilization and thermal efficiency [18]. However, the influence of L_c/D_c on the recirculation regions is not fully understood.

In light of the needs above, the present paper reports on an experimental investigation of the iso-thermal flow-fields generated with a Multiple Impinging Jets in a Cylindrical Chamber, termed "MIJCC". The aims of the current study are: (a) to identify the influence of the aspect ratio L_c/D_c on the mean flow-fields within a cylindrical chamber with multiple-jets; and (b) to characterize the dependence of the characteristics of large-scale recirculation zones on the aspect ratio L_c/D_c.

Methodology

A schematic diagram of the experimental MIJCC configuration is shown in Figure 2. The cavity of the experimental model consists of a cylindrical chamber with a conical expansion, connected with a secondary concentrator (SC). The geometric parameters are given in Table 1.

The length of the MIJCC chamber were $L_c = 148$ mm, 111 mm and 74 mm, resulting in an aspect ratio of $L_c/D_c = 2$, 1.5 and 1. In addition, the chamber length of our previous work $L_r = 225$ mm, resulting in $L_r/D_c = 3$, was chosen as reference cases for comparison with the present study (labelled with an asterisk in Table 2).

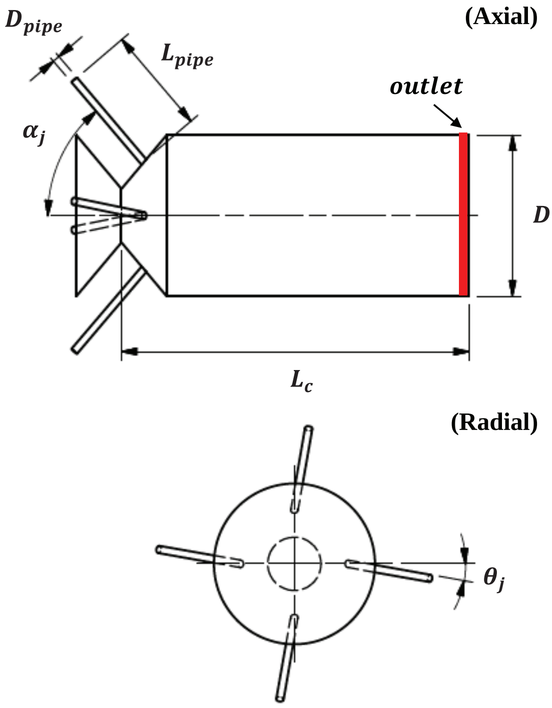

Figure 2. Schematic diagram of the configuration of the Multiple Impinging Jets in a Cylindrical Chamber (MIJCC).

Dimensions	Description	Value
D_c	Chamber diameter	74 mm
L_c	Chamber length	148, 111, 74 mm
L_r	Reference chamber length	225 mm
L_{pipe}	Inlet pipe length	150 mm
D_{pipe}	Inlet pipe diameter	3.35 mm
α_j	Jet inclination angle	25°
θ_j	Jet azimuthal angle	5°

Table 1. Values of the key geometric parameters of the experimental models.

Experimental case No.	Configurations	Confinement aspect ratio, L_c/D_c
1	MIJCC-05-LD20	2
2	MIJCC-05-LD15	1.5
3	MIJCC-05-LD10	1
4*	MIJCC-05-LD30	3

Table 2. The notation for the configurations investigated experimentally in the present study.

Particle Image Velocimetry (PIV) was employed under iso-thermal conditions at ambient temperature, with water as the working fluid to avoid deposition of tracer particles onto confining walls. The entire device was fully submerged into a rectangular water tank to minimize optical distortion. The water from the outlets was discharged into the water tank, which overflowed to a reservoir. The discharged fluid was reinjected through the jets using a water pump, a frequency converter and flowmeters, resulting in a closed-loop system.

The inlet jet bulk injection velocity at the nozzle exit (U_e) was fixed at 2.8 m/s for each nozzle, leading to an inlet jet Reynolds number $Re_D = 10{,}500$. This ensures that the inlet flow is within the fully turbulent regime. The inclined jets were introduced through long straight pipes with a length-to-diameter ratio, $L_{pipe}/D_{pipe} = 46$, which is sufficient to closely approach a fully-developed inflow condition at the exit of the inlet nozzles [14] and thus generate a well-defined inflow condition to the chamber.

The flow was seeded with hollow glass spheres of 12 µm in diameter and with a specific gravity of 1.1. The resultant Stokes number (Sk_D) was estimated to be $Sk_D = 0.003$ (where ρ_p is the particle density). This is sufficiently low to enable the particles to follow the flow down to length scales that can be resolved with the PIV measurement.

The optical arrangement and the measurement region are shown schematically in Figure 3. The source of illumination for the PIV measurements was a double-head, pulsed Nd:YAG laser (Quantel Brilliant B), operating at a fixed pulsing frequency of 10 Hz and a maximum power of approximately 400 mJ. The laser was operated in the frequency-doubled mode to provide a wavelength of 532 nm. The thickness of the light sheet was estimated to be 1.5 mm at the focal line.

The images were captured with a Charged Coupled Device (CCD) camera with an array of 1920 × 1080 pixels, which provides the axial (u) and radial (v) instantaneous velocity components with an image size of 118 mm (L_i) × 66 mm (W_i). A minimum of 3000 PIV images (12 bits) was recorded for each measurement. The image-processing was performed with an in-house PIV code in MATLAB, with an interrogation window size of 32 × 32 pixels, leading to a spatial resolution of 2 mm in each direction. A multi-grid correlation algorithm with 50% overlap was applied to all cases. All erroneous vectors were removed from the ensemble. The overall uncertainty of the mean velocity field was calculated to be 5%.

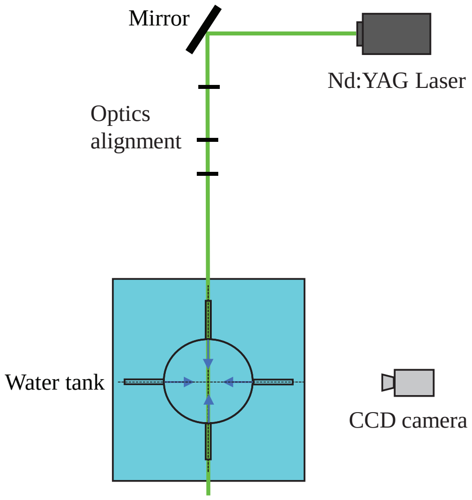

Figure 3. Experimental layout for the PIV measurements, together with the optical arrangement.

Results and discussion

Figure 4 presents the contours of measured mean axial velocity (U_x) normalized by the nozzle exit velocity (U_e), showing the streamlines, labelled with arrows to indicate flow direction (white arrows), and magnitude (colour map) for the configuration of $\alpha_j = 25^\circ$ and $\theta_j = 5^\circ$ with (a) $L_c/D_c = 2$, (b) $L_c/D_c = 1.5$, and (c) $L_c/D_c = 1$. The dashed line (in white colour) denotes the upstream end of the exit plane. It can be seen that a central resulting jet flow (enclosed with red dashed box) occurs in all cases downstream from a merging point of the four inlet jets. This resulting jet generates an external recirculation zone (ERZ), whose vortex core is marked with a black "×", running almost the full length of the chamber. It can also be seen that the position of the ERZ depends strongly on the value of L_c/D_c. For example, the axial location of the ERZ vortex-core relative to the throat location, x_{core}, increases from $x_{core}/L_c = 0.36$ to 0.40 and then reduces to $x_{core}/L_c = 0.27$ as L_c/D_c is reduced from 2 to 1 [Fig. 4(a), (b) and (c), respectively], with the distance between the ERZ vortex-core and the bluff end-wall reduces to $x_{end}/L_c \approx 0.09$ at $L_c/D_c = 1.5$ and remains approximately the same for $L_c/D_c = 1$. In addition, this decrease in L_c/D_c also increases the radial location of the ERZ core from $r_{core}/D_c = 0.28$ at $L_c/D_c = 2$ to $r_{core}/D_c = 0.4$ at $L_c/D_c = 1$. These findings are attributed to the effect of jet impingement on the bluff end-wall that influences the development of the resulting jet flow, and is consistent with previous studies with an unconfined single jet [7].

The results in Figure 4 also show that a reduction in L_c/D_c leads to ≈ 30% increase in the velocity magnitude of the jets upstream from the merging point (above the red dashed-box). This is attributed to the reduced flow oscillation at and upstream from the merging point as L_c is decreased. That is, a shorter length of the chamber tends to restrict both the "in-plane" and "out-of-plane" motion of the four inlet-jets, which in turn inhibits the flow oscillation associated with the interaction between inlet-jets.

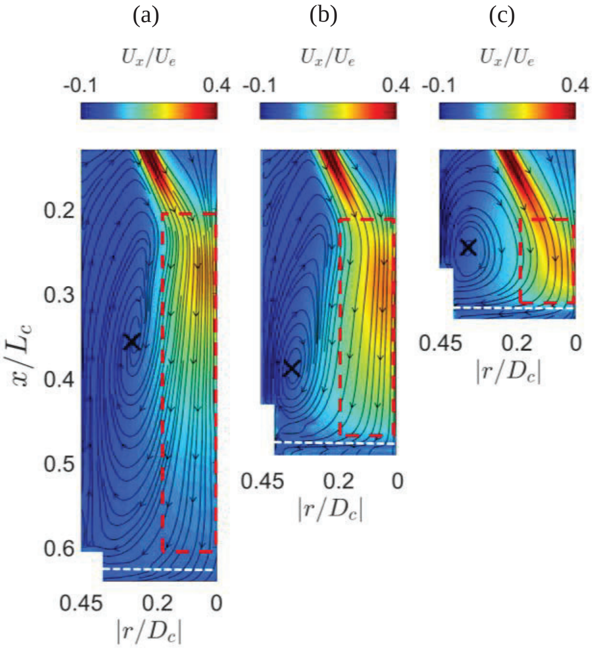

Figure 4. Mean axial velocity (U_x) normalized by the bulk mean jet exit velocity (U_e), showing the streamlines, labelled with arrows to indicate flow direction (black arrows), and magnitude (colour map), for (a) $L_c/D_c = 2$, (b) $L_c/D_c = 1.5$, and (c) $L_c/D_c = 1$.

Figure 5 presents the evolution of dimensionless mean axial velocity (U_c/U_e) along the axis of the MIJCC device for all investigated conditions. The PIV data from our previous work [12] of $L_c/D_c = 3$ is also included. The dotted lines refer to the locations of the bluff end-wall. We define the jet merging point, P_{mer}, to be the location of the maximum mean axial velocity along the centreline of the chamber [$(U_c/U_e)_{max}$]. It can be seen that $(U_c/U_e)_{max} \approx 0.25$ at $x/L_r = 0.27$ for all cases, implying that L_c/D_c does not change the location of the merging point or its corresponding velocity magnitude. However, downstream from P_{mer}, the evolution of U_c/U_e is strongly influenced by L_c/D_c. For example, as L_c/D_c reduces from 2 to 1.5, the decay rate of U_c/U_e decreases significantly. This is possibly caused by the effect of end-wall on the development of resulting jet that reduces the entrainment rate between the jet and surrounding fluids. Importantly, for $L_c/D_c = 1$ where the bluff end-wall closely approaches the location of P_{mer}, the central resulting jet is almost absent [also see Fig 4(c)] due to the confinement effect from the cylindrical walls, while the decay of U_c/U_e is the highest for all cases. Hence, it can be concluded that the aspect ratio of L_c/D_c significantly inhibits the axial development of the central resulting jet for $L_c/D_c < 2$.

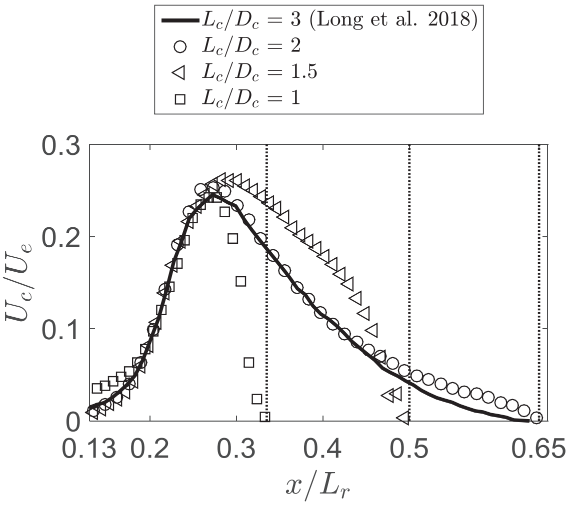

Figure 5. Evolution of mean axial velocity along the centerline of the Multiple Impinging Jets in a Cylindrical Chamber (MIJCC), normalized by the bulk mean velocity (U_c/U_e) as functions of chamber length for all experimental cases. For clarity, the figure only presents one in two data points.

Figure 6 presents the effect of L_c/D_c on the recirculation rate ($Kv = \dot{m}_{ent}/\dot{m}_{in}$) within the MIJCC configurations. Here $\dot{m}_{ent} = \int_0^\infty 2\pi r\rho U_{ent}\, dr$ is the total mass flow rate of fluid transported upstream through a plane orthogonal to the axis at the plane x/L_c, while $\dot{m}_{in}$ refers to the total inlet mass flow rate of fluid. The entrainment velocity, U_{ent}, is the negative axial velocity ($U_x < 0$) within the chamber. It can be seen that a single hump profile, approximately corresponding with the axial extent of the ERZ, occurs for all cases, while the location of the peak value of K_v [$(K_v)_{max}$] coincides well with the location of the vortex-core in the ERZ (x_{core}). For $L_c/D_c = 2$ to 1.5, a decrease in L_c/D_c leads to a decrease in the axial extent of K_v throughout the chamber ($x/L_r = 0.13$ to 0.65), although the magnitude of $(K_v)_{max}$ for these two cases remains the same (occurring at $x/L_r = 0.38$). However, as L_c/D_c is further decreased to $L_c/D_c = 1$, the value of $(K_v)_{max}$ increases significantly (~ 25%) and its location moves further upstream to $x/L_r = 0.2$ due to the confinement effect caused by the chamber length. Hence, the axial profile of K_v appears similar for $L_c/D_c \geq 2$, while as L_c is further reduced to 1, the value and distribution of K_v is strongly restricted by the chamber length and bluff end wall.

The results in Figure 6 also shows that the value of $(K_v)_{max}$ exceeds 3 for all cases considered here. This finding is important for the development of practical combustion applications, particularly those employing combustion in the MILD (moderate or intense low-oxygen dilution) regime [18]. This is because the value of $K_v = 3$, in addition to the presence of a large and uniform recirculation zone, is crucial for achieving desirable mixing, heat transfer and quasi-homogeneous temperature distribution for applications employing MILD (such as the HSRC).

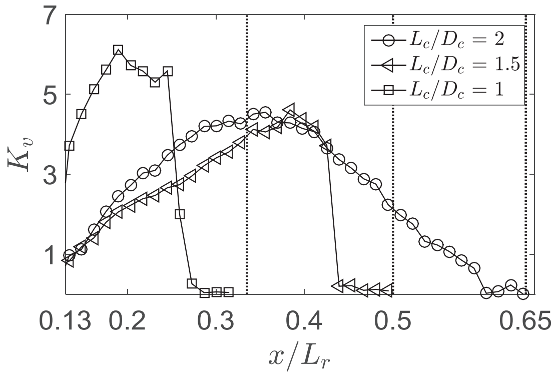

Figure 6. Evolution of the recirculation rate (K_v) along the centerline of the Multiple Impinging Jets in a Cylindrical Chamber (MIJCC) as a function of the normalized reference chamber length (x/L_r).

Conclusions

An experimental study was carried out to investigate the iso-thermal flow field within a cylindrical chamber featuring multiple-jets with an inclination angle $\alpha_j = 25^\circ$ and an azimuthal angle $\theta_j = 5^\circ$. The aspect ratio of chamber length to diameter (L_c/D_c) from 2 to 1 was assessed in the present study. The key outcomes of the study are as follows:

1. For a given value of D_c, the mean velocity field depends strongly on the value of L_c as L_c/D_c is reduced from 2 to 1. This causes a significant reduction in the axial location and the velocity magnitude of the external recirculation zone (ERZ).
2. A decrease in L_c/D_c from 2 to 1 was found to increase 30% of the velocity magnitude near to the merging point, which highlights the reduction in the large-scale oscillations as L_c/D_c is reduced.
3. The maximum value of the recirculation rate of the ERZ (K_v) was found to increase by 25% as L_c/D_c reduces from 2 to 1, with the axial extent of K_v reduces 50%.
4. The value of K_v exceeds 3 for all cases, which is crucial for achieving desirable mixing, heat transfer and quasi-homogeneous temperature for solar thermal applications utilising combustion in the MILD regime.

Acknowledgments

The authors would like to acknowledge the support of the Australian Research Council, FCT Combustion Pty. Ltd. and Vast Solar Pty. Ltd. through the ARC Linkage grant LP110200060. Mr. Shen Long acknowledges the financial support of the Australian Government Research Training Program.

References

[1] Boushaki, T. & Sautet, J.C., Characteristics of flow from an oxy-fuel burner with separated jets: influence of jet injection angle. *Exp. Fluids*, **48**, 2010, 1095-1108.

[2] Chammem, T., Mhiri, H. & Vauquelin, O., Experimental and computational investigation of Reynolds number effect on the longitudinal ventilation in large enclosure of twin inclined jets. *Build. Environ*., **67**, 2013, 87-96.

[3] Chinnici, A., Tian, Z.F., Lim, J.H., Nathan, G.J. & Bassam, B.B., Comparison of system performance in a hybrid solar receiver combustor operating with MILD and conventional combustion. Part I: Solar-only and combustion-only employing conventional combustion." *Sol. Energy,* **147**, 2017, 489-503.

[4] Chinnici, A., Tian, Z.F., Lim, J.H., Nathan, G.J. & Bassam, B.B., Comparison of system performance in a hybrid solar receiver combustor operating with MILD and conventional combustion. Part II: Effect of the combustion mode. *Sol. Energy,* **147**, 2017, 479-488.

[5] Cox, G., Multiple jet correlations for gas turbine engine combustor design. *J. Eng. Power,* **98**, 1976, 265-272.

[6] Gao, Z., Han, J., Xu, Y., Bao, Y. & Li, Z., Particle image velocimetry (PIV) investigation of flow characteristics in confined impinging jet reactors. *Ind. Eng. Chem. Res.,* **52**, 2013,11779-11786.

[7] Guo, T., Rau, M.J, Vlachos, P.P. & Garimella, S.V., Axisymmetric wall jet development in confined jet impingement. *Phys. Fluids,* **29**, 2017, 025102.

[8] Hussein, H. J., Capp, S.P. & George, W.K., Velocity measurements in a high-Reynolds-number, momentum-conserving, axisymmetric, turbulent jet. *J. Fluid Mech.,* **258**, 1994, 31-75.

[9] Koepf, E., Villasmil, W. & Meier, A., High Temperature Flow Visualization and Aerodynamic Window Protection of a 100-kW th Solar Thermochemical Receiver-reactor for ZnO Dissociation. *Energy Procedia,* **69**, 2015, 1780-1789.

[10] Lim, J. H., Nathan, G.J., Hu, E. & Bassam, B.B., Analytical assessment of a novel hybrid solar tubular receiver and combustor. *Appl. Energy,* **162**, 2016, 298-307.

[11] Long, S., Lau, C.W.T., Chinnici, A., Tian, Z.F., Bassam, B.B. & Nathan, G.J., Experimental and numerical investigation of the iso-thermal flow characteristics within a cylindrical chamber with multiple planar-symmetric impinging jets. *Phys. Fluids,* **29**, 2017, 105111.

[12] Long, S., Lau, C.W.T., Chinnici, A., Tian, Z.F., Bassam, B.B. & Nathan, G.J., Iso-thermal flow characteristics of rotationally symmetric jets generating a swirl within a cylindrical chamber. *Phys. Fluids,* **30**, 2018, 055110.

[13] Nathan, G.J., Battye, D.L. & Ashman, P.J., Economic evaluation of a novel fuel-saver hybrid combining a solar receiver with a combustor for a solar power tower. *Appl. Energy,* **113**, 2014, 1235-1243.

[14] Nikuradse, J., Gesetzmäßigkeiten der turbulenten Strömung in glatten Rohren. *Forsch. Geb. Ingenieurwes.,* **4**, 1933, 44-44.

[15] Tanaka, E. , The interference of two-dimensional parallel jets: 1st report, experiments on dual jet. *Bull. JSME,* **13**, 1970, 272-280.

[16] Tanaka, E. , The interference of two-dimensional parallel jets: 2nd report, experiments on the combined flow of dual jet. *Bull. JSME,* **17**, 1974, 920-927.

[17] Tanaka, E. & Nakata, S., The Interference of Two-Dimensional Parallel Jets: 3rd Report, The Region near the Nozzles in Triple Jets. *Bull. JSME,* **18**, 1975, 1134-1141.

[18] Wünning, J.A. & Wünning, J.G., Flameless oxidation to reduce thermal NO-formation. *Prog. Energy Combust. Sci.,* **23**, 1997, 81-94.